An Investigation of the Interaction Between Graphene and Hydrated Ions

A dissertation presented

by

Donald George Dressen II

to

The Committee on Higher Degrees in Biophysics

in partial fulfillment of the requirements

for the degree of

Doctor of Philosophy

in the subject of

Biophysics

Harvard University

Cambridge, Massachusetts

May 2016

Dissertation Advisor:
Professor Jene Golovchenko

Author:
Donald George Dressen II

An Investigation of the Interaction Between Graphene and Hydrated Ions

Abstract

The ability of graphene and carbon nanotubes to generate an electric potential from flowing fluids has attracted much interest [1–7]. The effect is thought to occur because certain ionic and molecular species bind to the surface of these materials more strongly than others. Although several physical models have been proposed, none has yet been rigorous enough to be confirmed by experiment [4, 6, 7]. In this work, I describe an electromechanical device, *i.e.* a supercapacitive electrical energy generator (SCEEG) made with graphene electrodes, that generates electricity from oscillating droplets of electrolyte solutions and ionic liquids. I provide a theoretical model of how the graphene SCEEG (G-SCEEG) works that quantitatively agrees with experimental results. More importantly, the model allows one to characterize electrochemically-useful properties of the interaction between graphene and hydrated ions from the device's experimentally measured output. The identity of the ions that preferentially adsorb to graphene as well as the effective surface density and effective binding energy of these ions can all be determined using the G-SCEEG. Additionally, both the capacitance per unit area and the surface potential of the graphene-solution interface can also be determined.

Although this work focuses on a SCEEG device whose electrodes are made from graphene, the electrodes can, in principle, be made from any conductive material, *e.g.* metals, such as gold, and semiconductors, such as indium-tin-oxide [8]. All SCEEGs described in this thesis, however, work by exchanging charge between two supercapacitors, *i.e.* capacitors that spontaneously form at the interface between an electrode and an electrolyte solution (or ionic liquid) as a result

of ionic adsorption. Charge exchange occurs not by charging and discharging these interfacial capacitors but instead by increasing and decreasing their capacitance. This is accomplished mechanically as a moving droplet wets and dewets the electrodes. The changing interfacial capacitance acts as a source of current; the flow of current through the device's internal impedance creates an electric potential; and, when connected to an external load, the SCEEG is then capable of generating electric power.

I show that a G-SCEEG can generate a peak power of up to $7\ \mu$W from the oscillatory motion of two $20\ \mu$L droplets of 6.0 M HCl. I demonstrate that the device can be successfully modeled as a source of alternating current that is in parallel with a time-varying internal impedance. Using this model and the G-SCEEG's output, I determine that the chloride anions in 6.0 M HCl adsorb to graphene with the greatest effective surface density (5.6×10^{12} ions/cm^2) and induce in it the largest charge density (900 nC/cm^2) of all the solutions I studied. These chloride anions adsorb to graphene with an effective binding energy of 350 meV, in turn producing an electric potential of 690 mV at the graphene-solution interface. I also find that the density and the sign of the surface charge induced in graphene are dependent on the ionic species present in each solution, the concentration and pH of the solution, and the presence of multi-layers in the graphene electrodes with the solution's pH providing the greatest effect.

Finally, I describe in this dissertation the study of the Raman spectral properties of suspended mono- and multi-layer graphene membranes and the use of graphene and graphite to electrostatically trap DNA from an aqueous solution. I conclude by explaining the unique methods I developed during the course of this work including the synthesis of large-grain graphene using chemical vapor deposition (CVD) and the transfer of large areas of CVD-grown graphene to hydrophobic substrates.

Contents

Listing of figures

List of Tables

To all those who have pushed me to see the universe through different eyes.

... The only true voyage of discovery, the only fountain of Eternal Youth, would be not to visit strange lands but to possess other eyes, to behold the universe through the eyes of another, of a hundred others, to behold the hundred universes that each of them beholds, that each of them is...

– Marcel Proust

Acknowledgments

To successfully practice the art of science one must stand on the shoulders of the giants who came before him, be they those of scientists or otherwise. Throughout the duration of this dissertation I have enjoyed the support of many broad shoulders. I owe a debt of gratitude to the advisors, mentors, teachers, colleagues, friends, and family who prepared me for and accompanied me along this journey. I am forever grateful for the roles, big and small, that they played in this accomplishment.

A special thanks goes to my advisor, Professor Jene Golovchenko, for having the confidence in me to allow me to develop and explore my own ideas, even if they often ended in failure. Above all he taught me to embrace the challenges associated with solving difficult scientific problems and to rigorously question my own assumptions. I would like to thank Professors Lene Vestergaard Hau and Daniel Branton for being avid proponents of efficient and cogent scientific thought and communication. Their feedback and guidance were instrumental in my development as a scientist. I also thank the other members of my committee, Professors Adam Cohen and Hector Abruña, for their guidance and inspiration. Further, I thank Michael Burns, Stanley Cotreau, Alessandra Ferzoco, and James MacArthur for sharing their time, expertise, and equipment with me.

My friends and colleagues in the Golovchenko and Hau groups, past and present, helped me cope with the hardships of experimental science and provided me with timely comedic relief. I owe special thanks to Lu Bo, Fernando Albertorio, Tommi Hakala, Jules Gardener, Christopher Russo, David Hoogerheide, Anpan Han, Dimitar Vlassarev, Slaven Garaj, Rui Zhang, Jesse Crossno, Tony Zhou, Ryan Rollings, Andrew Mutter, Aaron Kuan, Tamas Szalay, Edlyn Levine, Gaku Nagashima, Stephen Fleming, Peter Frisella, Ray Aubut, Eric Brandin, and Jane Salant. Eric Brandin deserves extra recognition for helping me to construct, and then to survive, some of my more dangerous experiments.

I have been humbled by the generosity of the Ashford Family and their commitment to the fellows they support. I thank them for believing in me.

I want to thank Michele Jakoulov and Professor James Hogle for treating me like family. The Harvard Biophysics Program is a first-class scientific training program because of their dedication.

I count Mauricio Carneiro and Pan-Pan Jiang among my closest friends, and I thank them for their unwavering support and enthusiasm.

Beth, Kirk, and Brooke have always been a source of happiness and love. I am forever indebted to them for their continued confidence in me. I thank my parents for being my first and most important teachers. They showed me the value of hard work and the power of curiosity. And finally to my incredible wife Ally, I owe the most gratitude. I could not have done it without her love.

WISE MEN IN THEIR BAD HOURS

Wise men in their bad hours have envied
The little people making merry like grasshoppers
In spots of sunlight, hardly thinking
Backward but never forward, and if they somehow
Take hold upon the future they do it
Half asleep, with the tools of generation ...

– Robinson Jeffers

1

Introduction

1.1 Motivation: From sequencing DNA to generating electricity

As unrelated as it may seem, the work described in this dissertation originated with the goal of trying to sequence DNA with a graphene nanopore. The hope was to find a way to electrostatically control the motion a molecule of DNA as it moved along the surface of graphene and towards a nanopore in the graphene's lattice. A nanopore is a nanometer-scale aperture that is either created in a thin, free-standing membrane of a solid-state material or that exists naturally in a transmembrane protein. To date nanopores have been heavily investigated as a means to detect

individual biological molecules and, more recently, have become the basis for the next-generation of DNA sequencing technology.

Although the cost of sequencing DNA continues to decrease rapidly, current sequencing technologies are still plagued by slow sequencing rates, short read lengths, and the need for costly reagents and extensive computational analyses [9]. A DNA sequencing device based on electrophoretically driving individual molecules of single-stranded DNA through a nanopore promises to solve these problems by directly detecting an electric signal for each nucleotide as it passes through the pore [9]. Much progress has been made recently in using nanopore-containing transmembrane proteins, *i.e.* biopores, in such devices and commercial biopore sequencing instruments are currently under development [10–13]. Despite this technological achievement, nanopores fabricated from solid-state materials offer several important advantages. They are more amenable to large-scale fabrication using well-established micro- and nano-fabrication methods and are more stable over a wide range of environmental conditions [9]. Additionally, two-dimensional solid-state materials such as graphene, hexagonal boron nitride, and molybdenum disulfide are especially attractive because their atomic thickness provides the highest spatial resolution for detecting individual nucleotides. Graphene nanopores in particular have been the focus of much experimental work [14, 15].

Graphene is a two-dimensional, zero-gap semiconductor (also known as a semimetal) made of carbon and has generated significant interest because of its exceptional electric, thermal, and mechanical properties [16]. The ability of graphene to exist as a freestanding membrane despite being only a single atom thick makes it particularly well-suited for studying single molecules using nanopores. Although it has been theoretically calculated that the atomic thickness of a graphene nanopore can provide sufficient spatial resolution to distinguish between neighboring nucleotides in DNA [14], the temporal resolution of the current amplifier used to detect the electric signal is still orders of magnitude too slow to resolve adjacent nucleotides. Attempts to overcome this lim-

itation by reducing the velocity of the DNA as it moves through, or translocates, the pore have thus far been insufficient [17, 18]. In addition, conformational and diffusional fluctuations by the DNA lead to an undesirable spread in the distribution of translocation times [19]. Both the large temporal uncertainty and the low temporal resolution currently preclude the ability of a graphene nanopore to accurately distinguish between nucleotides.

Electrically controlling the motion of DNA using the graphene membrane surrounding the nanopore was seen as a way to address both the temporal uncertainty and resolution problems. The idea was straightforward: if the DNA-graphene interaction could be made sufficiently strong such that it suppressed conformational and diffusional fluctuations while at the same time still weak enough to allow the DNA to translocate through a nanopore with a controllable velocity then these temporal problems could be solved simultaneously. Additionally, such control would enable DNA to be ratcheted through the pore a single nucleotide at a time and would allow for signal integration over long enough timescales to very accurately identify each nucleotide.

Before the DNA-graphene interaction could be effectively manipulated and controlled, however, the nature of the interaction needed to first be understood. Based on work done by others [20, 21], the interaction between the nucleobases of single-stranded DNA and graphene is thought to be dominated by π-π stacking, resulting in base-dependent adsorption energies of $\simeq 1$ eV. In comparison, the energy needed to translate a nucleobase between adjacent graphene lattice sites was found to be an order of magnitude less, $\simeq 0.1$ eV. This suggests that nucleobases can be confined to a graphene surface while still being able to move in plane. Relatively little is known, however, about the effect that the cyclic deoxyribose and the negatively-charged phosphate moieties of the DNA have on this interaction. In fact, even the nature of the interaction between graphene and water and graphene and simple hydrated ions has yet to be unambiguously resolved [22–24]. Adding further complication, the impact of graphene's supporting substrate on the ability of graphene to interact with molecules and ions is also unresolved [25–27].

In spite of these remaining unknowns, preliminary attempts were made at perturbing the DNA-graphene interaction electrostatically. The aim was to trap DNA on and to repel DNA from the surface of graphene by biasing it relative to a buffer solution. Because DNA has a net negative charge (DNA phosphate groups have a $pK_a \simeq 0$), positive and negative voltages were used to attract and repel the DNA, respectively. Once they were interacting with the graphene surface, DNA molecules were then moved along the surface using electrophoresis. Trapping, repelling, and electrophoresis were each successfully demonstrated using fluorescence microscopy and fluorescently-labeled DNA. However, technical problems including defective and multi-layer graphene, unwanted substrate interactions, and organic-polymer contamination prevented the experiments from providing meaningful quantitative results.

Significant effort was made to solve these technical challenges by developing better experimental protocols. The number of grain-boundary defects, and subsequently the amount of polymer contamination, were decreased by developing a protocol for synthesizing large-grain graphene that was free of multi-layers. More rigorous annealing and cleaning methods were also followed to ensure that the graphene was as free of contaminants as possible. To mitigate unwanted substrate effects a protocol was developed for transferring graphene to a hydrophobic surface.

During the development of these methods, however, Dhiman et al. published an article that purportedly showed that an electric potential could be generated across a sheet of graphene as an electrolyte solution was flowed over it [4]. This effect was similar to that seen previously in carbon nanotubes (CNTs) [1–3]. A possible mechanism for the effect was that hydrated ions in solution were electrostatically coupling to charge carriers in the graphene/CNTs and dragging them along the direction of flow [1,4]. This effect was particularly interesting to those in the field of solid-state nanopore sequencing because if it were real it could potentially be used in reverse to control poly-anionic DNA molecules on the surface of graphene by simply flowing current through it. A concerted effort was therefore made to replicate their results. Based on my own ex-

periments as well as those of Yin et al. [5], it was quickly determined, however, that the effect was a result of a flaw in the initial experimental setup and a lack of proper control experiments. Fixing this flaw showed that graphene was incapable of generating a voltage from flowing aqueous electrolytes.

1.2 Graphene, aqueous electrolytes, and electricity

Recently, more rigorous experiments have shown that voltages can in fact develop across graphene if droplets of electrolyte solution are dragged across its surface or if graphene is actively moved into and out of an electrolyte bath [6, 7]. While differences in the adsorption energies of different ionic species on graphene are thought to give rise to this effect, the lack of a quantitative model prevents this idea from being confirmed. Disagreement between molecular dynamics and density functional theory calculations adds to the uncertainty of the effect's mechanism [5–7, 24].

Out of my unsuccessful effort to replicate the results of Dhiman et al., my advisor, Prof. Jene Golovchenko, and I have developed a graphene device that is also able to generate electricity from the motion of electrolyte solutions. More importantly, however, the device's behavior can be modeled accurately enough to quantitatively match experimental results. Not only has this device proved capable of generating electric current, voltage, and power from oscillating droplets of electrolyte solutions, it has also proved to be a unique way for studying the interaction between those solutions and graphene.

Our device is a type of supercapacitive electrical energy generator (SCEEG), a name I coined for any device consisting of a system of electrically-connected capacitors that exchange charge in such a way as to generate an alternating current. The mechanism of action of an SCEEG is straightforward: by repeatedly moving charge between two capacitors connected in series, *e.g.* by simultaneously increasing the capacitance one capacitor while decreasing the capacitance of the other and *vice versa*, an alternating current is produced; this in turn generates an AC voltage across the device's internal impedance; when flowing through an external load the alternating current is also a source of electric power.

At first it may seem that SCEEGs are physically unrealizable, especially if one tries to fathom how the capacitances of serial capacitors could be forced to change selectively and synchronously

with one another to exchange charge. In fact, such an onerous task of shuttling charges back and forth between capacitors seems best suited for an army of Maxwell's "intelligent demons" in a Gedankenexperiment [28]. One might be even more skeptical of the device's existence if I said that it needs no externally-applied voltage in order to operate. Despite these initial misgivings, however, SCEEG devices actually do exist and do so without requiring either an external voltage or an invocation of charge-shuttling demons. Although the SCEEG requires no external voltage, it still needs an external input of energy. In the two embodiments of SCEEG devices described to date (the first by Moon et al. [8] and the second by me in this thesis) the energy input comes from the mechanical motion of oscillating droplets of liquids. The SCEEG is therefore an electromechanical transducer, converting oscillatory mechanical energy into oscillatory electric energy. The SCEEGs in this thesis are symmetric, meaning that the electrodes and the mechanism by which they exchange charge are identical. Moon et al.'s SCEEG is asymmetric; both the electrodes and their charge transfer mechanism are different.

Fig. 1.1 (p. 8) shows the three symmetric SCEEGs described in this thesis in addition to Moon et al.'s asymmetric SCEEG. Whereas Moon et al.'s SCEEG has indium-tin-oxide (ITO) electrodes (one with a top layer of polytetrafluoroethylene and one without), our symmetric graphene (G-SCEEG) and gold (Au-SCEEG) devices consist of two adjacent sheets of graphene and gold, respectively. In the case of the G-SCEEGs the graphene electrodes are supported by a hydrophobic substrate (glass treated with octadecyltrichlorosilane) and separated from each other by a small gap. Evaporated metal contacts allow the graphene sheets to be electrically connected to one another through an external circuit. The Au-SCEEG consists of 50-nm thick gold evaporated onto bare borosilicate glass. A 1-nm thick layer of evaporated titanium is used to promote adhesion of the gold.

The presence of an electrolyte solution or room-temperature ionic liquid across the gap in the electrodes completes the circuit. Spontaneous and asymmetric adsorption of the ions onto the

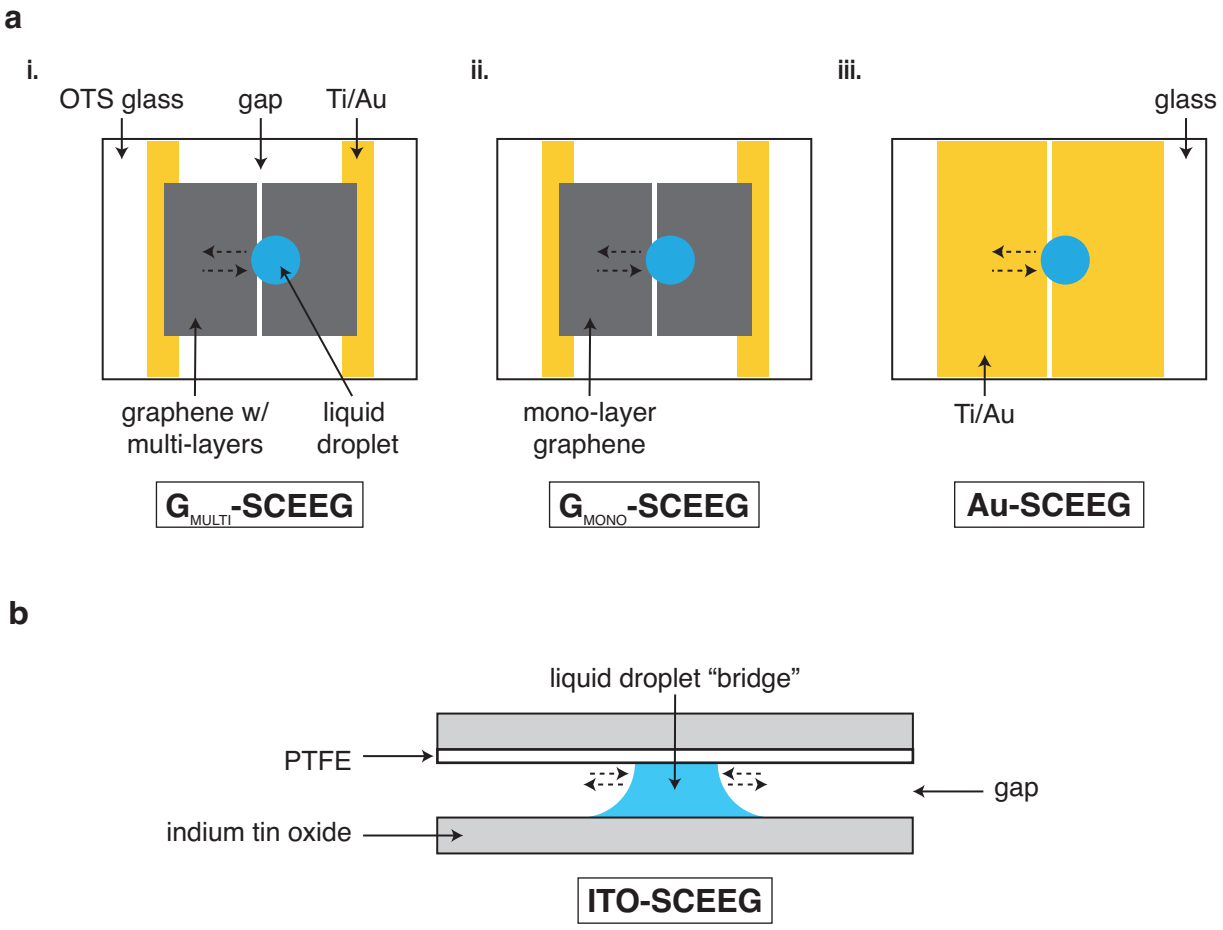

Figure 1.1: SCEEG devices. a, Plan view of the three symmetric SCEEG devices (G_{MULTI}-SCEEG, G_{MONO}-SCEEG, and Au-SCEEG) described in this thesis. Their electrodes are made of: (**i.**) graphene with 10–20% of its area containing multi-layers of various layer number; (**ii.**) mono-layer only graphene; and (**iii.**) 50-nm thick gold on a 1-nm thick titanium adhesion layer. The two devices with graphene electrodes use a glass substrate that has been functionalized with octadecyltrichlorosilane (OTS). The device with Au electrodes uses bare glass. **b**, Cross-sectional view of the asymmetric SCEEG device of Ref. [8]. Its electrodes are made of indium tin oxide (ITO). The top ITO electrode is coated in polytetrafluoroethylene (PTFE).

electrodes leads to an excess of one ionic species at the surface. A net charge develops which effectively creates a charged capacitor at the interface between the electrolyte and the electrodes, *i.e.* an interfacial supercapacitor. Electricity is generated as the droplet's area of contact with the electrode changes. Ions are adsorbed when the contact area increases and desorbed when it decreases, charging and discharging the interfacial capacitor on each half of the device, respectively, and generating a current. No need for Maxwell's demon.

As simple as the mechanism of an SCEEG device is, however, the device has only recently been described in the literature. To my knowledge, Moon et al.'s February 2013 article titled, "Electrical power generation by mechanically modulating electrical double layers" was the first published account of such a device. This publication came approximately eight months after I first generated current with an early version of the G-SCEEG by mechanically dragging droplets of electrolyte across its surface [29]. Although Moon et al. provide a differential equation to describe the voltage output of their ITO-SCEEG, they fail to take into account the reactance of the capacitors when expressing the device's internal impedance. This significant oversight calls into question the conclusions they draw on how the ITO-SCEEG's output scales with various experimental parameters. Further, they provide no analytical solution to the differential equation, making the task of verifying their conclusions difficult.

On the other hand, by properly accounting for the reactance of the capacitors I find that a simple model circuit consisting of an alternating current source in series with a resistor and a time-varying capacitor accurately predicts the dynamic behavior of both the ITO- and G-SCEEG devices. Additionally, an analytical expression for the G-SCEEG's short-circuit current allows the density and sign of the surface charge induced in graphene by the solution to be determined, thus providing insights into the nature of the interaction between graphene and hydrated ions as well as the parameters that influence it. Perhaps most interesting is that the G-SCEEG allows the identity of the adsorbed ion to be determined as well as its effective binding energy to graphene. The

G-SCEEG also provides a simple way to determine properties of the electric double layer that forms at the graphene's surface such as its capacitance per unit area and its surface potential.

1.3 Graphene: wonder material or wonderfully hyped?

Since the discovery of a simple method for isolating graphene, an atomically-thin allotrope of carbon, from bulk graphite, graphene's fascinating properties have generated much interest both in the fundamental physics describing its unique behavior as well as in its potential application as a transparent and highly conductive material [16]. In addition to its outstanding electrical and thermal conductivities, graphene is the strongest material ever measured [30]. Clearly, graphene is a uniquely interesting material for many reasons besides it extreme thinness and in the decade after graphene was first successfully isolated in 2004, the level of scientific interest in this two-dimensional material has been staggering. With sustained exponential growth in the number of published scholarly articles mentioning the word graphene in their titles, the graphene "gold rush" is well underway [31]. This burgeoning stockpile of research has shown graphene to have many fascinating properties, but it has also ascribed to graphene attributes which are not entirely justified in retrospect. Nowhere is this more evident than in the field of research to which the work in this dissertation belongs, namely the generation of electricity from the flow of electrolyte solutions over graphene surfaces. A lack of proper control experiments and an inclination towards convoluted, *ad hoc* theoretical models have needlessly muddled the explanation of this effect. The goal of this dissertation is to separate the hype from the physics and to provide a deeper understanding of the interaction between graphene and hydrated ions.

1.4 The organization of this thesis

The bulk of this dissertation is contained in Chapters 2 and 3. Chapter 2 focuses on the description of the SCEEG device in general and on the development and implementation of the G-SCEEG device in particular. The factors governing the electrical output of the G-SCEEG are explored; a theoretical model describing the SCEEG's output is provided that quantitatively agrees with the device's measured output. Several applications of the G-SCEEG are explored such as energy harvesting and detecting standing waves on the surface of a droplet. The chapter concludes with the characterization of several of the physical and chemical properties of the device's graphene electrodes.

Chapter 3 focuses on describing the interaction between graphene and hydrated ions based on inferences from G-SCEEG's output. The identity of adsorbed ions and their effective surface density are determined. The ion's effective binding energy to graphene is also be determined. Additionally, electrochemically-useful details about the interface between a graphene electrode and an electrolyte solution are measured such as the capacitance per unit area and the surface potential.

Chapter 4 is the result of a collaborative project between a fellow Harvard graduate student, Tony Zhou, and me. We show that mono-crystalline graphene can be suspended over large-area apertures in an insulating substrate. We also study the properties of suspended mono- and multi-layer graphene using Raman spectroscopy.

Chapter 5 contains the preliminary results on electrostatically trapping DNA on and repelling DNA from the surface of graphene. As I previously mentioned, this was the project that began my odyssey into understanding how ions and graphene interact.

In Chapter 6, I explain the unique methods I developed during the course of this thesis. Included is a method for synthesizing large-grain, mono- and multi-layer graphene using chemical

vapor deposition (CVD) and a method for transferring CVD-grown graphene onto hydrophobic substrates.

Finally, in Chapter 7, I summarize the conclusions from this work and speculate on the future use of SCEEGs in both electrochemistry and energy harvesting applications.

... Foolishly reduplicating

Folly in thirty-year periods; they eat and laugh too,

Groan against labors, wars and partings,

Dance, talk, dress and undress; wise men have pretended

The summer insects enviable;

One must indulge the wise in moments of mockery ...

– Robinson Jeffers

2

The SCEEG device

2.1 Chapter overview

This chapter provides a comprehensive description of the supercapacitive electrical energy generator (SCEEG) while specifically focusing on the behavior of SCEEGs made with graphene electrodes (G-SCEEGs). The main objectives of the chapter are to:

(i) introduce the different types of SCEEGs and their mechanisms of action.

(ii) provide a mathematical model that quantatively captures the dynamics and the scaling be-

havior of the SCEEG's electrical output.

(**iii**) provide data demonstrating how the electrical output of the G-SCEEG varies with different experimentally-accessible parameters.

(**iv**) discuss several applications of the G-SCEEG such as harvesting energy from mechanical vibrations and detecting standing waves on the surface of liquid droplets.

A comprehensive characterization of the G-SCEEG's physical and chemical properties using optical microscopy, Raman spectroscopy, X-ray photoelectron spectroscopy (XPS), and I-V measurements is also provided. The chapter concludes with a comparison of the electrical output of SCEEGs whose electrodes are made with different materials, *i.e.* mono-layer graphene, graphene with regions of multi-layers, and gold.

2.2 Types of SCEEG devices

In general, a SCEEG is any system of serially-connected supercapacitors which generates an alternating current by repeatedly exchanging charge between adjacent supercapacitors. Supercapacitors (also known as electrochemical capacitors, electric double layer capacitors, and ultracapacitors) are capacitors that form as a result of a separation of charge at the interface between an electrode and either an electrolyte solution or an ionic liquid [32]. Because of this, the term 'supercapacitor' is used interchangeably with the term 'interfacial capacitor' throughout this thesis. The reason these capacitors are labeled 'super' is because their energy density is several orders of magnitude higher than conventional dielectric capacitors [33]. The supercapacitors discussed in this thesis are those that form spontaneously when an electrode, such as graphene, is exposed to these particular liquids. The separation of charge that results from the preferential adsorption of one ionic species from the liquid to the electrode's surface leads to the spontaneous formation of

these capacitors. Such separation of charge also gives rise to an electric potential at the surface of the electrode which is commonly referred to as the electrode's surface potential.

The fundamental unit of a SCEEG device consists of a single pair of serially-connected supercapacitors (outlined in a red box in Fig. 2.1, p. 17), but similar devices can be made, more broadly, from capacitors of any type. This single pair of supercapacitors can be added to other pairs in both series and parallel to create more complex SCEEG devices. Assuming that adjacent capacitors, C_{i} and C_{j}, are both initially charged due to a mechanism such as ionic adsorption, the conservation of electric charge, q, demands that the removal of an infinitesimal amount of charge, dq, from one capacitor be offset by the addition of dq to the other, *i.e.* $dq = dq_{\mathrm{i}} = -dq_{\mathrm{j}}$. From the definition of capacitance this implies that, $dq = d\left(C_{\mathrm{i}}\,\Phi_{\mathrm{i}}\right) = -d\left(C_{\mathrm{j}}\,\Phi_{\mathrm{j}}\right)$, where Φ_{i} and Φ_{j} are the surface potentials across the supercapacitors C_{i} and C_{j}, respectively.

With this in mind it is evident that charge can be exchanged between the capacitors, and thus current can flow through the device, using several different mechanisms. As demonstrated in Fig. 2.2 those mechanisms include:

(a) *changing the electric potential,* $dq = C_i\,d\Phi_i = -C_j\,d\Phi_j$*:* the voltage across one of the SCEEG's capacitors is decreased while the voltage across an adjacent capacitor is simultaneously increased, *i.e.* synchronous charging and discharging of nearest-neighbor capacitors; the capacitance of each capacitor remains constant.

(b) *changing the capacitance,* $dq = \Phi_i\,dC_i = -\Phi_j\,dC_j$*:* the capacitance of one capacitor is decreased while the capacitance of an adjacent capacitor is simultaneously increased; the voltage across each remains constant.

(c) *changing both the capacitance and the electric potential,* $dq = C_i\,d\Phi_i + \Phi_i\,dC_i = -C_j\,d\Phi_j - \Phi_j\,dC_j$*:* both the capacitance and the voltage of adjacent capacitors are changed.

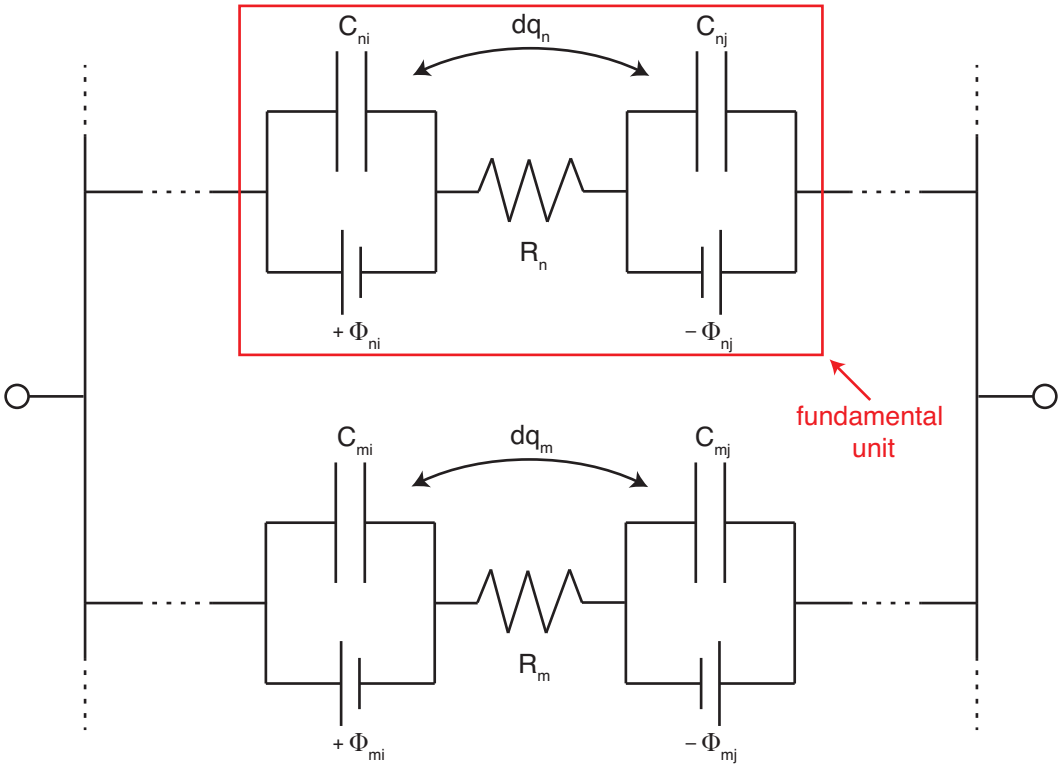

Figure 2.1: General SCEEG circuit model. The fundamental unit (red box) of the SCEEG's circuit model is a single pair of serially-connected supercapacitors, C_{ni} and C_{nj}, each of which is charged by the surface potentials, Φ_{ni} and Φ_{nj}, respectively. In the steady state, $\Phi_{\mathrm{ni}} = -\Phi_{\mathrm{nj}}$. Serially-connected supercapacitors repeatedly exchange an infinitesimal amount of charge, dq, in response to a repeating, infinitesimal change in either their capacitances or their surface potentials (or both), *i.e.* $dq = d\left(C_{\mathrm{i}}\,\Phi_{\mathrm{i}}\right) = -\,d\left(C_{\mathrm{j}}\,\Phi_{\mathrm{j}}\right)$. The repeated exchange of charge generates an alternating current (for the sake of simplicity the capacitive current sources are not explicitly shown in the circuit model). More complex SCEEGs can be created by adding additional pairs of capacitors in both series and parallel as indicated by the dashed lines.

(d) *changing the capacitance of one and the electric potential of another,* $dq = \Phi_i\, dC_i = -C_j\, d\Phi_j$*:* the capacitance of one capacitor is decreased while the voltage across an adjacent capacitor is simultaneously increased and *vice versa*.

Each of the above mechanisms assumes that the electrode-liquid interfaces making up the SCEEG's supercapacitors are ideally polarizable, *i.e.* no charge transfer occurs across the interface and there is no flow of so-called faradiac current.

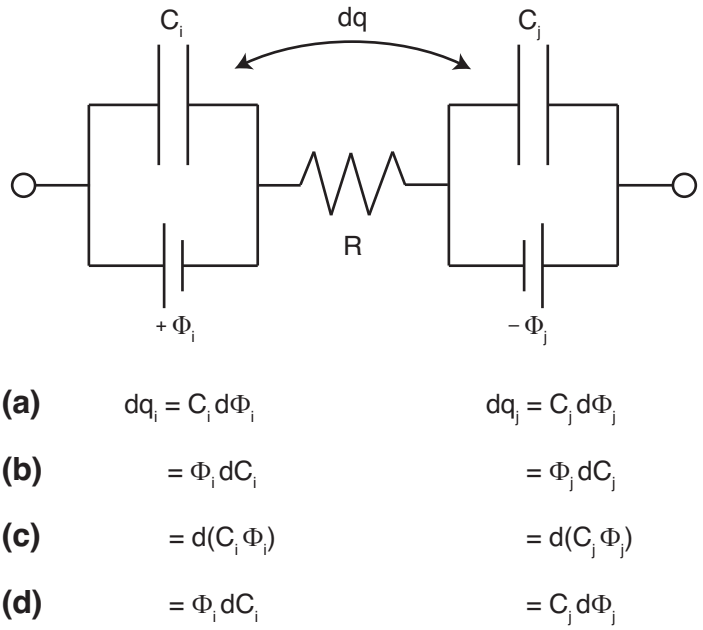

Figure 2.2: Charge transfer mechanisms. An infinitesimal amount of charge, dq, can be exchanged between the supercapacitors of a SCEEG using any of the four mechanisms listed in (**a**)–(**d**). Conservation of charge requires that $dq = dq_{\mathrm{i}} = -\,dq_{\mathrm{j}}$. Again, for the sake of simplicity the capacitive current sources are not explicitly shown in the circuit model.

If the supercapacitors are forced to repeatedly exchange charge back and forth, the SCEEG generates an alternating short-circuit current. The SCEEG simultaneously generates an open-circuit AC voltage as a result of this current flowing through its internal resistance and capacitive reactance. However, when no current is flowing and the device is in a steady state, there is no net open-circuit voltage because $\Phi_{\mathrm{i}} = -\Phi_{\mathrm{j}}$. Furthermore, a SCEEG is capable of generating electric power when it is connected to an external load as demonstrated later in this chapter.

To the best of my knowledge the only embodiments of the SCEEG that have been described to date are the three devices detailed in this thesis and the single device published by Moon et al. in 2013 [8]. All four of these SCEEGs are similar in that they consist of only two serially-connected supercapacitors.[1] The supercapacitors form spontaneously when the SCEEG's two electrodes are exposed to the same liquid droplet. In addition to forming supercapacitors at the electrode-solution interface, the droplet also electrically connects the electrodes to one another by spanning the gap between them. Due to its finite conductivity, the droplet acts as a resistor in series with the two interfacial supercapacitors. Finally, all SCEEGs depend on the droplet's motion to supply the impetus for the exchange of charge to occur.

The SCEEGs differ significantly, however, in the material from which their electrodes are made and in the mechanism by which the moving droplet exchanges charge between the supercapacitors. Moon et al.'s device has electrodes made from the semiconductor indium tin oxide (ITO) with one of the electrodes coated with polytetrafluoroethylene (PTFE), causing it to be hydrophobic. Their ITO-SCEEG uses the movement of a deionized water droplet to transfer charge between the electrodes by changing the capacitance of the supercapacitor at the PTFE-coated electrode. This generates a current which then causes a simultaneously change in the voltage across the bare ITO electrode. The ITO-SCEEG operates, therefore, via the $\Phi_{\mathrm{i}} dC_{\mathrm{i}} = -C_{\mathrm{j}} d\Phi_{\mathrm{j}}$ mechanism.[2]

Unlike Moon et al.'s ITO-SCEEG, two of the SCEEG devices described in this thesis were made using the semimetal graphene (G) as the electrode material and the other was made using the noble metal gold (Au). The two graphene SCEEGs differ from each other in that one contains regions of multilayer graphene ($\mathrm{G_{MULTI}}$-SCEEG) whereas the other contains only monolayer graphene ($\mathrm{G_{MONO}}$-SCEEG). Despite the difference in their electrodes, the Au-SCEEG and both

[1] For an illustration of all four SCEEGs, see Fig. 1.1 (p. 8).

[2] For illustrations of Moon et al.'s ITO-SCEEG, see Figs. 1.1 (**c**) (p. 8), 2.9 (p. 48), and 2.12 (p. 71).

G-SCEEGs function via the ΦdC mechanism, *i.e.* charge transfer occurs when a moving droplet of electrolyte solution causes a simultaneous change in the capacitance of both of the SCEEG's interfacial supercapacitors.

2.2.1 Symmetric vs. asymmetric SCEEGs

It is convenient to classify a SCEEG as being either *symmetric* or *asymmetric*. For a SCEEG to be symmetric it must satisfy the following two criteria:

(i) Both of its capacitors must have the same capacitance per unit area, c_0, *i.e.* the SCEEG's electrodes are made of the same material and are exposed to the same solution.

(ii) The mechanism by which the individual capacitors exchange charge must be identical, *i.e.* both capacitors use the ΦdC mechanism, etc.

SCEEGs not meeting both of these criteria are labeled asymmetric. By this definition then, only the $\Phi_{\mathrm{i}} dC_{\mathrm{i}} = -C_{\mathrm{j}} d\Phi_{\mathrm{j}}$ mechanism of those listed above is exclusive to asymmetric SCEEGs. The G- and Au-SCEEGs described in this thesis are symmetric because their capacitors exchange charge via the ΦdC mechanism and have the same value of c_0. Conversely, Moon et al.'s ITO-SCEEG is asymmetric both because its capacitors have different values of c_0 and because it uses the $\Phi_{\mathrm{i}} dC_{\mathrm{i}} = -C_{\mathrm{j}} d\Phi_{\mathrm{j}}$ mechanism.

2.3 Physical model

A detailed discussion of the physical model describing the SCEEG is limited here to include only the two types of SCEEGs that have been developed so far: the symmetric SCEEG using the ΦdC mechanism, *i.e. symmetric* ΦdC *SCEEG*, and the asymmetric SCEEG using the $\Phi_{\mathrm{i}} dC_{\mathrm{i}} = -C_{\mathrm{j}} d\Phi_{\mathrm{j}}$ mechanism, *i.e. asymmetric* $\Phi_i dC_i = -C_j d\Phi_j$ *SCEEG*.

2.3.1 Symmetric ΦdC SCEEG

The symmetric ΦdC SCEEG is shown in Fig. 2.3 (p. 22). This SCEEG contains a pair of serially-connected supercapacitors which use the ΦdC mechanism of charge transfer. According to the model presented in the figure, when an electrolyte solution is in contact with the SCEEG's electrodes, one of the ionic species of the electrolyte preferentially and spontaneously adsorbs on the electrode's surface. This asymmetric ionic adsorption induces an image charge of density σ at the surface of the electrode that is of opposite sign as that of the adsorbed ions. The attractive, electrostatic force between the adsorbed ions and the induced image charge effectively binds the ions to the electrode's surface, creating a condensed layer (also known as a Stern or Helmholtz layer) of immobile ions at the surface.

In addition to the attractive, electrostatic force that the ions experience near the electrode's surface, the ions are also subject to a randomly fluctuating force caused by collisions with solvent molecules. The resultant of these two forces acts on non-adsorbed ions to create a layer of mobile ions that extends away from the electrode's surface and into the bulk of the solvent. This layer is termed the diffuse layer (also known as the Gouy-Chapman layer) and has a characteristic length scale, λ_{D}, called the Debye length (typically, $\lambda_{\mathrm{D}} \simeq 1$–$100$ nm) [34].

Taken together, the layer of induced charge in the electrode and the layers of charge in the solution form what is called an electric double layer (EDL) at the electrode-solution interface. Be-

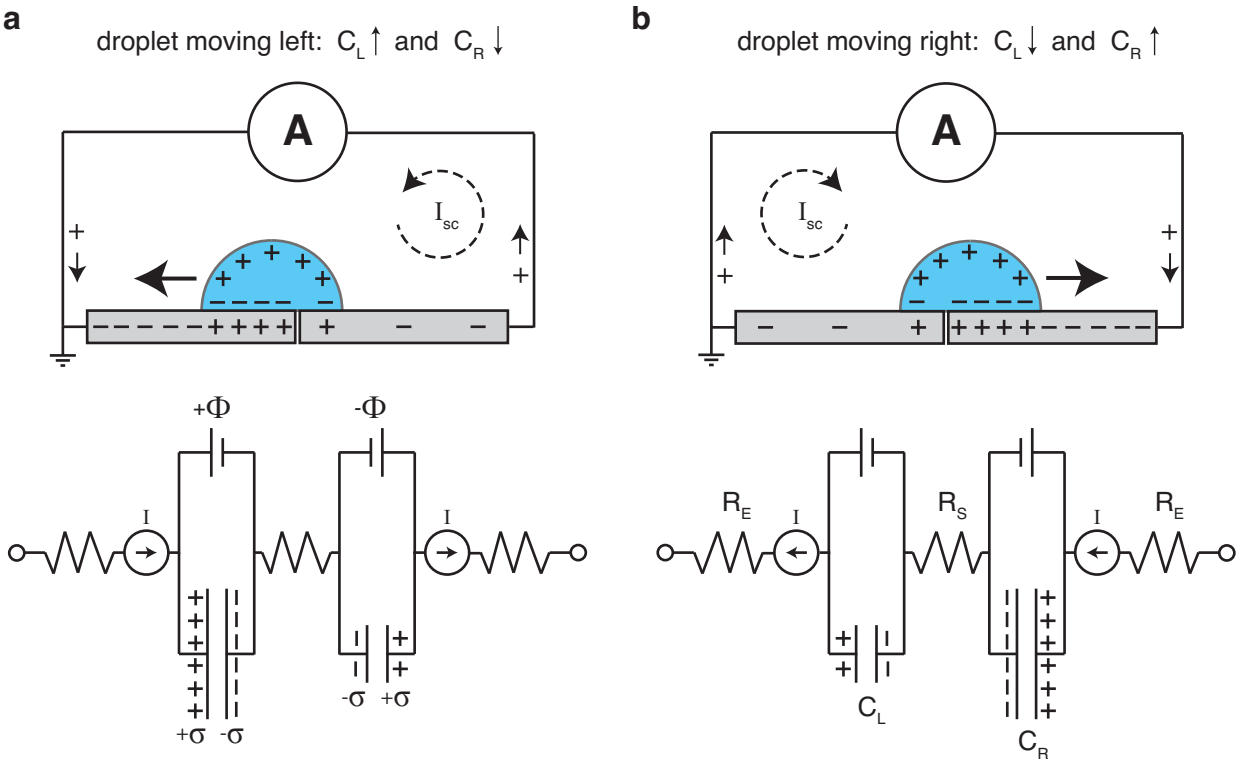

Figure 2.3: Physical model of the symmetric ΦdC SCEEG. Anions $(-)$ in a droplet of electrolyte solution (blue) adsorb to the surface of the SCEEG's electrodes (grey), inducing in them a positive image charge density, $+\sigma$, and generating a surface potential, Φ. The compensating positive charge in solution is distributed along the air-droplet interface by the cations $(+)$. The compensating negative charge in the electrode is distributed along the electrode's surface. **a**, As the droplet moves from the right to the left electrode, the capacitance of the left interfacial capacitor increases while that of the right decreases. During this process positive charge is removed from the right electrode and deposited on the left, generating a counterclockwise flow of short-circuit current, I_{sc}, through the circuit as measured by an ammeter. **b**, As the droplet moves to the right, the opposite occurs and a clockwise current is generated. The interfacial capacitor at each electrode acts as both a capacitor and a current source, I. Impeding the flow of current are resistors and time-varying capacitors connected to each other in series: R_{E}, resistance of the electrode; R_{S}, resistance of the solution; and C_{L} and C_{R}, capacitances of the left and right interfacial capacitor, respectively. The size of the interfacial capacitors in each circuit represents the relative magnitude of their capacitance.

cause there is thought to be more than two total layers of charge at the interface, EDL is a misnomer. Despite this, the term is still widely used in the literature due to historical precedent. EDL can still be considered accurate, however, in the contrived sense that the combination of a "solid-phase" and a "liquid-phase" layer of charge form a "double" layer of charge at the interface.

For the case depicted in Fig. 2.3, it is the anions of the electrolyte that form the EDL by specifically binding to the surface of the electrodes and thus inducing in them a positive charge density. The cations on the other hand are repelled from the region near the positively-charged electrode.[3] Because the solution is a conductor, the positive charge that is excluded from the double layer distributes itself at the air-solution interface in the form of an increased concentration of cations. The compensating negative charge in the electrode also distributes itself at the surface, save for the area immediately underneath the droplet. If the electrode is two-dimensional, however, as is the case with graphene, the compensating charge does not distribute itself exclusively at the electrode's perimeter [35]. Instead, the charge is distributed throughout the area of the electrode with its density increasing significantly near the perimeter.[4]

The accumulation of net charge in both the electrode and in the EDL near the interface is analogous to the build up of charge that occurs on a parallel-plate capacitor when it is subjected to an applied voltage. It is convenient, therefore, to model the electrode-solution interface as an electric double-layer capacitor (EDLC) [37]. Unlike a typical capacitor which is charged by applying an external potential, the EDLC is charged by the asymmetric adsorption of ions on the electrode's surface and the charge density, σ, that this, in turn, induces in electrode.

The resulting separation of charge across the interface generates an electric field and, as a re-

[3] For a more detailed discussion on the properties of the EDL see Chapter 3, Sect. 3.2 (p. 115) and, in particular, Fig. 3.1 (p. 117).

[4] In general, it is difficult to analytically express the distribution of charge on a conductor. However, for the case of an infinitely-long, two-dimensional conductor in the $x\,y$ plane that straddles the y axis from $x = -a$ to $x = a$, the surface charge density, σ, is distributed according to $\sigma(x) = \lambda \,/\, 2\,\pi\,\sqrt{a^2 - x^2}$, where λ is the charge per unit length along the y axis [36]. The surface charge density increases monotonically away from the y axis and diverges as $x \to \pm a$.

sult, a surface potential, Φ. So long as the interface remains electrochemically inert, *i.e.* there is no heterogeneous charge transfer across it, both Φ and σ are assumed to be constant for a given electrolyte solution. EDLCs are implicitly represented in the circuit diagrams of Fig. 2.3. Because two-dimensional electrodes, such as graphene, have a quantum capacitance (owing to their relatively low density of states), the entire graphene-solution interface is actually a serial combination of a quantum capacitor and an EDLC. To account for this addition, the capacitor at the graphene-solution interface is more generally referred to as a supercapacitor, or interfacial capacitor, throughout this thesis. Due to the way in which the interfacial capacitors of the symmetric SCEEG are oriented relative to each other, their surface potentials sum to zero when the system is in the steady state. For a stationary droplet, this means there is no net voltage drop across the SCEEG.

2.3.1.1 *Short-circuit current, I_{sc}*

The separation of charge that occurs across a parallel-plate capacitor gives rise to a uniform electric field, $\vec{E}$, between the capacitor's plates. This field stores energy with a density of $w = \epsilon\,\epsilon_0\,|\vec{E}|^2/\,2$, where ϵ and ϵ_0 are the relative and vacuum permittivities, respectively.[5] From the expression for w, it is easily shown that the total energy, W, stored in the parallel-plate capacitor is:

$$W = \frac{1}{2}\,C\,V^2 \tag{2.1}$$

where C is the capacitance and V is the voltage drop across the capacitor. Because of the way in which it stores energy, a charged capacitor can be considered a non-ideal source of voltage if the external voltage used to charge it is abruptly removed. The energy expended by the external voltage source to overcome the back electromotive force (emf) of the charging capacitor is not irreversibly dissipated but is instead recovered upon turning off the external source.[6] When connected in series to a load resistor of resistance $R_{\rm L}$, a capacitive voltage source transfers its stored energy to the load in the form of a current, which dissipates power in the resistor according to $P_{\rm L} = I^2\,R_{\rm L}$. The transfer of energy from the capacitor to the load effectively discharges the capacitor, causing the electric potential across it to exponentially decay over a characteristic timescale, $\tau_{\rm RC} = R\,C$:

$$V(t) = V_0\,\exp\left(-\,t\,/\,\tau_{\rm RC}\right) \tag{2.2}$$

Rather than discharging its interfacial capacitors in this way, however, a ΦdC SCEEG generates short-circuit current by mechanically changing the capacitance of its interfacial capacitors. Dur-

[5] Because the system is static, it is equivalent to think of the total energy, W, as arising from the particular way in which the charge is distributed on the surface of the capacitor's plates, *i.e.* $W = \int \sigma\,V\,da\,/\,2$, where V is the full electric potential of the system [36, 38].

[6] In contrast, energy is stored in the form of a magnetic field, $\vec{B}$, with a density of $w = |\vec{B}|^2/\,2\,\mu_0$, when a current flows through an inductor of inductance L. Because this stored energy can be expressed as $W = L\,I^2/\,2$, an inductor can be considered a non-ideal source of current once the external current flowing through it stops [36].

ing this process, the voltage across each interfacial capacitor, *i.e.* the surface potential Φ, does not exponentially decay according to Eq. (2.2) (p. 25), but instead remains approximately constant. As shown in Fig. 2.3 (p. 22), the way in which the interfacial capacitors are oriented means that there is no net voltage drop across the device when it is in a steady state, *i.e.* $\Phi_{\mathrm{L}} = -\Phi_{\mathrm{R}}$.

The SCEEG changes the capacitance of its interfacial capacitors by simultaneously changing the area of overlap, $A(t)$, between the droplet and each of its electrodes. Ideally, this happens such that the area change occurring at one electrode is equal but opposite to the area change occurring at the other electrode, *i.e.* $\dot{A}_{\mathrm{L}}(t) = -\dot{A}_{\mathrm{R}}(t)$. Taking the derivative with respect to time of the definition of capacitance, $q = C\,\Phi$, and assuming that both Φ and the capacitance per unit area, c_0, of the interfacial capacitors are constant, the expression describing the short-circuit current generated by each interfacial capacitor is:

$$\boxed{I_{\mathrm{sc}}(t) = \Phi\,\dot{C}(t) = \sigma\,\dot{A}(t)} \tag{2.3}$$

where

$$\dot{C}(t) \equiv \dot{C}_{\mathrm{L}}(t) = -\dot{C}_{\mathrm{R}}(t) \tag{2.4}$$

$$\dot{A}(t) \equiv \dot{A}_{\mathrm{L}}(t) = -\dot{A}_{\mathrm{R}}(t) \tag{2.5}$$

$$\Phi \equiv \Phi_{\mathrm{L}} = -\Phi_{\mathrm{R}} \tag{2.6}$$

and where the surface charge density, σ, is defined as:

$$\sigma \equiv c_0\,\Phi \tag{2.7}$$

Due to both the conservation of charge and the way in which the interfacial capacitors are connected, the current generated by one interfacial capacitor must equal that generated by the other,

i.e. $I_{\text{sc,L}}(t) = I_{\text{sc,R}}(t)$.

The assumption that Φ remains constant during this process is true only if the interfacial capacitors are able to perfectly absorb the charge flowing into them by changing their capacitance. If not, charge will accumulate on the interfacial capacitors in excess of the the steady-state charge density and the value of Φ will change accordingly. It is posited in this model that any change in Φ is small enough and short-lived enough to be safely neglected in the expression for $I_{\text{sc}}(t)$.[7] As discussed in the subsequent section, however, small changes in Φ cannot be neglected when modeling the SCEEG's open-circuit voltage. This is because any non-zero net voltage drop across the device's capacitive reactance is entirely a result of these small changes.

Even though the charged interfacial capacitors of the SCEEG store energy in the form of an electric field, it is the kinetic energy of the droplet that is responsible for moving charge from one electrode to the other. As illustrated in Fig. 2.3 (**a**), when the droplet moves to the left the area of overlap between it and the left electrode increases. As a result, the total amount of charge on the left interfacial capacitor increases. The area of overlap between the droplet and the right electrode, however, simultaneously decreases, reducing the amount of charge on the right interfacial capacitor. Because the two electrodes are connected to each other through an external circuit, the movement of charge from the right interfacial capacitor to the left generates a counterclockwise flow of current. In Fig. 2.3 (**b**), the opposite occurs; as the droplet moves to the right, the current flows clockwise from the left to the right electrode. For a continually oscillating droplet, an alternating current is generated. Because the moving droplet transfers charge from one interfacial capacitor to the other over a given amount of time, *e.g.* one half of the period of an oscillating droplet, it is intuitive to think of the droplet, and the SCEEG in general, as a non-ideal cur-

[7] Because charge is uniformly distributed over the interfacial capacitor's entire area, any amount of charge added to the interfacial capacitor that is much less than the total stored charge will only slightly change σ and, hence, Φ. Also, any excess charge density on the interfacial capacitor will likely quickly desorb from it and return to the bulk solution, *i.e.* equilibration of σ is assumed to occur on a timescale that is shorter than the period of the droplet's oscillation.

rent source.[8] While treating the SCEEG as a current source simplifies the analysis of its circuit model, as demonstrated throughout the remainder of this chapter, it is perhaps more accurate to think of the device as a source of electrical energy. This is because it has a finite, non-zero internal impedance and, as a result, can be considered a source of both short-circuit current, $I_{\text{sc}}(t)$, and open-circuit voltage, $V_{\text{oc}}(t)$.[9]

2.3.1.2 *Open-circuit voltage, V_{oc}*

The SCEEG generates an open-circuit voltage, $V_{\text{oc}}(t)$, from the flow of current through its internal impedance, $R(t)$, and capacitive reactance, $X(t)$, both of which are, in general, functions of time. $V_{\text{oc}}(t)$ is, therefore, the sum of the voltage drops across the device's equivalent resistance and equivalent reactance:

$$V_{\text{oc}}(t) = V_{\text{R}}(t) + V_{\text{X}}(t) \tag{2.8}$$

Although it was assumed in the derivation of $I_{\text{sc}}(t)$ above that the surface potential across each interfacial capacitor is independent of time, the model of $V_{\text{oc}}(t)$ treats the total voltage drop across the equivalent reactance, $V_{\text{X}}(t)$, as if it were time-dependent. This is done to account for the possibility that the flow of current can lead to an accumulation of charge, in excess of the steady-state charge density, on each interfacial capacitor even as this excess charge is being effectively absorbed by the interfacial capacitor's changing capacitance. If the interfacial capacitors were able to perfectly absorb each unit of charge flowing into them by changing their capacitances, their surface potentials would remain constant and they would present no impediment to the flow of current. As a consequence, there would be no net voltage drop across both of them. Although

[8] Separately, however, each charged interfacial capacitor can still be considered a non-ideal source of voltage as previously discussed. Additionally, it is evident from Eq. (2.1) that the energy stored in an interfacial capacitor changes as its capacitance changes. The change in the interfacial capacitor's capacitive energy is much more a consequence of the droplet's motion than a result of any small change in its surface potential.

[9] This argument is supported by the equivalence of the Norton and Thevenin representations of circuits that contain non-ideal sources. See Ref. [39] for more details.

current is generated only from the region of the interfacial capacitor whose area is changing, it is the entire area of the interfacial capacitor that contributes to impeding the current. This means that the reactance of interfacial capacitors is significant and must be explicitly included in the model of the SCEEG's open-circuit voltage.

Another way to think about this is that, due to the way in which they are oriented, the total voltage drop across the interfacial capacitors is the difference between the magnitudes of their surface potentials. This difference is equal to $V_{\mathrm{X}}(t)$, *i.e.* $V_{\mathrm{X}}(t) = \Phi_{\mathrm{L}}(t) - \Phi_{\mathrm{R}}(t)$. Because Φ_{L} and Φ_{R} have the same value in the steady-state, $V_{\mathrm{X}}(t)$ is entirely a result of the change in these surface potentials away from the steady state. Any such change, therefore, cannot be outright neglected without also completely neglecting $V_{\mathrm{X}}(t)$.

With this in mind, the voltage drop across $R(t)$ is easily found using Ohm's law and Eq. (2.3) (p. 26):

$$V_{\mathrm{R}}(t) = I(t)\, R(t) = \sigma\, R(t)\, \dot{A}(t) \tag{2.9}$$

and the voltage drop across $X(t)$ is found using the definition of capacitance:

$$q(t) = C_{\mathrm{eq}}(t)\, V_{\mathrm{X}}(t) \tag{2.10}$$

where $C_{\mathrm{eq}}(t)$ is the equivalent capacitance of the SCEEG. Solving Eq. (2.10) for $V_{\mathrm{X}}(t)$ and writing $q(t)$ as the integral of $I(t)$ with respect to time gives:

$$V_{\mathrm{X}}(t) = \frac{1}{C_{\mathrm{eq}}(t)} \int_0^t I(t')\, dt' \tag{2.11}$$

Substituting the expression $I(t) = \sigma\, \dot{A}(t)$ from Eq. (2.3) into the integral of Eq. (2.11) gives a

simple expression for $V_{\mathrm{X}}(t)$:

$$V_{\mathrm{X}}(t) = \frac{\sigma}{C_{\mathrm{eq}}(t)} \int_0^t dA(t') = \sigma \, \frac{\Delta A(t)}{C_{\mathrm{eq}}(t)} \tag{2.12}$$

where

$$\Delta A(t) \equiv A_{\mathrm{L}}(t) - A_{L,0} = A_{R,0} - A_{\mathrm{R}}(t) \tag{2.13}$$

From Eqs. (2.9) and (2.12), Eq. (2.8) can then be expressed as:

$$\boxed{V_{\mathrm{oc}}(t) = V_{\mathrm{R}}(t) + V_{\mathrm{X}}(t) = \sigma \, \dot{A}(t) \left(R(t) + \frac{1}{C_{\mathrm{eq}}(t)} \, \frac{\Delta A(t)}{\dot{A}(t)} \right)} \tag{2.14}$$

2.3.1.3 *Time-dependent, internal impedance, Z^**

When one talks of electrical impedance one usually means a frequency-dependent quantity, $Z(\omega)$, that is quantitatively defined according to Ohm's law as the ratio of the of the voltage phasor, $\mathbf{V}$, to the current phasor, $\mathbf{I}$:

$$Z(\omega) = \frac{\mathbf{V}}{\mathbf{I}} \tag{2.15}$$

Strictly speaking, the impedance describes the opposition experienced by a sinusoidal current as it flows through a circuit [39]. In the case of the SCEEG's internal impedance, however, it is more appropriate to think of impedance as a function of time because the device's equivalent resistance and equivalent capacitance are, in general, both time-dependent. With this in mind, a time-dependent, internal impedance, $Z^*(t)$, can be defined for the SCEEG by taking the ratio of the its open-circuit voltage, $V_{\mathrm{oc}}(t)$, to its short-circuit current, $I_{\mathrm{sc}}(t)$. From Eqs. (2.3) (p. 26) and (2.14) this gives:

$$\boxed{Z^*(t) = \frac{V_{\mathrm{oc}}(t)}{I_{\mathrm{sc}}(t)} = R(t) + \frac{1}{C_{\mathrm{eq}}(t)} \, \frac{\Delta A(t)}{\dot{A}(t)}} \tag{2.16}$$

In general, $R(t)$ and $C_{\text{eq}}(t)$ are functions of time because they are both dependent on the area of overlap between the droplet and the electrodes, which itself is a function of time. As illustrated in the circuit diagrams of Figs. 2.3 (p. 22) and 2.4 (p. 32), the equivalent resistance consists of three resistors in series (one for each electrode and one for the bulk solution of the droplet):

$$\boxed{R(t) = R_{\text{E,L}}(t) + R_{\text{E,R}}(t) + R_{\text{S}}(t) = 2\,R_{\text{E}}(t) + R_{\text{S}}(t)} \tag{2.17}$$

Although the resistance of the electrode is normally time independent, if the electrode is made of a material whose resistance can be significantly altered by its environment, such as graphene, its resistance will change as its area of overlap with the droplet changes. Additionally, because the resistance of the droplet, $R_{\text{S}}(t)$, is dependent on both the droplet's conductivity, σ_{c}, and its geometry, *i.e.* its length, $l(t)$, and cross-sectional area, $A(t)$, the resistance will change in time as the droplet oscillates back and forth across the SCEEG:

$$R_{\text{S}}(t) \simeq \frac{1}{\sigma_{\text{c}}}\,\frac{l(t)}{A(t)} \tag{2.18}$$

The equivalent capacitance consists of two capacitors in series (one for each electrode-solution interface):

$$\boxed{C_{\text{eq}}(t) = \left(\frac{1}{C_{\text{L}}(t)} + \frac{1}{C_{\text{R}}(t)}\right)^{-1} = c_0\left(\frac{1}{A_{\text{L}}(t)} + \frac{1}{A_{\text{R}}(t)}\right)^{-1}} \tag{2.19}$$

If no external voltage is applied to the SCEEG and if the SCEEG's electrodes are inherently electrochemically inert to the liquid droplet, no electrochemical reaction will occur at the electrode-droplet interface, *i.e.* no faradaic current will flow between the electrode and the liquid. Under these conditions the interface is assumed to be ideally polarizable and is therefore modeled solely as a capacitor. If, however, an external voltage is applied or if the electrode material is electrochemically reactive, some faradaic current is expected due to the increased likelihood of a reduction-

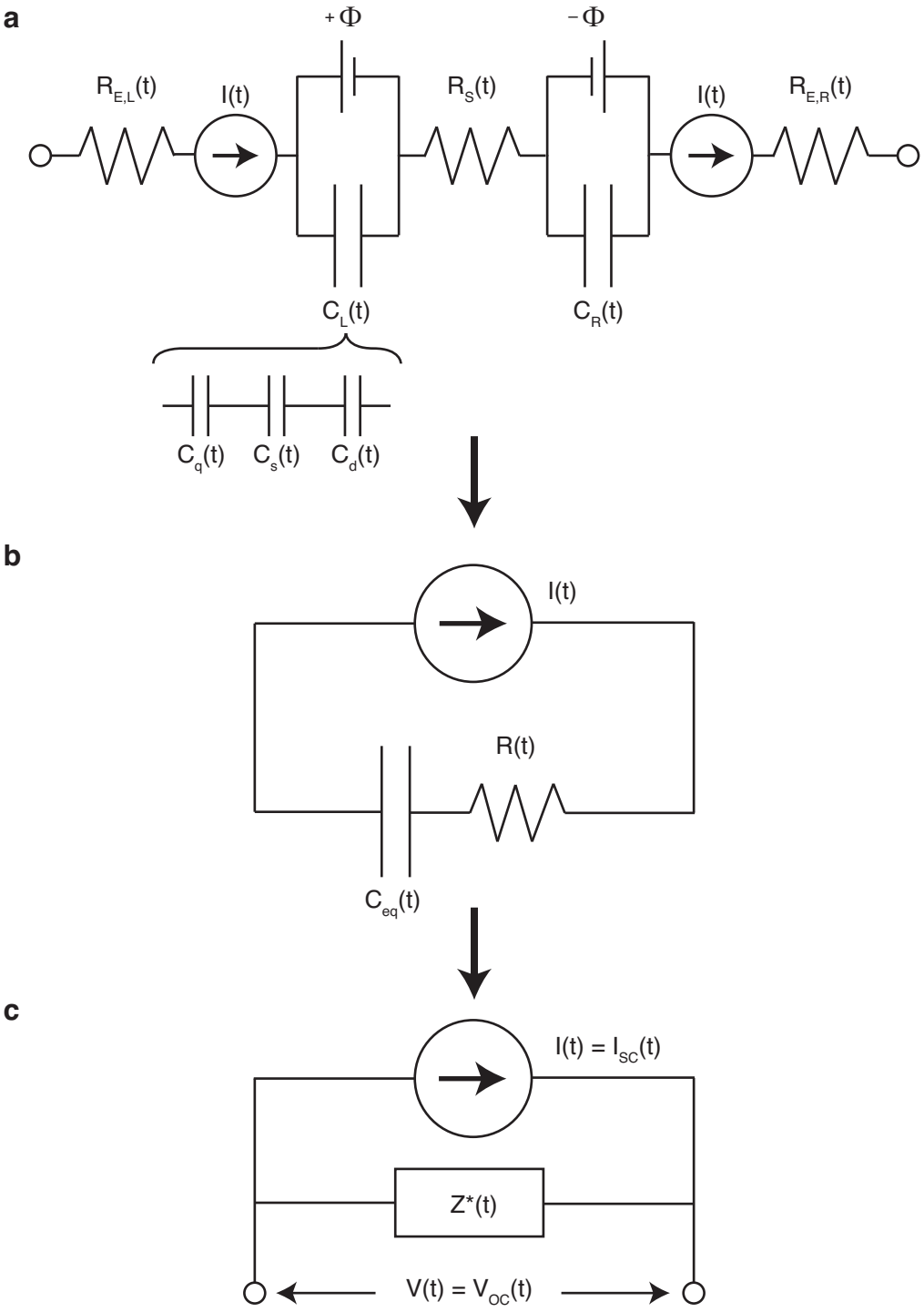

Figure 2.4: Equivalent circuit models. **a**, Illustration of the circuit model of the SCEEG explicity showing the interfacial series capacitance, $C_{\mathrm{q}}(t)$, $C_{\mathrm{s}}(t)$, and $C_{\mathrm{d}}(t)$, and the capacitive current sources, $I(t)$. **b**, Simplified circuit model representing the device's equivalent current source, $I(t)$, equivalent resistance, $R(t)$, and equivalent capacitance, $C_{\mathrm{eq}}(t)$. **c**, The Norton equivalent circuit with time-dependent impedance, $Z^*(t)$, and short-circuit current source, $I_{\mathrm{sc}}(t)$.

oxidation reaction occurring at the interface. In this case, the interface is best modeled as a capacitor in parallel with a faradaic resistor [37].[10] Because the basal plane of graphene is inherently electrochemically inert and because gold is a fairly inert noble metal, both the G-SCEEG and the Au-SCEEG devices are assumed to have ideally polarizable electrode-solution interfaces in the absence of an applied potential [40].

According to a generally accepted model of the electric double layer, its equivalent capacitance can be represented as two capacitors in series with one another [37]. As previously mentioned, one capacitor is due to a condensed layer of ions on the electrode's surface, called the Stern layer, and is referred to as the Stern capacitance, $C_{\mathrm{s}}(t)$. The other is due to a diffuse layer of ions, called the Debye layer, and is referred to as the Debye capacitance, $C_{\mathrm{d}}(t)$.[11] Because these two capacitors are connected in series they add in the usual way to give an equivalent EDL capacitance, $C_{\mathrm{EDL}}(t)$:

$$C_{\mathrm{EDL}}(t) = \left(\frac{1}{C_{\mathrm{s}}(t)} + \frac{1}{C_{\mathrm{d}}(t)} \right)^{-1} \tag{2.20}$$

In addition to $C_{\mathrm{s}}(t)$ and $C_{\mathrm{d}}(t)$, there exists another capacitance, $C_{\mathrm{q}}(t)$, that has up until this point has only been briefly mentioned. $C_{\mathrm{q}}(t)$ is the quantum capacitance (also referred to as the chemical capacitance) and is a consequence of the Pauli exclusion principle [41–43]. In order to add an electron to a conductor, energy must be provided to not only overcome the repulsive force between the added electron and the conductor's intrinsic electrons but to also place the electron in a higher energy state within the conductor's electronic band structure, as required by Pauli's principle. Adding an electron to the electronic band structure results in a change in the system's electrochemical potential, $\Delta\mu$ (also known as the Fermi level, E_{F}). If the density of electrons in the conductor's band structure, Δn_{e}, is changed as a result of a change in an applied electric po-

[10] See Fig. 2.10 (p. 61) for a circuit model of such an interface.

[11] See Chapter 3, Sect. 3.2.1 (p. 122) for a more detailed discussion of the Stern and Debye capacitances.

tential, ΔV, then the following expression for $\Delta\mu$ holds:

$$\Delta\mu = \frac{\Delta n_{\mathrm{e}}}{\rho_{\mathrm{s}}} = e\,\Delta V \tag{2.21}$$

where ρ_{s} is the density of states of the electrons and e is the fundamental unit of charge. From Eq. (2.21) and the definition of differential capacitance, $C' = \partial\, q \,/\, \partial V$, it is easily shown that the quantum capacitance can be written as:

$$C_{\mathrm{q,\,3D}} = \rho_{\mathrm{s}}\, e^2\, v \tag{2.22}$$

where v is the volume of the conductor.[12] For a two-dimensional electron gas (2DEG) or a two-dimensional conductive material like graphene of area A, Eq. (2.22) becomes:

$$C_{\mathrm{q,\,2D}} = \rho_{\mathrm{s}}\, e^2\, A \tag{2.23}$$

Because a three-dimensional conductor, no matter how thin, has a near infinite density of electronic energy states, its quantum capacitance is also nearly infinite. This means that an external electric field is unable to significantly penetrate the conductor's surface and, as a result, the screening length of a three-dimensional conductor can safely be assumed to be much shorter than any realistic film thickness [41].

In the case of an electrode exposed to an electrolyte solution, the quantum capacitance is in series with the equivalent electric double-layer capacitance because the sum of the voltage drops across them is equal to the total voltage drop across the interface. The true equivalent capacitance of the interface is therefore comprised of three separate capacitors, connected to each other in series as shown in Fig. 2.4 (**a**). The expression for the equivalent capacitance of the complete inter-

[12] See Chapter 3, Sect. 3.2.1 (p. 122) for a more thorough discussion on differential and quantum capacitances.

face, $C_{\mathrm{I}}(t)$, is then:

$$C_{\mathrm{I}}(t) = \left(\frac{1}{C_{\mathrm{q}}(t)} + \frac{1}{C_{\mathrm{EDL}}(t)} \right)^{-1} = \left(\frac{1}{C_{\mathrm{q}}(t)} + \frac{1}{C_{\mathrm{s}}(t)} + \frac{1}{C_{\mathrm{d}}(t)} \right)^{-1} \tag{2.24}$$

As mentioned above, for three-dimensional conductors, such as gold, that have a near infinite density of states the quantum capacitance is also nearly infinite. A capacitor with infinite capacitance effectively acts as short and contributes negligibly to the total serial capacitance as seen from the form of Eq. (2.24). Because of this, quantum capacitance does not play a significant role in the behavior of the Au-SCEEG or any SCEEG whose electrodes have a large density of states. For such electrodes Eq. (2.24) simplifies to Eq. (2.20). On the other hand, electrodes made of materials with a finite density of states like graphene can have a quantum capacitance that is of the same order of magnitude as that of the EDL [44]. As a result, the quantum capacitance does affect the behavior of the G-SCEEG.

In addition to simplifying the SCEEG's circuit model by determining the equivalent resistance and equivalent capacitance, the model can be further simplified using Norton's theorem. Because the model contains serially-connected sources and impedances, Norton's theorem permits the circuit in Fig. 2.4 (**b**) to be rewritten as the circuit in Fig. 2.4 (**c**), *i.e.* a single current source, $I(t)$, in parallel to a single internal resistnace, $Z^*(t)$. Although it is more intuitive to describe a SCEEG as a current source, Thevenin's theorem permits the circuit in (**c**) to be rewritten as a voltage source in series with $Z^*(t)$ as shown in Fig. 2.21 (p. 90).

2.3.1.4 *Mutual capacitance between the SCEEGs electrodes*

Although it is possible, using advanced photolithographic techniques, to fabricate electrodes that are separated by a gap of the same order of magnitude as the characteristic thickness of the diffuse layer ($\lambda_{\mathrm{D}} \sim 10^{-9}$ m), the mutual capacitance of the electrodes, C_{LR}, at this distance of sep-

aration is still orders of magnitude less than their interfacial capacitances because of their end to end orientation, *i.e.* $C_{\mathrm{L}} \simeq C_{\mathrm{R}} >> C_{\mathrm{LR}}$.[13] To see why this is so, consider the following argument: The electrode is a conductor so any excess charge it has accumulates at its surface. The surface density of the excess charge is greatest at the ends of the electrode owing to the large amount of curvature found there relative to the rest of the electrode.[14] For this reason the ends of the electrodes that are facing one another can be treated, approximately, as two infinitely long wires of radius $r = a$. If the wires are separated by a distance d, such that $d >> a$, with one having a linear charge density of $+\lambda$ and with the other having $-\lambda$, the potential difference, V, between them is:

$$V = \frac{\lambda}{\pi \epsilon \epsilon_0} \ln\left(\frac{d}{a}\right) \tag{2.25}$$

and their capacitance is given by:

$$C = \frac{q}{V} = \frac{\epsilon \epsilon_0 \pi}{\ln\left(\frac{d}{a}\right)} l \tag{2.26}$$

where l is the length of the wires [36]. Because the form of Eq (2.26) assumes the wires are infinite, the expression holds only for $l >> d$. Using values typical of SCEEGs with side-by-side electrodes ($\epsilon \sim 10^2$, $d \sim 10^{-6}$ m, $a \sim 10^{-9}$ m, and $l \sim 10^{-2}$ m), Eq. (2.26) estimates the mutual capacitance to be $\sim 10^{-11}$ F. Compared to the interfacial capacitance of each electrode ($C_{\mathrm{L}} \simeq C_{\mathrm{R}} \sim 10^{-7}$ F), the mutual capacitance is orders of magnitude smaller. It is therefore safe to neglect C_{LR} when modeling the SCEEG.

[13] This condition, along with the fact that the SCEEG's electrodes are held at roughly the same electric potential relative to the bulk of the droplet, $\Phi_{\mathrm{L}} \simeq \Phi_{\mathrm{R}}$, implies that the capacitance matrix, **C**, of the system is diagonal, *i.e.* $\mathbf{C} = \begin{bmatrix} C_{\mathrm{L}} + C_{\mathrm{LR}} & -C_{\mathrm{LR}} \\ -C_{\mathrm{RL}} & C_{\mathrm{R}} + C_{\mathrm{RL}} \end{bmatrix} \simeq \begin{bmatrix} C_{\mathrm{L}} & 0 \\ 0 & C_{\mathrm{R}} \end{bmatrix}$. For a more detailed discussion of the elements of the capacitance matrix, see Ref. [38].

[14] For a two-dimensional conductor the surface charge density is greatest near the perimeter as discussed in footnote 4 of this chapter (p. 23).

2.3.1.5 *Phase angle, ϕ*

A phase delay exists between the waveforms of $I_{\text{sc}}(t)$ and $V_{\text{oc}}(t)$ for any alternating short-circuit current that flows through an internal impedance consisting of a resistor and a capacitor in series. Specifically, $V_{\text{oc}}(t)$ trails $I_{\text{sc}}(t)$ by the angle, ϕ. As evident in Fig. 2.5, ϕ is a function of both time and frequency. Assuming that the waveforms are sinusoidal and can be represented as phasors, ϕ can be determined geometrically using an Argand diagram:

$$\boxed{\phi(t,\,\omega) = \tan^{-1}\left(-\frac{1}{\omega\,R(t)\,C_{\text{eq}}(t)}\right)} \tag{2.27}$$

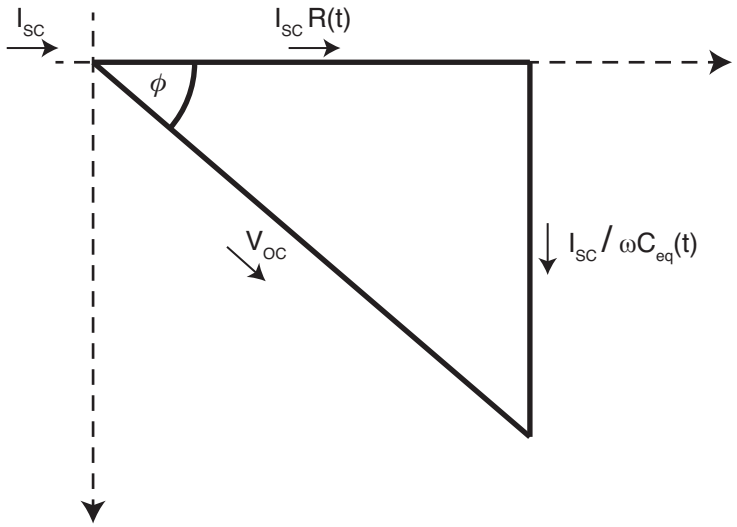

Figure 2.5: Argand diagram. Argand diagram of the phase angle, ϕ, between $I_{\text{sc}}(t)$ and $V_{\text{oc}}(t)$. I_{sc} and V_{oc} are the magnitudes of the phasors of the short-circuit current and open-circuit voltage, respectively. $R(t)$ and $C_{\text{eq}}(t)$ are the time-dependent equivalent resistance and capacitance, respectively, and ω is the angular frequency.

2.3.1.6 *Power dissipated in a load, P_L*

Because the SCEEG can generate both short-circuit current and open-circuit voltage it can also serve as a source of electric power. This is most easily understood by considering what happens when a load impedance, $Z_{\mathrm{L}}(t)$, is placed across the SCEEG's terminals. The resulting circuit changes from that in Fig. 2.6 (**a**) to that in Fig. 2.6 (**b**). In the presence of $Z_{\mathrm{L}}(t)$ the short-circuit current generated by the SCEEG is divided into two parallel branches. A portion of the current is shorted through the internal impedance of the device and the rest flows through the load.

From this figure it is clear that the voltage drop across the internal impedance and the load impedance must be equal. This equivalence means that the ratio of the current flowing through the load, $I_{\mathrm{L}}(t)$, to the total short-circuit current is:

$$\frac{I_{\mathrm{L}}(t)}{I_{\mathrm{sc}}(t)} = \left(1 + \frac{Z_{\mathrm{L}}(t)}{Z^{*}(t)}\right)^{-1} \tag{2.28}$$

From the common expression for electric power, $P = IV$, it is found that the instantaneous power dissipated in the load, $P_{\mathrm{L}}(t)$, is:

$$\boxed{P_{\mathrm{L}}(t) = I_{\mathrm{L}}(t)^2\, Z_{\mathrm{L}}(t) = \left(\frac{I_{\mathrm{sc}}(t)}{1 + \frac{Z_{\mathrm{L}}(t)}{Z^{*}(t)}}\right)^2 Z_{\mathrm{L}}(t)} \tag{2.29}$$

Using Eq. (2.55) it is found that the SCEEG delivers power to the load with an efficiency, $\eta(t)$, of:

$$\eta(t) = \frac{P_{\mathrm{L}}(t)}{P_{\mathrm{TOT}}(t)} = \left(1 + \frac{Z^{*}(t)}{Z_{\mathrm{L}}(t)}\right)^{-1} \tag{2.30}$$

It is worth noting here that the average power dissipated in the load, $\langle P_{\mathrm{L}} \rangle_{\mathrm{avg}}$, can be represented as:

$$\langle P_{\mathrm{L}} \rangle_{\mathrm{avg}} = \langle I_{\mathrm{L}} \rangle_{\mathrm{RMS}}\, \langle V_{\mathrm{L}} \rangle_{\mathrm{RMS}}\, \cos\phi \tag{2.31}$$

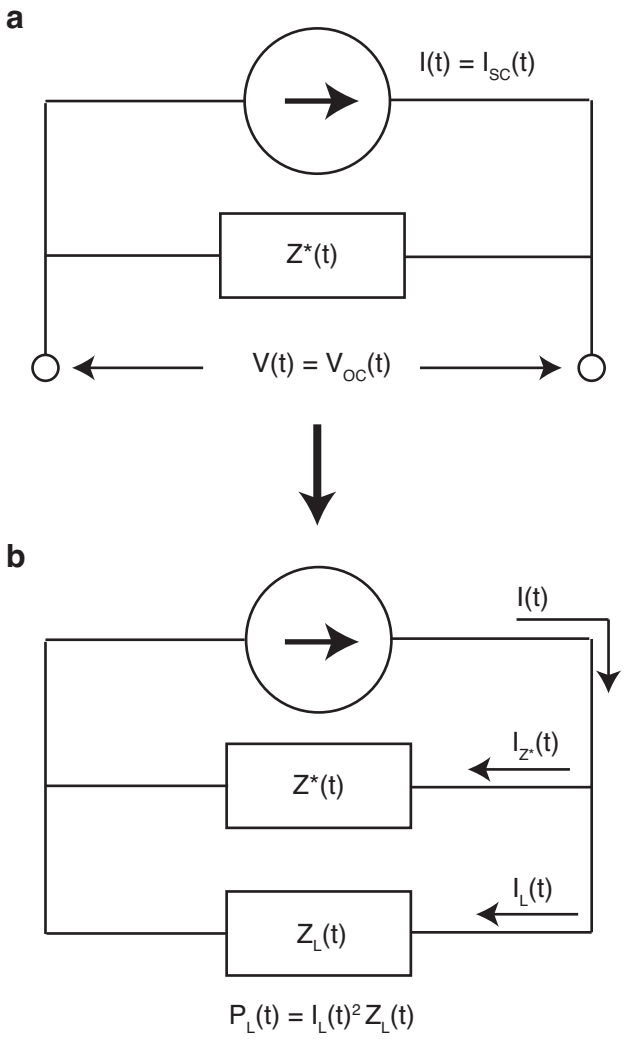

Figure 2.6: Circuit model with load impedance. Illustration of the Norton equivalent circuit of the SCEEG device, (**a**) without and (**b**) with a load impedance, $Z_{\mathrm{L}}(t)$. Power generated by the device is dissipated in the both the load impedance and internal impedance, $Z^*(t)$, as the currents $I_{\mathrm{L}}(t)$ and $I_{Z^*}(t)$, respectively, flow through them. The efficiency, η, of the SCEEG in delivering power to the load impedance is given by Eq. (2.30).

where $\langle I_{\mathrm{L}} \rangle_{\mathrm{RMS}}$ and $\langle V_{\mathrm{L}} \rangle_{\mathrm{RMS}}$ are the root-mean-square (RMS) averages of both the current and the voltage across the load, respectively. If the load is made up of reactive elements, *i.e.* capacitors and inductors, there will be a phase shift, ϕ, between $I_{\mathrm{L}}(t)$ and $V_{\mathrm{L}}(t)$. This phase shift results in a decrease in the real power dissipated in the load compared to the apparent power, $\langle P_{\mathrm{L}} \rangle_{\mathrm{avg}} = \langle I_{\mathrm{L}} \rangle_{\mathrm{RMS}} \langle V_{\mathrm{L}} \rangle_{\mathrm{RMS}}$, that the load would otherwise be expected to dissipate. Physically, the real power is always less than the apparent power for loads with complex impedances because reactive elements store energy, which can then be later recovered, instead of thermally dissipating it. The $\cos\phi$ term in Eq. (2.31) is called the power factor (PF) and it represents the factor by which the real value of $\langle P_{\mathrm{L}} \rangle_{\mathrm{avg}}$ is decreased from its apparent value for a given phase shift, $-\frac{\pi}{2} \leq \phi \leq \frac{\pi}{2}$ [39]:

$$\mathrm{PF} \equiv \cos\phi \tag{2.32}$$

Although it is most common for $0 \leq \mathrm{PF} \leq 1$, there are limited situations where $\mathrm{PF} < 0$ [45]. In experiments conducted so far with SCEEGs, the load has been entirely resistive and it has, therefore, been assumed that $\mathrm{PF} = 1$.

2.3.1.7 *Characteristic timescale of the ΦdC SCEEG's dynamics*

The time-dependent output of the ΦdC SCEEG is not dictated by the characteristic timescale that typically governs a circuit containing a resistor in series with a capacitor, *i.e.* $\tau_{\mathrm{RC}} = RC$. This is because the ΦdC SCEEG's capacitors are not charged or discharged by changing the potential drops across them. Instead, charge is added to and subtracted from the capacitors by changing their capacitance. To date this has been accomplished exclusively by changing the capacitor's area by a moving a droplet of liquid over an electrode. As long as the capacitor at the droplet-electrode interface forms on a timescale that is orders of magnitude faster than the period of the oscillating droplet and no faradaic current flows across the interface, the frequency at which the SCEEG generates short-circuit alternating current is limited only by the frequency of the droplet's motion.

For a droplet of electrolyte solution the timescale on which an electric double layer is formed is known as the Debye time, τ_{D}:

$$\tau_{\mathrm{D}} = \frac{\lambda_{\mathrm{D}}^2}{D} \tag{2.33}$$

and is the time required for a hydrated ion of diffusivity, D, to diffuse over a single Debye screening length, λ_{D}:

$$\lambda_{\mathrm{D}} = \sqrt{\frac{\epsilon\,\epsilon_0\,k_{\mathrm{B}}\,T}{2\,z^2\,e^2\,n_\infty}} \tag{2.34}$$

where ϵ is the relative permittivity of the solution, k_{B} the Boltzmann constant, T the temperature, z the charge state of the ions, e the charge of an electron, and n_∞ the average concentration of the ions in the bulk solution.[15] The Debye screening length is discussed in greater detail in Chapter 3.

The Debye time is a property of the electrolyte solution and is typically on the order of 10^{-9} to 10^{-6} s ($\lambda_{\mathrm{D}} \simeq$ 1–100 nm, $D \simeq 10^3$ μm^2/s) [34]. Due to the difficulties in translating a liq-

[15] Strictly speaking, the form of Eq. (2.34) is valid only for symmetric electrolytes, $z^- = z^+$.

uid droplet at high frequencies, *e.g.* viscous damping and irreversible droplet spreading [46–48], SCEEGs have only been implemented at frequencies < 1 kHz. The period of oscillation, T, at these frequencies is greater than 1 ms, resulting in $T >> \tau_{\mathrm{D}}$. Thus, for oscillation frequencies $< 10^6$–10^9 Hz the timescale of the SCEEG's dynamics is determined exclusively by T.

2.3.1.8 *Summary of analytical expressions*

The list below summarizes the analytical expressions describing the output of the symmetric ΦdC SCEEG. The equations have been generalized to include the case where $n \geq 1$ droplets are simultaneously oscillating in phase with each other.

$$I_{\mathrm{sc}}(t) = n\,\sigma \dot{A}(t) \tag{2.35}$$

$$V_{\mathrm{oc}}(t) = I_{\mathrm{sc}}(t)\,Z^{*}(t) \tag{2.36}$$

$$P_{\mathrm{L}}(t) = \left(\frac{I_{\mathrm{sc}}(t)}{1 + \frac{Z_{\mathrm{L}}(t)}{Z^{*}(t)}} \right)^2 Z_{\mathrm{L}}(t)$$

where

$$Z^{*}(t) = R(t) + \frac{1}{C_{\mathrm{eq}}(t)} \frac{\Delta A(t)}{\dot{A}(t)}$$

$$R(t) = 2\,R_{\mathrm{E}}(t) + \frac{R_{\mathrm{S}}(t)}{n} \tag{2.37}$$

$$C_{\mathrm{eq}}(t) = n\,c_0 \left(\frac{1}{A_{\mathrm{L}}(t)} + \frac{1}{A_{\mathrm{R}}(t)} \right)^{-1} \tag{2.38}$$

2.3.1.9 *Scaling of $\langle I_{sc}\rangle_{RMS}$, $\langle V_{oc}\rangle_{RMS}$, and $\langle P_L\rangle_{avg}$*

To analyze how the average output of a symmetric ΦdC SCEEG scales with the variables $A(t)$, n, and frequency of oscillation, f, it is helpful to assume that the area of overlap between a droplet and the left and right electrodes is sinusoidal in time:

$$A_{\mathrm{L}}(t) = A_{\mathrm{L,0}} + \alpha \sin(\omega\, t) \tag{2.39}$$

$$A_{\mathrm{R}}(t) = A_{\mathrm{R,0}} - \alpha \sin(\omega\, t) \tag{2.40}$$

where α is the amplitude of the area change, ω the angular frequency of oscillation ($\omega = 2\pi f$), and $A_{\mathrm{L,0}}$ and $A_{\mathrm{R,0}}$ the average areas of overlap between the droplet and the left and right electrode, respectively.[16] Using this assumption, Eqs. (2.16), (2.35), (2.36), and (2.38) become:

$$Z^*(t,\, \omega) = R + \frac{1}{j\, \omega\, C_{\mathrm{eq}}(t)} \tag{2.41}$$

$$I_{\mathrm{sc}}(t,\, \omega) = \sigma\, n\, \omega\, \alpha \cos(\omega\, t) \tag{2.42}$$

$$V_{\mathrm{oc}}(t,\, \omega) = I_{\mathrm{sc}}(t,\, \omega)\ Z^*(t,\, \omega) \tag{2.43}$$

$$C_{\mathrm{eq}}(t) = n\, c_0 \left(\frac{\left[A_{\mathrm{L,0}} + \alpha \sin(\omega\, t)\right]\left[A_{\mathrm{R,0}} - \alpha \sin(\omega\, t)\right]}{A_{\mathrm{L,0}} + A_{\mathrm{R,0}}} \right) \tag{2.44}$$

where R and ω are assumed to be constant in time and j is the imaginary unit. It is interesting to note that although Eqs. (2.41) – (2.43) are functions of time, they are also explicitly dependent on

[16] Except for the small, abrupt changes in the overlap area caused by pinning of the droplet to the electrode's surface and the slight asymmetries between $\dot{A}_{\mathrm{L}}(t)$ and $\dot{A}_{\mathrm{R}}(t)$ that this causes, this is generally a reasonable assumption to make.

frequency.[17] Unlike the frequency dependence, however, the time dependence for each is purely oscillatory. As a result, for a constant angular frequency, ω, the equations only change appreciably over half a period of oscillation, $T \,/\, 2 = \pi \,/\, \omega$.

For determining how the SCEEG's output scales, it is essential to eliminate the oscillatory time dependence of the equations above by averaging quadratically over time. The root-mean-square (RMS) of Eq. (2.42) over a single period of oscillation is:

$$\langle I_{\text{sc}} \rangle_{\text{RMS}} = \frac{\sqrt{2}}{2} \, \sigma \, n \, \omega \, \alpha \tag{2.45}$$

It is clear from Eq. (2.45) that $\langle I_{\text{sc}} \rangle_{\text{RMS}}$ scales linearly with all four variables σ, n, ω, and α. Unlike $\langle I_{\text{sc}} \rangle_{\text{RMS}}$, analytical expressions for $\langle V_{\text{oc}} \rangle_{\text{RMS}}$ and $\langle P_{\text{L}} \rangle_{\text{avg}}$ cannot be written due to the form of the internal impedance, $Z^*(t, \omega)$. It is possible, however, to analyze their scaling behaviors by numerically averaging them over time.

Fig. 2.7 shows log-log plots of the computed value for $\langle V_{\text{oc}} \rangle_{\text{RMS}}$ as a function of the peak-to-peak area change, the number of droplets, and the frequency of oscillation. Parameters used in the calculations were chosen to match those of the experiments involving a 20 μL droplet of 1 M HCl oscillating on the G_{MULTI}-SCEEG device. The values of the parameters are listed below in Table 2.1 (p. 46).[18] The plots of Fig. 2.7 show that $\langle V_{\text{oc}} \rangle_{\text{RMS}}$ scales linearly with the peak-to-peak area change and is also linear for large values of both the droplet number and the frequency. $\langle V_{\text{oc}} \rangle_{\text{RMS}}$ scales sub-linearly with droplet number when the number is less than 10 and is independent of frequency when the frequency is less than 100 Hz. Although the scaling behavior of $\langle V_{\text{oc}} \rangle_{\text{RMS}}$ vs. area change agrees with the experimental data in Fig. 2.19 (p. 87), the scaling

[17] Mathematical expressions dependent on both time and frequency are said to be functions of the time–frequency domain and are useful in certain signal-processing applications. See Refs. [49] and [50]. Expressions with time-frequency dependence similar to Eq. (2.42) (p. 43) are also found when taking derivatives with respect to time of the equations describing the displacement of simple harmonic motion [51].

[18] See Fig. 2.19 (p. 87) for the experimental data.

behavior of $\langle V_{\rm oc}\rangle_{\rm RMS}$ vs. droplet number appears to disagree with it. This could simply be due, however, to the lack of enough data points to make an accurate comparison.

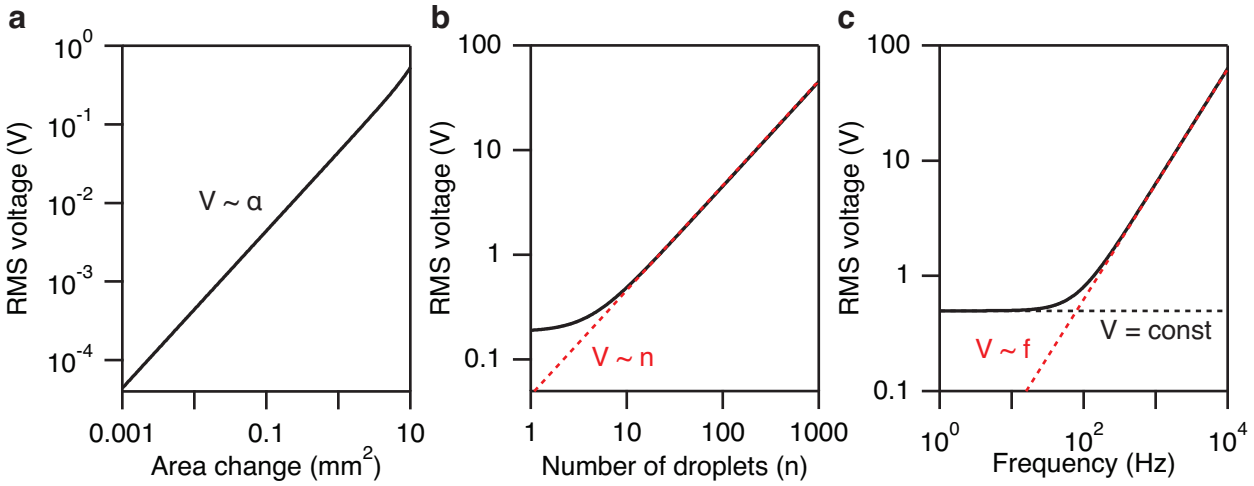

Figure 2.7: Scaling of $\langle V_{\rm oc}\rangle_{\rm RMS}$. Log-log plots of $\langle V_{\rm oc}\rangle_{\rm RMS}$ vs. (**a**) peak-to-peak area change, 2α, (**b**) number of droplets, n, and (**c**) frequency, f. For most values of each of these parameters, $\langle V_{\rm oc}\rangle_{\rm RMS}$ scales linearly.

Fig. 2.8 shows log-log plots of the computed value for $\langle P_{\rm L}\rangle_{\rm avg}$ as a function of the peak-to-peak area change, the number of droplets, and the frequency of oscillation. Again, parameters used in the calculations were chosen to match those of the experiments involving a 20 μL droplet of 1 M HCl oscillating on the G_{MULTI}-SCEEG device. The values of the parameters are listed below in Table 2.1 (p. 46).[19] The plots show that $\langle P_{\rm L}\rangle_{\rm avg}$ scales quadratically with the peak-to-peak area change. It is also quadratic for large values of droplet number. For droplet numbers less than 10, $\langle P_{\rm L}\rangle_{\rm avg}$ scales linearly. For frequencies less than 10 and greater than 100 Hz, $\langle P_{\rm L}\rangle_{\rm avg}$ scales quadratically with frequency. Between 10 and 100 Hz, however, $\langle P_{\rm L}\rangle_{\rm avg}$ is linear in frequency. The scaling behavior of $\langle P_{\rm L}\rangle_{\rm avg}$ with the peak-to-peak area change and droplet number agrees with the experimental data in Fig. 2.20 (p. 89).

[19] See Fig. 2.20 (p. 89) for the experimental data.

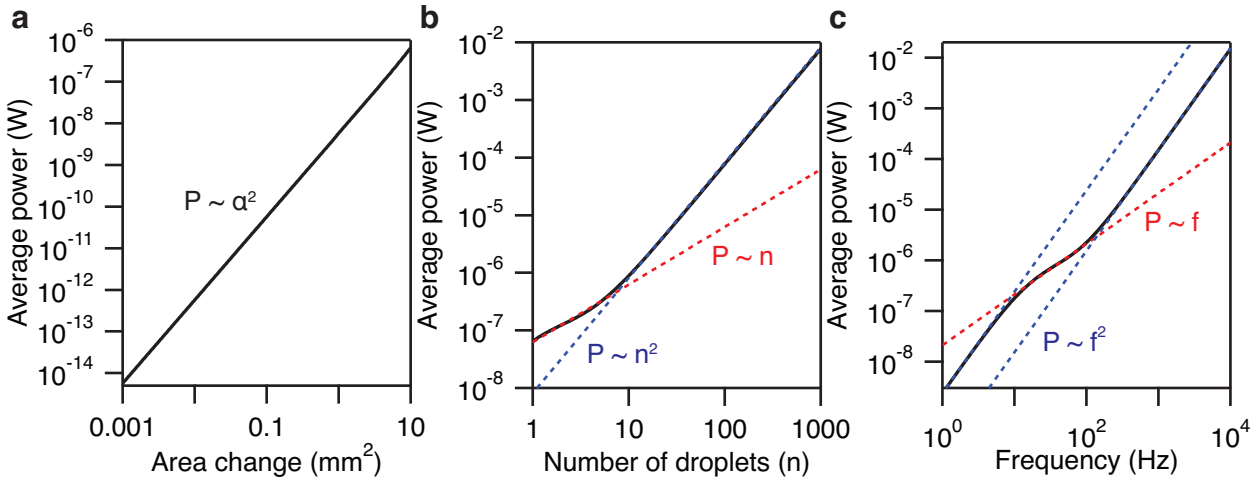

Figure 2.8: Scaling of $\langle P_L \rangle_{avg}$. Log-log plots of $\langle P_L \rangle_{avg}$ vs. (**a**) peak-to-peak area change, 2α, (**b**) number of droplets, n, and (**c**) frequency, f. For most values of each parameter, $\langle P_L \rangle_{avg}$ scales like the square of the parameter.

Parameter	Value (a)	Value (b)	Value (c)	Units	Source
2α	–	2.4	10	mm^2	Figs. 2.19, 2.20 (pp. 87, 89)
n	1	–	1	droplet	
f	30	30	–	Hz	
$A_{L,0}$	10	5.4	10	mm^2	
$A_{R,0}$	10	5.4	10	mm^2	
$Z_L(t) = R_L$	150	150	150	kΩ	
R	50	50	50	kΩ	Table 2.2 (p. 64)
σ	570	570	570	nC/cm^2	Table 3.4 (p. 153)
c_0	10	10	10	nF/mm^2	Table 3.5 (p. 158)
R_S	30	30	30	Ω	Eq (2.18) (p. 31)

Table 2.1: Parameters used in the numerical calculations of $\langle V_{oc} \rangle_{RMS}$ and $\langle P_L \rangle_{avg}$. The parameters and their values used in the numerical calculations of (**a**)–(**c**) of both Figs. 2.7 and 2.8. Values were chosen to coincide with those from experiments. In the experiments, $Z_L(t)$ was due exclusively to R_L, which was assumed to be constant in time. R_S was estimated from the conductivity and geometry of the droplet ($\sigma_c \simeq 280$ mS/cm [52], $l \simeq 4$ mm, $A \simeq 5$ mm^2 $\rightarrow R_S \simeq 30$ Ω)

2.3.2 Asymmetric $\Phi_{\mathrm{i}} dC_{\mathrm{i}} = -C_{\mathrm{j}} d\Phi_{\mathrm{j}}$ SCEEG

The asymmetric $\Phi_{\mathrm{i}} dC_{\mathrm{i}} = -C_{\mathrm{j}} d\Phi_{\mathrm{j}}$ SCEEG is shown in Fig. 2.9. Like the symmetric ΦdC SCEEG, this device contains a pair of serially-connected interfacial capacitors. The top interfacial capacitor uses the ΦdC mechanism of charge transfer while the bottom uses the $Cd\Phi$ mechanism. By definition, the interfacial capacitors have different capacitances per unit area, c_0. As previously mentioned, asymmetric ionic adsorption on the electrodes induces an image charge of density σ at the surface of the electrodes that is of opposite sign as that of the adsorbed ions. In general, the surface charge density induced in the top electrode is not equal to that which is induced in the bottom electrode for this device, *i.e.* $\sigma_{\mathrm{T}} \neq \sigma_{\mathrm{B}}$. Spontaneous charge separation across each interface generates an electric field, $\vec{E}$, and, in turn, a surface potential, Φ. When the device is in a steady state and there is no relative motion between it and the droplet wetting it, the surface potentials of the top and bottom interfaces are equal but opposite, *i.e.* $\Phi_{\mathrm{T}} = -\Phi_{\mathrm{B}}$, and there is no net voltage drop across the SCEEG.

2.3.2.1 *Summary of analytical expressions*

The analytical expressions describing the output of the asymmetric $\Phi_{\mathrm{i}} dC_{\mathrm{i}} = -C_{\mathrm{j}} d\Phi_{\mathrm{j}}$ SCEEG are similar to those describing the output of the symmetric ΦdC SCEEG. The expressions are summarized in the list below and are generalized to include the case where $n \geq 1$ droplets are

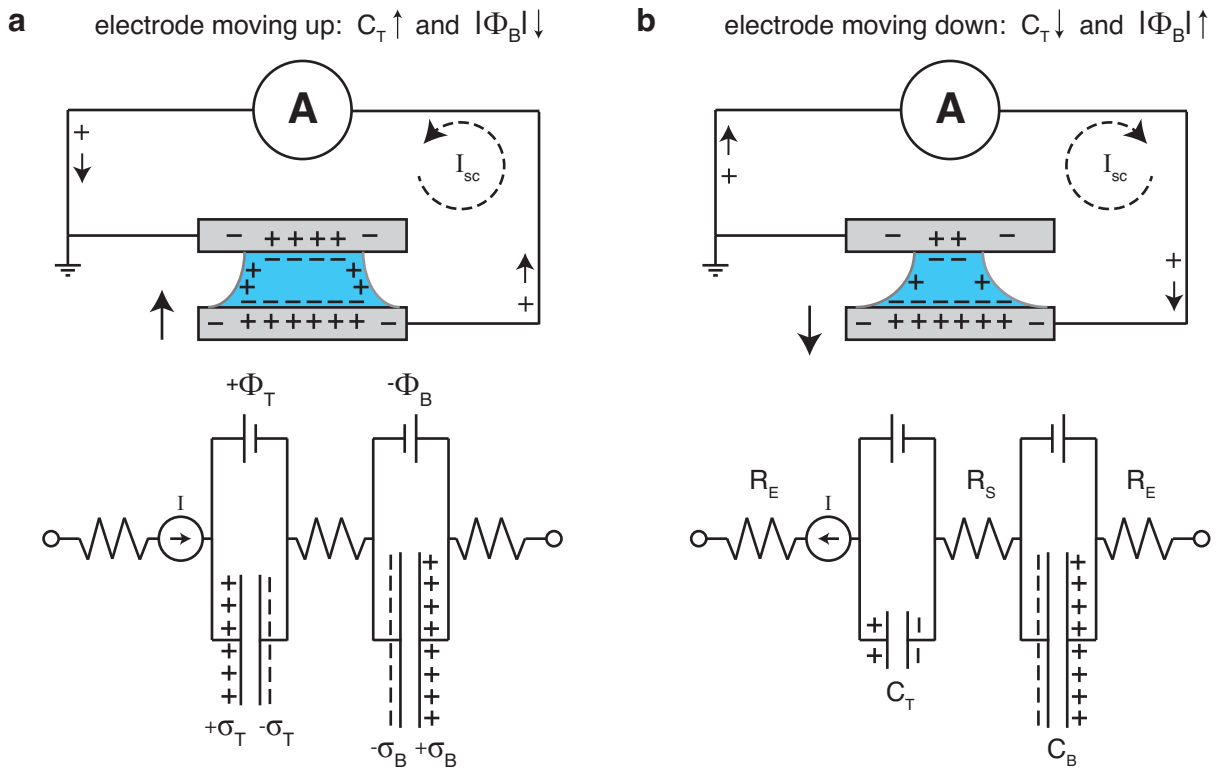

Figure 2.9: Physical model of the asymmetric $\Phi_i dC_i = -C_j d\Phi_j$ SCEEG. Anions $(-)$ in a droplet "bridge" of electrolyte solution (blue) adsorb to the surface of the SCEEG's electrodes (grey), inducing in them positive image charge densities, $+\sigma_T$ and $+\sigma_B$, and generating surface potentials, Φ_T and Φ_B. The compensating positive charge in the solution is carried by the cations $(+)$ to the lateral surfaces of the droplet and is distributed along the air-droplet interface. The compensating negative charge in the electrode is distributed along the electrode's surface. **a**, As the bottom electrode moves upward, the capacitance of the top interfacial capacitor increases while that of the bottom remains constant. During this process positive charge is removed from the bottom electrode and deposited on the top, generating a counterclockwise flow of short-circuit current, I_{sc}, through the circuit as measured by an ammeter. The magnitudes of the surface potential, $|\Phi_B|$, and the surface charge density, $|\sigma_B|$, of the bottom electrode decrease as a result. **b**, As the electrode moves downward, the opposite occurs and a clockwise current is generated. The interfacial capacitor at the top electrode acts as both a capacitor and a current source, I. Impeding the flow of current are resistors and capacitors connected to each other in series: R_E, resistance of the electrode; R_S, resistance of the solution; and C_T and C_B, capacitances of the top and bottom interfacial capacitor, respectively. The size of the interfacial capacitors in each circuit represents the relative magnitude of their capacitance.

simultaneously oscillating in phase with each other.

$$I_{\text{sc}}(t) = n\,\sigma_{\text{T}}\,\dot{A}_{\text{T}}(t) \tag{2.46}$$

$$V_{\text{oc}}(t) = I_{\text{sc}}(t)\,Z^{*}(t)$$

$$P_{\text{L}}(t) = \left(\frac{I_{\text{sc}}(t)}{1+\frac{Z_{\text{L}}(t)}{Z^{*}(t)}}\right)^{2} Z_{\text{L}}(t)$$

where

$$Z^{*}(t) = R(t) + \frac{1}{C_{\text{eq}}(t)}\,\frac{\Delta A_{\text{T}}(t)}{\dot{A}_{\text{T}}(t)}$$

$$R(t) = 2\,R_{\text{E}}(t) + \frac{R_{\text{S}}(t)}{n}$$

$$C_{\text{eq}}(t) = n\left(\frac{1}{c_{0,\text{T}}\,A_{\text{T}}(t)} + \frac{1}{c_{0,\text{B}}\,A_{\text{B}}}\right)^{-1} \tag{2.47}$$

2.3.2.2 *Short-circuit current, I_{sc}*

The asymmetric $\Phi_{\text{i}} dC_{\text{i}} = -C_{\text{j}} d\Phi_{\text{j}}$ SCEEG generates current when the capacitance of its top interfacial capacitor is changed. This is accomplished by moving the bottom electrode up and down, which subsequently changes the area of overlap between the droplet bridge and the top electrode. Because the droplet is pinned to the bottom electrode, the area of overlap there remains constant and, as a result, the bottom interfacial capacitor generates no current. For the same arguments provided in Sect. 2.3.1.1 (p. 25), the moving droplet, and the asymmetric SCEEG in

general, can be thought of as a non-ideal source of current and the expression for $I_{\text{sc}}(t)$ is:

$$\boxed{I_{\text{sc}}(t) = n\,\sigma_{\text{T}}\,\dot{A}_{\text{T}}(t)}$$

For this equation to hold, however, the image charge that is induced in the top electrode by the adsorption of ions must traverse the SCEEG and end up on the bottom electrode as soon as the receding droplet forces the ions bound to the top electrode to desorb. As the droplet dewets the top electrode, the ions that were once adsorbed to the interface are redistributed throughout the droplet with any remaining net charge density distributing itself at the air-droplet interface. The image charge that was once induced in the electrode by these ions, however, can do one of two things: it can either move to the bottom electrode, generating a short-circuit current and increasing both the surface potential and charge density of the bottom interfacial capacitor in the process, or it can redistribute itself in the top electrode such that it remains near the electrode-droplet interface, increasing both the surface potential and charge density of the top interfacial capacitor but generating no short-circuit current. In either case, ions from the solution will adsorb to the electrode-droplet interface in response to the added image charge there.

To a first approximation, whether the excess image charge redistributes itself in the top electrode or moves to the bottom electrode depends on which process is energetically favorable, *i.e.* which process requires the least amount of energy. From Eq. (2.1) (p. 25), the total energy stored in the top and bottom interfacial capacitors, assuming they can both be treated as parallel-plate capacitors, is:

$$W_{\text{TOT}} = W_{\text{T}} + W_{\text{B}} = \frac{1}{2}\left(\frac{q_{\text{T}}^2}{C_{\text{T}}} + \frac{q_{\text{B}}^2}{C_{\text{B}}}\right) \tag{2.48}$$

If an excess amount of image charge, δq, were suddenly added to the interfacial capacitor of the

top electrode, the change in energy of the system, $\Delta W_{\text{TOT,T}}$, would be:

$$\Delta W_{\text{TOT,T}} = \frac{\delta q}{2\,C_{\text{T}}}\left(\delta q + 2\,q_{\text{T}}\right) \tag{2.49}$$

Similarly, if the same amount of excess charge were added to the interfacial capacitor of the bottom electrode, the change in energy of the system, $\Delta W_{\text{TOT,B}}$, would be:

$$\Delta W_{\text{TOT,B}} = \frac{\delta q}{2\,C_{\text{B}}}\left(\delta q + 2\,q_{\text{B}}\right) \tag{2.50}$$

From the ratio, S, of $\Delta W_{\text{TOT,T}}$ to $\Delta W_{\text{TOT,B}}$,

$$S \equiv \frac{\Delta W_{\text{TOT,T}}}{\Delta W_{\text{TOT,B}}} = \frac{C_{\text{B}}}{C_{\text{T}}}\left(\frac{\delta q + 2\,q_{\text{T}}}{\delta q + 2\,q_{\text{B}}}\right) \tag{2.51}$$

one can determine whether it is energetically favorable for an excess amount of image charge, δq, to remain on the top electrode or to traverse the device to the bottom electrode in the event that the area of overlap between the droplet and the top electrode suddenly decreases. For $S > 1$, it is energetically favorable for the image charge to traverse the circuit to the bottom electrode as this requires the least amount of energy.[20] For $S < 1$, the opposite is true and the image charge will remain in the top electrode. For the case where $S = 1$, both processes are equally as energetically favorable and the kinetics of each will dictate which process is dominant.

[20] Because Moon et al.'s asymmetric ITO-SCEEG device has been empirically shown to generate short-circuit current, as inferred from its ability to generate a voltage drop across a load, the excess image charge must move to the bottom interfacial capacitor when the capacitance of the top interfacial capacitor decreases and, therefore, it must be that $S > 1$. This is consistent with the fact that $C_{\text{B}} \,/\, C_{\text{T}} \sim 10^2$ for the device. See Sect. 2.3.3.2 (p. 70) and Table 2.3 (p. 73) for more details.

2.3.2.3 *Open-circuit voltage, V_{oc}*

By definition, the capacitance of only one of the interfacial capacitors of the asymmetric $\Phi_{\mathrm{i}} dC_{\mathrm{i}} = -C_{\mathrm{j}} d\Phi_{\mathrm{j}}$ SCEEG changes. In the example in Fig. 2.9 (p. 48) this is the top capacitor. Assuming that this change in capacitance does in fact result in the generation of short-circuit current and that $c_{0,\mathrm{B}}$ is constant, the surface potential of bottom interfacial capacitor, Φ_{B}, must change to ensure that charge is conserved. Unlike the symmetric ΦdC SCEEG, no excess charge can be absorbed by the bottom interfacial capacitor without also altering Φ_{B}. Thus, the following relation must be true:

$$I_{\mathrm{sc}}(t) = \Phi_{\mathrm{T}} \dot{C}_{\mathrm{T}} = C_{\mathrm{B}} \dot{\Phi}_{\mathrm{B}} \tag{2.52}$$

Solving Eq. (2.52) for $\dot{\Phi}_{\mathrm{B}}$ and integrating with respect to time to find $\Phi_{\mathrm{B}}(t)$ yields:

$$\Phi_{\mathrm{B}}(t) = \Phi_{\mathrm{T}} \left(\frac{c_{0,\mathrm{T}}}{c_{0,\mathrm{B}}} \right) \left(\frac{\Delta A_{\mathrm{T}}(t)}{A_{\mathrm{B}}} \right) + \Phi_{\mathrm{B},0} \tag{2.53}$$

where $\Phi_{\mathrm{B}}(t = 0) = \Phi_{\mathrm{B},0}$. It is assumed in Eqs. (2.52) and (2.53) that C_{T} itself does not impede the flow of $I_{\mathrm{sc}}(t)$. As previously discussed, however, this is the ideal case and is only true if C_{T} perfectly absorbs all charge flowing into it by changing its capacitance.

Because $\Phi_{\mathrm{T}} = -\Phi_{\mathrm{B},0}$, the change in Φ_{B} is equal to the net voltage drop across the interfacial capacitors:

$$\boxed{\Delta\Phi_{\mathrm{B}}(t) = \Phi_{\mathrm{B}}(t) + \Phi_{\mathrm{T}} = \Phi_{\mathrm{T}} \left(\frac{c_{0,\mathrm{T}}}{c_{0,\mathrm{B}}} \right) \left(\frac{\Delta A_{\mathrm{T}}(t)}{A_{\mathrm{B}}} \right)} \tag{2.54}$$

The effect of the change in Φ_{B} on the SCEEG's open-circuit voltage is captured in the form of the asymmetric SCEEG's time-dependent equivalent capacitance, $C_{\mathrm{eq}}(t)$. The expression for $\Delta\Phi_{\mathrm{B}}(t)$ is not equivalent, however, to the expression for the total voltage drop across the capacitive reactance, $V_{\mathrm{X}}(t)$, because $\Delta\Phi_{\mathrm{B}}(t)$ does not include the capacitive reactance of the top interfacial

capacitor, *i.e.*

$$\left[\Delta\Phi_{\mathrm{B}}(t) = \sigma_{\mathrm{T}}\,\frac{\Delta A_{\mathrm{T}}(t)}{C_{\mathrm{B}}}\right] \;\neq\; \left[V_{\mathrm{X}}(t) = \sigma_{\mathrm{T}}\,\frac{\Delta A_{\mathrm{T}}(t)}{C_{\mathrm{eq}}}\right]$$

The form of $V_{\mathrm{X}}(t)$ better describes the actual behavior of the SCEEG because any current through the device will be impeded by the reactance of both the bottom and top capacitors.

Although the expressions for the time-dependent, internal impedance, $Z^{*}(t)$, and internal resistance, $R(t)$, retain their familiar forms,

$$\boxed{Z^{*}(t) = R(t) + \frac{1}{C_{\mathrm{eq}}(t)}\,\frac{\Delta A_{\mathrm{T}}(t)}{\dot{A}_{\mathrm{T}}(t)}}$$

$$\boxed{R(t) = 2\,R_{\mathrm{E}}(t) + \frac{R_{\mathrm{S}}(t)}{n}}$$

the expression for the equivalent capacitance, $C_{\mathrm{eq}}(t)$, is changed to reflect the time-independence of the bottom interfacial capacitor's capacitance:

$$\boxed{C_{\mathrm{eq}}(t) = n\left(\frac{1}{c_{0,\mathrm{T}}\,A_{\mathrm{T}}(t)} + \frac{1}{c_{0,\mathrm{B}}\,A_{\mathrm{B}}}\right)^{-1}}$$

Like the symmetric ΦdC SCEEG, the expression for the open-circuit voltage is again given by:

$$\boxed{V_{\mathrm{oc}}(t) = I_{\mathrm{sc}}(t)\,Z^{*}(t)}$$

2.3.2.4 *Power dissipated in a load, P_L*

As before, from the common expression for electric power, $P = I\,V$, one finds that the instantaneous power, $P_{\mathrm{L}}(t)$, dissipated in a complex load impedance, $Z_{\mathrm{L}}(t)$, is:

$$\boxed{P_{\mathrm{L}}(t) = I_{\mathrm{L}}(t)^2\, Z_{\mathrm{L}}(t) = \left(\frac{I_{\mathrm{sc}}(t)}{1 + \frac{Z_{\mathrm{L}}(t)}{Z^*(t)}}\right)^2 Z_{\mathrm{L}}(t)}$$

whereas the average power, $\langle P_{\mathrm{L}} \rangle_{\mathrm{avg}}$, dissipated in that load is:

$$\langle P_{\mathrm{L}} \rangle_{\mathrm{avg}} = \langle I_{\mathrm{L}} \rangle_{\mathrm{RMS}}\ \langle V_{\mathrm{L}} \rangle_{\mathrm{RMS}}\ \cos\phi$$

2.3.2.5 *Characteristic timescale of the $\Phi_i dC_i = -\,C_j d\Phi_j$ SCEEG's dynamics*

Although one of the $\Phi_{\mathrm{i}} dC_{\mathrm{i}} = -\,C_{\mathrm{j}} d\Phi_{\mathrm{j}}$ SCEEG's capacitors is charged and discharged, *i.e.* the bottom capacitor across which the voltage drop increases and decreases, the timescale of the device's output is dictated primarily by the period of oscillation, T, of the capacitance of the top capacitor. Like the ΦdC SCEEG, this is again due to the fact that the changing capacitance acts as an alternating current source with period T. This current source forces a charging/discharging response in the opposing capacitor instead of allowing it to naturally charge/discharge on the usual timescale of $\tau_{\mathrm{RC}} = RC$. Because the oscillation period is usually much longer than the Debye time, *i.e.* $T >> \tau_{\mathrm{D}}$, the change in capacitance and, hence, the generated current are limited only by the timescale of T.[21]

There is a situation in the operation of the device, however, where τ_{RC} does influence the timescale of the SCEEG's output. If the decreasing capacitance of the top interfacial capacitor forces the bottom interfacial capacitor to charge but does not then force that capacitor to discharge by sub-

[21] See Sect. 2.3.1.7 (p. 41) for a discussion of the Debye time.

sequently increasing its capacitance, the bottom interfacial capacitor will discharge naturally until both its surface potential and charge density (assuming its capacitance per unit area, c_0, remains constant) reach their steady state values, $\Phi_{\mathrm{B},0}$ and $\sigma_{\mathrm{B},0}$, respectively. The process of discharging the bottom interfacial capacitor can occur through one of two possible mechanisms:

1. **Generation of I_{sc} over a characteristic timescale of τ_{RC}**

   If the RC time constant, τ_{RC}, is much shorter than the characteristic timescale of ionic desorption, τ_{d}, *i.e.* the timescale over which ions, whose concentration is in excess of its steady-state value, desorb from the interface as a result of thermal fluctuations, the excess charge stored on the bottom interfacial capacitor, $q_{\mathrm{ex}} \equiv \Delta\sigma_{\mathrm{B}}\, A_{\mathrm{B}} = \sigma_{\mathrm{T}}\, \Delta A_{\mathrm{T}}$, will be converted into electric current. In turn, the current will ultimately be dissipated in the device's internal resistance in the form of electric power. Mathematically, the time-dependent discharge of the excess voltage, $V_{\mathrm{ex}}(t)$, and excess charge, $q_{\mathrm{ex}}(t)$, of the bottom interfacial capacitor and the resulting excess current, $I_{\mathrm{ex}}(t)$, can all be written as functions that decrease exponentially in time:

$$V_{\mathrm{ex}}(t) = V_{\mathrm{ex},0} \exp\left(-\,t\,/\tau_{\mathrm{RC}}\right) \tag{2.55}$$

$$q_{\mathrm{ex}}(t) = q_{\mathrm{ex},0} \exp\left(-\,t\,/\tau_{\mathrm{RC}}\right) \tag{2.56}$$

$$I_{\mathrm{ex}}(t) = I_{\mathrm{ex},0} \exp\left(-\,t\,/\tau_{\mathrm{RC}}\right) \tag{2.57}$$

where

$$\tau_{\mathrm{RC}} \equiv R\, C_{\mathrm{eq}} \tag{2.58}$$

$$V_{\mathrm{ex,0}} \equiv \Delta\Phi_{\mathrm{B}} = \frac{\Delta\sigma_{\mathrm{B}}}{c_{\mathrm{0,B}}} \tag{2.59}$$

$$I_{\mathrm{ex,0}} \equiv \frac{V_{\mathrm{ex,0}}}{R} = \frac{\Delta\sigma_{\mathrm{B}}}{R\, c_{\mathrm{0,B}}} \tag{2.60}$$

$$q_{\mathrm{ex,0}} \equiv -\, I_{\mathrm{ex,0}}\ \tau_{\mathrm{RC}} = -\,\frac{\Delta\sigma_{\mathrm{B}}\, C_{\mathrm{eq}}}{c_{\mathrm{0,B}}} \tag{2.61}$$

Both the excess surface potential, $\Delta\Phi_{\mathrm{B}}$, and the excess charge, $\Delta\sigma_{\mathrm{B}}$, on the bottom interfacial capacitor will exponentially decay over the characteristic timescale τ_{RC} until their steady state values, $\Phi_{\mathrm{0,B}}$ and $\sigma_{\mathrm{0,B}}$, are reached.

2. **Ionic desorption over a characteristic timescale of τ_{d}**

   On the other hand, if $\tau_{\mathrm{d}} << \tau_{\mathrm{RC}}$, the excess ionic charge stored on the bottom interfacial capacitor will decay before it can generate any meaningful current flow through the device. The excess charge on the bottom interfacial capacitor will be removed as ions desorb from the interface, a process that continues until the stead-state density of the ions is reached. While this will create a small current over a short distance in the direction normal to the interface, the probabilistic nature of thermally-driven desorption makes it unlikely that this process will generate a concerted flow of image charge large enough to produce a short-circuit current at the device level.

   According to the Langmuir adsorption model, the rate of desorption, r_{d}, is equal to the prod-

uct of the desorption reaction rate constant, k_{d}, and the relative concentration of bound ions, Θ_{r}, *i.e.* $\Theta_{\mathrm{r}} = \Theta \,/\, \Theta_{\mathrm{sat}}$ where Θ is the number of occupied binding sites and Θ_{sat} is the total number of occupied binding sites at saturation. Assuming the rate of the desorption reaction is first order in Θ_{r},[22] the expression for r_{d} is:

$$r_{\mathrm{d}} = \frac{d\Theta}{dt} = -\, k_{\mathrm{d}}\, \Theta_{\mathrm{r}} \tag{2.62}$$

where

$$k_{\mathrm{d}} = \nu\, \exp\left(-\, E_{\mathrm{d}} \,/\, k_{\mathrm{B}}\, T\right) \tag{2.63}$$

In Eq. (2.63), ν is the frequency factor, *i.e.* the number of successful desorption attempts per unit time, $k_{\mathrm{B}}\, T$ is the thermal energy of the system, and E_{d} is the activation energy for the desorption reaction [54]. E_{d} can be thought of as being approximately equal to the binding energy of the ions to the interface, *i.e.* $E_{\mathrm{d}} \simeq E_{\mathrm{B}}$. In general, Eq. (2.63) is known as the Arrhenius equation and it is widely used to describe how the rate of a chemical reaction depends on temperature.

To find the characteristic timescale of desorption, τ_{d}, one integrates Eq. (2.62) with respect to time to find an expression for $\Theta(t)$. Doing so gives:

$$\Theta(t) = \Theta_0\, \exp\left(-\, t \,/\, \tau_{\mathrm{d}}\right) \tag{2.64}$$

where

$$\tau_{\mathrm{d}} \equiv \frac{\Theta_{\mathrm{sat}}}{k_{\mathrm{d}}} = \frac{\Theta_{\mathrm{sat}}}{\nu}\, \exp\left(E_{\mathrm{d}} \,/\, k_{\mathrm{B}}\, T\right) \tag{2.65}$$

[22] The order, x, of a reaction with respect to a reactant A is defined as the exponent to which the concentration of A, $[A]$, is raised in the rate equation, *i.e.* $r = k\, [A]^x$. The total reaction order, n, is the sum of the exponents of all the concentration terms appearing in the rate equation. For $r = k\, [A]^x\, [B]^y$, $n = x + y$ [53].

Because each bound ion carries a charge, $q = z$, where z is the charge state of the ion, the desorption of charge, in excess of that in the steady state, from the interfacial capacitor can be written using Eq. (2.64):

$$q_{\text{ex}}(t) = z\,\Theta_{\text{ex}}(t) = q_{\text{ex,0}}\,\exp\left(-\,t\,/\,\tau_{\text{d,ex}}\right) \tag{2.66}$$

where

$$q_{\text{ex,0}} \equiv z\,\Theta_{\text{ex,0}} = z\,\left(\Theta_{\text{i}} - \Theta_0\right) \tag{2.67}$$

$$\tau_{\text{d,ex}} \equiv \frac{\Theta_{\text{ex,sat}}}{\nu_{\text{ex}}}\,\exp\left(E_{\text{d,ex}}\,/\,k_{\text{B}}\,T\right) \tag{2.68}$$

and where $\Theta_{\text{ex,0}} = \Theta_{\text{i}} - \Theta_0$ is the initial number of bound ions that is in excess of the number in the steady-state, Θ_0.

Because ions fall into a potential energy "well" as they absorb to the interface, they release energy in the process. This energy is the binding energy, E_{B}, of the ion to the interface and represents the energetic barrier that must then be overcome for the ions to escape the well and desorb.[23] For this reason, the rate of desorption at the interface is much slower than the rate of absorption. However, when concentrated at the interface in excess of their steady-state density, overcrowding of the ions results in the excess ions being less strongly bound to the electrode because of their mutual repulsion of one another. This reduces the energetic barrier to desorption and, as a result, increases the desorption rate.

[23] On average, the ions likely experience an attractive, screened Coulomb potential arising from their electrostatic attraction to image charges in the electrode and from their ability to screen the resulting electric field. This potential is effective over a long range because it scales as $\sim \left(e^{-\,r\,/\,\lambda_{\text{D}}}\right)\,/\,r$, where λ_{D} is the Debye length and r is the distance to the interface. Additionally, the ions experience a short-range, repulsive potential due to their finite size and mutual repulsion that scales as $\sim 1\,/\,r^n$, where $n \to \infty$ [38, 55].

The two discharge mechanisms listed above are believed to occur regularly during the normal operation of the SCEEG as a result of transient pinning of the droplet to the top electrode. For $\tau_{\text{RC}} << \tau_{\text{d}} \sim T$, however, the current and voltage generated by these transient pinning events decays too quickly to meaningfully contribute to $I_{\text{sc}}(t)$ and $V_{\text{oc}}(t)$.[24] Similarly, if $\tau_{\text{d}} << \tau_{\text{RC}} \sim T$, uncompensated changes in the area of overlap at the top electrode negligibly impact the SCEEG's current and voltage outputs.

[24] In Ref. [8], $\tau_{\text{RC}} \simeq 5 - 10$ ms and $T = 33$ ms.

2.3.3 Experimental verification of the model

The physical models for the symmetric ΦdC and asymmetric $\Phi_{\mathrm{i}} dC_{\mathrm{i}} = -C_{\mathrm{j}} d\Phi_{\mathrm{j}}$ SCEEGs that were developed in Sects. 2.3.1 (p. 21) and 2.3.2 (p. 47) were compared to experimental data in order to determine their veracity. The symmetric ΦdC SCEEG model was compared to data that was taken using the $\mathrm{G_{MULTI}}$-SCEEG device whereas the asymmetric $\Phi_{\mathrm{i}} dC_{\mathrm{i}} = -C_{\mathrm{j}} d\Phi_{\mathrm{j}}$ SCEEG model was compared to data that was taken by Moon et al.'s ITO-SCEEG device. In both cases, the model sufficiently matched the data so as to prove that the two are at least in qualitative agreement.

2.3.3.1 *Symmetric ΦdC SCEEG*

The physical model of the symmetric ΦdC SCEEG proposed in Sect. 2.3.1 (p. 21) was experimentally verified in two different ways. In the first, the circuit model was tested by applying an external AC potential to a $\mathrm{G_{MULTI}}$-SCEEG device. Fig. 2.10 shows the current flowing through the device in response to such a potential. The G-SCEEG was connected to a function generator which supplied an AC voltage ramp and the resulting current was measured using a Keithley 427 current amplifier connected in series with the device (input resistance $\simeq 15\ \Omega$).

Due to the externally applied voltage, charge transfer between the graphene electrode and the electrolyte droplet is more likely to occur. Therefore, the droplet-graphene interface is modeled in Fig. 2.10 (**a**) as a capacitor, C, in parallel with a faradaic resistor, R_{F}, of finite resistance *i.e.* the interface is no longer assumed to be ideally polarizable. In the experiment, however, a fast voltage ramp rate, ν, and a narrow potential range, $V_{\text{p-p}}$, were used in an attempt to prevent electrochemical reactions, and the resulting faradaic current they create, from occurring ($\nu = 100$ V/s and $V_{\text{p-p}} = 500$ mV). For the sake of completeness, the surface potential, Φ, across the interfacial capacitors is also shown in the figure.

According to this circuit model, the response current, $I(t)$, to the voltage ramp, $V(t) = \nu\, t$,

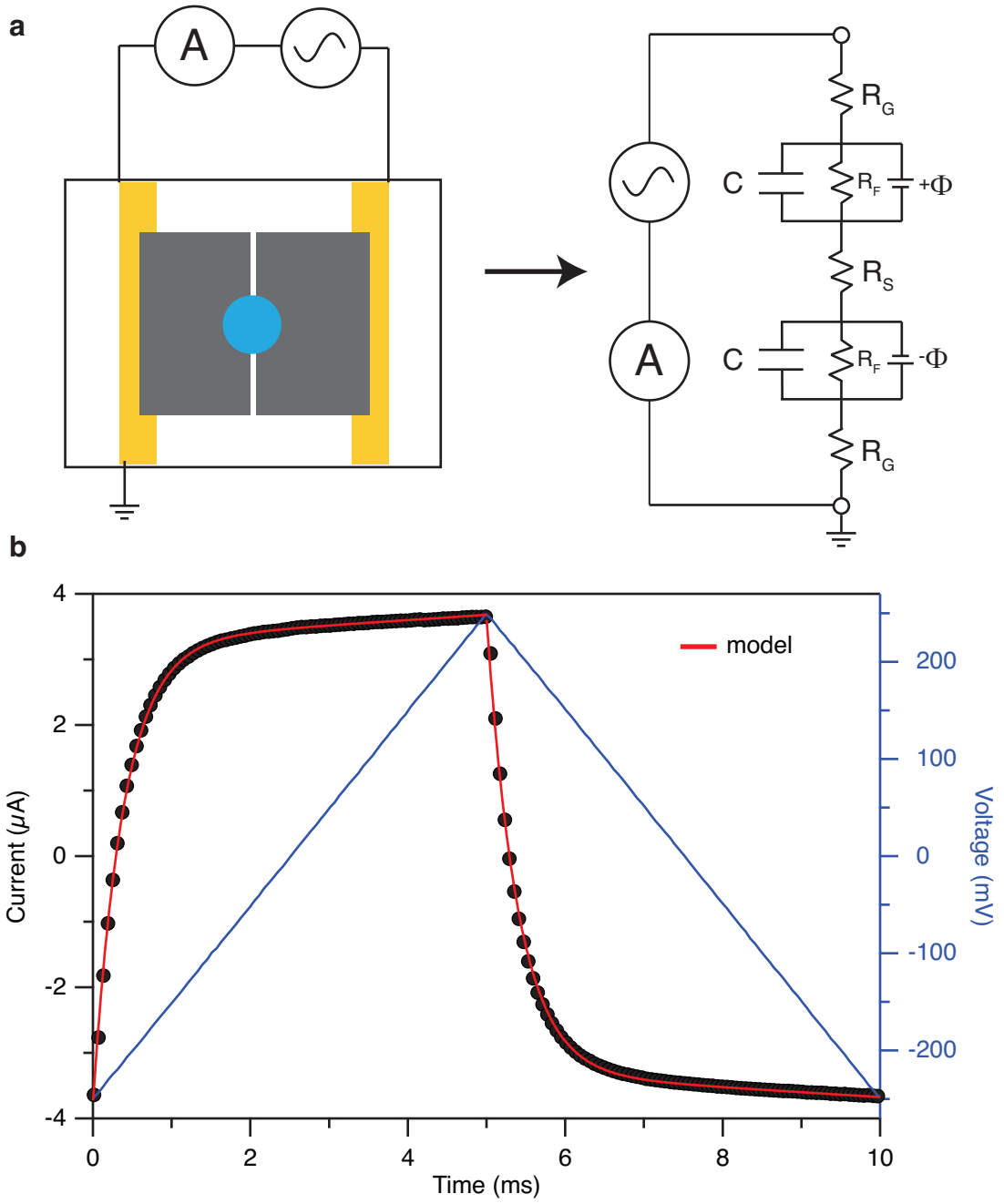

Figure 2.10: G-SCEEG response to an applied AC potential. **a**, Illustration of the G-SCEEG device connected in series to a ammeter and an AC voltage source (left) and its equivalent circuit model (right). Because an external voltage is applied across the device, the droplet-graphene interface is modeled as a capacitor, C, in parallel with a faradaic resistance, R_{F}. The surface potential, Φ, across each interface is also shown and is due to the natural accumulation of ions that occurs at the graphene's surface. **b**, Current vs. time response (black dots) of the G-SCEEG due to an applied AC voltage ramp (blue line). The red line represents a fit of the data using Eq. (2.73) for both positive and negative values of ν. Droplet $= 15$ μL of 1 M HCl, frequency $= 100$ Hz, $\nu = \dot{V}(t) = \pm 100$ V/s.

should obey the following first-order differential equation:

$$\dot{I}(t) + \left[\frac{2\,R_{\mathrm{F}} + R}{R_{\mathrm{F}}\,R\,C}\right] I(t) = \frac{\nu}{R}\left(1 + \frac{t}{R_{\mathrm{F}}\,C}\right) \tag{2.69}$$

Here, ν is the slope of the voltage ramp, $\nu \equiv \dot{V}(t)$, and R is the equivalent resistance of the device ($R = 2\,R_{\mathrm{G}} + R_{\mathrm{S}}$).

Eq. (2.69) is derived by applying both of Kirchhoff's circuit laws to the circuit in Fig. 2.10 (**a**). Kirchhoff's laws give:

$$V(t) = V_{\mathrm{R}}(t) + 2\,V_{\mathrm{R_FC}}(t) \tag{2.70}$$

$$I(t) = I_{\mathrm{C}}(t) + I_{\mathrm{R_F}}(t) \tag{2.71}$$

where $V_{\mathrm{R}}(t)$ and $V_{\mathrm{R_FC}}(t)$ are the voltage drops across the device's equivalent resistance, R, and a single $R_{\mathrm{F}}\,C$ loop, respectively. $I_{\mathrm{C}}(t)$ and $I_{\mathrm{R_F}}(t)$ are the currents through branches of the $R_{\mathrm{F}}\,C$ loop containing the capacitor, C, and the faradaic resistor, R_{F}, respectively. Using Ohm's law, $V = I\,R$, the definition of capacitance, $q = C\,V$, and Eq. (2.70), Eq. (2.71) can be rewritten as:

$$I(t) = \frac{C}{2}\frac{d}{dt}\big[V(t) - I(t)\,R\big] + \frac{V(t) - I(t)\,R}{2\,R_{\mathrm{F}}} \tag{2.72}$$

Collecting and rearranging the terms in Eq. (2.72) and using the relation $V(t) = \nu\,t$ results in Eq. (2.69). Because Eq. (2.69) is a first-order ordinary differential equation, it can be solved by integrating it with respect to time after first determining the appropriate integrating factor.[25] For

[25] The differential equation $y' + P(x)\,y = Q(x)$ can be made integrable if the following integrating factor is found: $e^{\,\mu(x)}$, where $\mu(x) = \int P(x)\,dx$. Multiplying $y(x)$ by $e^{\,\mu(x)}$ in the equation above and integrating both sides with respect to x gives the following solution: $y(x) = e^{-\,\mu(x)} \int e^{\,\mu(x)}\,Q(x)\,dx$. See Ref. [56] or any other textbook on mathematical physics for more details.

the initial condition $I(t=0)=0$, the solution is:

$$\boxed{I(t)=\frac{\nu}{2\,R_{\mathrm{F}}+R}\left[t+R_{\mathrm{F}}\,C\left[\frac{R}{2\,R_{\mathrm{F}}+R}-1\right]\left(\exp\left(-\frac{2\,R_{\mathrm{F}}+R}{R_{\mathrm{F}}\,R\,C}t\right)-1\right)\right]} \tag{2.73}$$

When the equivalent faradaic resistance is much greater than the equivalent resistance of the device, *i.e.* $2\,R_{\mathrm{F}} >> R$, Eq. (2.73) simplifies to:

$$I(t)=\frac{\nu}{2\,R_{\mathrm{F}}}t+\frac{\nu\,C}{2}\left[1-\exp\left(-\frac{2}{R\,C}t\right)\right] \tag{2.74}$$

Because $V(t)=\nu\,t$, Eq. (2.74) can be rewritten as a function of V:

$$I(V)=\frac{1}{2\,R_{\mathrm{F}}}V+\frac{\nu\,C}{2}\left[1-\exp\left(-\frac{2}{\nu\,R\,C}V\right)\right] \tag{2.75}$$

Eq. (2.75) shows that $I(V)$ is the sum of two terms: the first is linear in voltage and is due to current flowing through the faradaic resistors; the second saturates with voltage and is due to the charging of the capacitors. The second term is dominant for small voltages whereas the first term dominates for large voltages. This behavior is clearly evident in the current trace of Fig. 2.10 (**b**). Fig. 2.10 (**b**) is a plot of $I(t)$ that was measured when an AC voltage ramp was applied to the G-SCEEG containing a 15 μL droplet of 1 M HCl. The red line is a fit of the data using Eq. (2.73) with C, R_{F}, and R as free fitting parameters. The quality of the fit suggests that the circuit model accurately represents the G-SCEEG. From this fit, the fitting parameters were determined to be: $C=68$ nF, $R_{\mathrm{F}}=640$ kΩ, and $R=12$ kΩ. Because the droplet is stationary in this experiment, C, R_{F}, and R are all assumed to be constant in time. This is not true, however, for an oscillating droplet. In that case, C and R are generally functions of time, $C(t)$ and $R(t)$, as previously discussed in Sect. 2.3.1.

The second way the symmetric ΦdC SCEEG model was experimentally verified was by com-

paring Eqs. (2.35) and (2.36) to the G-SCEEG's output for $I_{sc}(t)$ and $V_{oc}(t)$, respectively.[26] Shown in Fig. 2.11 (p. 65) are time traces of $I_{sc}(t)$ and $V_{oc}(t)$ for a 30 μL droplet of 6 M HCl oscillating at 33 Hz. Superimposed on each of these is the time trace predicted by the model. Values for the parameters used in the model are given below in Table 2.2. The only parameter that was adjusted to best fit the model to the data was the internal resistance, R. R was treated as a fitting parameter, and was assumed to be constant, because the change in resistance of the graphene electrodes when they are exposed to a droplet of 6 M HCl is unknown. The value of R that produced the best fit of the model to the trace of $V_{oc}(t)$ was $R \simeq 50$ kΩ. Based on Fig. 2.27 (p. 102) ($2\,R_E \simeq 14$ kΩ) and on the conductivity and geometry of the droplet ($\sigma_c \simeq 850$ mS/cm [52], $l \simeq 3$ mm, $A \simeq 10$ mm^2; using Eq. (2.18), $R_S \simeq 4\ \Omega$), this estimate seems reasonable. Interestingly, this value of R is approximately equal to $\langle V_{oc}(t)\rangle_{RMS} \,/\, \langle I_{sc}(t)\rangle_{RMS} \simeq 50$ kΩ, suggesting that the device's capacitive reactance only minimally contributes to its average impedance.

Parameter	Value	Units	Source
n	1	droplet	experiment
R	50	kΩ	fitting parameter
σ	900	nC/cm^2	Table 3.4 (p. 153)
c_0	15	nF/mm^2	Table 3.5 (p. 158)

Table 2.2: Parameters used in the model of $I_{sc}(t)$ and $V_{oc}(t)$. The parameters, and their values, used to calculate the time traces of the model (red circles) in Fig. 2.11. Values for the model were chosen to coincide approximately with those that were experimentally determined (where applicable, they can be found in the tables of Chapter 3). R, however, was treated as a free fitting parameter. The value of R that was used was that which resulted in the best fit of the model to the data.

Instead of treating R as a fitting parameter, however, it is possible to calculate it from Eq. (2.16) using the experimentally measured time traces of $I_{sc}(t)$, $V_{oc}(t)$, $A(t)$, and $\dot{A}(t)$:

$$R = \left\langle \frac{V_{oc}(t)}{I_{sc}(t)} - \frac{1}{C_{eq}(t)} \frac{\Delta A(t)}{\dot{A}(t)} \right\rangle_{avg} \tag{2.76}$$

[26] See Fig. 2.14 (p. 77) for an illustration of a typical experiment.

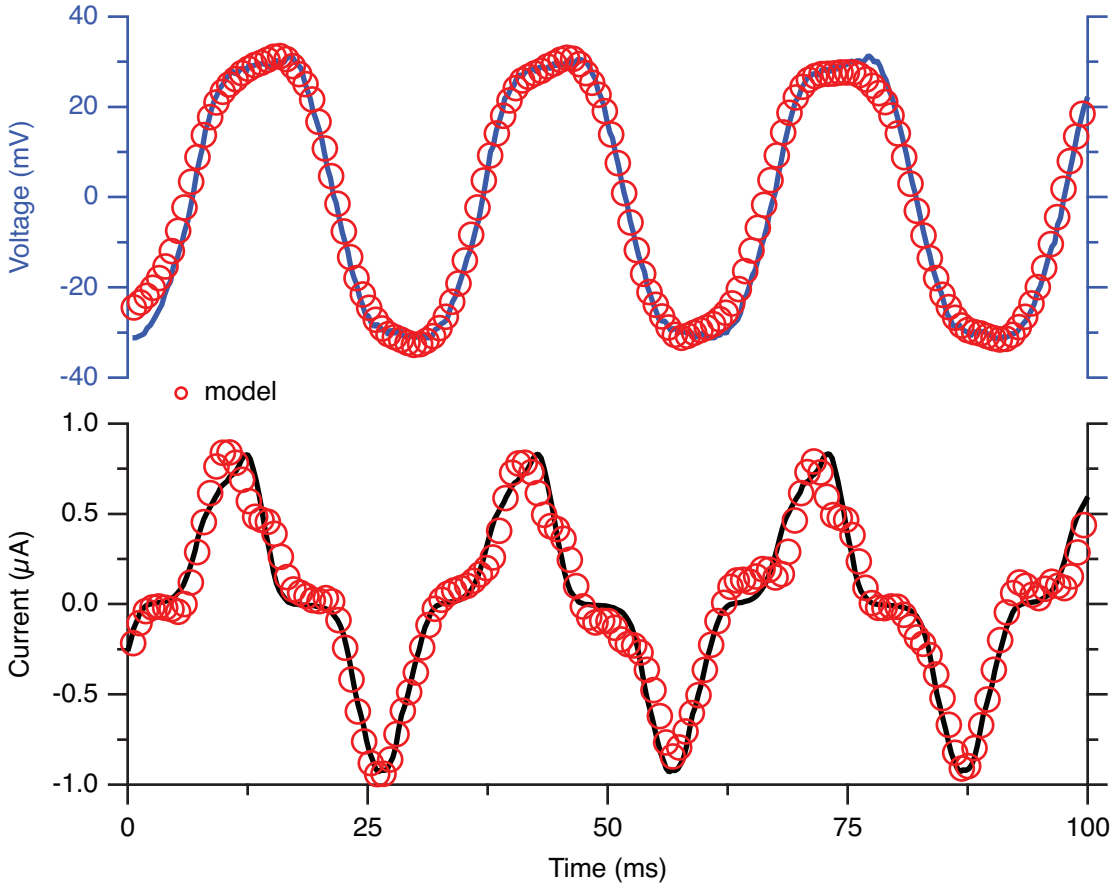

Figure 2.11: G-SCEEG physical model vs. data. Comparing Eqs. (2.35) (p. 42) and (2.36) (p. 42) (both represented as red circles) to the time traces of $I_{\text{sc}}(t)$ (black line) and $V_{\text{oc}}(t)$ (blue line), respectively, shows that the physical model accurately describes the time-dependent behavior of the device. Droplet $= 30$ μL of 6 M HCl, oscillation frequency $= 33$ Hz. Values for $A(t)$ and $\dot{A}(t)$ were experimentally determined and used in the model. Values used for other model parameters are listed in Table 2.2 (p. 64). The area data used in the model of $V_{\text{oc}}(t)$ were resampled such that amplitude modulations occurring at frequencies > 33 Hz were removed.

Computing a value for R using Eq. (2.76) requires that the relative phase shifts between all the oscillatory terms be accurately known. Due to experimental constraints, however, these phase shifts could only be roughly estimated. As a result, it is believed that treating R as a free fitting parameter is a more accurate way of determining its value.

Because the motion of the droplet is oscillatory but not strictly sinusoidal, the areas of overlap, $A_{\mathrm{L}}(t)$ and $A_{\mathrm{R}}(t)$, between the droplet and the left and right graphene electrodes, respectively, were experimentally measured as a function of time and their average magnitude was subsequently used in the model.[27] The average magnitude of their rates of change, $\dot{A}(t)$, was calculated from the area data and also used in the model. If the G-SCEEG were ideally symmetric then $\dot{A}_{\mathrm{L}}(t) = -\dot{A}_{\mathrm{R}}(t)$ for all time t. The area data showed, however, that $\dot{A}_{\mathrm{L}}(t) \simeq -\dot{A}_{\mathrm{R}}(t)$ over the course of the experiment. When $\dot{A}_{\mathrm{L}}(t) \neq -\dot{A}_{\mathrm{R}}(t)$ the G-SCEEG behaves in a manner similar to an asymmetric $\Phi_{\mathrm{i}} dC_{\mathrm{i}} = -C_{\mathrm{j}} d\Phi_{\mathrm{j}}$ SCEEG, *i.e.* a change in capacitance at one interfacial capacitor results in a change in surface potential at the other. In this situation charge must still be conserved, meaning the amount of charge that is removed from the left electrode must be equal to the amount that is added to the right. If charge is removed from the left electrode by decreasing its area of overlap with the droplet, $\dot{A}_{\mathrm{L}}(t) < 0$, but the overlap area with the right electrode (and hence the interfacial capacitance) stays constant, $A_{\mathrm{R}}(t) = A_{\mathrm{R}}$, the surface potential of the right electrode, Φ_{R}, must increase according to:

$$I_{\mathrm{sc}}(t) = C_{\mathrm{R}}\,\dot{\Phi}_{\mathrm{R}} = \Phi_{\mathrm{L}}\,\dot{C}_{\mathrm{L}} \tag{2.77}$$

The resulting change in surface potential of the right electrode, $\Delta\Phi_{\mathrm{R}}(t)$, is:

$$\Delta\Phi_{\mathrm{R}}(t) = \Phi_{\mathrm{L}} \left(\frac{\Delta A_{\mathrm{L}}(t)}{A_{\mathrm{R}}} \right) \tag{2.78}$$

[27] The area data were obtained using video of the droplet's motion relative to the SCEEG which was recorded using a digital microscope and a strobe light. See Fig. 2.16 (p. 81) for a photograph of the experimental setup.

where c_0 is assumed to be identical for each interfacial capacitor and, therefore, falls out of Eq. (2.78). For small, asymmetric changes in area, *i.e.* $\Delta A_{\mathrm{L}}(t) << A_{\mathrm{R}}$, it is clear that the change in surface potential is negligible, *i.e.* $\Delta\Phi_{\mathrm{R}}(t) \simeq 0$.

Eq. (2.78) assumes that any uncompensated change in area of the left interfacial capacitor will result in a current that traverses the device and charges the right interfacial capacitor. As previously mentioned in Sect. 2.3.2.2 (p. 49), however, this only occurs if it is energetically favorable to do so. Whether the excess image charge, δq, is deposited on the right interfacial capacitor or remains on the left can be determined by applying Eq. (2.51) (p. 51) to the symmetric ΦdC SCEEG:

$$S \equiv \frac{\Delta W_{\mathrm{TOT,L}}}{\Delta W_{\mathrm{TOT,R}}} = \frac{C_{\mathrm{R}}}{C_{\mathrm{L}}}\left(\frac{\delta q + 2\,q_{\mathrm{L}}}{\delta q + 2\,q_{\mathrm{R}}}\right) = \frac{\left(\frac{\delta q}{A_{\mathrm{L}}} + 2\,\sigma\right)}{\left(\frac{\delta q}{A_{\mathrm{R}}} + 2\,\sigma\right)} \tag{2.79}$$

where it is assumed that both the left and right interfacial capacitors have the same charge density, σ, prior to the addition of δq. As evident by Eq. (2.79), $S > 1$ when $A_{\mathrm{R}} > A_{\mathrm{L}}$, $S < 1$ when $A_{\mathrm{L}} > A_{\mathrm{R}}$, and $S = 1$ when $A_{\mathrm{R}} = A_{\mathrm{L}}$. Therefore, excess image charge will only move from the left to the right electrode, and thus change Φ_{R} in the process, if $A_{\mathrm{R}} > A_{\mathrm{L}}$. Otherwise, the excess image charge will stay on the left electrode and cause Φ_{L} to change.[28]

Assuming $A_{\mathrm{R}} > A_{\mathrm{L}}$, the process of charging the right interfacial capacitor is not a natural response of the circuit, but is instead a response that is forced by the change in capacitance of the left capacitor. The dynamics of circuit are, therefore, dictated by the timescale over which this change occurs and not by the characteristic RC time constant, $\tau_{\mathrm{RC}} = RC$. However, if the right capacitor is not forced to discharge by a subsequent change in capacitance of the left capacitor, the excess charge on the right interfacial capacitor will naturally decay, either by generating a short-circuit current or by desorption of ions from the interface. As discussed in Sect. 2.3.2.5 (p. 54), the dominant mechanism of discharge is that which occurs over the shortest timescale.

[28]Unless, of course, $A_{\mathrm{R}} = A_{\mathrm{L}}$ and neither is energetically favored. In this case, the kinetics of adding δq to each interfacial capacitor dictates which surface potential ends up changing.

From Table 2.2 (p. 64), it is determined that $\tau_{\text{RC}} \simeq 5$ ms for the SCEEG device whose $V_{\text{oc}}(t)$ and $I_{\text{sc}}(t)$ data are displayed in Fig. 2.11 (p. 65). Unfortunately, it is difficult to accurately estimate τ_{d} because the values of the variables in Eq. (2.68) on p. 58 are unknown. However, assuming $\Theta_{\text{ex,sat}} \simeq \sigma A \simeq 1 \times 10^{10}$ ions/mm^2 $\cdot$ 30 mm^2 $= 3 \times 10^{11}$ ions (Table 3.4, p. 153), $E_{\text{d,ex}} \simeq E_{\text{B}} \simeq 300$ meV (Table 3.6, p. 160), and $k_{\text{B}} T \simeq 30$ meV, the frequency factor would have to be $\nu_{\text{ex}} > 10^{18}$ ions/s in order for $\tau_{\text{d}} < \tau_{\text{RC}}$. Frequency factors for desorption are typically on the order of $10^9 - 10^{18}$ s^{-1} so it is very likely that $\tau_{\text{d}} > \tau_{\text{RC}}$ [57, 58].

If $\tau_{\text{RC}} < \tau_{\text{d}}$, any excess charge density (and, thus, excess surface potential) on the interfacial capacitors will naturally decay by generating a short-circuit current through the device's internal impedance until the excess charge eventually desorbs back into the droplet or is absorbed by an appropriate change in capacitance. Because the SCEEG has both resistive and reactive components, an imbalance in the surface potentials of the SCEEG's interfacial capacitors is equivalent to applying an input voltage signal across the terminals of an RC circuit.

In general, an RC circuit acts as a low-pass filter.[29] The circuit attenuates the magnitude of all components of an input voltage signal that oscillate with a frequency greater than the cutoff frequency, $f_{\text{c}} = 1 \,/\, 2\,\pi\,\tau_{\text{RC}}$ [39]. This means that only changes in the SCEEG's charge density that occur at frequencies less than f_{c} will result in fluctuations in $I_{\text{sc}}(t)$ and $V_{\text{oc}}(t)$. All higher frequency changes will be filtered out because the natural charging/discharging process will occur too slowly for the changes to be reflected in the device's output. For the device represented in Fig. 2.11 (p. 65), $f_{\text{c}} \simeq 30$ Hz. Because the cutoff frequency is less than the driving frequency, $f_{\text{drive}} = 33$ Hz, the movement of the droplet forces the surface potentials to change before any excess potential is allowed to naturally decay. This is likely the main reason why there does not ap-

[29] In contrast, an RC circuit does not behave as a low-pass filter when connected to an ideal, alternating current source. The input and output currents for such a circuit are identical. The magnitude of output voltage, however, is attenuated for high angular frequencies, ω, of the current source because the magnitude of the circuit's complex impedance, $|Z| = \sqrt{R^2 + 1 \,/\, \omega^2\, C^2}$, decreases monotonically as it asymptotically approaches $|Z| \to R$ for $\omega \to \infty$.

pear to be any amplitude modulation occurring at frequencies greater than f_{drive} in the time traces of $I_{\text{sc}}(t)$ and $V_{\text{oc}}(t)$.

On the other hand, if $\tau_{\text{d}} < \tau_{\text{RC}}$, no short-circuit current will be generated because excess charge will desorb back into solution before it has time to travel through the device. For the SCEEG represented in Fig. 2.11 this means that, regardless of whether τ_{d} is greater or less than the period of the droplet's motion, there will again be no modulation in the amplitude of the time traces of $I_{\text{sc}}(t)$ and $V_{\text{oc}}(t)$ at frequencies greater than f_{drive}.

To account for the attenuation of high-frequency amplitude modulations, the area data used in the model of $V_{\text{oc}}(t)$ were resampled to remove fluctuations occurring at frequencies > 33 Hz. As evident in Fig. 2.11, the resulting model accurately captures the dynamics of the G-SCEEG's output.

2.3.3.2 *Asymmetric $\Phi_i dC_i = -C_j d\Phi_j$ ITO-SCEEG*

The utility of the mathematical model describing the asymmetric $\Phi_{\rm i} dC_{\rm i} = -C_{\rm j} d\Phi_{\rm j}$ SCEEG was evaluated by comparing it to the experimental data published for an ITO-SCEEG by Moon et al. [8]. Their device and experimental setup are depicted in Fig. 2.12. The figure has been reprinted with permission from their original publication. As mentioned previously, their device differs from the G-SCEEG in the following ways: (i) the electrodes are made from the semiconductor indium-tin-oxide (ITO); (ii) the top ITO electrode is coated with a thin layer of PTFE, rendering it hydrophobic and permitting an aqueous droplet to move across it; (iii) the bottom electrode is uncoated ITO over which an aqueous droplet does not freely move; the droplet is effectively pinned to its surface; (iv) the PTFE-coated electrode is stacked on top of the bare electrode such that they are separated by a narrow gap; droplets are placed in between the electrodes in such a way that they bridge the gap; the height of the gap is then mechanically oscillated to cause the area of overlap between the droplet and the top PTFE-coated electrode to change; (v) the only solution tested on the device is deionized water which has a much larger resistivity than electrolyte solutions; and (vi) the device is large enough to simultaneously support 33 separate 40 μL droplets.

Fig. 2.13 shows how the asymmetric $\Phi_{\rm i} dC_{\rm i} = -C_{\rm j} d\Phi_{\rm j}$ SCEEG model in Sect. 2.3.2 above compares to Moon et al.'s experimental data. Most of the values for the parameters used in the model were taken from Ref. [8] and are provided in Table 2.3 (p. 73). When the value of a parameter was not explicitly mentioned in Ref. [8] a reasonable estimate was made. Because the capacitance of top, PTFE-coated electrode, $C_{\rm T}(t)$, is much less than that of the bottom, uncoated electrode, $C_{\rm B}$, the following simplification was made to Eq. (2.47) of the model:

$$C_{\rm eq}(t) = n \left(\frac{1}{c_{0,\rm T}\, A_{\rm T}(t)} + \frac{1}{c_{0,\rm B}\, A_{\rm B}} \right)^{-1} \simeq n\, c_{0,\rm T}\, A_{\rm T}(t) \tag{2.80}$$

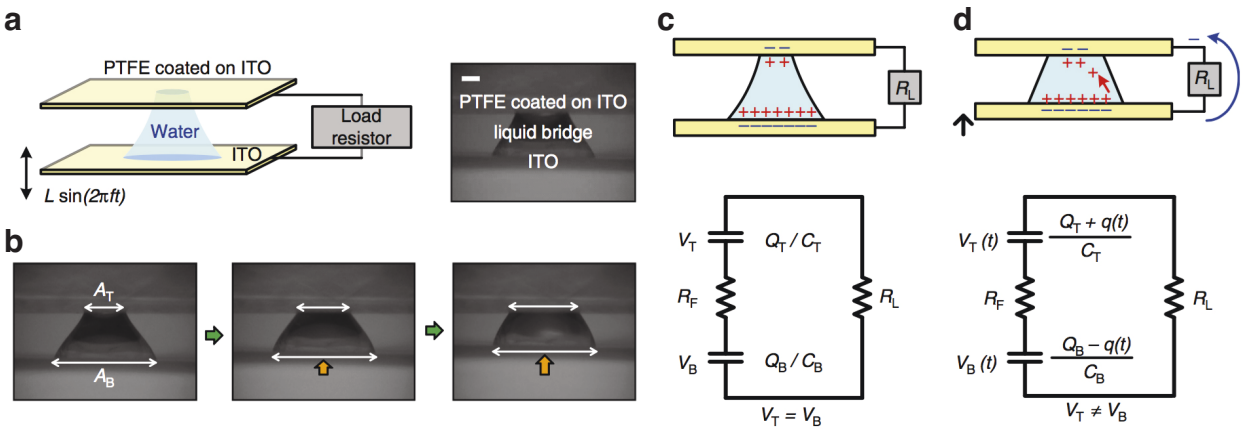

Figure 2.12: Moon et al.'s ITO-SCEEG device and experimental setup. **a**, Experimental setup and **b**, video images of water bridge over time. Scale bar, 1 mm. Charge distributions on interfacial capacitors and corresponding equivalent electrical circuits **c**, when the water bridge height is fixed in time (equilibrium state) and **d**, at the very moment when the two plates are approaching each other (non-equilibrium state). Within a couple of periods after the vibration starts, the system reaches a steady state. Figure and figure caption reprinted with permission from Macmillan Publishers Ltd: Nature Communications. Moon, J. K., et al. Nature Communications 4, 1487 (2013), copyright 2013.

In general, the model agrees well with Moon et al.'s data. Significant disagreement between the model and the data only occurs in the frequency-dependent data for frequencies greater than 15 Hz. This is likely due to the droplets not maintaining a constant area change as the frequency is increased in the experiment. This explanation is supported by the observations of Fig. 2.18. Although Moon et al. provide a differential equation that they claim represents the voltage that is generated across a load resistor connected to their device, their equation neglects the reactance of the device's capacitance. The conclusions they draw from this equation are flawed as a result.

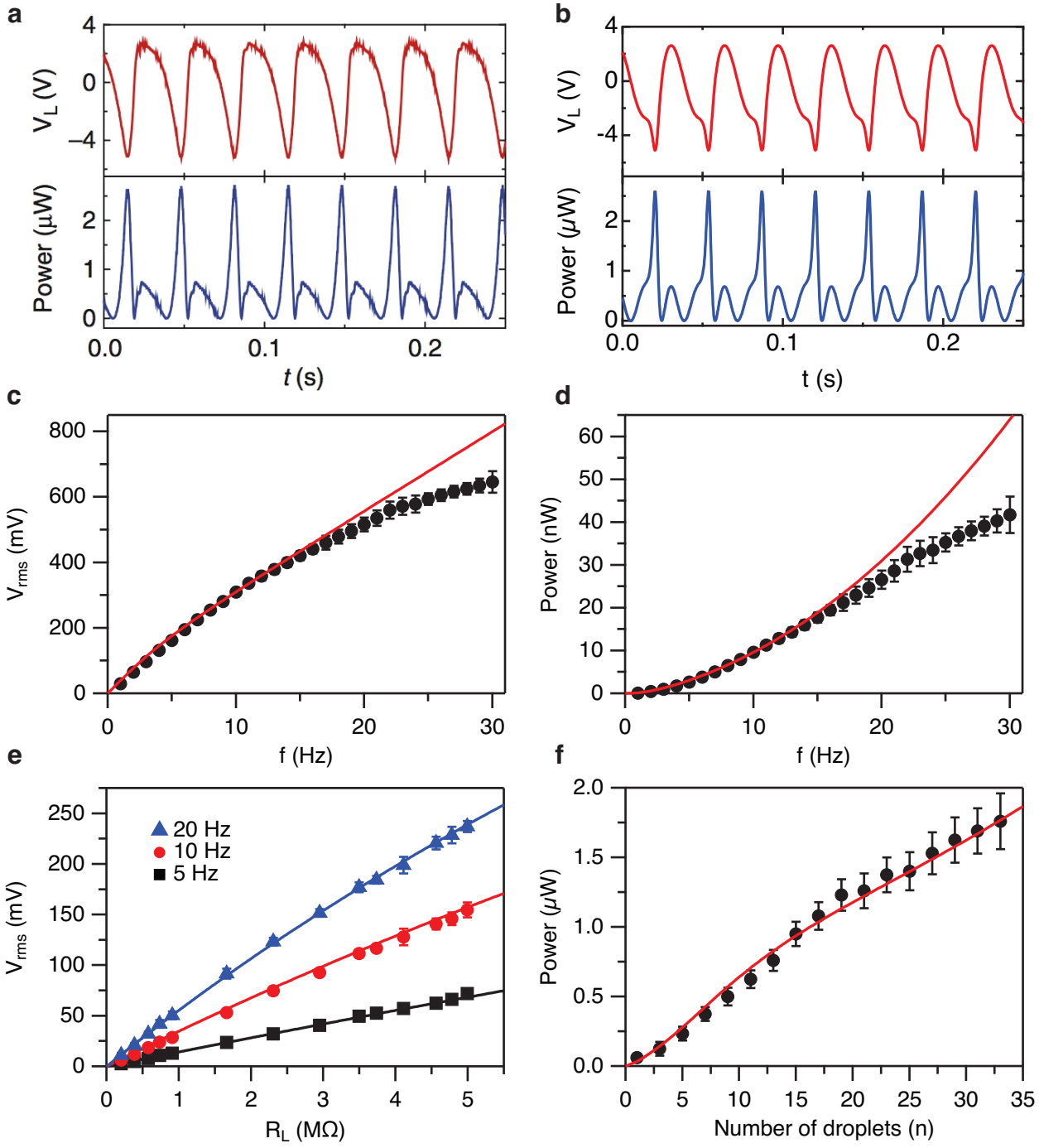

Figure 2.13: Comparison of asymmetric $\Phi_i dC_i = -C_j d\Phi_j$ SCEEG model to data from Moon et al. a, Data of voltage and power output *vs.* time from Moon et al.'s ITO device. **b**, Voltage and power time traces produced using asymmetrical SCEEG model. **c** - **f**, Comparison of Moon et al.'s experimental data (solid symbols) with the asymmetrical SCEEG model (solid lines). Moon et al.'s figure [Fig. (**a**) above] and data are reprinted and adapted, respectively, with permission from Macmillan Publishers Ltd: Nature Communications. Moon, J. K., et al. Nature Communications 4, 1487 (2013), copyright 2013.

Parameter	Value		Units
	Ref. [8]	**Model**	
σ_{T}	$-$	63	pC/mm^2
α	$-$	$8.9-14.2$	mm^2
f	$1-30$	$1-30$	Hz
n	$1-35$	$1-35$	droplets
R	$-$	16	MΩ
R_{S}	$-$	15	MΩ
R_{L}	10	10	MΩ
$c_{0,\mathrm{T}}$	62	62	pF/mm^2
$c_{0,\mathrm{B}}$	2.3	2.3	nF/mm^2
$\langle A_{\mathrm{T}} \rangle_{\mathrm{avg}}$	10	$10-15$	mm^2
$\langle A_{\mathrm{B}} \rangle_{\mathrm{avg}}$	28	28	mm^2

Table 2.3: Parameters used in the model of ITO-SCEEG. The parameters and their values from Ref. [8] used to model the ITO-SCEEG in Fig. 2.13 (solid lines). When not explicitly mentioned in Ref. [8], values for the parameters were estimated to give the best fit of the model to the data.

2.3.4 The role of the streaming current, I_{str}, and streaming potential, V_{str}

Due to the electromechanical nature of the SCEEG, it is natural to wonder if the short-circuit current, I_{sc}, and open-circuit voltage, V_{oc}, that the device generates is a consequence of the streaming potential effect. In general, the streaming potential is an electrokinetic phenomenon whereby the flow of an electrolyte solution over a solid surface, such as the walls of a glass capillary, generates an electric potential. An applied hydrostatic pressure gradient is generally treated as the source of the solution's flow. Not only does the gradient cause the volume of solution to flow but it also generates a current, I_{str}, called the streaming current [59, 60]. I_{str} is a result of the flow of mobile ionic charge in the diffuse layer of the EDL in the direction from high to low pressure. The mobile charge accumulates with increasing density down the gradient, *i.e.* at the low-pressure end of the system, leading to a separation of charge and, ultimately, to the formation of a potential, V_{str}, called the streaming potential.[30]

For an axial pressure gradient, $\vec{\nabla} P = (\partial P / \partial z)\ \hat{z} = -\ (\Delta P / l)\ \hat{z}$, applied to an electrolyte solution with viscosity, η_s, and bulk conductivity, $\sigma_{c,0}$, in a cylindrical capillary of radius, R_c, and length, l, the expressions for I_{str} and V_{str} are:

$$I_{str} = -\frac{\epsilon\,\epsilon_0\,\pi\,R_c^2}{\eta_s\,l}\,\Phi_d\,\Delta P \tag{2.81}$$

$$V_{str} = \frac{\epsilon\,\epsilon_0}{\eta_s\,\sigma_{c,0}}\,\Phi_d\,\Delta P \tag{2.82}$$

where ϵ and ϵ_0 are the relative and vacuum permittivities, respectively, and Φ_d is the voltage drop across the diffuse layer.[31]

[30] The streaming potential effect is the opposite of the electro-osmotic effect, *i.e.* electro-osmosis is the flow of fluid that results from an applied electric potential gradient.

[31] The form of Eq. (2.82) assumes that the radius of the cylinder, R_c, is much greater than the Debye length of the diffuse layer, λ_D, *i.e.* $R_c >> \lambda_D$. For a derivation of Eq. (2.82), see Appendix B, Sect. B.4 (p. 229).

Because $\sigma_{c,0}$ increases and Φ_d decreases (due to compression of the diffuse layer) with increasing concentration of the electrolyte, both I_{str} and V_{str} should decrease as the electrolyte's concentration increases. However, if the surface conductance, G_s, of the capillary is non-negligible, the expression for V_{str} becomes:

$$V_{str} = \frac{\epsilon\,\epsilon_0}{\eta_s\,(\sigma_{c,0} + 2\,G_s\,/\,R_c)}\,\Phi_d\,\Delta P \tag{2.83}$$

and there is a maximum in the plot of V_{str} vs. concentration [60].

Although Eqs. (2.81)–(2.83) describe the streaming potential for a cylindrical geometry, the scaling of I_{str} and V_{str} with $\sigma_{c,0}$ and Φ_d is also thought to apply to a planar surface like that of the SCEEG's electrodes. Thus, if the streaming current and potential played a significant role in the output of the SCEEG, I_{sc} and V_{oc} would decrease as the concentration of the electrolyte increased. As evident in Figs. 2.17 (p. 83), 2.19 (p. 87), and 3.6 (p. 144) and Table 2.4 (p. 110), however, I_{sc} and V_{oc} increase with increasing concentration of HCl and NaCl. It is assumed, therefore, that the streaming potential effect does not play a significant role in the SCEEG's short-circuit current and open-circuit voltage output.

2.4 The G-SCEEG device

As previously mentioned in Chapter 1, the two types of SCEEG devices built to date are electromechanical transducers, converting the mechanical energy of an oscillating droplet into electrical energy. Specifically, the G-SCEEG generates alternating current, voltage, and power from the mechanical oscillation of droplets of electrolyte solutions over a bifurcated graphene sheet. The bifurcation prevents the graphene from acting as short in the circuit. This permits the generation of significant open-circuit voltage ($\simeq 500$ mV, RMS), short-circuit current ($\simeq 6$ μA, RMS), and dissipated power ($\simeq 600$ nW, avg.) from the oscillation of a single 20 μL droplet. The following is a brief description of the steps involved in its fabrication. For more detailed descriptions of the methods, see Chapter 6 (p. 187) and Appendix A (p. 211).

Fabrication of the G-SCEEG begins with a piece of borosilicate glass (20 $\times$ 25 $\times$ 1 mm) that has been cleaned using a piranha etch solution and oxygen plasma. The glass serves as the supporting substrate for the graphene electrodes. Two parallel, rectangular gold contacts (3 $\times$ 20 mm, thickness: 50 nm Au on 1 nm Ti) are first evaporated onto the top surface of the glass such that they are 1.2 mm apart. All exposed surfaces of the glass are then functionalized with a self-assembled monolayer (SAM) of octadecyltrichlorosilane (OTS), rendering them hydrophobic.

It was determined that the G-SCEEG needed a hydrophobic substrate in order to facilitate the motion of an aqueous droplet across its surface. Because graphene at least partially assumes the wetting properties of its supporting substrate [22, 25–27, 61], the hydrophobic OTS SAM prevents aqueous droplets from spreading out over the graphene while also maintaining the droplets' hemispherical shape. In contrast, aqueous droplets in contact with graphene which is supported by a hydrophilic substrate, e.g. SiO_2, wet the graphene more readily and are effectively pinned to the graphene's surface.[32]

[32] For an example, see Fig. 3 (**b**) in Ref. [26]

A 10 × 15 mm sheet of large-grain (average diameter = 0.75–1.5 mm), CVD-grown graphene is transferred to the OTS glass such that it overlaps both Au contacts. A 5–10 μm gap is subsequently made in the graphene to create two electrically isolated sheets. Two types of large-grain graphene were used to make G-SCEEGs in this work. The first contained patches of multi-layer graphene domains over 10–20% of its surface and is subsequently referred to as large-grain, multi-layer (LG-Multi) graphene. The second was devoid of multi-layer areas and is referred to as large-grain, mono-layer (LG-Mono) graphene.[33]

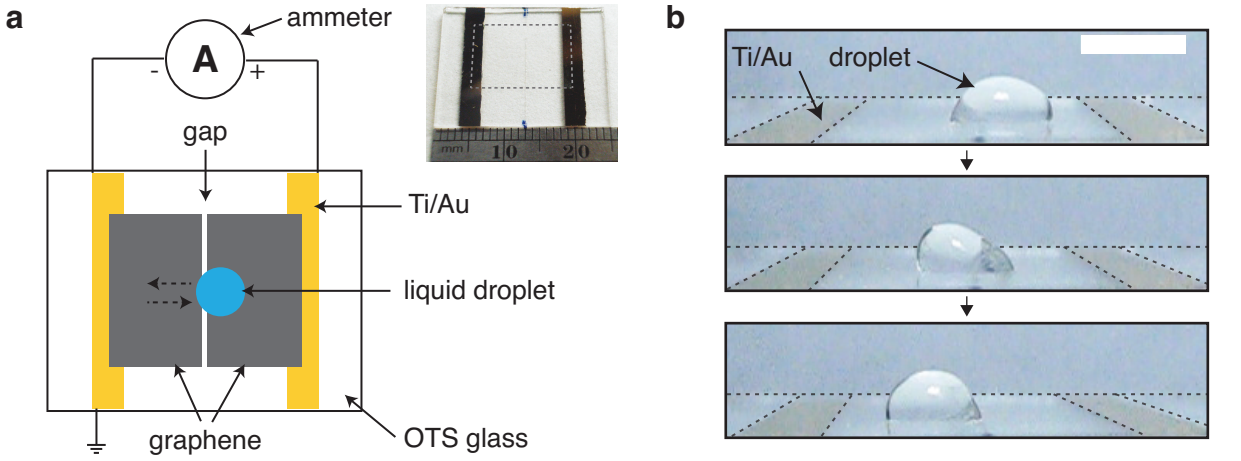

Figure 2.14: The G-SCEEG device. **a**, Illustration of the G-SCEEG device (white rectangle) connected to an ammeter. (**inset**) Photograph of the device. The dashed line demarcates the location of the graphene. **b**, Sequence of video images showing a 20 μL droplet of 1 M NaCl moving from right to left across the gap in the graphene (roughly halfway between the two Ti/Au contacts). Scale bar: 5 mm.

The final step in fabrication is to mark the location of the gap in the graphene by etching a thin line on the bottom side of the glass with either a laser or a diamond-coated scribe. This mark is used to determine both the relative motion between the device and the droplet and the area of overlap between the droplet and each graphene sheet during oscillation. Fig. 2.14 provides an illustration and a photograph of the finished device as well as a sequence of video images showing a 20 μL droplet of 1 M NaCl moving from right to left across it. The electric output generated by

[33] See Fig. 2.29 (p. 104) for optical micrographs of each type.

the droplet's motion is measured by connecting the appropriate meter (or amplifier-meter pair) across the device's gold contacts.

2.4.1 Generating electricity

Two necessary conditions were discovered for the G-SCEEG to continuously generate either alternating current, voltage, or power: (i) the area of overlap between the droplet and at least one graphene sheet must be changing, and (ii) the droplet must maintain contact with both graphene sheets. Time traces representing typical short-circuit current (I_{sc}), open-circuit voltage (V_{oc}), and power dissipated in a load (P_L) generated by a G-SCEEG made from LG-Multi graphene are given in Fig. 2.15. Unless otherwise noted all data in this section was taken using the G_{MULTI}-SCEEG. For each trace, a 20 μL droplet of 1 M NaCl was oscillated at 30 Hz using a sinusoidal waveform. The maximum peak-to-peak area change of the droplet over either sheet of graphene was 8.5 mm^2. The load resistance, R_L, used for the measurement of the power output was 150 kΩ.

Both the physical parameters of the experiment and the chemical properties of the electrolyte solution were found to significantly affect the G-SCEEG's electric output. Significant physical parameters include: (i) the change in the area of overlap between the droplet and each graphene sheet; (ii) the number of concurrently oscillating droplets on the device; (iii) the driving frequency of the speaker; (iv) the magnitude of the load resistance; and (v) the presence of areas of multilayer graphene. Chemical properties such as the type and concentration of the electrolyte as well as the pH of the solution were also shown to be significant. The rest of this section focuses primarily on how the G-SCEEG's behavior changes with those physical parameters whereas Chapter 3 provides a detailed account of the chemical effects. Unless otherwise noted, data presented in this section were taken using a G-SCEEG made from LG-Multi graphene.

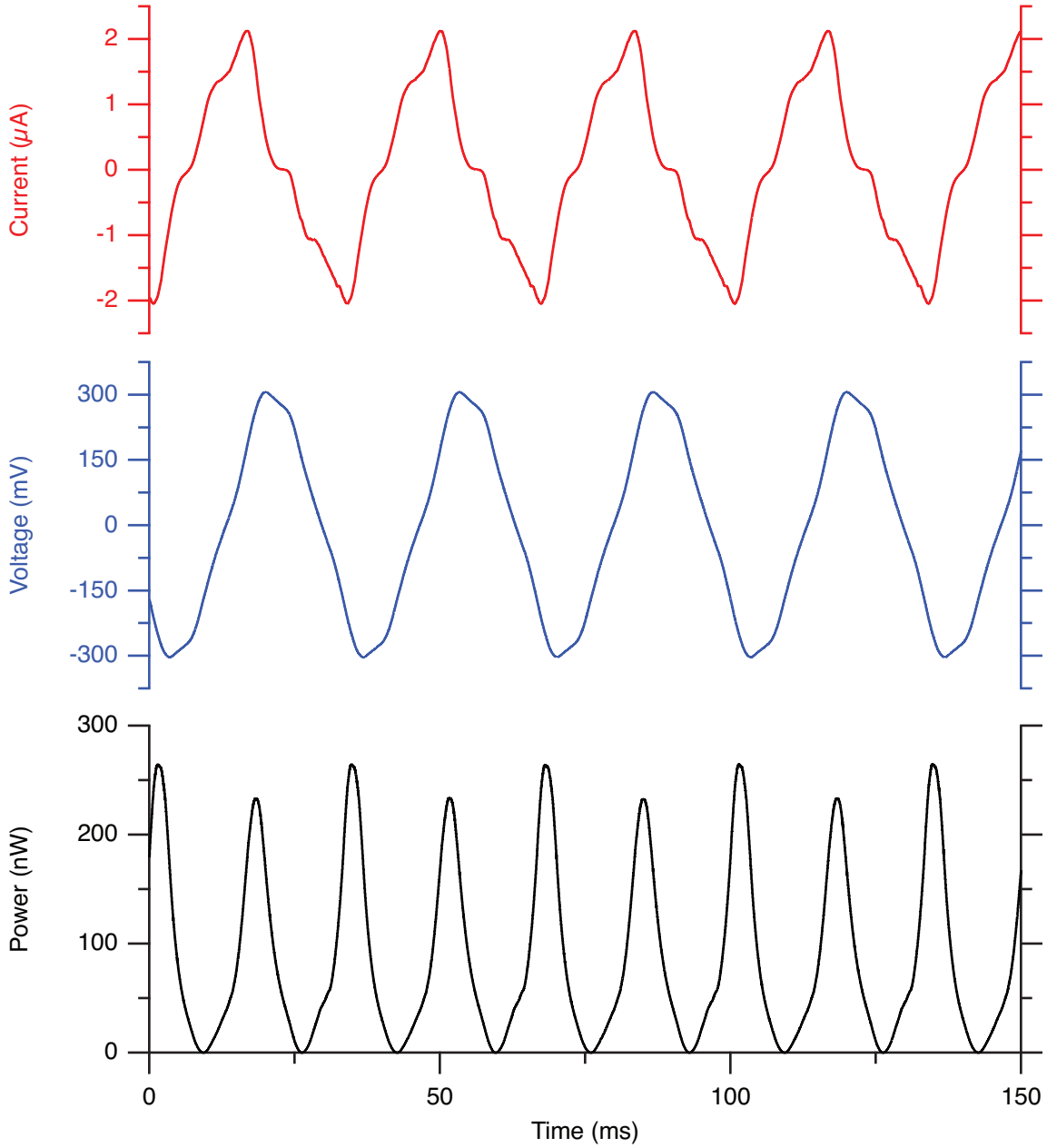

Figure 2.15: Typical G-SCEEG output vs time. I_{sc}, V_{oc}, and P_L as a function of time for a 20 μL droplet of 1 M NaCl oscillating at 30 Hz over a G-SCEEG made from LG-Multi graphene. The peak-to-peak area change of the droplet with each graphene sheet is 8.5 mm^2. $R_L = 150$ kΩ.

2.4.1.1 *Experimental setup*

The droplet of electrolyte solution is driven back and forth across the G-SCEEG by mechanically oscillating it using a small bass speaker connected to a function generator and an audio power amplifier. Fig. 2.16 shows the basic experimental setup. The G-SCEEG is mounted on a fiberglass stage which is in turn mounted to the dust cap of the speaker. The droplet's inertia allows it to move relative to the G-SCEEG even though the G-SCEEG itself is being driven by the speaker. A window has been cut into the bottom of the stage to allow the droplet's motion to be imaged from below using a compact digital microscope (Aven Mighty Scope 5M USB Digital Microscope). The microscope also functions as a strobe light as its six light-emitting diodes (LEDs) are pulsed using a separate function generator. The strobe light enables the oscillating droplet's motion to be imaged without the need for a high-speed camera. An accelerometer is used to measure the acceleration of the device during the experiment. The setup is supported by a vibration isolation table and contained within a plastic purge box. The purge box allows the chemical composition of the atmosphere surrounding the experiment to be controlled by continuously flowing in a gas of choice.

Unless otherwise noted, all experiments described in this chapter were performed under a wet-N_2 atmosphere, i.e. N_2 gas which has been bubbled through deionized water. Also, all electrolyte solutions were sparged with helium (He) prior to use. Purging the box with N_2 and sparging the solutions with He were done to prevent the concentration of dissolved CO_2, and in turn the pH, of the electrolyte solutions from fluctuating appreciably during oscillation. Because pH was determined to significantly alter the output of the G-SCEEG, purging and sparging were necessary for the reproducibility of most experiments involving the device.

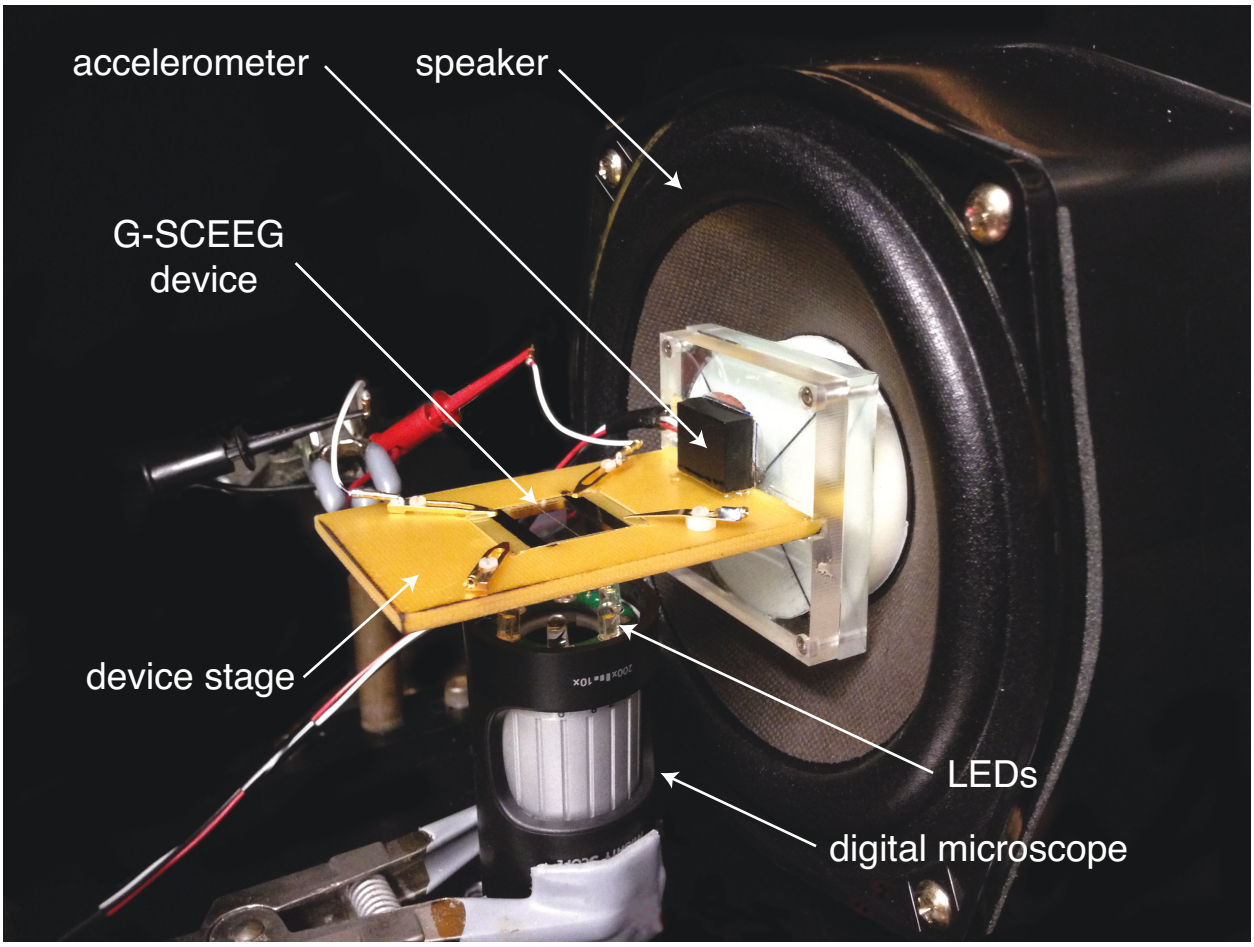

Figure 2.16: Basic experimental setup. A photograph showing the basic experimental setup including a G-SCEEG mounted on the device stage. Not shown are the function generators (providing the input waveforms to the speaker and the LEDs of the digital microscope), the audio amplifier, the vibration isolation table, and the plastic purge box.

2.4.1.2 *Short-circuit current, I_{sc}*

I_{sc} was measured using a Keithley 427 current amplifier connected to an Axon Instruments Digidata 1322A digitizer. Fig. 2.17 shows how I_{sc} changes as a function of area change and droplet number. Fig. 2.17 (**a**) plots the root-mean-square (RMS) short-circuit current ($\langle I_{sc} \rangle_{RMS}$) vs. area change for four different electrolyte solutions: 1 M NaCl, 1 M HCl, 1 M HNO_3, and 6 M HCl. The change in area was altered by adjusting the gain setting on the audio amplifier. It is clear from the plot that $\langle I_{sc} \rangle_{RMS}$ scales linearly with the change in area for each solution and that 6 M HCl generates the greatest amount of current followed by 1 M HNO_3, 1 M HCl, and 1 M NaCl.

Fig. 2.17 (**b**) shows a similar scaling behavior. The plot shows that $\langle I_{sc} \rangle_{RMS}$ scales linearly with the number of droplets of 1 M HCl that are concurrently oscillating on the G-SCEEG. The finite size of each graphene sheet and the difficulty in preventing multiple droplets from merging into a single large one limited the maximum number of droplets that could concurrently oscillate to 3×10 μL. The time trace in Fig. 2.17 (**c**) gives the maximum I_{sc} generated by a G-SCEEG to date. Two 20 μL droplets of 6 M HCl produced a peak-to-peak short-circuit current of 40 μA (11 μA RMS) while oscillating at 30 Hz. The change in area of each droplet was approximately 14 mm^2.

In addition to determining how $\langle I_{sc} \rangle_{RMS}$ scales with the change in area and the number of droplets, $\langle I_{sc} \rangle_{RMS}$ was also measured as a function of driving frequency. Fig. 2.18 (**a**) is a plot of $\langle I_{sc} \rangle_{RMS}$ vs. frequency for a 20 μL droplet of 1 M HCl. A lock-in amplifier was used to measure the $\langle I_{sc} \rangle_{RMS}$ that was generated at the same frequency as the driving frequency. Because $\langle I_{sc} \rangle_{RMS}$ scales with the change in area, an attempt was made to hold the area change constant vs. frequency by using a feedback control circuit. A photo-interrupt sensor was placed towards the end of the stage (left end of the stage in Fig. 2.16) and was used as part of a proportional-integral-derivative (PID) feedback controller connected to the speaker's amplifier. During the frequency sweep the gain

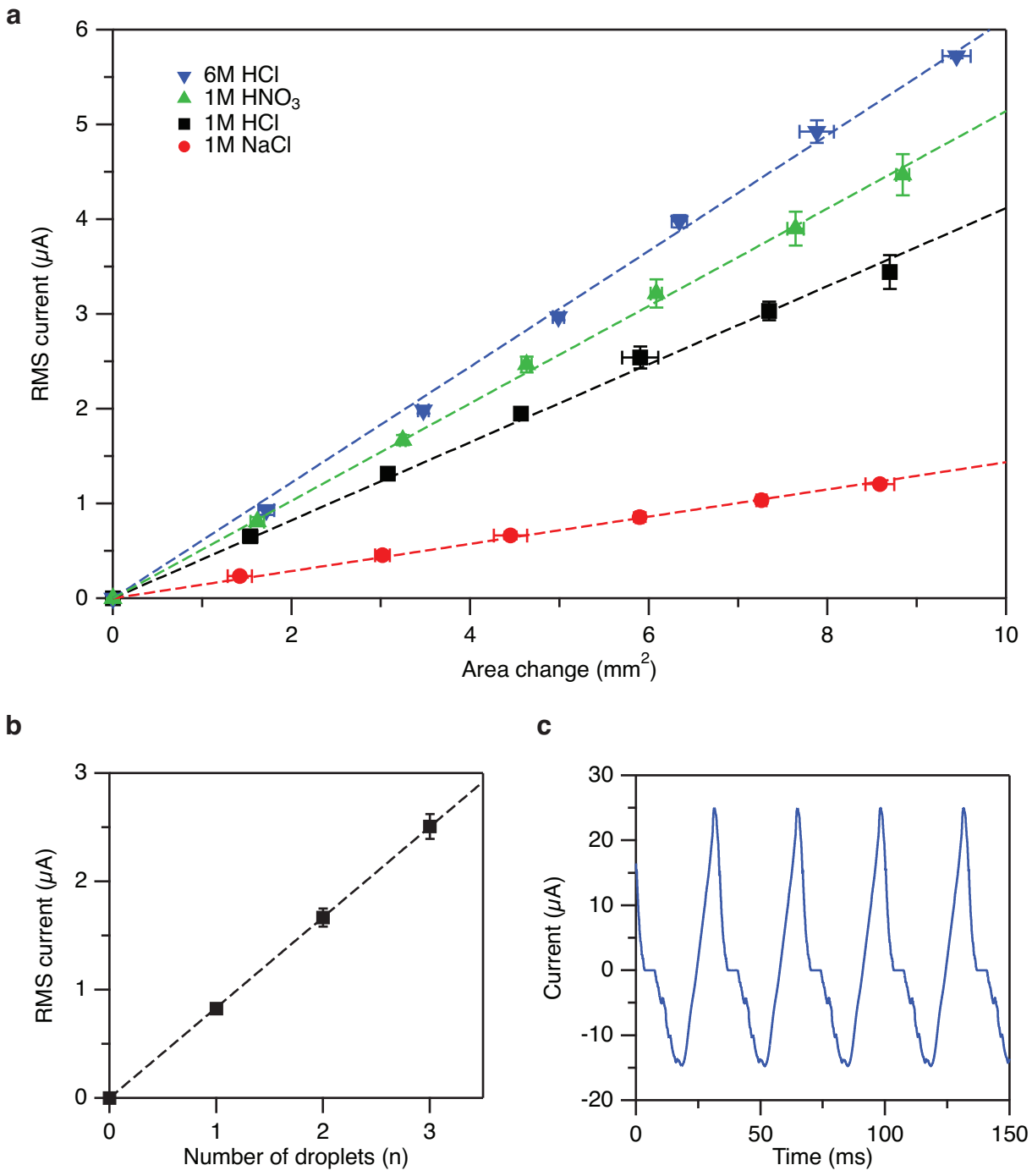

Figure 2.17: Scaling of $\langle I_{sc}\rangle_{RMS}$ and maximum I_{sc} output. a, Scaling of $\langle I_{sc}\rangle_{RMS}$ with the peak-to-peak change in area of the droplet on each half of the device for different electrolyte solutions. Droplet volume = 20 μL, oscillation frequency = 30 Hz. **b**, Scaling of $\langle I_{sc}\rangle_{RMS}$ with the number of droplets of 1 M HCl. Individual droplet volume = 10 μL, oscillation frequency = 30 Hz. **c**, Maximum I_{sc} output achieved ($I_{sc,pk\text{-}pk}$ = 40 μA, $\langle I_{sc}\rangle_{RMS}$ = 11 μA). Solution = 6 M HCl, droplet volume = 2 × 20 μL, oscillation frequency = 30 Hz, area change = 2 × 14 mm^2. Error bars represent the standard deviation of measurements made in triplicate.

on the audio amplifier was adjusted to maintain a constant RMS output voltage from the photo-interrupter. A one-to-one correspondence between the photo-interrupter output voltage and the displacement of the device stage ensured that stage's RMS displacement was held approximately constant throughout the sweep. 10–310 Hz was the largest frequency range over which the RMS displacement could be kept constant while also maintaining a displacement magnitude large enough to generate current.

As evident in the plot of Fig. 2.18 (**a**) current is generated only at certain driving frequencies, *i.e.* 30, 110, 160, 200, 210, and 300 Hz. For all frequencies > 30 Hz, current is generated when the driving frequency is equal to a resonant frequency of a particular standing wave on the droplet's surface, causing the droplet to oscillate. At 30 Hz the droplet experiences the largest RMS displacement across the device but none of its standing wave modes is on resonance.[34] At all frequencies which generate current the droplet moves relative to the device while maintaining contact with each graphene sheet. For all other frequencies no relative motion is observed. Splitting of the current signal into two or more peaks near a resonant frequency is most likely due movement of the droplet that is not strictly side to side. Because of the design of the speaker the droplet experiences some front to back motion. This motion likely distorts the geometry of the droplet enough to cause a splitting of the resonant frequency. Figs. 2.18 (**b**) and (**c**) show the effect of the electrolyte and the droplet's volume, respectively, on $\langle I_{sc} \rangle_{RMS}$ vs. frequency. The volume of the droplet effects the number of current-generating frequencies and their spectral position more significantly than the change in electrolyte.[35]

[34] See the insets of Fig. 2.26 (**a**) (p. 101) for photographs of standing waves on a 5 μL droplet.

[35] See Sect. 2.4.2.2 (p. 96) for a more detailed discussion of the detection of resonant modes using the G-SCEEG.

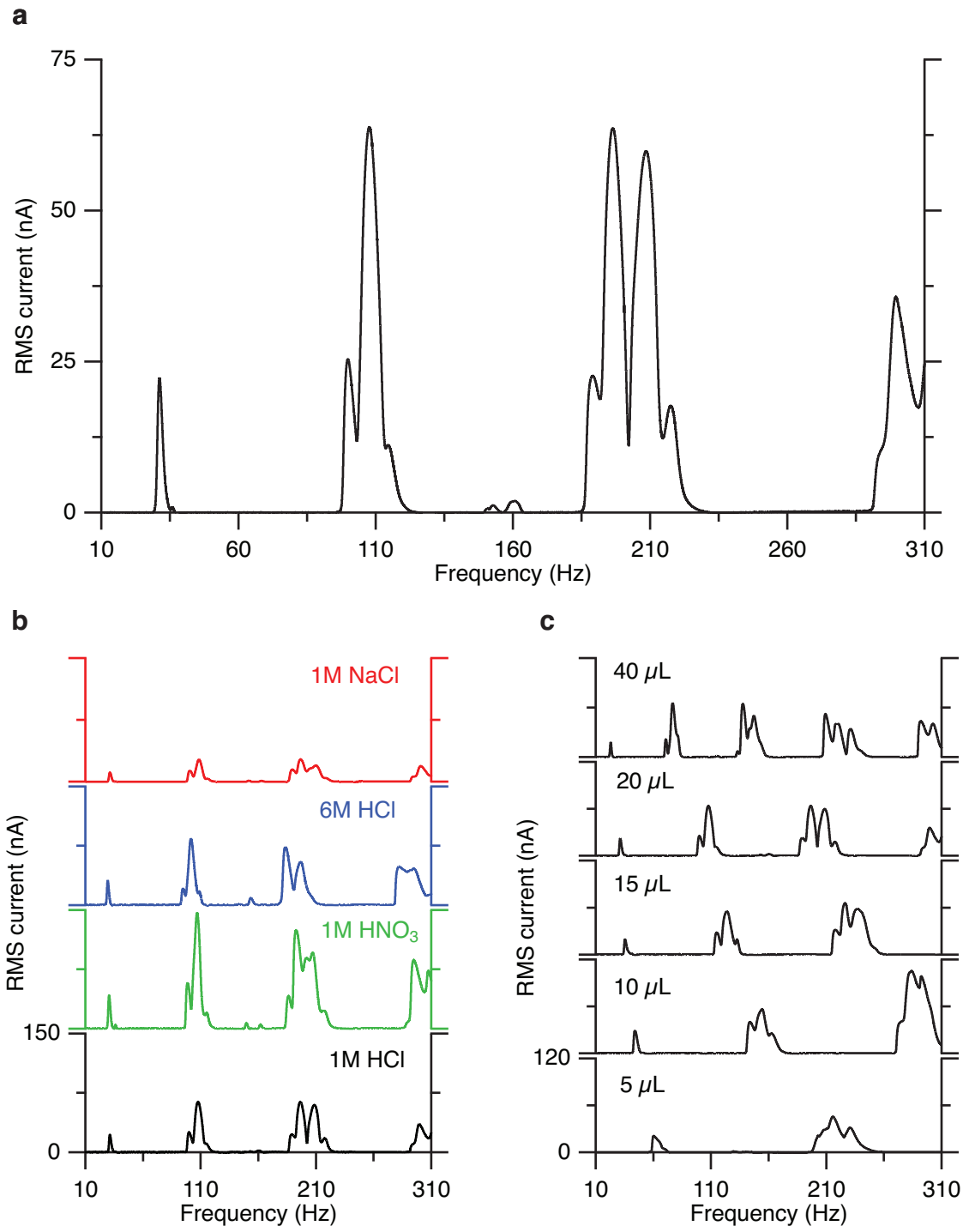

Figure 2.18: Scaling of I_{sc} vs. frequency. **a**, Scaling of $\langle I_{sc} \rangle_{RMS}$ with the frequency of oscillation. Current is generated only at or near resonant frequencies of standing waves on the droplet's surface. Splitting of the current peaks is likely caused by front to back movement of the droplet. Droplet = 20 μL of 1 M HCl. **b**, $\langle I_{sc} \rangle_{RMS}$ vs. frequency for different electrolyte solutions. Droplet volume = 20 μL. **c**, $\langle I_{sc} \rangle_{RMS}$ vs. frequency for different droplet volumes of 1 M HCl. RMS displacement for all measurements was held constant at $\sim$10 μm.

2.4.1.3 *Open-circuit voltage, V_{oc}*

V_{oc} was measured by directly connecting the G-SCEEG to the Axon digitizer (1 MΩ input resistance). Fig. 2.19 shows how V_{oc} changes as a function of area change and droplet number. Fig. 2.19 (**a**) plots the RMS open-circuit voltage ($\langle V_{oc} \rangle_{RMS}$) as a function of area change for 1 M NaCl, 1 M HCl, 1 M HNO_3, and 6 M HCl. Unlike $\langle I_{sc} \rangle_{RMS}$, 1 M HNO_3 generates the greatest $\langle V_{oc} \rangle_{RMS}$ followed by 6 M HCl, 1 M HCl, and 1 M NaCl. Like $\langle I_{sc} \rangle_{RMS}$, however, $\langle V_{oc} \rangle_{RMS}$ scales linearly with the change in area. The plot of $\langle V_{oc} \rangle_{RMS}$ vs. droplet number in Fig. 2.19 (**b**) appears to demonstrate that $\langle V_{oc} \rangle_{RMS}$ also scales linearly with droplet number. Device constraints, however, again limited the number of droplets to a maximum of 3×10 μL which prevents the scaling behavior from more accurately being determined. The time trace in Fig. 2.19 (**c**) gives the maximum V_{oc} generated by a G-SCEEG to date. Two 20 μL droplets of 1 M HNO_3 produced a peak-to-peak open-circuit voltage of 2.2 V (0.7 V RMS) while concurrently oscillating at 30 Hz.

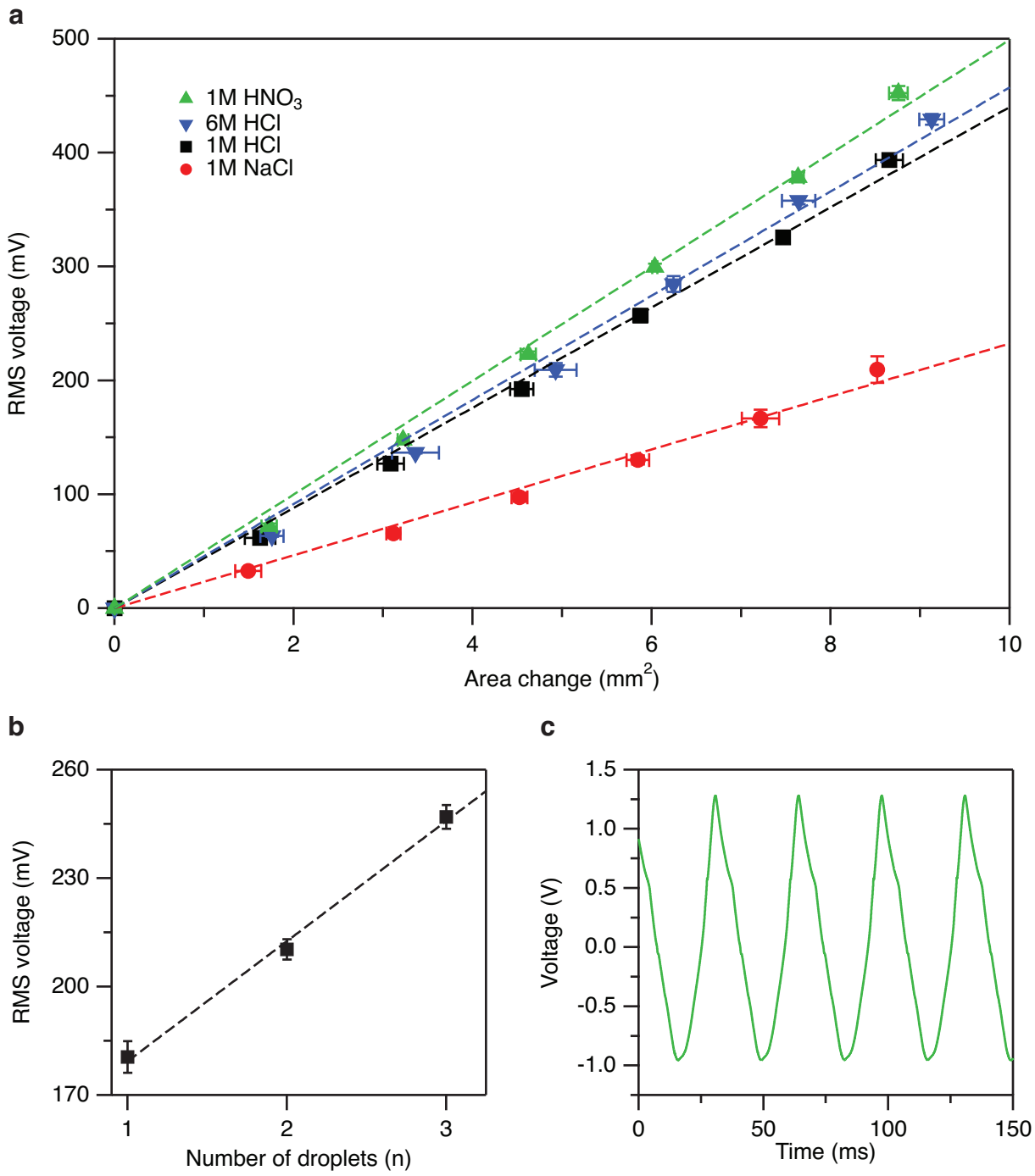

Figure 2.19: Scaling of $\langle V_{oc}\rangle_{RMS}$ and maximum V_{oc} output. a, Scaling of $\langle V_{oc}\rangle_{RMS}$ with the peak-to-peak change in area of the droplet on each half of the device for different electrolyte solutions. Droplet volume = 20 μL, oscillation frequency = 30 Hz. **b**, Scaling of $\langle V_{oc}\rangle_{RMS}$ with the number of droplets of 1 M HCl. Individual droplet volume = 10 μL, oscillation frequency = 30 Hz. **c**, Maximum V_{oc} output achieved ($V_{oc,pk\text{-}pk}$ = 2.2 V, $\langle V_{oc}\rangle_{RMS}$ = 0.7 V). Solution = 1 M HNO_3, droplet volume = 2 x 20 μL, oscillation frequency = 30 Hz. Error bars represent the standard deviation of measurements made in triplicate.

2.4.1.4 *Power dissipated in a load, P_L*

$P_{\mathrm{L}}(t)$ is calculated from the current passing through a load resistor, $I_{\mathrm{L}}(t)$, and the resistance of that load, R_{L}, using the following expression:

$$P_{\mathrm{L}}(t) = I_{\mathrm{L}}^2(t)\, R_{\mathrm{L}} \tag{2.84}$$

In the G-SCEEG experiment, $I_{\mathrm{L}}(t)$ was measured by placing the Keithley 427 current amplifier in series with R_{L}. The input resistance, R_{I}, of the current amplifier is $\simeq 15\ \Omega$ at a gain of 10^6 V/A, the gain setting used in the experiment. Because $R_{\mathrm{L}} >> R_{\mathrm{I}}$, the contribution of R_{I} to the total load resistance is negligible and was therefore neglected when determining $P_{\mathrm{L}}(t)$ from Eq. (2.84). Fig. 2.20 shows how $P_{\mathrm{L}}(t)$ changes as a function of area change and droplet number for a constant load resistance of 150 kΩ. Fig. 2.20 (**a**) plots the average power, $\langle P_{\mathrm{L}} \rangle_{\mathrm{avg}}$, dissipated in the 150 kΩ load as a function of area change for 1 M NaCl, 1 M HCl, 1 M HNO_3, and 6 M HCl. For this load, 1 M HNO_3 generates the greatest $\langle P_{\mathrm{L}} \rangle_{\mathrm{avg}}$ followed by 6 M HCl, 1 M HCl, and 1 M NaCl. $\langle P_{\mathrm{L}} \rangle_{\mathrm{avg}}$ was calculated using the following variation of Eq. (2.84):

$$\langle P_{\mathrm{L}} \rangle_{\mathrm{avg}} = \left\langle I_{\mathrm{L}} \right\rangle_{\mathrm{RMS}}^2 R_{\mathrm{L}} \tag{2.85}$$

As evident in the figure, $\langle P_{\mathrm{L}} \rangle_{\mathrm{avg}}$ scales quadratically with the change in area for each solution. This is unsurprising given the linear scaling behavior of $I_{\mathrm{sc,RMS}}$ and the form of Eq. (2.85). The plot of $\langle P_{\mathrm{L}} \rangle_{\mathrm{avg}}$ vs. droplet number in Fig. 2.20 (**b**) suggests that $\langle P_{\mathrm{L}} \rangle_{\mathrm{avg}}$ also scales linearly with droplet number. The time trace in Fig. 2.20 (**c**) gives the maximum P_{L} generated by a G-SCEEG to date. Two 20 μL droplets of 6 M HCl produced a maximum power of 7 μW (1.6 μW avg.) while concurrently oscillating at 30 Hz.

For the purpose of determining how $\langle P_{\mathrm{L}} \rangle_{\mathrm{avg}}$ varies with R_{L} it is most convenient to use Thevenin's

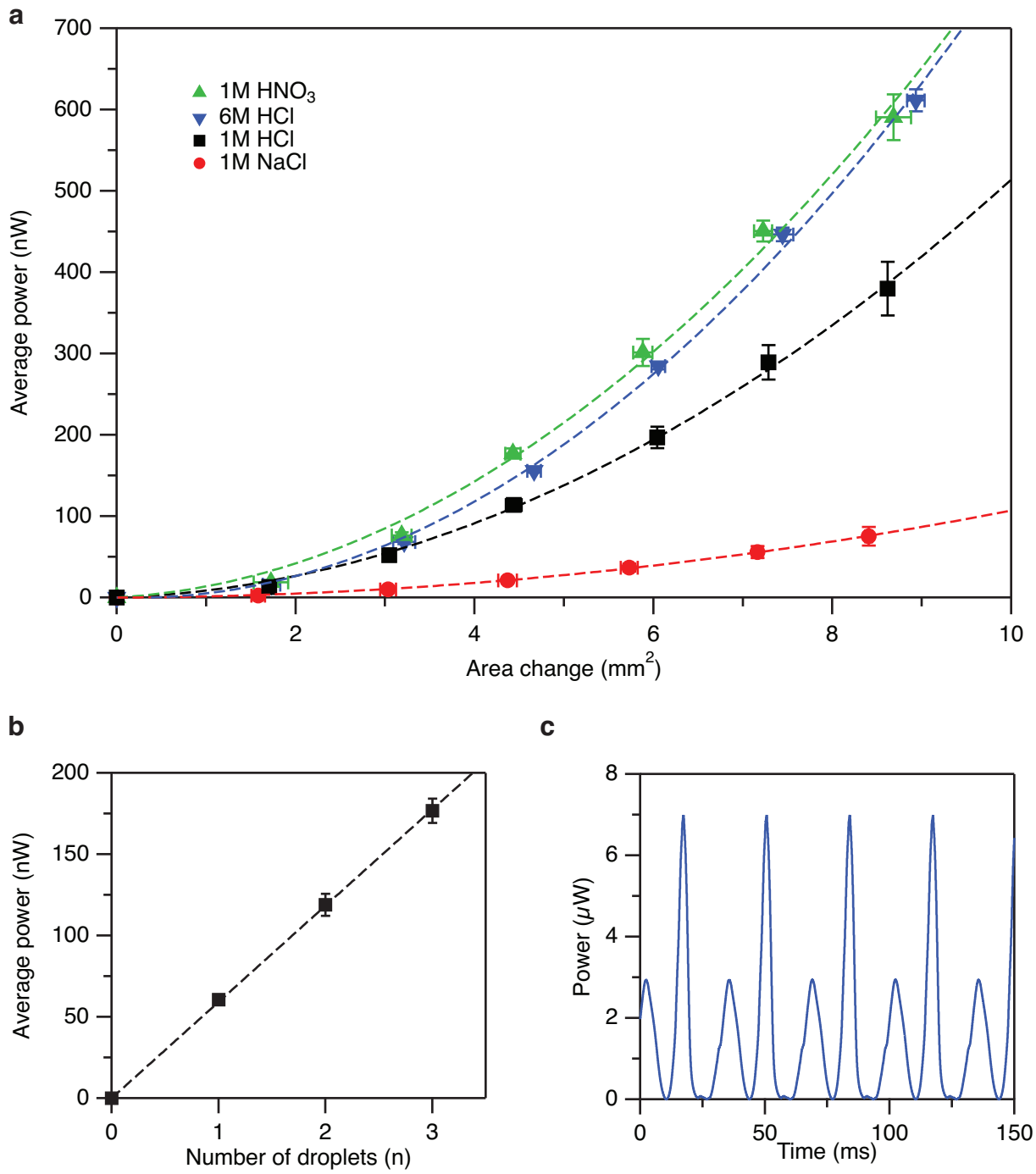

Figure 2.20: Scaling of P_L and maximum P_L output. a, Scaling of $\langle P_L \rangle_{avg}$ with the peak-to-peak change in area of the droplet on each half of the device for different electrolyte solutions. Droplet volume = 20 μL, oscillation frequency = 30 Hz. **b**, Scaling of $\langle P_L \rangle_{avg}$ with the number of droplets of 1 M HCl. Individual droplet volume = 10 μL, oscillation frequency = 30 Hz. c, Maximum P_L output achieved ($P_{L,max}$ = 7 μW, $\langle P_L \rangle_{avg}$ = 1.6 μW). Solution = 6 M HCl, droplet volume = 2 x 20 μL, oscillation frequency = 30 Hz. R_L = 150 kΩ for each set of data.

theorem to treat the G-SCEEG as an AC voltage source with open-circuit voltage $V_{\text{oc}}(t)$ and a constant average internal source impedance, $\langle Z \rangle_{\text{avg}}$, as depicted in Fig. 2.21. Assuming $V_{\text{oc}}(t)$ is sinusoidal with a constant amplitude $|V_{\text{oc}}|$, then the following expression describes $\langle P_{\text{L}} \rangle_{\text{avg}}$ as a function of R_{L}:

$$\langle P_{\text{L}} \rangle_{\text{avg}} = \frac{1}{2} \left(\frac{|V_{\text{oc}}|}{|\langle Z \rangle_{\text{avg}} + R_{\text{L}}|} \right)^2 R_{\text{L}} \tag{2.86}$$

Eq. (2.86) is derived from Eq. (2.85) by noting the following concerning the current passing through the load:

$$\langle I_{\text{L}} \rangle_{\text{RMS}} = \langle I_{\text{L}} \sin(\omega t) \rangle_{\text{RMS}} = \frac{\sqrt{2}}{2} |I_{\text{L}}| \tag{2.87}$$

$$|I_{\text{L}}| = \frac{|V_{\text{oc}}|}{|\langle Z \rangle_{\text{avg}} + R_{\text{L}}|} \tag{2.88}$$

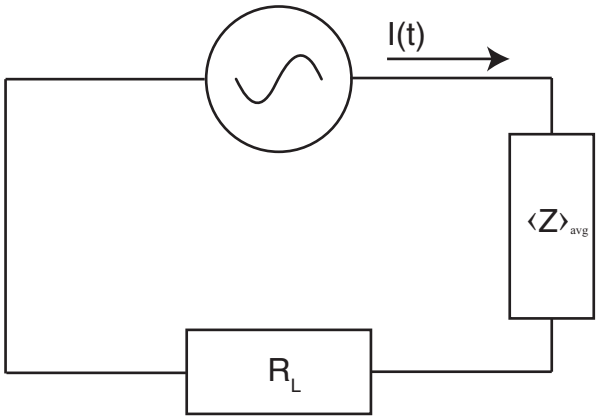

Figure 2.21: Circuit model of G-SCEEG as an AC voltage source. According to Thevenin's theorem the G-SCEEG can be modeled as an AC voltage source in series with an average internal impedance, $\langle Z \rangle_{\text{avg}}$ (assuming the voltage source is sinusoidal), and a load resistance, R_{L}.

It can be shown from Eq. (2.86) that $\langle P_{\text{L}} \rangle_{\text{avg}}$ is maximized when $R_{\text{L}} = \langle Z \rangle_{\text{avg}}$. This maximum is observed in the plot of Fig. 2.22 (**a**). Fig. 2.22 (**a**) shows how $\langle P_{\text{L}} \rangle_{\text{avg}}$ changes as a function of R_{L} for $R_{\text{L}} = 15 - 1680\ \text{k}\Omega$. A variable resistor was used as the load for most data points and

its resistance was measured using a multimeter. $I_{\mathrm{L}}(t)$ was measured using a Keithley 427 current amplifier and $\langle P_{\mathrm{L}} \rangle_{\mathrm{avg}}$ was calculated from Eq. (2.85). The dashed black line in Fig. 2.22 (**a**) represents a fit of the data using Eq. (2.86). From this fit, it was determined that $\langle Z \rangle_{\mathrm{avg}} = 100$ kΩ and $|\mathrm{V_{oc}}| = 165$ mV. The blue line in Fig. 2.22 (**a**) shows the efficiency, η, of the transfer of power from the G-SCEEG to the load. It is defined as the ratio of the power dissipated in the load to the total generated power:

$$\eta = \frac{P_{\mathrm{L}}}{P_{\mathrm{TOT}}} = \left(1 + \frac{\langle Z \rangle_{\mathrm{avg}}}{R_{\mathrm{L}}}\right)^{-1} \tag{2.89}$$

Although $\langle P_{\mathrm{L}} \rangle_{\mathrm{avg}}$ is maximized when $R_{\mathrm{L}} = \langle Z \rangle_{\mathrm{avg}}$, only half of the generated power is transferred to the load at this value. The other half is dissipated in the device's internal impedance.

Fig. 2.22 (**b**) plots $\langle P_{\mathrm{L}} \rangle_{\mathrm{avg}}$, dissipated in a load resistance of 170 kΩ, as a function of time. A 20 μL droplet of 1 M HCl oscillating at 28 Hz with an initial area change of 3.5 mm^2 was used. This data was taken under normal atmospheric conditions and without sparging the electrolyte with He. The initial increase in $\langle P_{\mathrm{L}} \rangle_{\mathrm{avg}}$ could be due to changes in the concentration and pH of the droplet brought on by evaporation. Oscillations in $\langle P_{\mathrm{L}} \rangle_{\mathrm{avg}}$ after 30 min. are likely due to changes in the average position of the droplet relative to the gap in the graphene as asymmetric droplets have been observed to generate large spikes in power. Despite significant evaporation of the droplet, the G-SCEEG is still able to generate close to 80 nW of power after 60 min.

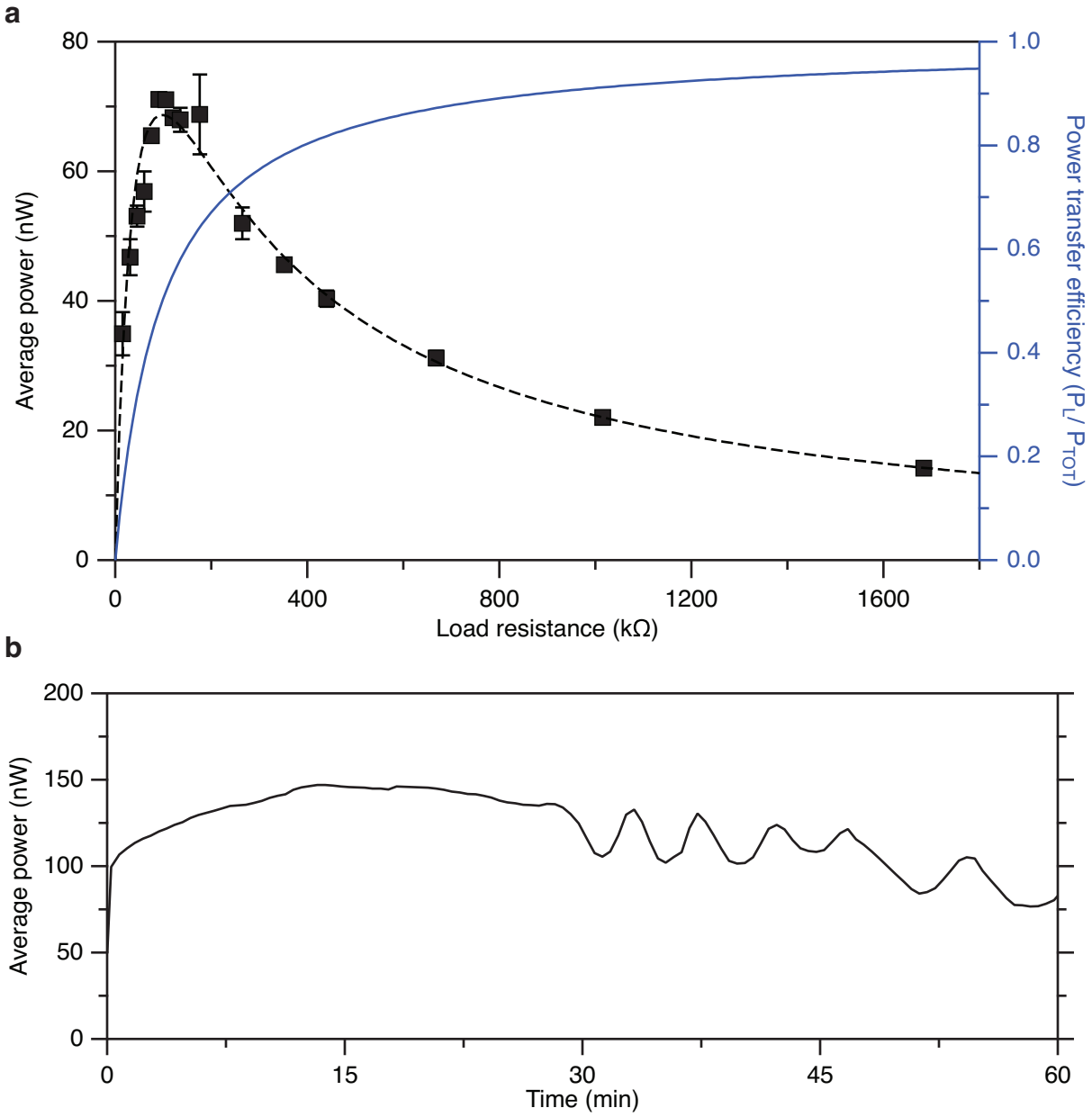

Figure 2.22: $\langle P_{\mathrm{L}} \rangle_{\mathrm{avg}}$ **vs.** R_{L} **and vs. time. a**, $\langle P_{\mathrm{L}} \rangle_{\mathrm{avg}}$ (black squares) as a function of the load resistance (average power was calculated from the measured RMS value of $I_{\mathrm{L}}(t)$). The dashed black line is a fit of the data to Eq. (2.86). The blue line represents the power transfer efficiency, *i.e.* the ratio of the power dissipated in the load to the total power generated by the G-SCEEG, $P_{\mathrm{L}} \,/\, P_{\mathrm{TOT}}$, and was calculated using Eq. (2.89). Droplet volume $= 20$ μL of 1 M HCl, oscillation frequency $= 28$ Hz, peak-to-peak area change $= 3.5$ mm^2. Where they are not visible, error bars are smaller than the dimensions of the data point's symbol. **b**, $\langle P_{\mathrm{L}} \rangle_{\mathrm{avg}}$ as a function of time for a 20 μL droplet of 1 M HCl oscillating at 28 Hz under normal atmospheric conditions. Oscillations are due to changes in the droplet's average position as it evaporates. $R_{\mathrm{L}} = 170$ kΩ. Initial area change $= 3.5$ mm^2.

2.4.2 Applications

2.4.2.1 *Energy harvesting*

One application of the G-SCEEG can be found in harvesting energy from sources of mechanical vibration. SCEEGs represent a novel form of micro-energy harvesting device whose mechanism of action markedly differs from that of piezoelectric, electromagnetic, thermoelectric, pyroelectric, photovoltaic, and triboelectric devices [62, 63]. According to Ref. [64], a white paper put forth by the company Texas Instruments in 2008, industrial and human sources of vibrational energy have estimated energy densities of 100 and 4 μW/cm^2, respectively. Because it has been demonstrated that the G-SCEEG can generate electric power in excess of 1 μW, such sources of vibrational energy could be harvested by G-SCEEGs to realistically replace batteries in powering small electronic devices or other ultra-low-power (ULP) technologies [63–65]. Additionally, larger amounts of electric power, on the scale of mW, can be reasonably achieved if the G-SCEEG is scaled up in the various ways that are modeled in Fig. 2.8 (p. 46). These include increasing the change in the overlap area, the number of simultaneously oscillating droplets, and the frequency of the droplet's oscillation.

A key aspect to consider before using the G-SCEEG to harvest energy, however, is the efficiency, η_{c}, with which it converts mechanical energy into electrical energy. When exposed to two 20 μL droplets of 6.0 M HCl, it is conservatively estimated that the $\mathrm{G_{MULTI}}$-SCEEG's efficiency is $\eta_{\mathrm{c}} = 0.4\,\%$. This was determined by estimating the average power input, $\langle P_{\mathrm{in}} \rangle_{\mathrm{avg}}$, that the sinusoidal vibration source needs to provide in order to overcome the dissipative forces acting on the droplets. To find $\langle P_{\mathrm{in}} \rangle_{\mathrm{avg}}$, the scalar product between the droplets' sinusoidal velocity, $\vec{v}$, and the sum of the dissipative forces acting on the droplets, *i.e.* the sum of the quadratic drag force, $\vec{f}_{\mathrm{d}}$, and the force of kinetic friction, $\vec{f}_{\mathrm{k}}$, was first determined and then subsequently averaged over half of the period of oscillation.

Assuming the displacement vector of a single droplet's center of mass as a function of time t is $\vec{x}(t) = \Lambda \cos(\omega\, t - \delta)\, \hat{x}$:

$$\vec{v}(t) = -\,\omega\, \Lambda\, \sin(\omega\, t - \delta)\, \hat{x} \tag{2.90}$$

$$\vec{f}_{\text{d}}(t) = \frac{1}{2}\, c_{\text{d}}\, \rho_{\text{m}}\, A_{\text{c}}\, v^2(t)\, \hat{x} \tag{2.91}$$

$$\vec{f}_{\text{k}} = \mu_{\text{k}}\, m\, g\, \hat{x} \tag{2.92}$$

and the required input power, P_{in}, is:

$$P_{\text{in}} = \left(\vec{f}_{\text{d}} + \vec{f}_{\text{k}}\right) \cdot \vec{v} \tag{2.93}$$

$$= \left[\frac{c_{\text{d}}\, \rho_{\text{m}}\, A_{\text{c}}\, \omega^3\, \Lambda^3}{2}\right] \sin^3(\omega\, t - \delta) + \left[\omega\, \mu_{\text{k}}\, m\, g\, \Lambda\right] \sin(\omega\, t - \delta) \tag{2.94}$$

where c_{d} is the drag coefficient, ρ_{m} the mass density of the droplets, A_{c} the frontal cross-sectional area of a single droplet, m is the mass of a single droplet, ω the angular frequency, Λ the amplitude of displacement, μ_{k} the coefficient of kinetic friction, δ the angular phase, and g the gravitational constant. The negative sign is neglected as it is understood that power is always being input into the system to overcome the dissipative forces.

The average input power, $\langle P_{\text{in}} \rangle_{\text{avg}}$, required to overcome the dissipative forces over one half of the period of the droplets' oscillation, $t = T\,/\,2 = \pi\,/\omega$, is then:

$$\langle P_{\text{in}} \rangle_{\text{avg}} = \frac{\omega}{\pi} \int_0^{\frac{\pi}{\omega}} \left(\vec{f}_{\text{d}} + \vec{f}_{\text{k}}\right) \cdot \vec{v}\, dt = \frac{2\,\omega\,\Lambda}{\pi} \left(\frac{c_{\text{d}}\, \rho_{\text{m}}\, A_{\text{c}}\, \omega^2\, \Lambda^2}{3} + m\, \mu_{\text{k}}\, g\right) \tag{2.95}$$

Based on the value for $\langle P_{\text{out}} \rangle_{\text{avg}}$ that was generated by two oscillating droplets of 6.0 M HCl (see

Fig. 2.20 (**c**) on p. 89), the efficiency, η_c, of the G_{MULTI}-SCEEG is:

$$\eta_c = \frac{\langle P_{out} \rangle_{avg}}{\langle P_{in} \rangle_{avg}} \simeq \frac{1.6\,\mu W}{400\,\mu W} = 0.4\,\% \tag{2.96}$$

where $c_d \simeq 0.5$, $\rho_m = 1000$ kg/m^3, $A_c = 2 \times 10^{-5}$ m^2 (total cross-sectional area of the two droplets), $m = 4 \times 10^{-5}$ kg (total mass of the two droplets), $\omega = 60\,\pi$ rad/s, $\Lambda = 3 \times 10^{-3}$ m, $\mu_k = 0.06$ [66], and $g \simeq 10$ m/s^2 were all estimated to match the experimental conditions.[36] Although the efficiency of the G-SCEEG, as configured, is low, it can be increased in a straightforward way if the geometry of the droplets is changed such that their drag coefficients and cross-sectional areas are reduced.

Overall, both the electrical output and the efficiency of the G_{MULTI}-SCEEG, as currently configured, are small compared to other energy harvesting devices such as triboelectric nanogenerators (TENGs) which rely on a mechanism of contact electrification. TENGs have demonstrated electrical outputs of 230 V, 15.5 μA/cm^2, and 128 mW/cm^3 and efficiencies between 10–39 % [67]. Because the G-SCEEG does not involve contact between solid materials, however, its lifespan will likely be much greater than that of TENGs and other energy harvesting devices that do rely on physical contact between solids. On the other hand, compared to other supercapacitive, energy-harvesting devices made from graphene and ITO, the G_{MULTI}-SCEEG generates orders of magnitude greater output (see Tables 2.4 (p. 110) and 2.5 (p. 111) for a direct comparison of the outputs of various supercapacitive energy-harvesting devices). Regardless of the energy harvesting mechanism employed, it is believed that micro-energy harvesting technologies will enable the design of smaller electronic devices if these technologies are able to successfully replace the need for batteries as it is ultimately the volume of the battery that currently determines the lower limit of the device's size.

[36] Note that when using these values, the magnitude of the force of kinetic friction is negligible compared to that of the quadratic drag force, *i.e.* $f_d >> f_k$.

2.4.2.2 *Detection of the resonant modes of standing capillary waves*

Another application of the G-SCEEG is the detection of standing capillary waves on the surface of a droplet of electrolyte solution. When a droplet is oscillated at a frequency that corresponds to a standing wave mode resonance, the droplet will move relative to the surface of the G-SCEEG. This movement generates short-circuit current in the G-SCEEG and allows the resonant mode to be identified. There are two ways in which the surface wave modes can be excited. Multiple resonant modes can be excited simultaneously by subjecting the droplet to a mechanical impulse. The frequencies of the excited modes can then be determined via Fourier analysis of the resulting $I_{sc}(t)$ time trace. This is similar to the method used in Fourier transform spectroscopy. Alternatively, the modes can be selectively excited one-by-one by oscillating the droplet at specific frequencies. The frequencies at which measurable current is produced are those that correspond to resonant modes. This is similar to the method used in dispersive spectroscopy.

Fig. 2.23 shows the results of the Fourier transform method. Fig. 2.23 (**a**) displays the current vs. time that is generated by mechanically plucking a 1 μL droplet of 0.5 M NaCl containing 12.5% (v/v) glycerol that is initially resting on the center of a multi-layer G-SCEEG device with a finely-pointed glass capillary tube. The pluck simultaneously excites multiple resonant modes of standing waves on the droplet's surface which results in the particular current vs. time waveform of part (**a**). Taking the Fourier transform of (**a**) gives the power spectral density shown in Fig. 2.23 (**b**). Peaks in the power spectral density correspond to the resonant frequencies of the standing wave modes.

According to Ref. [47], the dispersion relation that describes standing waves on the surface of a freely suspended liquid droplet surround by a uniform fluid is given by the following expression:

$$f^2 = \left[\frac{\gamma}{4\,\pi^2\,\rho_{\mathrm{m}}\,r^3}\right] \mathrm{n}\,(\mathrm{n}-1)\,(\mathrm{n}+2) \tag{2.97}$$

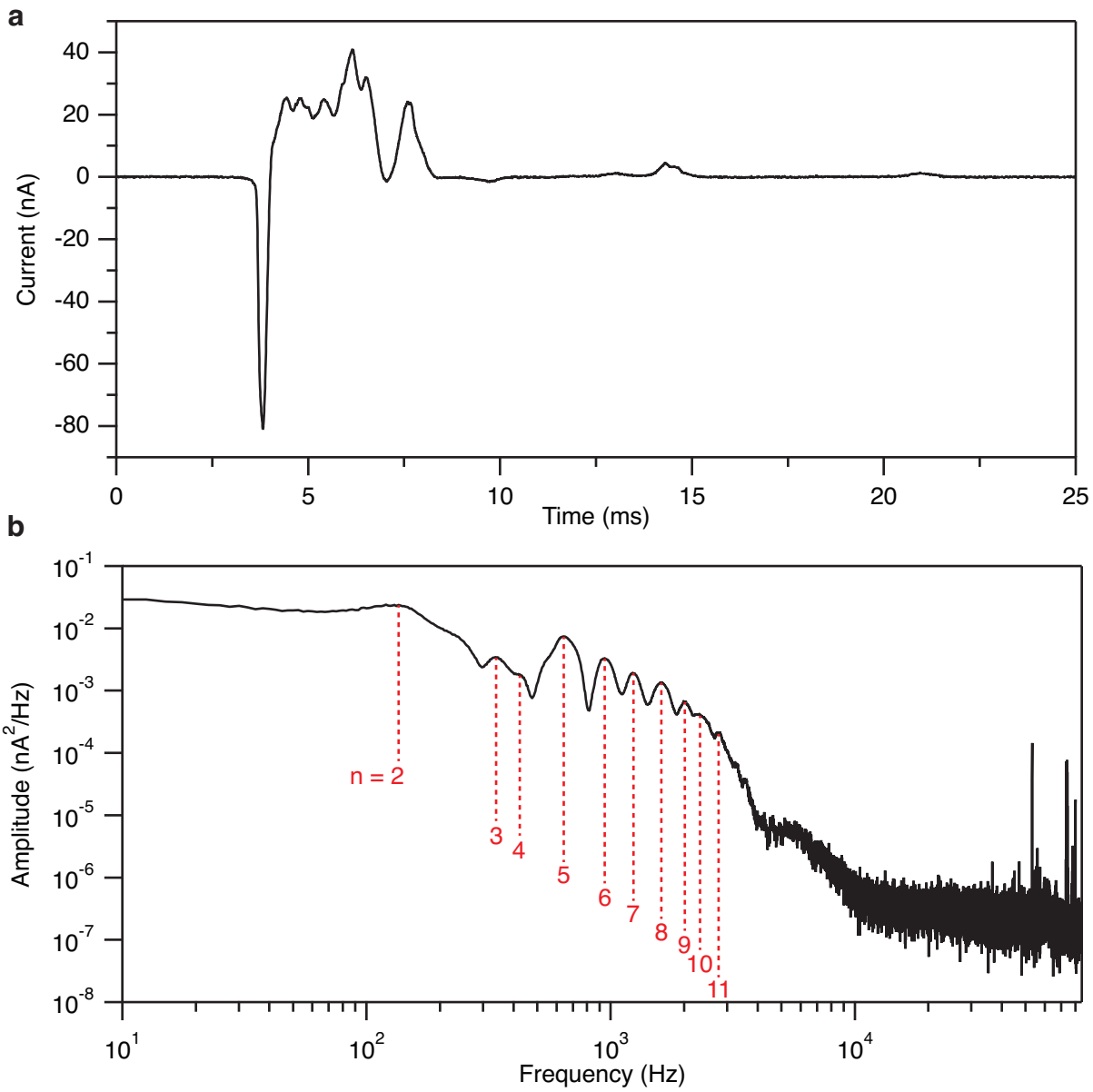

Figure 2.23: Simultaneous excitation of multiple surface capillary wave modes. **a**, I_{sc} vs. time of a 1 μL droplet of 0.5 M NaCl + glycerol (12.5% v/v) upon being mechanically plucked by a finely-pointed glass capillary tube. **b**, Power spectral density of current trace in (**a**) showing peaks due to the excitation of different surface capillary wave modes which have been labeled n $= 2$–11.

where n is the mode number, γ is the surface tension, ρ_{m} is the mass density of the liquid, and r is the radius of the droplet. According to Eq. (2.97), f^2 scales linearly with $\mathrm{n}\,(\mathrm{n}-1)\,(\mathrm{n}+2)$. Although the droplet in the experiment is resting on the G-SCEEG and is not freely suspended, the linear scaling of f^2 with $\mathrm{n}\,(\mathrm{n}-1)\,(\mathrm{n}+2)$ still holds for the data in Fig. 2.23 (**b**). This is clearly demonstrated in Fig. 2.24 (p. 98). Note that because the $\mathrm{n} = 1$ mode corresponds to translation of the droplet and not to a standing wave mode, the values of n from $\mathrm{n} = 2$–11 were assigned to the peaks in Fig. 2.23 (**b**) starting with the peak at 135 Hz.

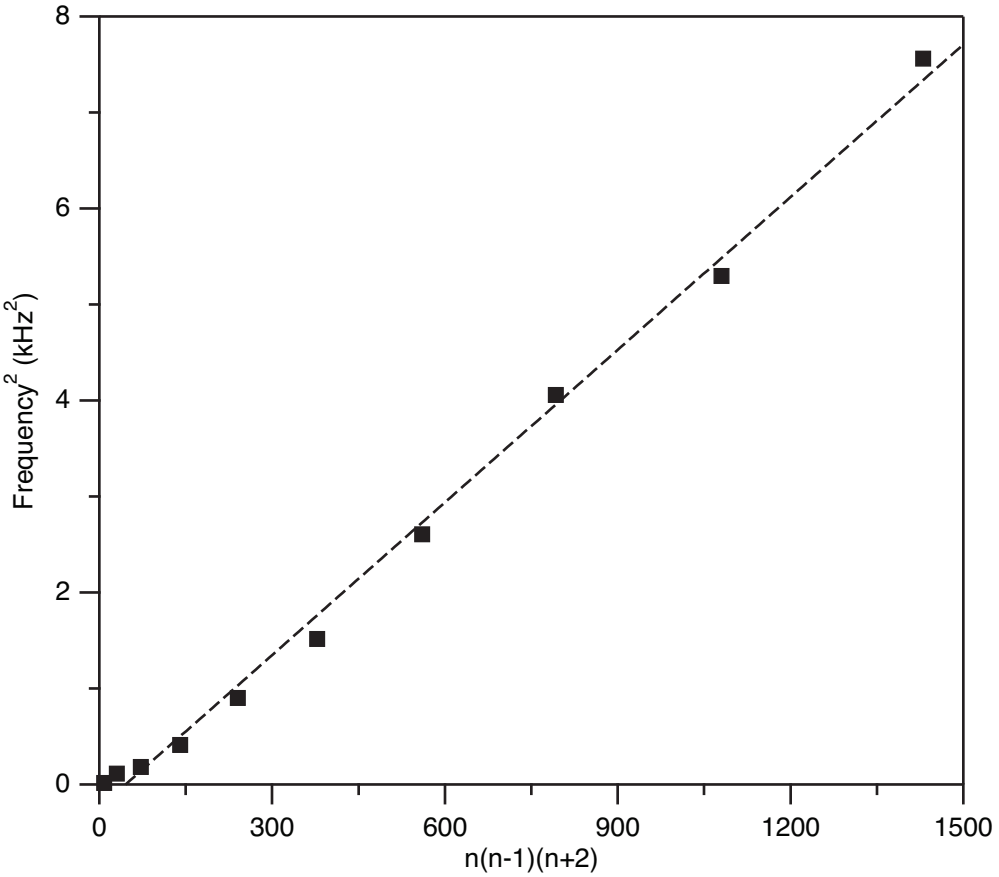

Figure 2.24: Estimation of the radius of curvature. The radius of curvature for a 1 μL droplet of 0.5 M NaCl + glycerol (12.5% v/v) can be estimated from the plot of the mode frequency squared vs. the mode parameter, $\mathrm{n}\,(\mathrm{n}-1)\,(\mathrm{n}+2)$. Data taken from Fig. 2.23. The radius was estimated to be $\simeq 0.7$ mm.

For $\gamma = 72$ mN/m and $\rho_{\mathrm{m}} = 1050$ kg/m^3, the radius of curvature, r, of the droplet was es-

timated from the slope of the linear fit of the data in Fig. 2.24 to be $\simeq 0.7$ mm. This underestimates the actual radius of curvature which was measured to be 1 mm. The fact that the droplet on the G-SCEEG is only hemispherical whereas Eq. (2.97) assumes a completely spherical droplet likely accounts for this discrepancy.

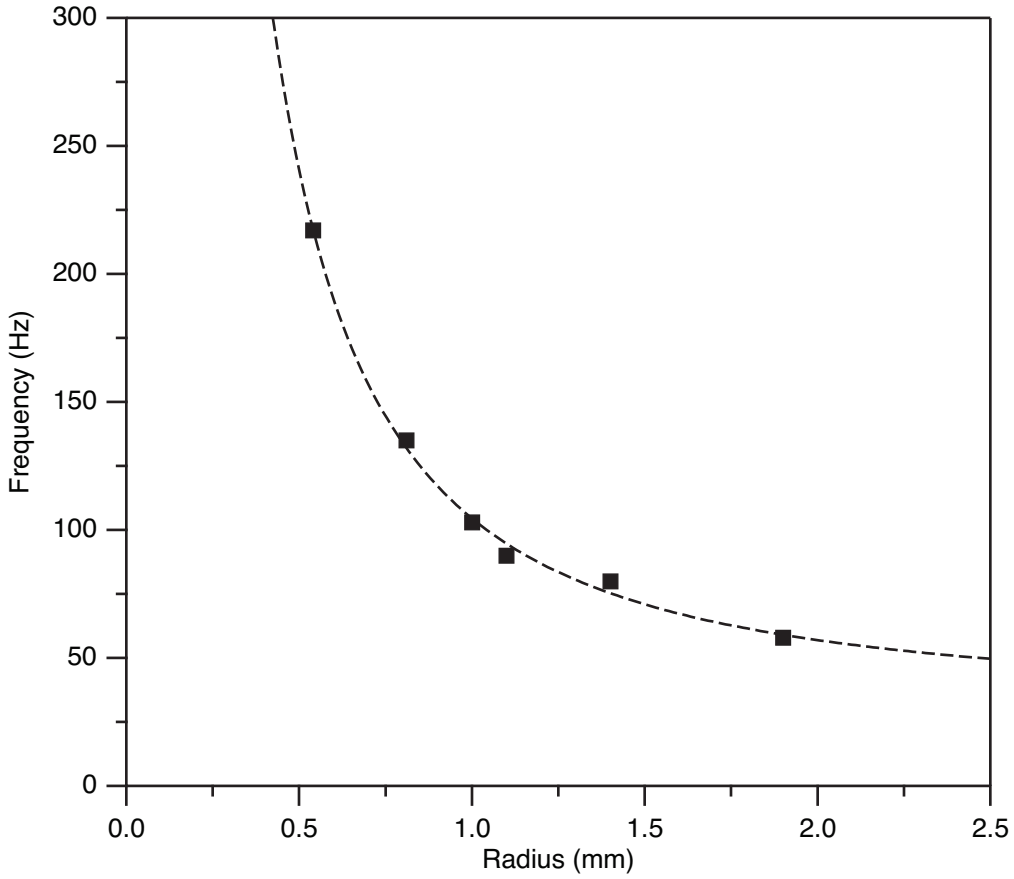

Figure 2.25: Scaling of n $= 2$ resonant mode frequency with radius of curvature. Plotting the frequency of the n $= 2$ resonant mode vs. radius of curvature of different volumes of 0.5 M NaCl $+$ glycerol (12.5% v/v) droplets shows the characteristic scaling of surface capillary waves. The dashed line is a fit of the data to a power-law function showing that $f \propto r^{-3/2}$.

The Fourier transform method of detecting resonant modes is further confirmed in Fig. 2.25 by plotting the frequency of the n $= 2$ mode vs. the radius of curvature of different volumes of droplets. The radius of curvature was measured from photographs of the profile of the the droplets

resting on the G-SCEEG. Droplets of volume 0.5, 1, 2, 3, 5, and 10 μL were used. The dashed line represents a fit of the data to a power-law function with an exponent of $-3/2$. As evident by the dashed line and as predicted by the dispersion relation, $f \propto r^{-3/2}$.

The results of the dispersive method of detecting the resonant modes are shown in Fig. 2.26. Fig. 2.26 (**a**) is the RMS current that is generated as the driving frequency is scanned from 10–510 Hz for a 5 μL droplet of 1.0 M NaCl on the multi-layer G-SCEEG. A lock-in amplifier was used to measure the current. The lock-in amplifier was used to filter out frequencies of the generated current that were not within several Hertz of the driving frequency. The photographs in (**a**) capture the outline of the droplet's motion at the first three odd resonant modes, *i.e.* $\mathrm{n} = 1, 3$, and 5. As seen in the photograph, the $\mathrm{n} = 1$ mode corresponds to lateral translation of the droplet whereas the other two correspond to standing waves on the droplet's surface. The linearity of f^2 vs. $\mathrm{n}\,(\mathrm{n}-1)\,(\mathrm{n}+2)$ is again demonstrated in Fig. 2.26 (**b**) for different volumes of droplets of 1 M NaCl. Several data points in (**b**) represent even resonant modes that were detected by oscillating the droplets and the G-SCEEG vertically with the speaker in addition to horizontally.

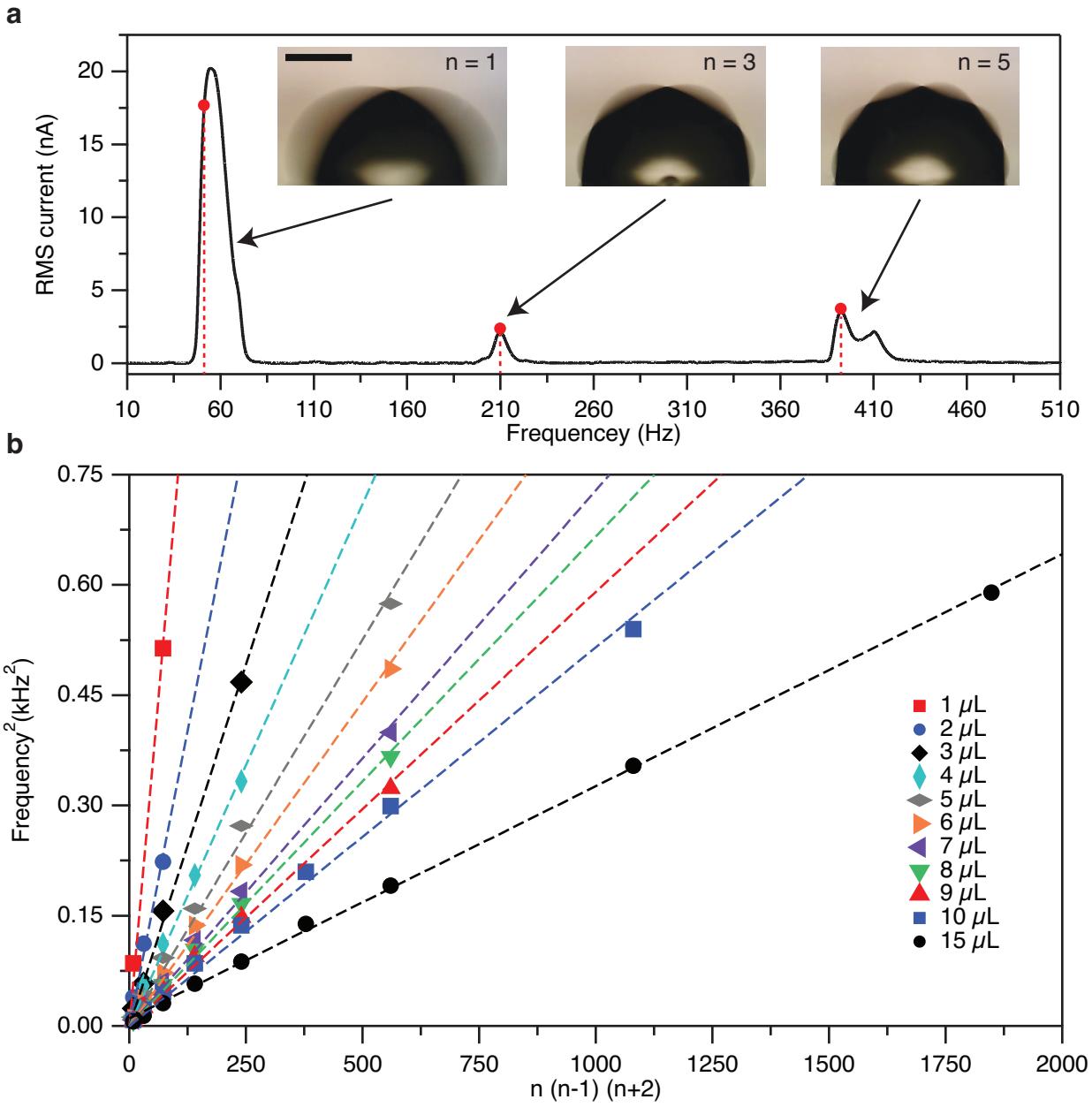

Figure 2.26: Selective excitation of individual surface capillary wave modes. **a**, $\langle I_{sc} \rangle_{RMS}$ vs. frequency of a 5 μL droplet of 1.0 M NaCl. The red dots and dashed lines mark the frequencies at which the phase shift between the input and output waveforms is $90°$, indicating that the surface wave is on resonance. A horizontal driving force excites only the odd resonant modes, *i.e.* n $= 1$, 3, and 5. Droplet images (insets) show the different surface capillary standing waves that are excited at each odd mode. Scale bar $= 1$ mm. **b**, Plot of frequency squared vs. the mode parameter, $n\,(n-1)\,(n+2)$, for different volumes of 1 M NaCl. Plot includes data from both odd (horizontal motion) and even (vertical motion) resonant modes.

2.4.3 Characterization of graphene electrodes

This section provides a characterization of several of the physical and chemical properties of the G-SCEEGs' graphene electrodes. In addition to the figure captions, further explanations are included where appropriate.

2.4.3.1 *Sheet resistance*

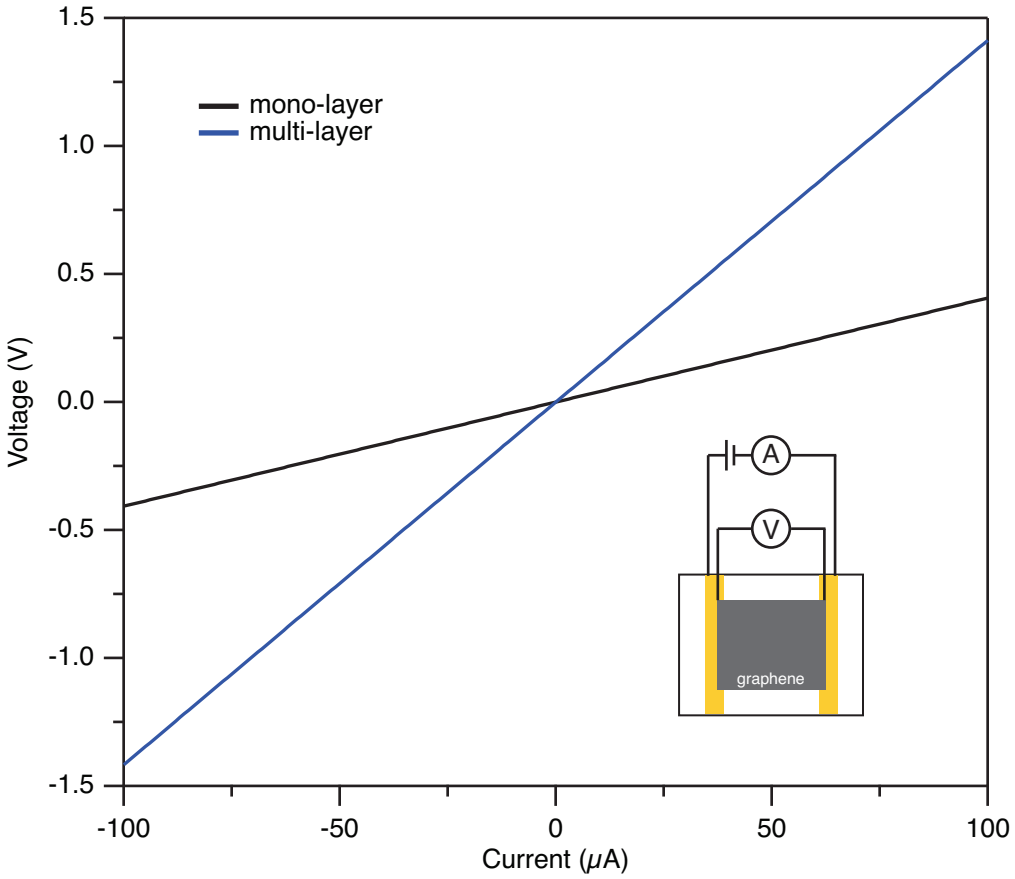

Figure 2.27: I-V curves of G-SCEEG devices. I-V curves measured using the four-point probe method of mono- and multi-layer G-SCEEG devices before bifurcation. The linearity of the curves indicates an ohmic contact between the Au contacts of the device and the graphene. The sheet resistances of the mono- and multi-layer devices were calculated to be and 3.7 and 14.2 k$\Omega/\square$, respectively.

2.4.3.2 *Charge-carrier density and mobility*

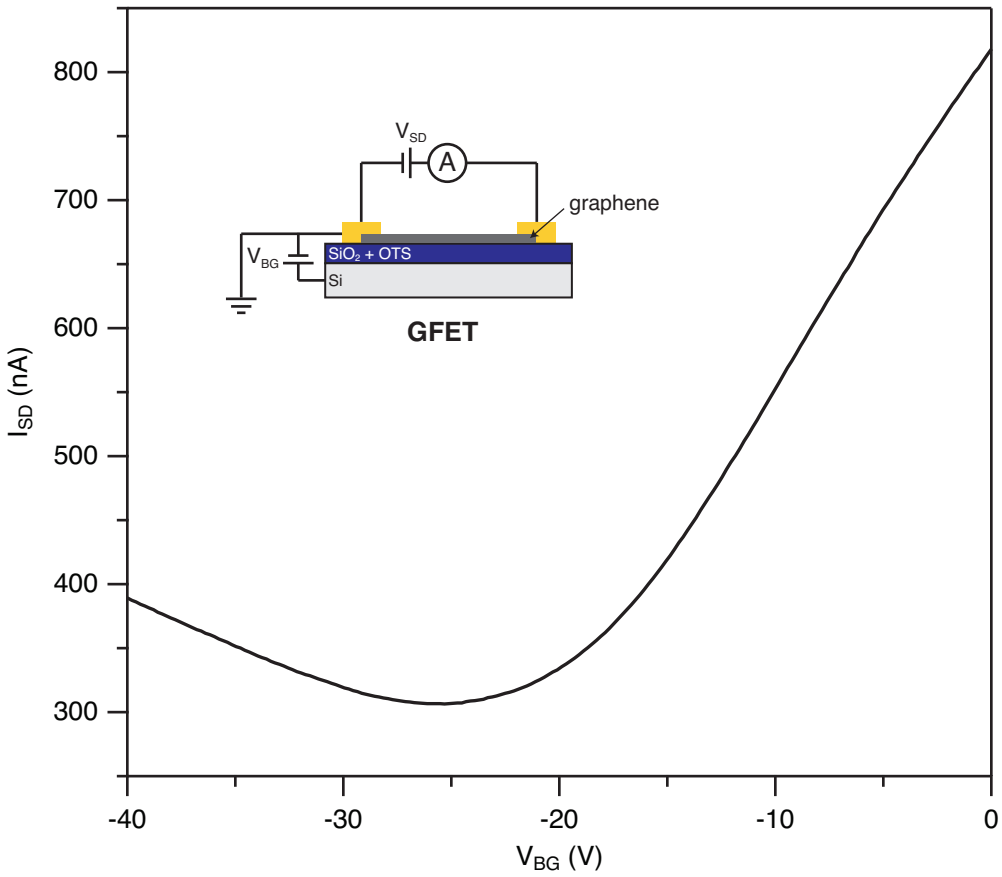

Figure 2.28: I_{SD} vs. V_{BG} for a large-grain, mono-layer graphene field-effect transistor (GFET). I_{SD} vs. V_{BG} for large-grain, mono-layer graphene on OTS-coated 300 nm SiO_2 on Si after being baked for 1 hr at $250°$C. $V_{SD} = 10$ mV, pressure $= 3 \times 10^{-5}$ mbar. The location of the current minimum indicates that the graphene is intrinsically n-doped with 2×10^{12} electrons per cm^2. Before being baked, however, it was determined that the graphene was p-doped with $> 3 \times 10^{12}$ holes per cm^2. From the slope of I_{SD} vs. V_{BG} to the right of the minimum the mobility of the electrons was determined to be 2000 cm^2/(V·s).

2.4.3.3 *Optical micrographs*

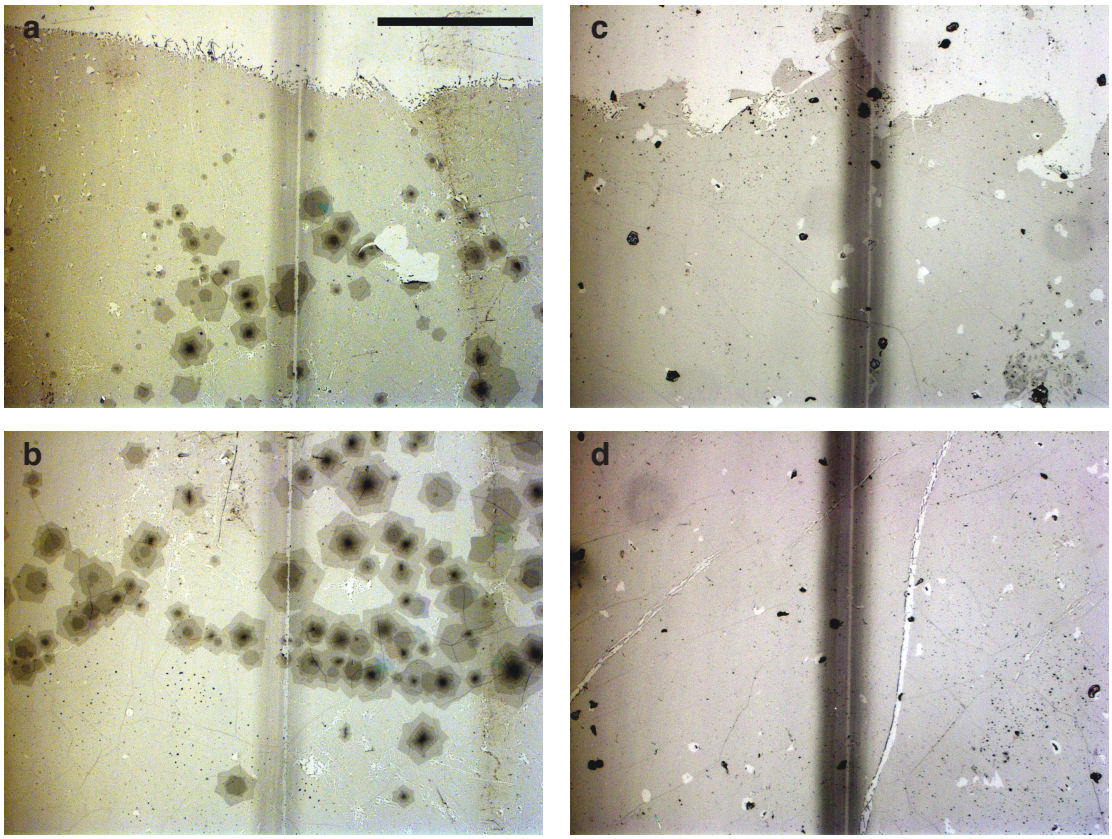

Figure 2.29: Optical micrographs of multi- and mono-layer G-SCEEG devices. Optical micrographs of the edge (**a** and **c**) and bulk (**b** and **d**) of multi-layer (left) and mono-layer (right) G-SCEEG devices taken with an inverted microscope. The gaps in the graphene are seen as vertical lines of lighter contrast located roughly in the middle of the images. Dark shadowing around the gaps is due to scoring of the back surface of the glass. Scale bar = 0.5 mm. Multi-layer graphene regions appear as hexagonal shapes of darker contrast. The darker the contrast the greater the number of layers. Contamination due to adsorbed PMMA and other particulates appears as dark specs. Folds appear as dark lines. Rips and tears show up as areas of lighter contrast.

2.4.3.4 *Raman spectral analysis*

Using Raman spectral analysis, Figs. 2.30 and 2.31 compare the large-grain, mono-layer (LGML) graphene used to make the G-SCEEG devices in this dissertation to graphene synthesized using a chemical vapor deposition (CVD) recipe that is commonly cited in the literature [15, 68]. Here, graphene synthesized using this common recipe is referred to as "standard" graphene. Raman analysis was done on both LGML and standard graphene that was supported by OTS- functionalized borosilicate glass. The Raman analysis on LGML graphene is representative of the mono-layer regions in large-grain graphene that also contains regions of multilayers. For Raman analysis of multi-layer regions, see Chapter 4, Sect. 4.4, Figs. 4.3 (p. 175) and 4.4 (p. 177). In both Figs. 2.30 and 2.31 below, the laser excitation photon energy was 2.33 eV at 8 mW and the laser spot size was 1–2 μm.

Fig. 2.30 (**a**) shows that the LGML graphene is less defective than standard graphene due to the notable lack of a D-peak at 1330 cm^{-1} in the LGML graphene's point spectrum. This is likely a result of a reduction in the number of grain boundaries in LGML graphene. The average diameter of graphene grains in LGML graphene is > 1 mm whereas it is approximately 10 μm in standard graphene. Fig. 2.30 (**b**) shows the probability density of the normalized D-peak intensity, I_D/I_G, over a 75×75 μm area. This further proves that LGML graphene is significantly less defective than standard graphene.

In addition to being more defective, standard graphene contains a significant amount of multi-layers. This is proven in the histograms of Figs. 2.30 (**c**)–(**e**). According to Kim et al. in Ref. [69], taken together the normalized G′-peak intensity ($I_{G'}/I_G$), the full-width half-maximum (FWHM) of the G′ peak, and the G′ peak's spectral shift all qualitatively demonstrate a significant amount of multi-layer graphene present in the standard graphene. It is estimated that at least 25% of the total area of standard graphene contains some number of multi-layers.[37]

[37] It is worth mentioning that the authors of Ref. [68] claim that only 5% of the total area of graphene synthesized

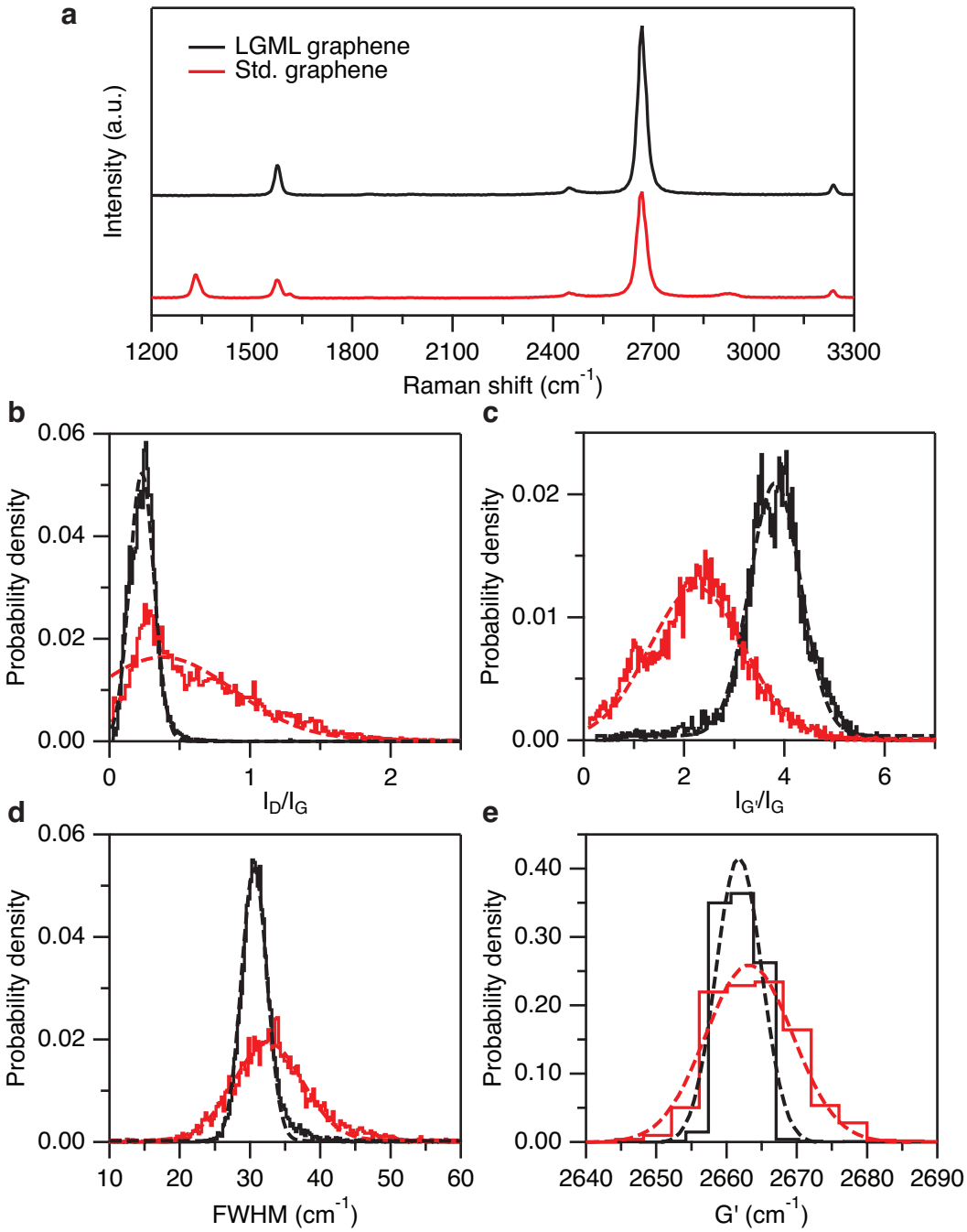

Figure 2.30: Raman spectral analysis of LGML vs. standard CVD graphene. a, Raman point spectra of LGML and standard CVD graphene. Histograms of: **b**, I_D/I_G **c**, $I_{G'}/I_G$ **d**, full-width half-maximum of G′ and **e**, spectral position of G′ peak of LGML and standard CVD graphene. Laser excitation photon energy $= 2.33$ eV at 8 mW and the laser spot size $= 1$–2 μm.

Comparing the Raman spectral maps of I_D/I_G and $I_{G'}/I_G$ in Fig. 2.31 visually demonstrates the relative amount of defects and multi-layers that the standard graphene has compared to the LGML graphene.

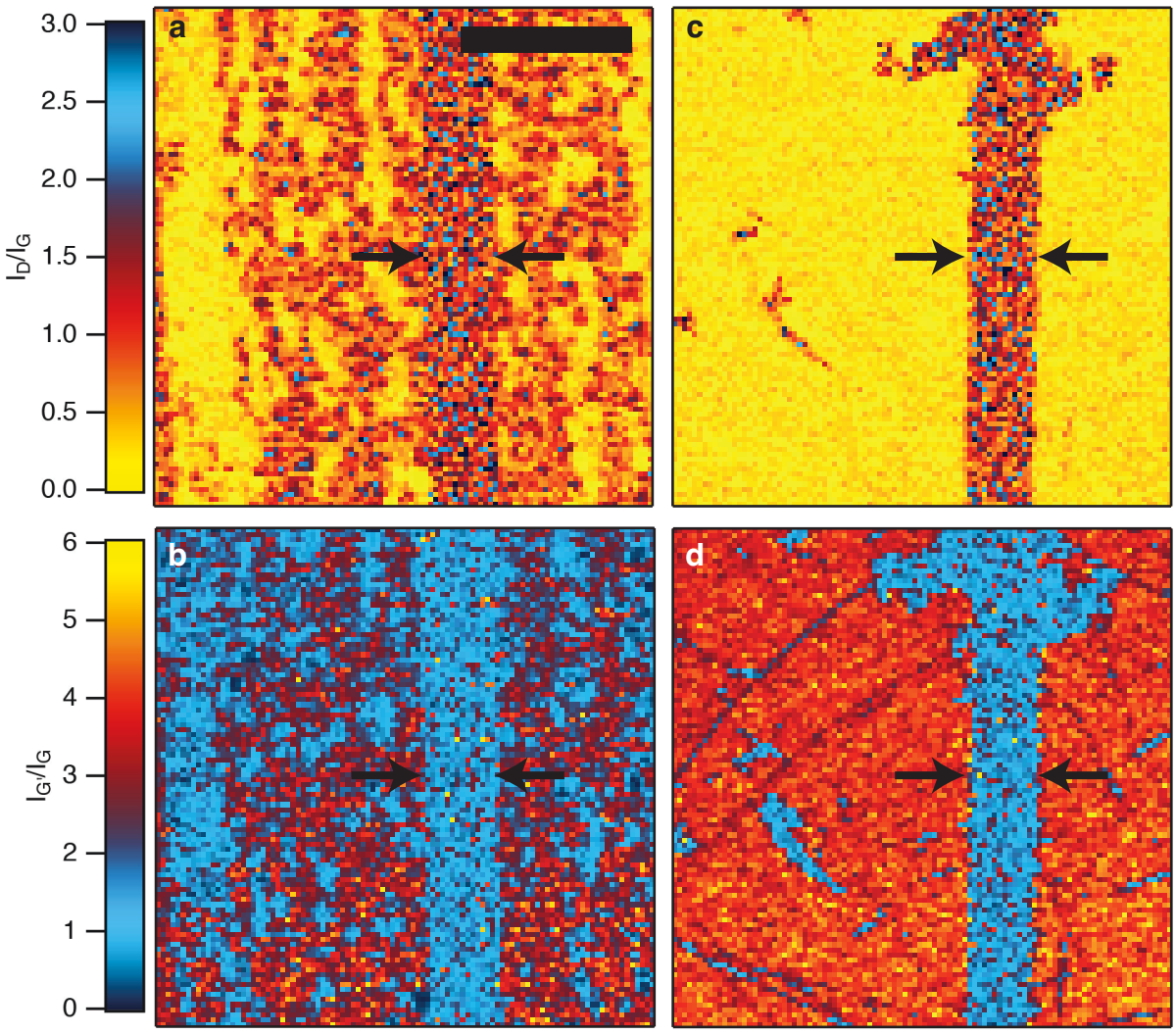

Figure 2.31: Raman maps of gap in LGML vs. standard CVD graphene. **a**, **c**, Map of I_D/I_G for standard and LGML CVD graphene, respectively, in the vicinity around the gap. Edges of the gap are demarcated with black arrows. **b**, **d**, Map of $I_{G'}/I_G$ for standard and LGML CVD graphene, respectively. Scale bar: 25 μm. Laser excitation photon energy $= 2.33$ eV at 8 mW and the laser spot size $=$ 1–2 μm.

using this protocol is covered with multi-layers.

2.4.3.5 *X-ray photoelectron spectral analysis*

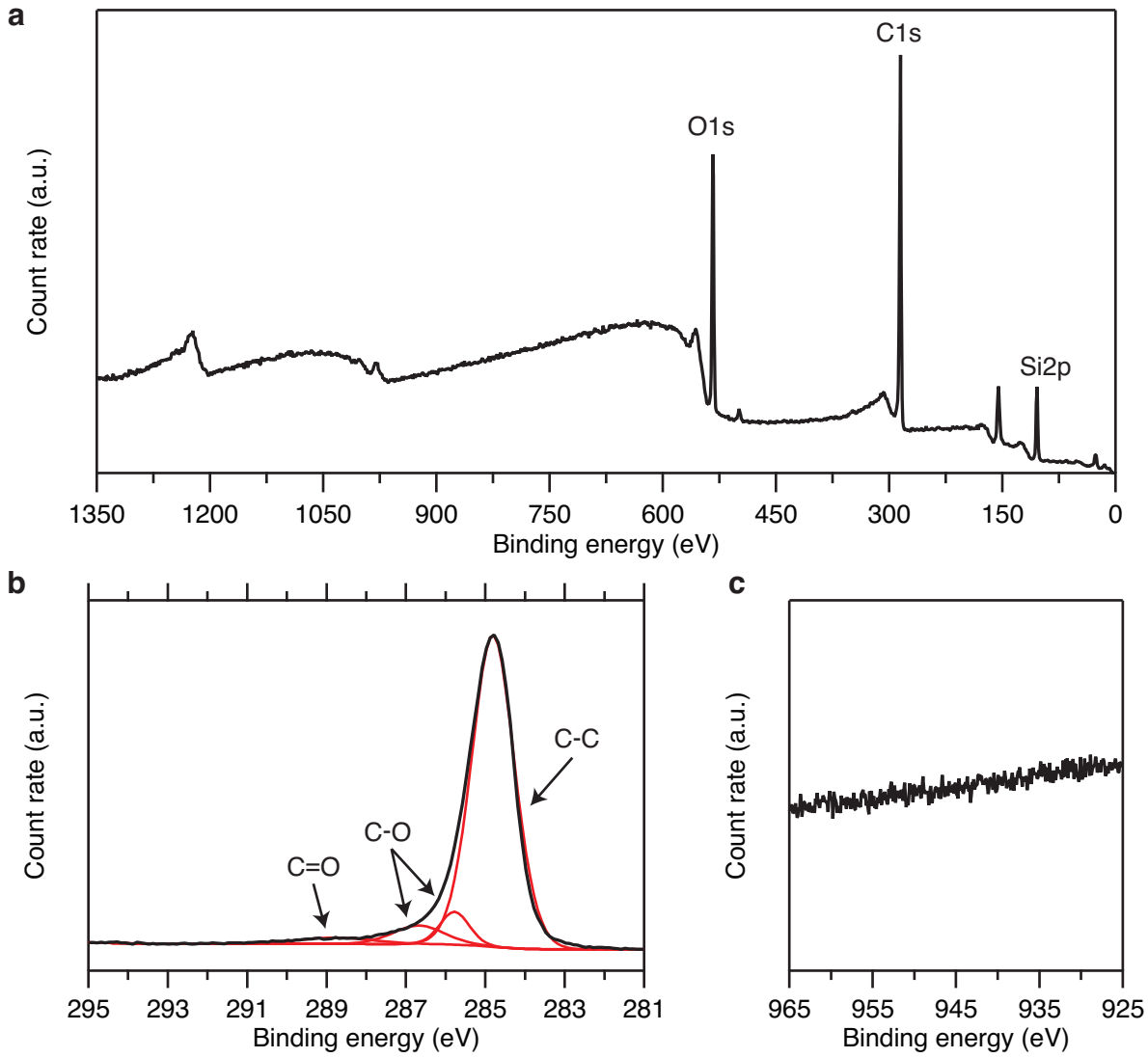

Figure 2.32: XPS analysis. a, XPS spectrum of mono-layer G-SCEEG device taken across the gap in the graphene. **b**, High-resolution spectrum of C1s peak. Red lines show the deconvolution of the peak into sub-peaks, each representing different types of carbon bonds that were detected. **c**, High-resolution spectrum of the Cu2p energy band showing no detectable amount of residual Cu. Beam diameter $= 400$ μm. X-ray source: Al K_α X-rays; X-ray energy: 1486.7 eV. The spectra qualitatively show that the graphene does not contain large quantities of oxygenated functional groups or residual Cu. The detection of oxygenated-carbon functional groups is likely the result of residual PMMA from the transfer process. The strong O1s and Si2p peaks in (**a**) are likely due to the borosilicate glass because the penetration depth of the X-rays is 10 nm and the thickness of the OTS is only 2.5 nm.

2.5 Comparison of symmetric SCEEG devices

As stated earlier in the chapter, G-SCEEG devices were fabricated using two types of large-grain graphene, one that contains areas of multi-layers (LG-Multi) and one that does not (LG-Mono). Fig. 2.33 (**a**) compares the RMS current generated by each as a function of the change in area when a 20 μL droplet of 1 M NaCl is oscillated at 30 Hz. In addition, Fig. 2.33 (**a**) compares both G-SCEEG devices with a similar symmetric SCEEG device, an Au-SCEEG, made not with graphene electrodes, but made instead with two thin sheets of Au (50 nm Au on 2.5 nm Ti) on borosilicate glass and separated by a 100 μm gap.

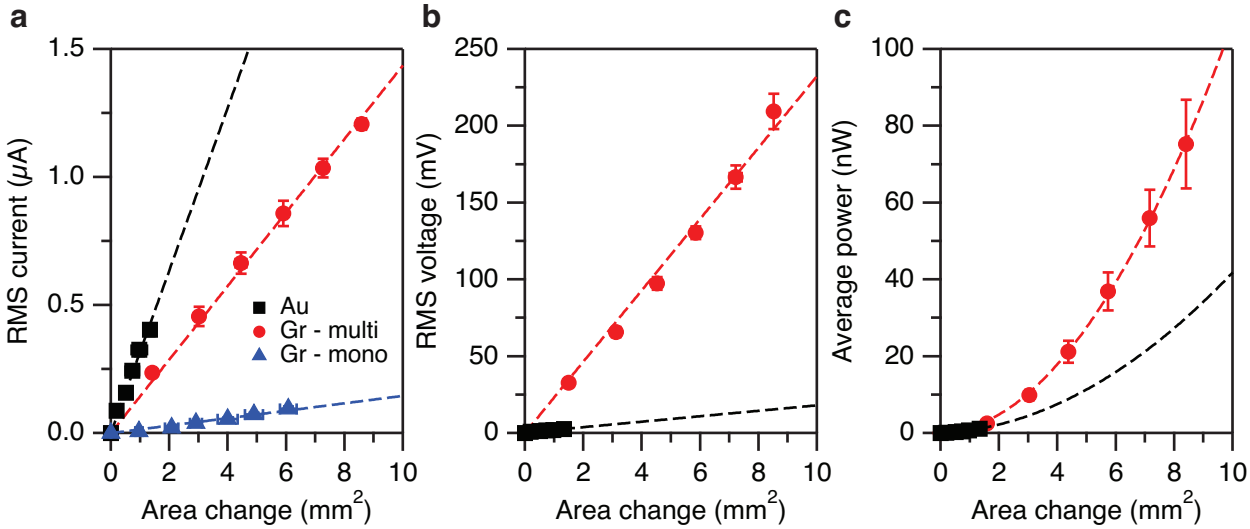

Figure 2.33: Comparison of SCEEG devices. **a**, $\langle I_{sc}\rangle_{RMS}$ **b**, $\langle V_{oc}\rangle_{RMS}$ and **c**, $\langle P_L\rangle_{avg}$ vs. peak-to-peak area change for Au (black squares), large-grain multi-layer graphene (red circles), and large-grain mono-layer graphene (blue triangles) SCEEG devices. Droplet volume = 20 μL of 1 M NaCl, oscillation frequency = 30 Hz. R_L = 150 kΩ for the G_{MULTI}-SCEEG and R_L = 1 kΩ for Au-SCEEG. The value of R_L was set to roughly match the internal impedance of each device. Where they are not visible, error bars are smaller than the dimensions of the data point's symbol.

Fig. 2.33 (**b**) and (**c**) show the RMS voltage and average power as a function of area change for only the G_{MULTI}- and Au-SCEEG devices. The Au-SCEEG produces the greatest current per unit area followed by the G_{MULTI}- and G_{MONO}-SCEEGs. Due to an increased tendency of the droplet to pin to the surfaces of both the Au-SCEEG and the G_{MONO}-SCEEG devices, the achievable

range of the area change was smaller for these devices. As a result, the G_{MULTI}-SCEEG produced the overall largest current of the three devices. As shown in parts (**b**) and (**c**) of Fig. 2.33, the G_{MULTI}-SCEEG also produced the overall largest voltage and power. In contrast to its current output, the Au-SCEEG produced significantly less voltage and power than the graphene device with multi-layer regions. This is likely due to the smaller internal resistance of the Au-SCEEG compared to the G_{MULTI}-SCEEG ($\simeq 1$ kΩ vs. $\simeq 150$ kΩ).

2.5.1 Comparison of electrical output

Table 2.4 below summarizes the electrical output of the three symmetric SCEEG devices that were studied. $\langle I_{sc} \rangle_{RMS}$ and $\langle V_{oc} \rangle_{RMS}$ have been normalized by the rate of change of the area and $\langle P_L \rangle_{avg}$ has been normalized by the square of the area's rate of change. Relative to Au and ITO,

Electrode material	Electrolyte solution	$\langle I_{sc} \rangle_{RMS}$ (nA·s/cm^2)	$\langle V_{oc} \rangle_{RMS}$ (mV·s/cm^2)	$\langle P_L \rangle_{avg}$ (nW·s^2/cm^4)
Multi-layer Gr	HCl (6.0 M)	1020 ± 20	80 ± 1	22 ± 1
	HNO_3	860 ± 10	86 ± 1	19 ± 1
	HCl	690 ± 20	76 ± 1	13 ± 1
	NaCl	240 ± 10	40 ± 1	2.8 ± 0.6
Mono-layer Gr	NaCl	27 ± 1	–	–
Au	NaCl	500 ± 30	3.5 ± 0.3	1.0 ± 0.3

Table 2.4: Comparison of the normalized output of symmetric SCEEG devices. The normalized electric output of symmetric SCEEG devices containing different electrode materials and using different electrolyte solutions. The values in red represent the largest measured outputs. All concentrations are 1.0 M unless otherwise noted. $R_L = 150$ kΩ and 1 kΩ for the power measurements made using the Gr- and Au-SCEEGs, respectively.

graphene seems to be uniquely suited as an electrode material for use in SCEEG devices for several reasons. First, graphene is relatively hydrophobic, especially when supported by a hydrophobic substrate. It's hydrophobicity means there is less friction opposing the motion of a volume of aqueous solution over it. Second, graphene's relatively high electrical resistance allows a SCEEG to support larger open-circuit voltages, increasing its maximum power output.

2.6 Comparison to other supercapacitive, energy-harvesting devices

Table 2.5 below summarizes the maximum (max.) and normalized (norm.) electrical output of the G_{MULTI}-SCEEG compared to other supercapacitive, energy-harvesting devices that have been described to date, *i.e.* the ITO-SCEEG, the graphene "waving potential" device (G-WP), and the graphene "drawing potential" device (G-DP) [6–8]. I_{sc} and V_{oc} have been normalized by the rate of change of the area and P_L has been normalized by the square of the area's rate of change. The G_{MULTI}-SCEEG significantly outperforms the normalized output of all other devices and is only eclipsed by the ITO-SCEEG in maximum voltage output. The presence of two separate graphene

Device	Electrolyte solution	I_{sc}		V_{oc}		P_L	
		max. (μA)	norm. (nA·s/cm^2)	max. (V)	norm. (mV·s/cm^2)	max. (μW)	norm. (nW·s^2/cm^4)
G_{MULTI}-SCEEG	HCl (6.0 M)	25	1020 ± 20	–	–	7	22 ± 1
	HNO_3 (1.0 M)	–	–	1.3	86 ± 1	–	–
ITO-SCEEG Ref. [8]	H_2O	$\simeq 1$	~ 10	$\simeq 5$	~ 10	3	~ 0.1
G-WP device Ref. [7]	NaCl (0.6 M)	11	~ 100	0.101	$\simeq 0.5$	N/A	N/A
G-DP device Ref. [6]	$CuCl_2$ (0.6 M)	$\simeq 1.7$	~ 10	$\simeq 0.03$	–	$\simeq 0.02$	~ 0.01
	NaF (0.6 M)	–	–	–	$\simeq 0.6$	–	–

Table 2.5: Comparison of the G_{MULTI}-SCEEG to other supercapacitive, energy-harvesting devices. The maximum (max.) and normalized (norm.) electric output of the G_{MULTI}-SCEEG compared to other supercapacitive, energy-harvesting devices described to date. When not explicitly reported in the literature, values were estimated based on stated experimental parameters. N/A signifies that no value was reported. The values in red represent the largest outputs. $R_L = 150$ kΩ, 10 MΩ, and 17.4 kΩ for the power measurements made using the G_{MULTI}-SCEEG, ITO-SCEEG, and G-DP device, respectively.

electrodes in the G_{MULTI}-SCEEG is likely responsible for its ability to outperform the G-WP and G-DP devices. This is because the single graphene electrode of the G-WP and G-DP devices acts as an electrical short. On the other hand, the G_{MULTI}-SCEEG outperforms the ITO-SCEEG likely because of graphene's ability to adsorb high densities of ions to its surface, especially at low pH. The ITO-SCEEG is able to generate larger maximum voltages than the G_{MULTI}-SCEEG, however, because of its ability to support a greater number of simultaneously oscillating droplets.

2.7 Chapter summary

1. A SCEEG generates current, voltage, and power from oscillating droplets of electrolyte solutions. A change in the area of contact between the droplet and the device's electrodes is necessary for this to occur.

2. A SCEEG can be accurately modeled using passive circuit elements. The device can be thought of as a current source in parallel with a time-varying internal impedance which is composed of a resistor and capacitor in series. Analytical expressions can be written for the short-circuit current, I_{sc}(t), open-circuit voltage, V_{oc}(t), and dissipated power, P_{L}(t), that the SCEEG generates.

3. The efficiency of the G_{MULTI}-SCEEG is estimated to be $0.4\,\%$. This will likely need to be improved if the G_{MULTI}-SCEEG is ever to function as useful energy-harvesting device.

4. Resonant modes of standing waves on the surface of a droplet can be readily detected using the short-circuit current generated by a G-SCEEG.

5. When exposed to droplets of 6.0 M HCl, the G_{MULTI}-SCEEG generates the greatest power output. The G_{MULTI}-SCEEG outperforms other SCEEGs made using ITO and Au electrodes. It also significantly outperforms similar supercapacitive, energy-harvesting devices made from graphene.

... Strength and desire possess the future,
The breed of the grasshopper shrills, ''What does the future
Mater, we shall be dead?'' Ah grasshoppers,
Death's a fierce meadowlark: but to die having made
Something more equal to the centuries
Than muscle and bone, is mostly to shed weakness ...

– Robinson Jeffers

3

The interaction between graphene and hydrated ions

3.1 Chapter overview

In this chapter, the electrical output of the graphene supercapacitive electrical energy generator (G-SCEEG) is used to deduce the nature of the interaction between graphene and hydrated ions. As alluded to in Chapter 2, the interaction between the ions of an electrolyte solution and

the graphene electrodes of the G-SCEEG is responsible for the G-SCEEG's ability to generate electricity. This makes it possible to determine both the effective surface density, σ_{n}, of the ions that spontaneously adsorb to the graphene's surface and the sign, $+$ or $-$, of the adsorbed ion's electric charge from the short-circuit current that the device produces. The main objectives of this chapter are to:

(i) describe the theoretical Gouy-Chapman (GC) model of the interface between a solid such as graphene and an electrolyte solution, including the modifications made to the model by Stern and Grahame.

(ii) determine both the sign, $+$ or $-$, of the electric charge of the ions of the electrolyte that adsorb to graphene as well as their effective surface density, σ_{n}, using data obtained from the G-SCEEG's short-circuit current.

(iii) experimentally demonstrate how the surface charge density, σ, induced in graphene by adsorbed ions depends on properties of the electrolyte solution such as the identity of the ions present, the ionic strength, and the pH; to show that the dependence of the surface charge density on ionic strength quantitatively agrees with the modified GC model.

(iv) determine the capacitance per unit area, c_0, of the graphene-electrolyte interface using data obtained by applying an AC voltage across the G-SCEEG.

(v) provide an estimate of the surface potential, Φ, across the graphene-solution interface as well as the effective surface binding energy, E_{B}, of hydrated Cl^- ions to graphene using the experimentally-determined values for σ and c_0.

It is worth noting here that the majority of the experimental data presented in this chapter was taken using the $\mathrm{G_{MONO}}$-SCEEG device. Where this is not true, the specific device that was used has been made explicitly clear.

3.2 Model of the graphene-electrolyte interface

As briefly mentioned in Chapter 2, when an electrode, such as graphene, is exposed to a solution of electrolyte, an electric double layer (EDL) can spontaneously form at the interface between the electrode and the solution. In general, an EDL can develop at the interface between an electrolyte solution (or ionic liquid) and any of the following:

1. A metal, semimetal, or semiconductor to which an electric potential has been applied relative to the solution.

2. A metal, semimetal, or semiconductor possessing an induced surface charge density due to the adsorption of ions.

3. A dielectric with fixed surface charge.

Although charging of the EDL at an electrode-solution interface can occur in different ways, *i.e.* ionization or dissociation of surface groups, adsorption or binding of ions to a previously uncharged surface, and charge transfer between dissimilar surfaces [55], for the graphene electrodes of the G-SCEEG device only adsorption/binding of ions is believed to occur in the absence of an externally applied voltage. This is because the bulk of the graphene is assumed to be ideally polarizable, *i.e.* no charge is transferred across the interface between the graphene and the solvated ions [70–75]. Another way of phrasing this is that, in the absence of an externally-applied potential, the electric potential of the graphene electrodes relative to the bulk solution is assumed to be below the reduction/oxidation potential of any of the ionic species present in the solution [76]. As a result, no electrochemical reactions are thought to occur and, hence, no faradaic currents are thought to exist.

The term EDL was purportedly first used by Helmholtz beginning in the middle of the 19th century to describe his theory on how charges and oriented dipoles distribute themselves at the

interface between a charged solid surface and an electrolyte solution [77, 78]. Helmholtz proposed that there are two layers of equal but opposite interfacial charge, one at the surface of the solid and one at the surface of the electrolyte, and that the ionic charge of the electrolyte effectively screens the charge on the solid. Furthermore, Helmholtz was one of the first to understand that these layers are separated by a distance of molecular order and that the separated layers of charge resemble the separation of charge that occurs on the plates of a charged capacitor [79].

Conceptually, Helmholtz's model of the EDL is quite simple. When an electrode (or a solid dielectric with a fixed surface charge) is exposed to an electrolyte solution, one species of ion in the electrolyte (the counterion) is attracted to charges of opposite sign that are induced at the surface of the electrode (or that are already presence at the surface, as is the case with fixed charges on a dielectric). As a result, the density of the counterions near the electrode's surface becomes greater relative to that in the bulk of the solution. The other ionic species in the electrolyte (the co-ion), *i.e.* the ion of opposite charge to that of the counterion, is repelled from the electrode's surface and its ionic density there becomes less than that in the bulk solution. As Helmholtz's term therefore suggests, the electric double layer is comprised of two layers of charge, the induced electronic charge layer at the surface of the electrode and the layer of counterions that is, in turn, bound to it.

Since Helmholtz first proposed his EDL model, however, it has undergone significant modifications and additions by the likes of Gouy, Debye, Hückel, Chapman, Stern, and Grahame [34]. Currently, one of the most widely accepted modern models of the EDL is the so-called modified Gouy-Chapman (GC) model [37]. Fig. 3.1 (p. 117) provides an illustration of the modified GC model of the interface between the surface of a conductive electrode and a symmetric electrolyte solution, *i.e.* an electrolyte solution in which each ionic species has the same charge state and the same concentration in the bulk of the solution.

As demonstrated in Fig. 3.1 (**a**), the modified GC model predicts that the EDL actually con-

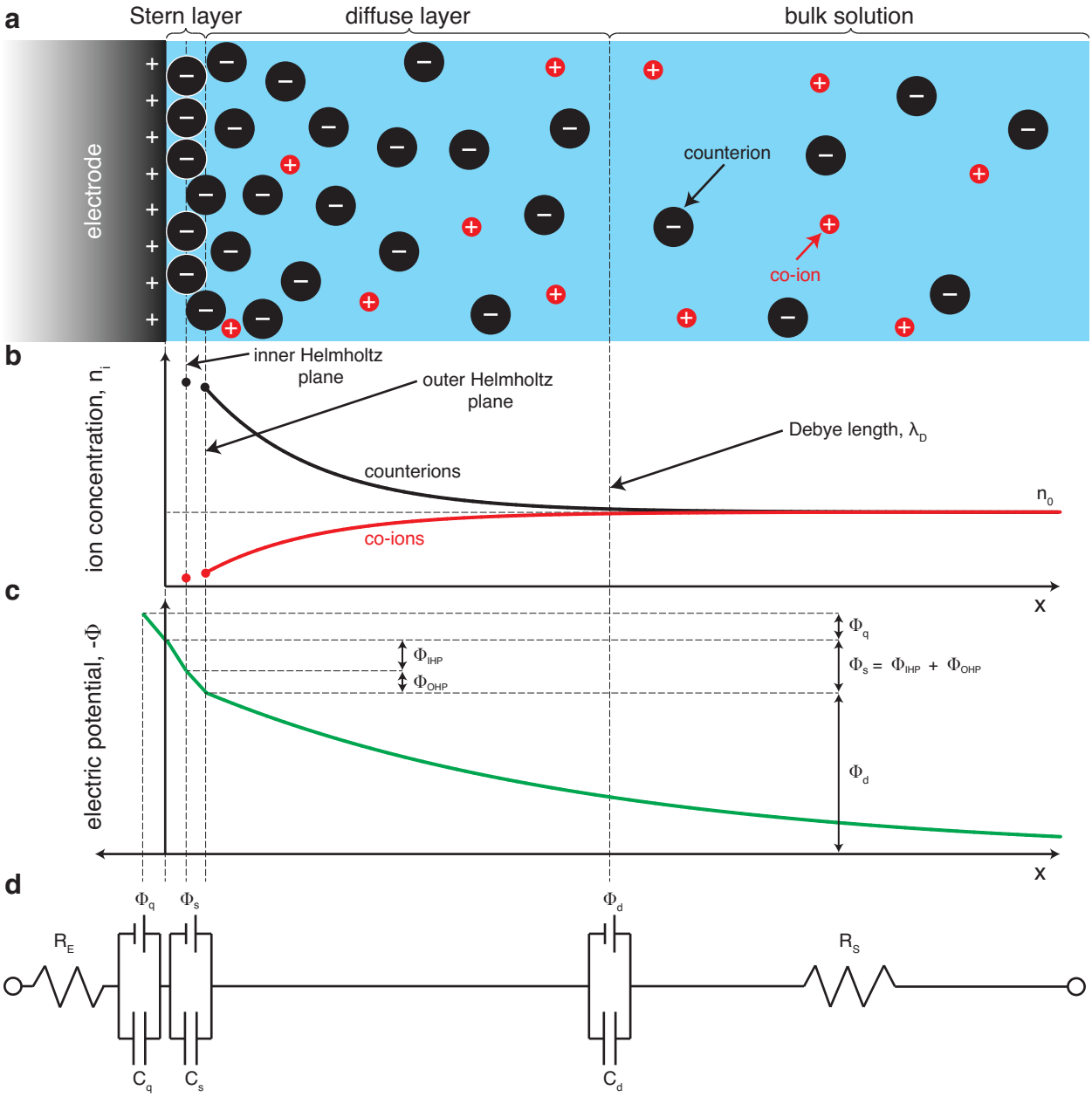

Figure 3.1: Modified Gouy-Chapman model of the interface between an electrode and an electrolyte solution. **a**, Illustration of the concentration of co-ions $(+)$ and counterions $(-)$ near the interface between an electrode and an electrolyte solution as described by the modified Gouy-Chapman (GC) model. Counterions outlined in white lack a hydration shell. **b**, The concentration, $n_i(x)$, of counterions (black line) and co-ions (red line) as a function of distance from the electrode's surface according to Eq. (3.9) (p. 122). n_0 is the ionic concentration of the bulk solution. **c**, The negative electric surface potential, $-\Phi(x)$, as a function of distance from the electrode's surface according to Eq. (3.8) (p. 121). Φ_q, Φ_s, and Φ_d are the potential drops across the quantum capacitance, the Stern layer, and diffuse layer, respectively. Φ_{IHP} and Φ_{OHP} are the potential drops across the inner and outer Helmholtz planes, respectively. The potentials are measured relative to that of bulk solution. **d**, Circuit model of the ideally-polarizable interface. R_E and R_S are the resistances of the electrode and the bulk solution, respectively. C_q, C_s, and C_d are the quantum, Stern layer, and diffuse layer capacitances, respectively.

sists of more than just two layers of charge; not only does the EDL include both an induced charge layer at the surface of the electrode (or a fixed layer of surface charge, as in the case of a dielectric) and a condensed ionic charge layer at the electrode-solution interface (also called the Stern layer), but it is also hypothesized to include a diffuse layer of increased ionic charge density that exists between the interface and the bulk of the solution [37, 80]. Additionally, the condensed, Stern layer itself can be thought of as two separate layers, the so-called inner and outer Helmholtz planes, based on whether or not the ions in the layer are surrounded by shells of water molecules (inner Helmholtz plane = bare ions, outer Helmholtz plane = hydrated ions).[1] The ions of the Stern layer are considered immobile and are either chemically or physically bound to the surface (or both). The ions of the diffuse layer, on the other hand, are mobile; they are subject to Brownian motion due to collisions with the surrounding solvent while also simultaneously being electrostatically attracted to the electrode. The ions of the condensed layer are bound tightly to the surface while those of the diffuse layer create an ionic cloud that extends out from the surface and into the solution.

Although it is now common practice to model the electrolyte near the interface as forming separate condensed and a diffuse layers of ions, the original GC model neglected the condensed layer and described only the solution's diffuse layer [37]. The original GC model still proves useful, however, in that it provides analytical expressions, through the use of the Poisson-Boltzmann equation, for the distribution of ions in the diffuse layer, for the electrostatic potential across the diffuse layer, for the diffuse layer's characteristic screening length, *i.e* the Debye length, λ_D, and for the layer's differential capacitance.

Despite the utility of the original GC model, the model is unphysical because it predicts a di-

[1]Note that because of all the additional layers of charge in the modified GC model of the EDL, the term "electric double layer" is no longer accurate. Due to historical precedent, however, EDL continues to be widely used in the literature when referring to such charged interfaces, regardless of the number of layers of charge the interface is presumed to have.

vergent differential capacitance for the diffuse layer as the potential drop across the layer becomes arbitrarily large [34]. It was not until Stern and Grahame modified the model by including a condensed layer of ions that this flaw was rectified. Stern and Grahame claimed that ions can come into direct contact with the electrode and, as a result, can specifically adsorb to it by losing their solvation shells. These ions form the inner Helmholtz plane (IHP) which is defined as the plane that passes through the centers of the specifically adsorbed ions. Another claim they made was that ions could adsorb onto the electrode without first needing to lose their hydration shells. These ions form the outer Helmholtz plane (OHP) which is defined as the plane that passes through the centers of the solvated ions at the distance of their closest approach to the electrode.

Due to Stern's and Grahame's insight, the IHP and OHP are treated as parallel layers of condensed, largely immobile ions in the modified GC model of the EDL. This enables them to be modeled collectively as a single parallel-plate capacitor which is, in turn, in series with the capacitance of the diffuse layer. The capacitance of the Stern and diffuse layers are considered to be connected in series because of the additive nature of the voltage drops across each of them:

$$\Phi_{\text{EDL}} = \Phi_{\text{s}} + \Phi_{\text{d}} \tag{3.1}$$

where Φ_{EDL}, Φ_{s}, and Φ_{d} are the potential drops across the EDL, the Stern layer, and the diffuse layer, respectively. Using the definition of capacitance, $q = \Phi_{\text{i}} C_{\text{i}}$, where q is the net charge in both the Stern and the diffuse layers, Eq. (3.1) becomes:

$$\frac{q}{C_{\text{EDL}}} = \frac{q}{C_{\text{s}}} + \frac{q}{C_{\text{d}}} \tag{3.2}$$

$$\frac{1}{C_{\text{EDL}}} = \frac{1}{C_{\text{s}}} + \frac{1}{C_{\text{d}}} \tag{3.3}$$

where C_{s} and C_{d} are the capacitances of the Stern and diffuse layers, respectively, and where the equivalent capacitance of the electric double layer, C_{EDL}, is also referred to as the electric double layer capacitance/capacitor (EDLC).[2] Because C_{EDL} is found by taking the reciprocal of the sum of reciprocals of the individual, serially-connected capacitors, C_{s} and C_{d}, the equivalent capacitance does not diverge regardless of how large the potential drop across the diffuse layer is [37]. It instead approaches the parallel-plate capacitance of the condensed Stern layer as seen in Eq. (3.3) when $C_{\mathrm{d}} \to \infty$.

Figs. 3.1 (**b**) and (**c**) (p. 117) represent the ion concentration, $n_{\mathrm{i}}(x)$, and the electric potential, $\Phi(x)$, as functions of the distance from the conductor's surface, x, respectively, as predicted by the modified GC model. The behavior of both ion concentration and the electric potential drop over the diffuse layer, $\Phi_{\mathrm{d}}(x)$, is derived from the Poisson-Boltzmann equation. The Poisson-Boltzmann equation is first found by treating the net charge density, $\rho(x)$, as the difference between the Maxwell-Boltzmann distributions of the positive and negative ions, with each ion having a distance-dependent potential energy, $U(x) = z\,e\,\Phi_{\mathrm{d}}(x)$, where z is the charge state of the ion and e is the charge of an electron:

$$\rho(x) = z\,e\left[n_{+}(x) - n_{-}(x)\right] = -2\,z\,e\,n_0 \sinh\left(\frac{z\,e\,\Phi_{\mathrm{d}}(x)}{k_{\mathrm{B}}\,T}\right) \tag{3.4}$$

Eq. (3.4) assumes that the electrolyte is symmetric, *i.e.* both ionic species have the same bulk concentration and the same net charge. This expression for $\rho(x)$ is then inserted into Poisson's equation, $\nabla^2\Phi_{\mathrm{d}} = -\rho(x)\,/\,\epsilon\,\epsilon_0$, where ϵ is the relative permittivity of the solution and ϵ_0 is the permittivity of vacuum, to give:

$$\nabla^2\Phi_{\mathrm{d}} = \frac{2\,z\,e\,n_0}{\epsilon\,\epsilon_0} \sinh\left(\frac{z\,e\,\Phi_{\mathrm{d}}}{k_{\mathrm{B}}\,T}\right) \tag{3.5}$$

[2]Note that typical values of $c_{\mathrm{EDL},0}$, the equivalent capacitance of the electric double layer per unit area, for graphene exposed to ionic liquids and gels are $\simeq$ 40–200 nF/mm^2 [44, 81].

If the thermal energy is much greater than the potential energy, *i.e.* $k_{\mathrm{B}}\,T >> z\,e\,\Phi_{\mathrm{d}}$, the exponential term in Eq. (3.5) can be replaced with a Taylor series expansion to first order. This is called the Debye-Hückel approximation and it linearizes the otherwise non-linear Poisson-Boltzmann equation:

$$\nabla^2 \Phi_{\mathrm{d}} \simeq \frac{1}{\lambda_{\mathrm{D}}^2}\,\Phi_{\mathrm{d}} \tag{3.6}$$

$$\lambda_{\mathrm{D}} \equiv \sqrt{\frac{\epsilon\,\epsilon_0\,k_{\mathrm{B}}\,T}{2\,z^2\,e^2\,n_0}} \tag{3.7}$$

where λ_{D} is the Debye length (for a 1 M concentration of a symmetric electrolyte whose ions are singly charged, such as HCl, $\lambda_{\mathrm{D}} \simeq 0.3$ nm at $T = 25^{\circ}$C; for 6 M HCl, $\lambda_{\mathrm{D}} \simeq 0.1$ nm). The Debye-Hückel approximation is useful in that it enables an analytical solution to be written for Eq. (3.5), which can otherwise only be solved numerically.

As demonstrated later in this chapter, however, the potential energies, *i.e.* binding energies, at the interface between graphene (containing multi-layer regions) and the electrolyte solutions of 1.0 M HCl, 1.0 M NaCl, and 6.0 M HCl ($\simeq$ 200–700 meV) are close to an order of magnitude larger than the thermal energy ($\simeq$ 30 meV). As a result, the Debye-Hückel approximation does not apply to these interfaces. On the other hand, the approximation does likely apply to the interfaces between many of the electrolyte solutions and mono-layer only graphene that were also studied.

When solving Eq. (3.6) for Φ_{d}, it is found that Φ_{d} decreases exponentially as a function of the distance, x, from the edge of the Stern layer ($x = x_{\mathrm{s}}$) to the bulk of the solution ($x \to \infty$):

$$\Phi_{\mathrm{d}}(x) = \Phi_{\mathrm{d},0}\,\exp\left(-\frac{x - x_{\mathrm{s}}}{\lambda_{\mathrm{D}}}\right) \tag{3.8}$$

Note that the boundary conditions ensure that $\Phi_{\mathrm{d}}(x = x_{\mathrm{s}}) = \Phi_{\mathrm{d},0}$ and $\lim_{x\to\infty} \Phi_{\mathrm{d}}(x) \to 0$. By definition, $\Phi_{\mathrm{d}}(x)$ is undefined for $x < x_{\mathrm{s}}$. For $U(x) = z\,e\,\Phi_{\mathrm{d}}(x)$, the i-th ion concentration, $n_{\mathrm{i}}(x)$, as a function of distance also exhibits exponential behavior:

$$n_{\mathrm{i}}(x) = n_{\mathrm{i},0}\ \exp\left(-\frac{U(x)}{k_{\mathrm{B}}\,T}\right) = n_{\mathrm{i},0}\ \exp\left[-\frac{z_{\mathrm{i}}\,e\,\Phi_{\mathrm{d},0}}{k_{\mathrm{B}}\,T}\ \exp\left(-\frac{x - x_{\mathrm{s}}}{\lambda_{\mathrm{D}}}\right)\right] \tag{3.9}$$

Both Eqs. (3.8) and (3.9) are plotted in Fig. 3.1 (p. 117). In line with physical intuition, the concentration of the counterions increases as one approaches the Stern layer while that of the co-ions decreases.

3.2.1 Interfacial capacitance

As previously mentioned, when not subject to an external electric potential, bulk graphene is an ideally-polarizable electrode because it is nearly electrochemically inert, *i.e.* no charge is transferred between it and any electrochemically reactive species in solution. As described in Chapter 2 (p. 35) and shown explicitly in this chapter in Fig. 3.1 (**d**) (p. 117), the relative inertness of graphene means that the interface between graphene and a solution of electrolyte can be modeled as a capacitor. More specifically, this capacitor is composed of three capacitances connected to each other in series: the quantum capacitance, C_{q}, the Stern layer capacitance, C_{s}, and the Debye diffuse layer capacitance, C_{d}.

Because the amount of charge in both the graphene and the diffuse layer does not, in general, scale linearly with the potential drops across each of them, C_{q} and C_{d} are defined as differential capacitances, $C'(V_0)$, *i.e.* capacitances that are found by evaluating the derivative of the accumu-

lated charge with respect to the applied potential at a given value of that potential, V_0: [3]

$$C'(V_0) \equiv \left. \frac{\partial q}{\partial V} \right|_{V=V_0} \tag{3.10}$$

In contrast, the amount of charge in the Stern layer is proportional to the potential drop across it and the expression for C_s is, therefore, found using the usual definition of capacitance. Mathematical expressions C_s, C_d, and C_q are provided below. Their derivations can be found in Appendix B (p. 220). The form of these expressions is useful for interpreting data on surface charge densities that are described in Sect. 3.4 (p. 132) of this chapter.

3.2.1.1 *Stern layer capacitance*

The Stern layer is due to the electrostatic attraction of one ionic species of an electrolyte to either a fixed charge or an induced image charge at the surface of an electrode (or other solid material) in such a way as to form a condensed layer of ions at the electrode's surface. Because of this the Stern layer is modeled as a parallel-plate capacitor whose capacitance is given by the following expression:

$$C_\mathrm{s} = \frac{\epsilon\,\epsilon_0}{d} A \tag{3.11}$$

and $c_{\mathrm{s},0} \equiv C_\mathrm{s} \,/\, A$ [36].

Typical values of $c_{\mathrm{s},0}$ that are used in theoretical models of aqueous electrolytes are $\simeq$ 50–3000 nF/mm^2 (assuming $\epsilon \simeq 6\,\epsilon_0$–$30\,\epsilon_0$ and $d \simeq 0.1$–1 nm) [37]. For metal and pyrolytic graphite electrodes, $c_{\mathrm{s},0} \simeq$ 100–200 nF/mm^2 [83].

[3] Eq. (3.10) is referred to as the Lippmann equation [80, 82].

3.2.1.2 *Debye diffuse layer capacitance*

The diffuse Debye layer is an accumulation of net charge extending away from the surface of the electrode and into the bulk electrolyte solution. The ions in this layer experience both an attractive electrostatic force and a randomly fluctuating force caused by collisions with the solvent molecules. When an electrode is exposed to an infinite reservoir of electrolyte solution, the diffuse layer can be thought of as a capacitor that separates the electrode's surface (voltage source) from the bulk solution (ground). The diffuse layer can, thus, be modeled as a capacitor because it stores charge in response to a potential drop [37]. The differential capacitance of this layer is given by the following expression:

$$C_{\mathrm{d}}(\Phi_{\mathrm{d,0}}) = A \left. \frac{\partial \sigma_{\mathrm{d}}}{\partial \Phi_{\mathrm{d}}} \right|_{\Phi_{\mathrm{d}}=\Phi_{\mathrm{d,0}}} = \frac{\epsilon\,\epsilon_0}{\lambda_{\mathrm{D}}} \left[\cosh\left(\frac{z\,e\,\Phi_{\mathrm{d,0}}}{2\,k_{\mathrm{B}}\,T} \right) \right] A \tag{3.12}$$

where

$$\lambda_{\mathrm{D}} \equiv \sqrt{\frac{\epsilon\,\epsilon_0\,k_{\mathrm{B}}\,T}{2\,z^2\,e^2\,n_0}}$$

and $c_{\mathrm{d,0}} \equiv C_{\mathrm{d}} \,/\, A$ [37].

Values of $c_{\mathrm{d,0}}$ for 1 M electrolyte solutions are typically > 1 μF/mm^2 [83].

3.2.1.3 *Quantum capacitance*

The quantum capacitance of a solid-state material originates in the change in chemical potential of the material's electrons when subject to a change in electric potential [41]. The change in chemical potential is only significant when the density of states is finite. Such is the case for a two-dimensional electron gas (2DEG) or a two-dimensional material like graphene. As shown in Chapter 2 (p. 34) the general expression describing the quantum capacitance in two-dimensional

materials is:

$$C_{\mathrm{q,\,2D}}(E_{\mathrm{F}}) = e^2\,\rho_{\mathrm{s}}(E_{\mathrm{F}})\,A \tag{3.13}$$

In the case of graphene the differential quantum capacitance is:

$$C_{\mathrm{q}}(\Phi_{\mathrm{q,0}}) = A\,\left.\frac{\partial\,\sigma}{\partial\Phi_{\mathrm{q}}}\right|_{\Phi_{\mathrm{q}}=\Phi_{\mathrm{q,0}}} = \frac{2\,e^2\,k_{\mathrm{B}}\,T}{\pi\,(\hbar\,v_{\mathrm{F}})^2}\,\ln\left[2\,\left(1+\cosh\left[\frac{e\,\Phi_{\mathrm{q,0}}}{k_{\mathrm{B}}\,T}\right]\right)\right]A \tag{3.14}$$

where $\Phi_{\mathrm{q,0}}$ is the entire electric potential drop across the graphene and $c_{\mathrm{q,0}} \equiv C_{\mathrm{q}}\,/\,A$ [81].

Typical values of $c_{\mathrm{q,0}}$ for graphene that have been experimentally measured are $\simeq$ 10–100 nF/mm^2 [44, 81].

3.3 Identifying ions that physically adsorb to graphene

Using the G-SCEEG, it is fairly straightforward to identify which of the ions in a solution of electrolyte, *i.e.* either the positively charged cation or the negatively charged anion, physically adsorbs to the device's graphene electrodes in greater density and, in turn, with larger binding energy, E_B.[4] Because the physically adsorbed ions induce an image charge of opposite sign in the G-SCEEG's graphene electrodes, the sign of the ions' electric charge can be determined simply by observing the sign of the short-circuit current that is generated as a droplet of electrolyte moves from the electrode connected to the current amplifier's negative lead to the electrode connected to the amplifier's positive lead. The identity of the physically adsorbed ions can then deduced from the sign of the short-circuit current and from the way in which the electrolyte is known to dissociate in water.

Chemically adsorbed ions, on the other hand, cannot be directly identified using the G-SCEEG because they do no induce an image charge in the device's electrodes. They instead change the number of charge carriers in the electrode, *i.e.* they dope the electrode. Their effect on the G-SCEEG's output can only be indirectly observed if such doping alters the interaction between graphene and any physically adsorbing ions that might be present. Two ions that are believed to chemically adsorb to graphene are the hydronium, H_3O^+, and the hydroxide, OH^-, ions. As discussed more thoroughly in Sect. 3.4.2 of this chapter (p. 138), reports in the literature suggest that H_3O^+ and OH^- bind so strongly with graphene as to form a covalent-like bond with it [5–7, 24]. As a result, charge is shared between the graphene and these ions, thus altering graphene's charge carrier density.

Fig. 3.2 (p. 128) presents two ways in which the sign of the electric charge of the physically adsorbed ions can be determined. The method in Fig. 3.2 (**a**) is the simplest to interpret. In this

[4] Note that physical adsorption is used here to mean adsorption that does not involve the sharing or transfer of charge. When such charge transfer does occur, it is termed chemical adsorption [55].

method, a droplet of electrolyte solution is first pipetted onto the graphene electrode that is connected to the current amplifier's negative lead. Using a glass capillary tube, the droplet is dragged across the gap (from left to right in the figure) to the graphene electrode connected to the current amplifier's positive lead. Simultaneously, the short-circuit current that this motion generates is recorded. For the droplet of 1 M HCl that is represented in the figure, a negative current is generated. Dragging the droplet in the opposite direction generates current with the opposite sign, *i.e.* positive current.

Based on the physical model of the G-SCEEG that is described in Fig. 2.3 (**b**) (p. 22), a droplet moving from left to right, *i.e.* from the electrode connected to the negative lead to the electrode connected to the positive lead, will generate a negative current only if the negatively charged anions physically bind more strongly to the graphene's surface than the positively charged cations. It is concluded, therefore, from Fig. 3.2 (**a**), and from what is known about the dissociation of HCl, that the chloride anions, Cl^-, of 1 M HCl are physically bound to graphene's surface, whereas the hydronium cations, H_3O^+, are likely chemically bound.

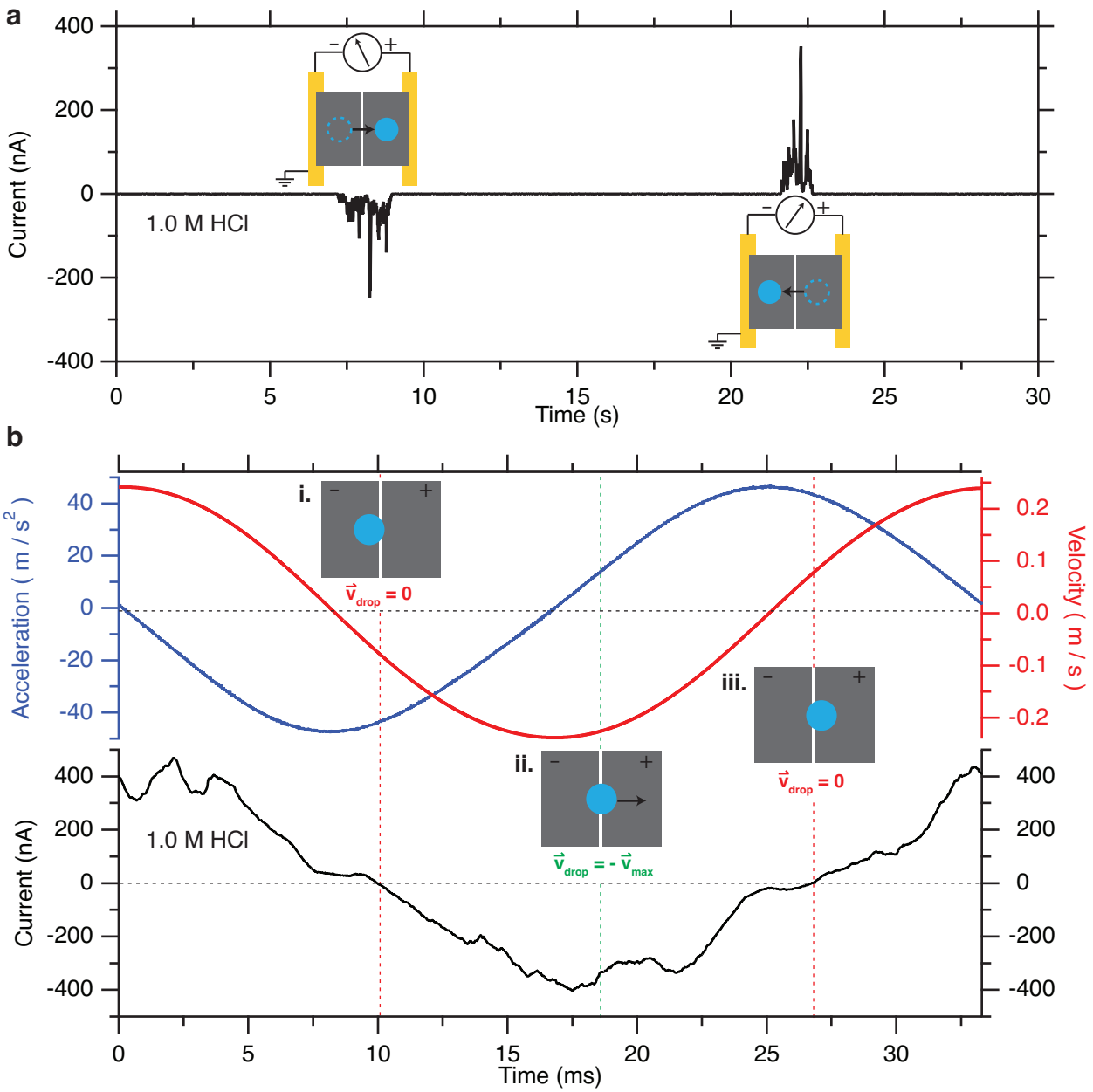

Figure 3.2: Sign of the electric charge of the physically adsorbed ions. The sign of the charge of the ions physically adsorbed to graphene was determined from the sign of $I_{sc}(t)$ using two separate methods. **a**, Method 1: The droplet was dragged from the graphene electrode connected to the negative lead of the current amplifier to the electrode connected to the positive lead (left to right), and vice versa. A 20 μL droplet of 1 M HCl resulted in negative current, meaning that the Cl^- ions are physically bound to graphene (the H_3O^+ ions are likely chemically bound). **b**, Method 2: The output of the speaker-mounted accelerometer (top traces; blue = acceleration, red = velocity) was used to determine the location of the droplet on the device as it moved from the left graphene electrode (**i.**), through its position of maximum velocity (**ii.**), and finally to the right graphene electrode (**iii.**). The sign of $I_{sc}(t)$ was determined between positions **i.** and **iii.** on the corresponding plot of $I_{sc}(t)$ vs. time (bottom, black trace). A 20 μL droplet of 1 M HCl again resulted in negative current. Oscillation frequency = 30 Hz, peak-to-peak area change = 5.5 mm^2, G-SCEEG device = mono-layer graphene.

The method in Fig. 3.2 (**b**) accomplishes the same task but allows the sign of the electric charge to be determined from the time trace of the alternating current generated by a freely oscillating droplet. In this method, the direction of the droplet's motion is determined from the acceleration and velocity of the device as measured by the speaker-mounted accelerometer. Based on visual observations of the droplet's motion using a strobe light, a $20\ \mu$L droplet of aqueous electrolyte oscillating at 30 Hz is slightly more than $180°$ out of phase with the motion of the device and the speaker, *i.e.* as the speaker is moving to the right the droplet is moving to the left but is slightly delayed. The accelerometer is mounted on the speaker so that it measures the greatest negative acceleration as the speaker is at its greatest displacement to the right; when the speaker is at its greatest displacement to the left, the accelerometer measures the greatest positive acceleration. This means that in the time between the negative and positive peaks in the acceleration's time trace, or during the time while the velocity is negative, the droplet moves from the electrode connected to the current amplifier's negative lead on the left to the electrode connected to the amplifier's positive lead on the right. The sign of the current generated by the G-SCEEG during this time is the same as the sign of the electric charge of the ions that are physically bound to the graphene's surface most strongly. For 1 M HCl the sign of the current was negative and it was again concluded that the Cl^- anions physically adsorb in greater density to graphene than the H_3O^+ cations because the H_3O^+ ions likely chemically adsorb. This result agrees with that obtained using the dragging method of part (**a**).

For most of the solutions studied in this thesis using the G_{MONO}-SCEEG device, both the signs of the electric charge of the physically adsorbed ions and the identities of those ions are listed in Table 3.1 (Sect. 3.4.6, p. 151).

3.3.1 Comparison of the adsorbed ions to those reported in the literature

Surprisingly, the identities of the physically adsorbed ions listed in Table 3.1 (Sect. 3.4.6, p. 151) mostly contradict those stated by Yin et al. in their studies on graphene and electrolyte solutions [5–7]. Yin et al. claim, using density functional theory (DFT) calculations and their experimental data, that the Cl^- anions of alkali chloride solutions are repelled from the surface of graphene and that the positively charged cations (Li^+, Na^+, and K^+) dominate the interfacial interaction. They do state, however, that the opposite is true for a solution of HCl; the H_3O^+ ions of HCl chemically adsorb to graphene by forming a covalent-like bond with it. The chemically adsorbed H_3O^+ ions increase the density of graphene's positive charge carriers, which, in turn, attract Cl^- ions to the graphene's surface. The Cl^- ion then dominates the physical interaction and is responsible for inducing a positive image charge in graphene. The data in Table 3.1 agree with this assessment of the Cl^- ion of HCl but disagree with that of the rest of the alkali chloride solutions. This is likely because Yin et al. did not include H_3O^+ ions in their calculations involving the alkali chloride solutions. H_3O^+ ions were present, however, in the solutions that were used in the G-SCEEG experiments as indicated by their pH values in the table.[5]

On the other hand, the results listed in Table 3.1 roughly agree with those of Cole et al. [24]. Cole et al. used classical molecular dynamics simulations to determine the distribution of charge density near a graphene surface when it was exposed to various electrolyte solutions. For an externally unbiased graphene sheet, they concluded the following:

1. For a solution of NaCl, the Cl^- anion accumulates in greater concentration near the graphene than the Na^+ cation.

[5]Note that the substrate Yin et al. used to support graphene, polyester terephthalate (PET), in their experimental device differs from the OTS-functionalized glass used in the G-SCEEG devices. A G-SCEEG was made using PET as the supporting substrate, however, and it was determined that this change did not affect which ionic species adsorbed to graphene.

2. For a solution of NaOH, the Na^+ cation accumulates in greater concentration near the graphene than the OH^- anion.

3. For a solution of HCl, the H_3O^+ cation accumulates in greater concentration near the graphene than the Cl^- anion.

Although their calculations did not taken into account chemical adsorption, their conclusions are qualitatively similar to those obtained using the G-SCEEG with the one caveat being the that for the solution of HCl, H_3O^+ is likely chemically adsorbed and Cl^- is likely physically adsorbed.

3.4 Induced surface charge density, σ

Now that methods for determining the sign of the the electric charge of the ions adsorbed to graphene have been established, it is fitting to want a method to calculate the charge density, σ, that is induced in graphene by the adsorbed ions. Upon inspection of Eq. (2.35) (p. 42), the magnitude of the induced charge density, $|\sigma|$, can be determined from the ratio of the magnitude of the G-SCEEG's short-circuit current, $|I_{\text{sc}}(t)|$, to the magnitude of the rate of change of the area of overlap between a single droplet and the graphene electrodes, $|\dot{A}(t)|$:

$$|\sigma| = \frac{|I_{\text{sc}}(t)|}{|\dot{A}(t)|} \tag{3.15}$$

Because both $I_{\text{sc}}(t)$ and $\dot{A}(t)$ are oscillatory, determining $|\sigma|$ from their experimentally-obtained time traces is most easily accomplished by averaging $|I_{\text{sc}}|$ and $|\dot{A}|$ over half a period of oscillation. Due to the difficulty in measuring $\dot{A}(t)$, however, the average of $|\dot{A}(t)|$ is estimated by dividing the peak-to-peak area change, $A_{\text{p-p}} = 2\,\alpha$, by half the period of oscillation, $T\,/\,2 = (2\,f)^{-1}$ where f is the oscillation frequency (the peak-to-peak area change occurs over half a period). Eq. (3.15) then becomes:

$$|\sigma| = \left(\frac{2}{T}\int_0^{\frac{T}{2}} |I_{\text{sc}}(t)|\; dt\right) \Bigg/ \left(\frac{2\,A_{\text{p-p}}}{T}\right) = \frac{\left\langle\, |I_{\text{sc}}| \,\right\rangle_{\text{avg}}}{4\,\alpha\,f} \tag{3.16}$$

Random error in the value of $|\sigma|$, introduced by the estimate $\left\langle|\dot{A}|\right\rangle_{\text{avg}} \simeq 4\,\alpha\,f$ or by other experimental factors, can be reduced by measuring $\left\langle\, |I_{\text{sc}}| \,\right\rangle_{\text{avg}}$ for different values of $A_{\text{p-p}}$ (while keeping f constant) and plotting the result. As evident in Eq. (3.15), $|\sigma|$ is then the slope of $\left\langle\, |I_{\text{sc}}| \,\right\rangle_{\text{avg}}$ vs. $\left\langle|\dot{A}|\right\rangle_{\text{avg}} \simeq 2\,f\,A_{\text{p-p}}$.

3.4.1 σ vs. electrolyte

By measuring the $\langle\, |I_{sc}| \,\rangle_{avg}$ output of the G_{MONO}-SCEEG as a function $A_{p\text{-}p}$, the magnitude of the surface charge density induced in mono-layer graphene by nearly 40 different electrolyte solutions was experimentally determined. The value of $|\sigma|$ and the sign of the electric charge induced in graphene for each of these solutions is listed later in this chapter in Table 3.1 (Sect. 3.4.6, p. 151). In this section, however, a detailed discussion is provided for the trends seen in $|\sigma|$ among the alkali chloride and sodium halide electrolytes only.

3.4.1.1 *Alkali chloride and sodium halide electrolytes*

The charge densities, σ, induced in graphene by 1 M solutions of the different alkali chloride and sodium halide electrolytes, as measured by using the G_{MONO}-SCEEG device, are shown in Fig. 3.3 (p. 136) and Fig. 3.4 (p. 137), respectively. The slopes of the average current magnitude vs. peak-to-peak area change in part (**a**) of both figures were used to calculate the charge densities shown in part (**b**) of both according to Eq. (3.16) (p. 132). The sign of σ in the figures is the sign of the induced charge in graphene, which is opposite the sign of the measured current. The sign of the electric charge of the ion that is most strongly bound to the graphene is, therefore, the same as that of the measured current as was previously discussed in Sect. 3.3 (p. 126). For example, the measured current is negative for all the electrolytes listed in Fig. 3.3 except for RbCl. This means that the Cl^- anion in all these solutions is more strongly bound to graphene than the alkali cation (the adsorbed Cl^- anion, in turn, induces in graphene a positive image charge).

Except for CsCl, moving down the alkali metal group in periodic table, from the hydronium (H^+) to the rubidium (Rb^+) cation, leads to less positive charge density in graphene. Moving down the halogen group, however, from the fluoride (F^-) to iodide (I^-) anion, leads to more positive charge density. For all solutions except RbCl and NaOH, the negatively charged anion is more strongly bound to graphene's surface than the positively charged cation. Without any ad-

ditional information, the trend in Fig. 3.3 (**b**) implies that as the radius of the cation gets larger the density of the chloride anion near the surface increases. Similarly, the trend in Fig. 3.4 (**b**) implies that as the anion's radius gets larger its density near the graphene surface increases. As discussed in Sect. 3.4.2 (p. 138), however, the trends are most heavily influenced by the pH of the electrolyte solutions and any effect due to the radius of the ions is likely small in comparison. In addition, the pH of the electrolyte solution is also thought to affect which ion, the cation or the anion, more strongly binds to the graphene for all but a few of the solutions that were studied.

Before discussing the effect of pH, it is worth exploring how the ion's radius might impact its ability to adsorb to graphene even if the radius ultimately plays a minor role. Possible explanations for radius-dependent contributions to the trends seen in Figs. 3.3 and 3.4 include:

1. As the radius of the bare cation increases from Li^+ to Cs^+ in Fig. 3.3, fewer unhydrated cations per unit volume are able to surround and shield the Cl^- anions, allowing the anions to more easily adsorb to the graphene (due to the large uncertainty in the radius of the hydrated proton [84], the hydronium cation has been left out of this discussion). This is opposite, however, to the trend observed in the figure. If one takes into account the cation's hydrated radius, this explanation does match the observed trend because the hydrated radius of the alkali cations decreases from Li^+ to Rb^+ with Rb^+ and Cs^+ having approximately the same hydrated radii [85].

2. As the anion's radius gets larger in Fig. 3.4, the anion becomes more easily polarized [86, 87], but its hydrated radius stays approximately the same [85]. With all else being equal, a more polarizable anion would likely lead to a stronger electrostatic attraction between the anion and the graphene.

3. Larger ions in general have hydration shells that are less compact and, as a result, are more loosely bound [88]. The ability of larger anions to more easily shed their hydration shells

could help explain the trend in the sodium halide data. It could also explain why the halide anions adsorb with greater density than the Na^+ cation. For all but the F^- anion, which is approximately equal to the Na^+ cation in both its hydrated and unhydrated radii, the Na^+ cation is smaller than its halide counterpart and thus has a more compact hydration shell that is more difficult to shed. Furthermore, the larger the alkali cation, the better its ability to shed its hydration shell, meaning an even greater concentration of such cations can surround the Cl^- anion and prevent it from adsorbing.

Again, despite the plausibility of these radius-dependent explanations, they likely only account for a small part of the observed trends.

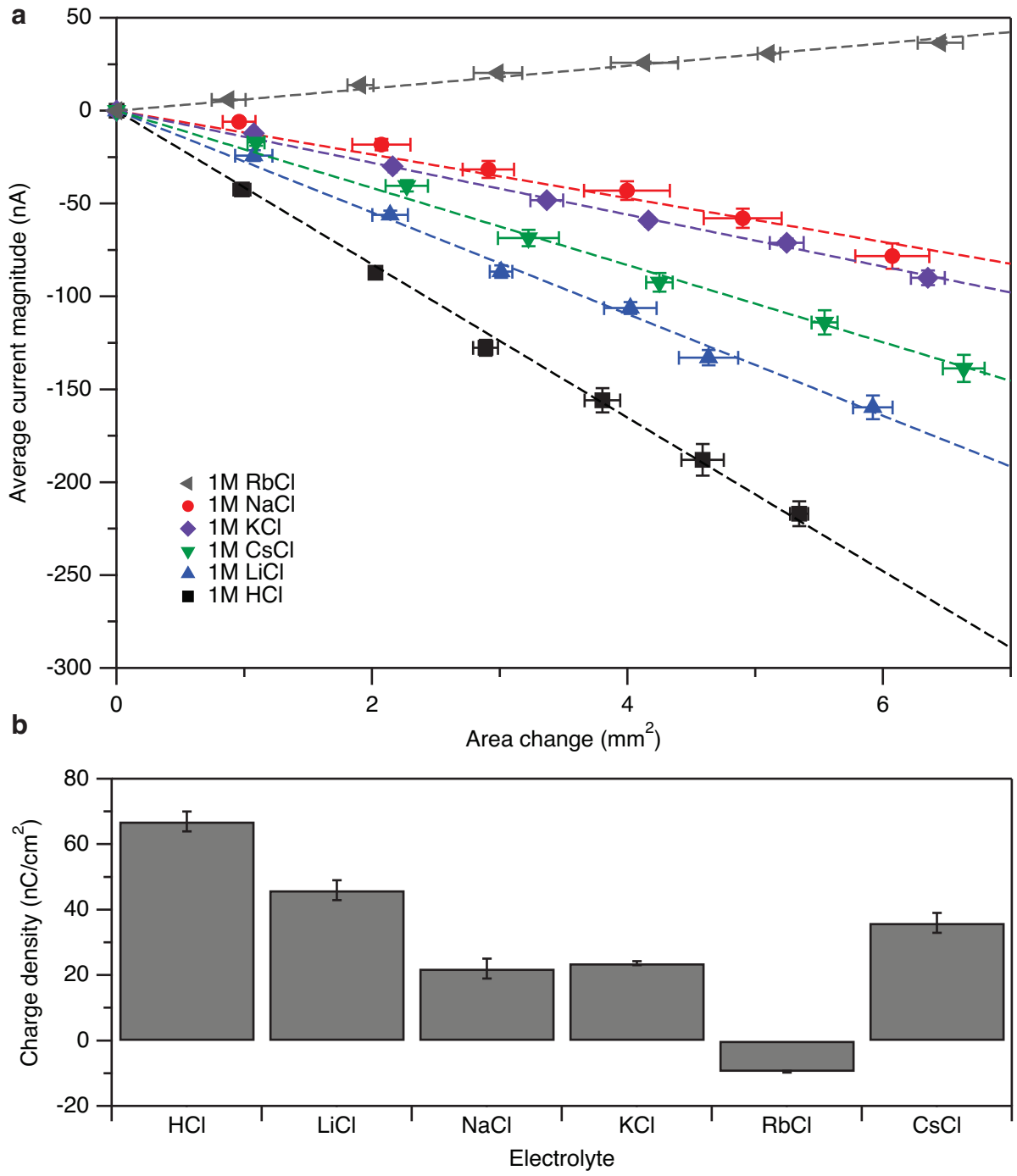

Figure 3.3: Surface charge density due to alkali chloride solutions. **a**, Average current magnitude vs. peak-to-peak area change (sign of the slope indicates the sign of the current). Droplet volume = 20 μL, oscillation frequency = 30 Hz. **b**, Induced charge density in graphene as a function of electrolyte. Where they are not visible, error bars are smaller than the dimensions of the data point's symbol.

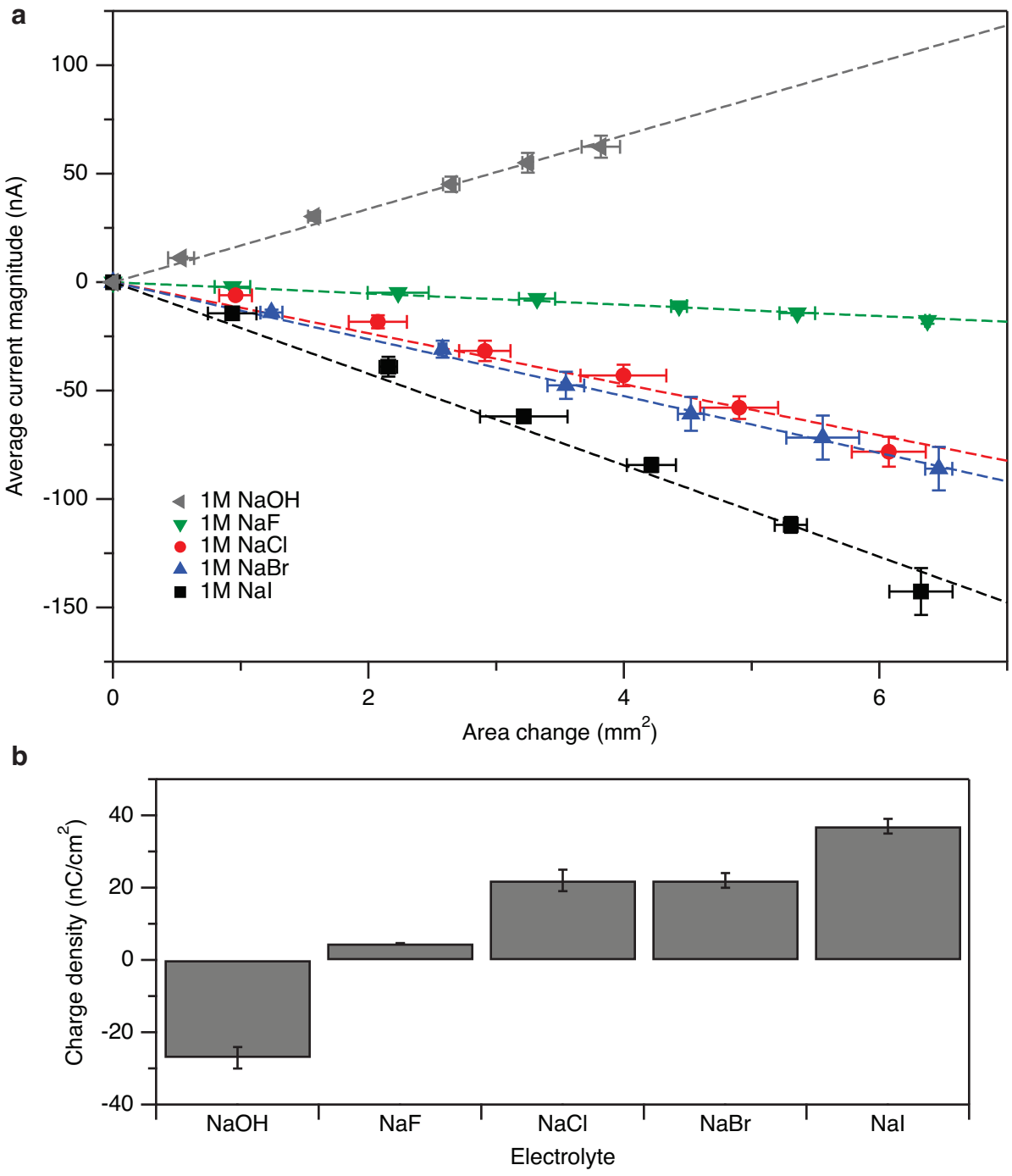

Figure 3.4: Surface charge density due to sodium halide solutions. a, Average current magnitude vs. peak-to-peak area change (sign of the slope indicates the sign of the current). Droplet volume = 20 μL, oscillation frequency = 30 Hz. **b**, Induced charge density in graphene as a function of electrolyte. Where they are not visible, error bars are smaller than the dimensions of the data point's symbol.

3.4.2 σ vs. pH

As mentioned in the last section, the induced charge density in graphene appears more significantly influenced by the pH of an electrolyte solution than it does by the radii (either hydrated or unhydrated) of the electrolyte's ions. This is demonstrated in a plot of the surface charge density vs. pH for all the alkali chloride and sodium halide solutions in Fig. 3.5 (**a**). The surface charge densities were taken from Figs. 3.3 (p. 136) and 3.4 (p. 137) and the pH of each droplet of solution was measured using a microelectrode after each droplet was oscillated. The pH of these solutions was not changed by acid/base titration. It is clear from the trend in this plot that the pH

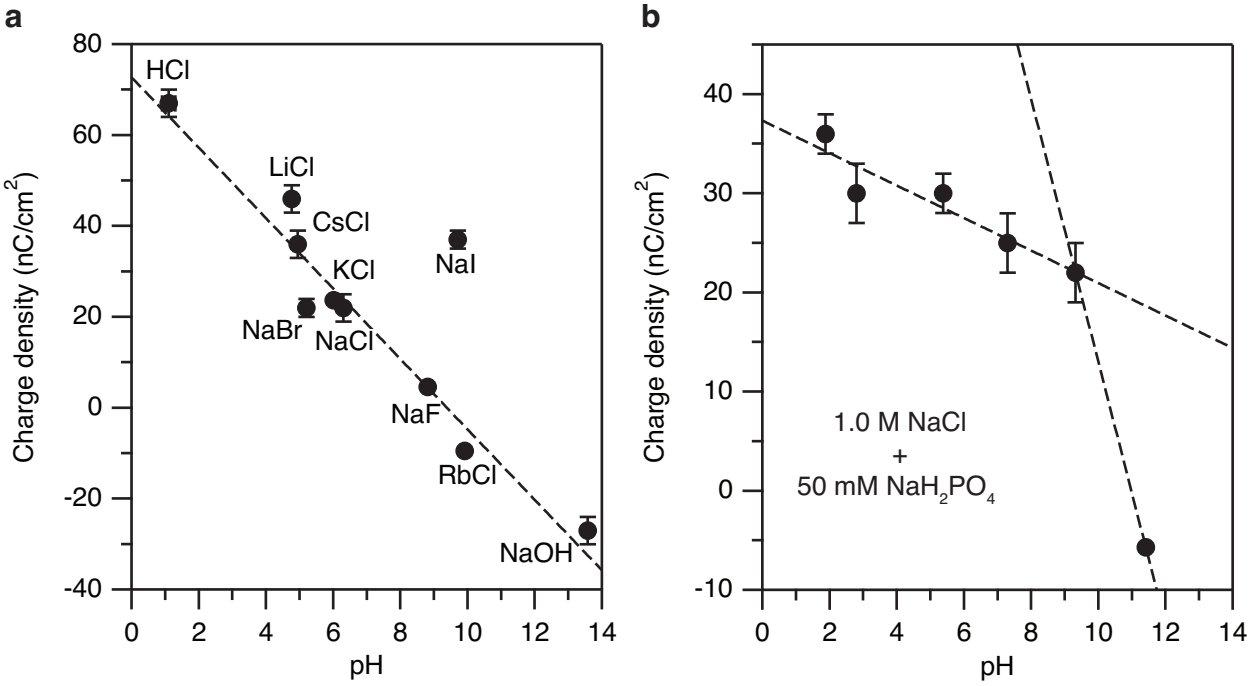

Figure 3.5: Surface charge density vs. pH. a, Induced charge density in graphene as a function of pH for alkali chloride and sodium halide electrolytes. All concentrations are 1.0 M. **b**, Induced charge density in graphene as a function of pH for 1.0 M NaCl buffered with 50 mM NaH_2PO_4. Where they are not visible, error bars are smaller than the dimensions of the data point's symbol.

appears to be the dominant factor influencing both the sign and the magnitude of the induced surface charge density with the charge density decreasing linearly with increasing pH. The only sig-

nificant outlier from this trend is the electrolyte NaI. This suggests that the I^- anion's interaction with graphene is not as heavily influenced by pH as the interactions between graphene and the other ions.

Fig. 3.5 (**b**) shows the effect of pH on induced surface charge density while controlling for the ionic species present in the electrolyte solution. The induced surface charge density is plotted vs. pH for 1.0 M NaCl solutions containing 50 mM of the buffer NaH_2PO_4. The pH was adjusted by adding small volumes of either 1 M HCl or 1 M NaOH. Due to experimental limitations, NaCl was the only electrolyte used to study the effect of pH in this way. As shown in the figure the induced surface charge density deceases linearly with pH for most of the pH values. The surface charge density induced in graphene by the solution with pH 11.4 does not agree with this trend, however, likely because of the abrupt change in the sign of the absorbed ion (from anion to cation) that occurs between pH $9 - 11.4$. Figs. 3.5 (**a**) and (**b**) both show that the pH can change which ion is most strongly interacting with graphene. In both cases when pH < 10 the dominant ion is the negatively charged anion and when the pH $\geq$ 10 the dominant ion is the positively charged cation.

The simplest explanation for the trends seen in Fig. 3.5 (p. 138) would be the protonation and deprotonation of oxygen- or nitrogen-containing functional groups in the graphene lattice or in the polymer contamination adsorbed to it. However, this explanation is unlikely for the following reasons:

1. If present in graphene, most of these functional groups would exist at the edges of the lattice [89]. Because the pH effect is determined by measuring a current per unit area, if these functional groups were responsible for the effect they would have to be distributed throughout the bulk of the graphene. Such graphene would be defective enough to show characteristic defect signatures when subject to both Raman and X-ray photoelectron spectroscopic analysis. As discussed in Section 2.4.3 (p. 102) and shown in Figs. 2.30 (p. 106) and 2.32

(p. 108), the data from such analyses refutes the functional-group protonation / deprotonation hypothesis.

2. The data show that for low pH solutions a positive surface charge is induced in graphene and vice versa for high pH solutions. If the effect were a result of protonation and deprotonation of functional groups in either the graphene lattice or in the polymer contamination adhered to the graphene, one would expect the signs of the surface charge for low and high pH to be reversed. This is because functional groups are protonated to a greater extent as the pH is lowered. By definition, protonation adds positive charge. This means that if functional groups were being protonated at low pH, there would be a net accumulation of positive charge in close proximity to the bulk of the graphene's lattice. In response, the graphene would become negatively charged (unless, of course, such functional groups altered the charge carrier density of the graphene by doping it instead of inducing in it an image charge). This, however, is the opposite of what is observed in the data. Furthermore, poly (methyl methacrylate) (PMMA), the polymer that was used in the transfer of graphene, does not contain any functional groups that are readily protonated or deprotonated.

3. It has been empirically shown that a room-temperature ionic liquid (RTIL), 1- ethyl -3-methylimidazolium tetrafluoroborate ($EMIMBF_4$), is capable of inducing a surface charge in graphene.[6] Because RTILs are not aqueous-based solutions and because the data in Fig. 3.8 were taken under an atmosphere of dry N_2, the effect of hydronium and hydroxide ions was effectively removed. The fact that surface charge is induced in graphene even in the absence of these ions is proof that, in general, protonation and deprotonation of functional groups is not a necessary requirement for charge induction. This further undermines the plausibility of the protonation / deprotonation argument for explaining the overall trend in

[6]See Fig. 3.8 (p. 148).

the dependence of surface charge density on pH.

In contrast, a plausible hypothesis for why pH affects the induced surface charge can be found in the unique way in which aqueous protons have been shown to interact with graphene. To date, nothing larger than a proton has shown the ability to migrate through an intact graphene lattice [90]. Instead of inducing in graphene a negative charge, an aqueous proton, because of its ability to pass through a graphene lattice under the influence of an applied electric potential, could become trapped in the lattice or otherwise interact with it strongly enough to remove an electron. The density of positive charge carriers would increase as a result and graphene would become more positively doped.[7] As the pH decreases and the concentration of protons increases, the graphene becomes more positively doped, *i.e.* p-doped, in this way. The larger density of positive charge carriers at low pH would enable anions of an electrolyte to induce a greater positive charge density in the graphene, ultimately increasing the concentration of the anions at the graphene's surface.

The modulation of the charge carrier density of a semiconductor or a semimetal, as is the case with graphene, by surface-bound dopants is termed surface transfer doping and has been well documented in the literature [91]. Graphene has been shown to be susceptible to surface transfer doping from many different types of dopants [92]. Attempts to determine the effect of pH on the charge carriers in graphene, however, have so far yielded mixed results with some questioning the significance with which surface transfer doping plays a role [72, 89, 93–97]. With the exception of Ref. [96], these studies have all employed a graphene field-effect transistor (GFET) to measure the change in charge carrier density as a function of pH.[8] The consensus appears to be that the charge carrier density in graphene is intrinsically insensitive to pH. Edge defects and the nature of the supporting substrate are thought to lead to graphene's sensitivity to pH. Defective

[7] In fact, it was theoretically calculated in Ref. [5] that protons bind to graphene with an energy similar to that of a covalent bond, a form of electron transfer between atoms.

[8] See Fig. 2.28 (p. 103) for an illustration of an experimental GFET setup.

graphene supported by a substrate with a fixed surface charge has been shown to become more positively doped at higher pH [89, 94, 95]. In each of these studies, however, an electrostatic gate was used to change graphene's charge carrier density. This was determined to cause specific adsorption of ions on the graphene's surface and was at least partially responsible for the pH sensitivity. Charging of the EDL at the solution-graphene interface by the electrostatic gate was also used to explain the pH-dependent doping effect.

Although the results in the literature seem to contradict those from the G-SCEEG, the G-SCEEG and GFET devices function in sufficiently different ways that this alone is likely responsible for the apparent contradiction. It is believed that in the absence of an external electric field, a supporting substrate with fixed surface charge, and defects in the graphene lattice (conditions all largely met by the G-SCEEG) aqueous protons positively dope graphene. This in turn enhances graphene's capacity for supporting positive surface charge density as induced by anions of an electrolyte. The fact that the intrinsic charge carrier density of graphene ($\sim 10^{12}$ cm^{-2}, Fig. 2.28) is within an order of magnitude of the charge number density induced in graphene by Cl^- ($\sim 10^{11}$ cm^{-2}, Fig. 3.3) supports this hypothesis.

3.4.3 σ vs. ionic strength

The effect that the concentration of the electrolyte solution has on the surface charge density is more straightforward to interpret. Fig. 3.6 (p. 144) is a log-log plot of the magnitude of the surface charge induced in graphene vs. the concentration of different NaCl solutions. For concentrations < 0.1 M, the magnitude of the charge density scales as the square root of the concentration (the dashed line through the data points over this concentration range has a slope of $1/2$ in the figure). For concentrations ≥ 0.1 M, however, the charge density scales weakly with concentration. In this plot, however, the pH is not strictly controlled. As listed in Table 3.3 (Sect. 3.3, p. 153), the pH is approximately the same for the solutions whose concentrations are < 0.1 M and more variable for those whose concentrations are ≥ 0.1 M.

The scaling behavior of σ vs. concentration in Fig. 3.6 can be best understood by examining Eq. (2.7) (p. 26). According to Eq. (2.7), the surface charge density, σ, is proportional to the equivalent capacitance per unit area of the interface, $\sigma \propto c_0$. Because the equivalent capacitance is equal to the reciprocal of the sum of the reciprocals of three different capacitances, it is dominated by the whichever capacitance is the smallest. According to Eq. (3.12) (p. 124), the expression for the capacitance per unit area of the diffuse layer, $c_{0,\mathrm{d}}$, is proportional to the square root of the concentration of the electrolyte, $c_{0,\mathrm{d}} \propto \sqrt{n_0}$. Therefore, Fig. 3.6 suggests that for concentrations < 0.1 M, the smallest capacitance is that due to the diffuse layer because the charge density scales as the square root of concentration over this concentration range (assuming that the surface potential, Φ, remains approximately constant):

$$\sigma = c_0 \, \Phi = \left(\frac{1}{c_{0,\mathrm{q}}} + \frac{1}{c_{0,\mathrm{s}}} + \frac{1}{c_{0,\mathrm{d}}} \right)^{-1} \Phi \simeq c_{0,\mathrm{d}} \, \Phi \propto \sqrt{n_0} \tag{3.17}$$

As concentration increases, however, the diffuse layer capacitance increases to a point where it is no longer the smallest. At a concentration of 0.1 M, the diffuse layer capacitance is roughly

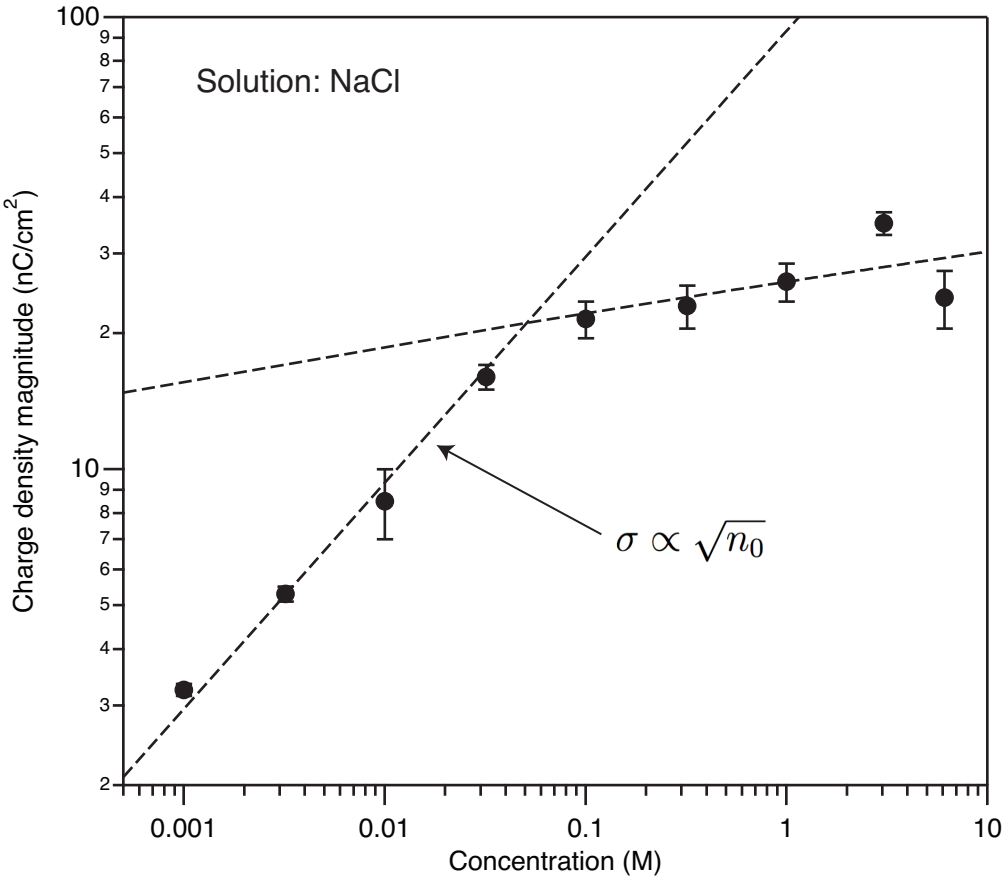

Figure 3.6: Surface charge density vs. NaCl concentration. A log-log plot of the magnitude of induced charge density in graphene as a function of NaCl concentration. The sign of the charge density is positive for all concentrations except 1 mM. The dashed line through the data points for concentrations < 0.1 M has a slope of $1/2$ indicating that the charge density scales as square root of concentration, $\sigma \propto \sqrt{n_0}$, over this concentration range. Where they are not visible, error bars are smaller than the dimensions of the data point's symbol.

equivalent to either the quantum capacitance or the Stern layer capacitance (or both) and no longer dominates the equivalent capacitance. As a result, the magnitude of the surface charge density is only weakly dependent on the concentration over this range.

3.4.4 σ vs. graphene multi-layers

In addition to the properties of the electrolyte solution, the presence of graphene multilayers also significantly influences the induced surface charge density. Fig. 3.7 compares the average current magnitude vs. the peak-to-peak area change for 1 M solutions of NaCl and HCl as measured by G-SCEEGs with (blue symbols) and without (black symbols) regions of multi-layer graphene. Note that $10-20\,\%$ of the area of the G_{MULTI}-SCEEG's graphene electrodes is covered in multi-layers ranging from $2-10$ layers thick.

As evident by the slopes of the linear fits of the data points, the induced surface charge density is almost an order of magnitude larger for graphene with multi-layers than for graphene without. Assuming that surface transfer doping is occurring between aqueous protons and graphene, one possible explanation for the increase in induced surface charge density could be that p-doping caused by the protons has an additive effect in regions of graphene multi-layers. Penetration of the protons through the basal plane of each graphene monolayer as well as lateral diffusion from the edges of the multi-layer stacks could cause each layer in the stack to become positively doped. This in turn would allow the multi-layer region to support a greater induced surface charge than an individual mono-layer. Because the multi-layer G-SCEEG device has between $10-20\,\%$ of its area covered in multi-layer graphene of varying numbers of layers, it is difficult to quantify the multi-layer effect from the data. G-SCEEG devices with a well defined number of graphene layers, *i.e.* bi-layer, tri-layer, *etc.*, are needed to help clarify this effect.

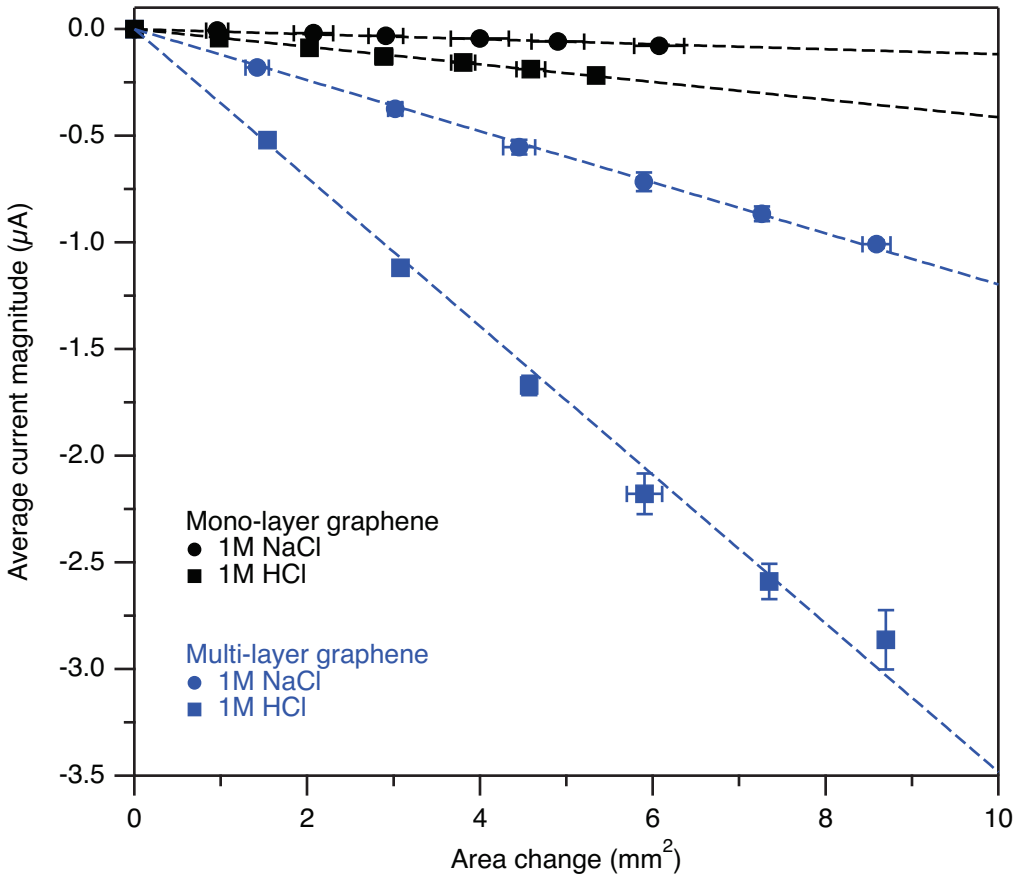

Figure 3.7: Surface charge density: multilayer vs. monolayer. Average current magnitude vs. peak-to-peak area change (sign of the slope indicates the sign of the current) for mono- vs. multi-layer graphene. Droplet volume $= 20$ μL, oscillation frequency $= 30$ Hz. Where they are not visible, error bars are smaller than the dimensions of the data point's symbol.

3.4.5 σ vs. other polar liquids

As a concluding proof-of-concept experiment that other polar liquids, including solutions containing charged biomolecules, can induce a measurable surface charge density in graphene, the average current magnitude vs. peak-to-peak area change was measured for the room-temperature ionic liquid (RTIL) 1-ethyl-3-methyl imidazolium tetrafluoroborate ($EMIMBF_4$) and an aqueous solution of 4–6 kb fragments of double-stranded DNA (500 μg/μL). Fig. 3.8 shows how these liquids compare. The black symbols represent the DNA solution and the blue symbols represent $EMIMBF_4$ and the G_{MULTI}-SCEEG device was used to collect the data for both liquids.

Due to the increased viscosity of both liquids, the range of peak-to-peak area changes was smaller than that achieved for the electrolyte solutions shown in Figs. 3.3 (p. 136) and 3.4 (p. 137). Neither liquid was sparged with He prior to being pipetted onto the G-SCEEG. This was because the concern about dissolved CO_2 affecting an aqueous solution's pH does not apply to $EMIMBF_4$ and because it was thought that sparging the solution of DNA could cause the DNA to fragment further. Without first sparging the DNA solution, its pH could not be accurately known throughout the course of the experiment and was not, therefore, measured. The DNA solution was desalted, *i.e.* the buffer solution it was stored in was replaced by deionized water, immediately before it was used in an attempt to prevent the ions of the buffer from affecting the measurement. It is likely, however, that some of the positively-charged ions of the buffer remained bound to the negatively charged DNA molecules during this process.

Interestingly, even in the absence of the p-doping effect caused by aqueous protons, the negatively charged BF_4^- anion appears to interact with graphene more strongly than the positively charged 1-ethyl-3-methyl imidazoium cation and induced in graphene a surface charge of $\sigma = 85 \pm 6$ nC/cm^2. This is significantly less than the surface charge induced by the 1.0 M electrolyte

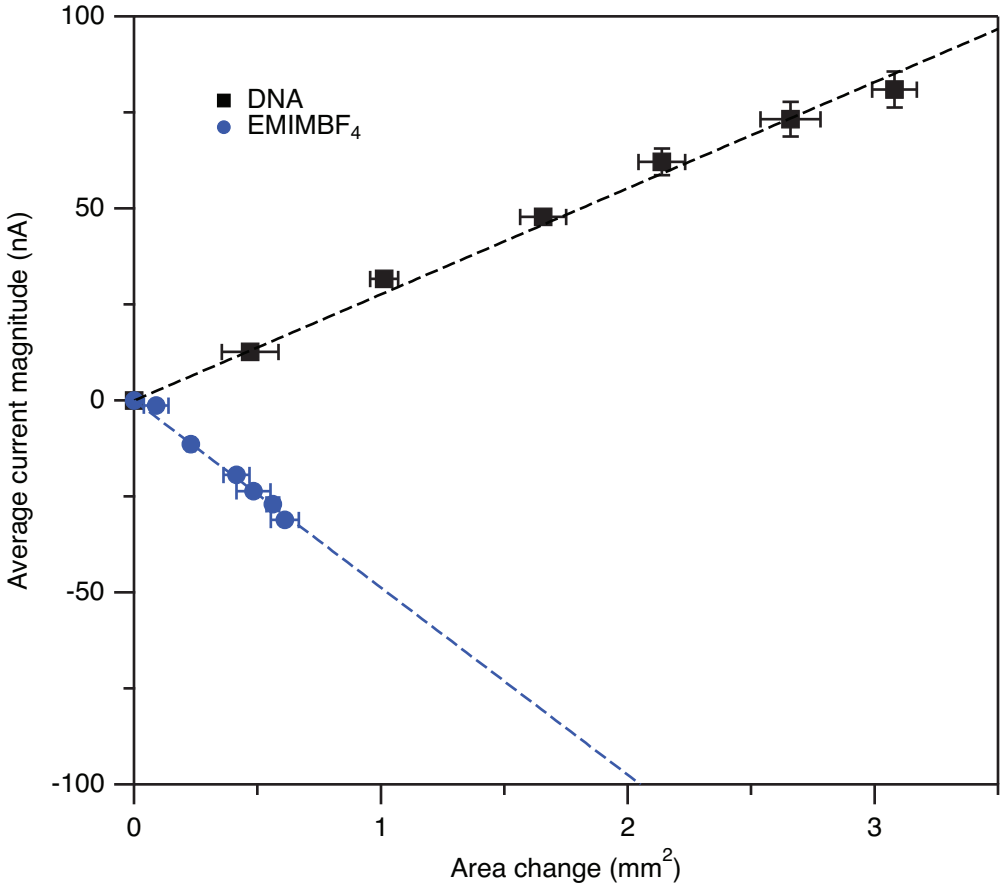

Figure 3.8: Surface charge density: EMIMBF$_4$ and DNA. Average current magnitude vs. peak-to-peak area change (sign of the slope indicates the sign of the current) for EMIMBF$_4$ and an aqueous solution of DNA. From the slopes in this plot the surface charge density induced in graphene by the DNA solution and EMIMBF$_4$ were found to be -45 ± 4 and 85 ± 6 nC/cm^2, respectively. Droplet volume $= 15$ μL, oscillation frequency $= 30$ Hz. Data taken with multi-layer G-SCEEG device. The DNA solution contained 4–6 kb fragments of double-stranded DNA at a concentration of 500 μg/μL was desalted prior to use. Where they are not visible, error bars are smaller than the dimensions of the data point's symbol.

solutions.[9] The reduction in induced surface charge is likely due to both the increased size of the BF_4^- anion and the lack of the p-doping enhancement caused by aqueous protons.

Also of interest is the sign of the surface charge induced in graphene by the DNA solution. DNA is negatively charged when dissolved in water and would be expected to induce in graphene a positive charge density if it were strongly interacting with it. Surprisingly, the solution of 4–6 kb double-stranded DNA fragments induced a surface charge of only $\sigma = -45 \pm 4$ nC/cm^2. Because the DNA was desalted, it is unclear which positive ion in the solution is responsible for inducing the negative charge density. Perhaps positively charged cations, such as the protonated form of tris- (hydroxymethyl) -aminomethane ($pK_a = 8$), from the original buffer solution remained bound to the DNA even after desalting and give rise to the negative charge density induced in graphene. Further experiments are needed to help clarify this result.

[9] See Table 3.4 (Sect. 3.4, p. 153).

3.4.6 Summary of surface charge densities

In summary, the G-SCEEG can be used to determine the sign and magnitude of the surface charge density induced in graphene by electrolyte solutions, room-temperature ionic liquids, and solutions containing charged biological molecules. The factors influencing the surface charge density induced in graphene by electrolyte solutions are: the type ionic species present, the concentration of ions in solution, the pH of the solution, and the presence of graphene multi-layers.

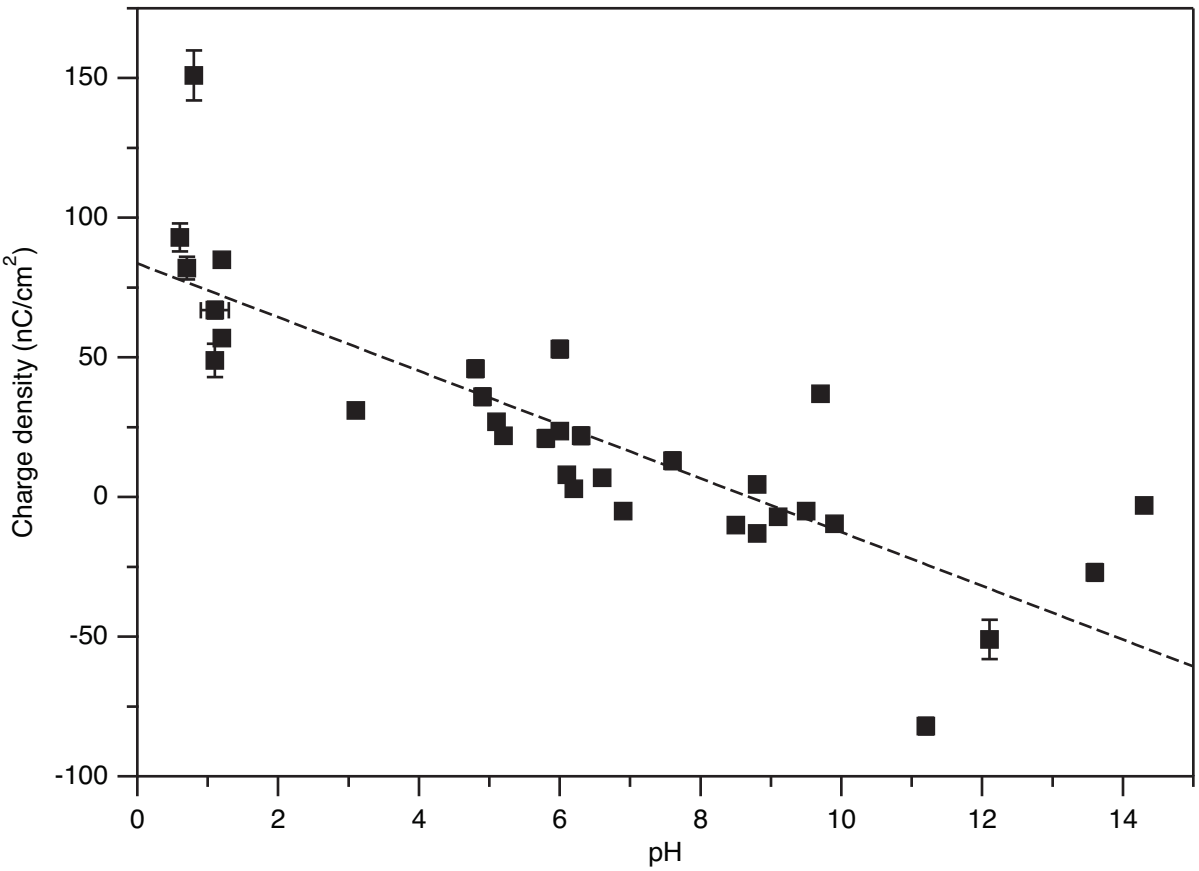

Figure 3.9: Surface charge density vs. pH for 1.0 **M electrolyte solutions.** Induced charge density in graphene as a function of pH for all 1.0 M electrolyte solutions that were studied. The data, including the identities of the solutions, are listed in Table 3.1 (p. 151). Where they are not visible, error bars are smaller than the dimensions of the data point's symbol.

In general, surface charge density decreases linearly with pH. The influence of pH appears to

Solution	pH (± 0.1)	Sign ($+/-$)	Charge density, σ (nC/cm^2)	Physically adsorbed ion	Surface density, σ_n ($\times 10^{10}$ ions/cm^2)
HCl (6.0 M)	-0.7	$+$	187 ± 4	Cl^-	120 ± 3
HNO_3	0.8	$+$	151 ± 9	$[NO_3]^-$	94 ± 6
$HClO_4$	0.6	$+$	93 ± 5	$[ClO_4]^-$	58 ± 3
H_3PO_4	1.2	$+$	85 ± 1	$[H_2PO_4]^-$	53 ± 1
H_2SO_4	0.7	$+$	82 ± 4	$[HSO_4]^-$ / $[SO_4]^{2-}$	51 ± 3
HCl	1.1	$+$	67 ± 3	Cl^-	42 ± 2
oxalic acid	1.2	$+$	57 ± 2	[bioxalate]$^-$	36 ± 1
$ZnCl_2$	6.0	$+$	53 ± 3	Cl^-	33 ± 2
citric acid	1.1	$+$	49 ± 6	$[C_6H_7O_7]^-$	31 ± 3
LiCl	4.8	$+$	46 ± 3	Cl^-	29 ± 2
NaI	9.7	$+$	37 ± 2	I^-	23 ± 1
CsCl	4.9	$+$	36 ± 3	Cl^-	23 ± 2
acetic acid	3.1	$+$	31 ± 2	$[CH_3CO_2]^-$	19 ± 1
NH_4Cl	5.1	$+$	27 ± 2	Cl^-	17 ± 1
KCl	6.0	$+$	23.7 ± 0.6	Cl^-	15 ± 1
NaCl	6.3	$+$	22 ± 3	Cl^-	14 ± 2
NaBr	5.2	$+$	22 ± 2	Br^-	14 ± 1
$MgCl_2$	5.8	$+$	21 ± 3	Cl^-	13 ± 2
NaSCN	7.6	$+$	13 ± 3	$[SCN]^-$	8 ± 2
benzoic acid (10 mM)	3.4	$+$	11 ± 1	[benzoate]$^-$	6.9 ± 0.6
$Mg(NO_3)_2$	6.1	$+$	8 ± 1	$[NO_3]^-$	5.0 ± 0.6
$NaClO_4$	6.6	$+$	7 ± 1	$[ClO_4]^-$	4.4 ± 2
NaF	8.8	$+ \rightarrow -$	4.6 ± 0.5	$F^- \rightarrow Na^+$	2.9 ± 0.3
$NaNO_3$	6.2	$+$	3 ± 1	$[NO_3]^-$	1.9 ± 0.6
KOH	14.3	$-$	-3 ± 3	K^+	2 ± 2
NH_4OH	9.5	$-$	-5 ± 1	$[NH_4]^+$	3.1 ± 0.6
H_2O (55 M)	8.7	$-$	-5 ± 1	$[H_3O]^+$	3.1 ± 0.6
Na_2SO_4	6.9	$-$	-5 ± 1	Na^+	3.1 ± 0.6
sodium acetate	9.1	$-$	-7 ± 1	Na^+	4.4 ± 0.6
trisodium citrate (1 mM)	8.7	$-$	-7 ± 1	Na^+	4.4 ± 0.6
RbCl	9.9	$-$	-9.5 ± 0.5	Rb^+	5.9 ± 0.3
$CaCl_2$	8.5	$-$	-10 ± 1	Ca^{2+}	3.2 ± 0.3
sodium oxalate (100 mM)	8.3	$-$	-12 ± 2	Na^+	7 ± 1
$MgSO_4$	8.8	$-$	-13 ± 1	Mg^{2+}	4.1 ± 0.3
NaOH	13.6	$-$	-27 ± 3	Na^+	17 ± 2
LiOH	12.1	$-$	-51 ± 7	Li^+	32 ± 4
Na_2CO_3	11.2	$-$	-82 ± 3	Na^+	51 ± 2

Table 3.1: Induced surface charge densities in mono-layer graphene. The sign and the density of the image charge induced by different solutions in mono-layer graphene as measured by the G_{MONO}-SCEEG. The identity of the physically adsorbed ion was deduced from the sign of the induced image charge and from the way in which the electrolytes are known to dissociate in water. All concentrations are 1.0 M unless otherwise noted. The symbol $+ \rightarrow -$ indicates that the sign of the induced charge briefly changes from $+$ to $-$ during half a period of oscillation. Solutions are listed in descending order of σ.

dominate the effect that the species of the ion has on the induced charge density for most types of ions studied. Exceptions include HNO_3, Na_2CO_3, LiOH, NaOH, KOH, NaI, $ZnCl_2$, acetic acid, citric acid, and oxalic acid as seen in Fig. 3.9 (p. 150) and Table 3.1 (p. 151). Surface charge density was found to scale as the square root of concentration for concentrations of NaCl < 0.1 M and is roughly independent of concentration for NaCl concentrations ≥ 0.1 M. This can be understood as the diffuse layer capacitance dominating the overall equivalent capacitance at low concentrations. As listed in Table 3.4 (p. 153) the presence of graphene multi-layers has a significant effect on the surface charge density and increases the charge density by an order of magnitude compared to mono-layer only graphene.

Solution	pH (± 0.1)	Sign ($+/-$)	Charge density, σ (nC/cm^2)	Physically adsorbed ion	Surface density, σ_n ($\times 10^{10}$ ions/cm^2)
NaCl + NaH_2PO_4	1.9	+	36 ± 3	Cl^-	23 ± 2
	2.8	+	30 ± 3	Cl^-	19 ± 2
	5.4	+	30 ± 2	Cl^-	19 ± 1
	7.3	+	25 ± 3	Cl^-	16 ± 2
	9.3	+	22 ± 3	Cl^-	14 ± 2
	11.4	−	-5.7 ± 0.5	Na^+	3.6 ± 0.3

Table 3.2: Induced surface charge densities vs. pH. The density and sign of charge induced by solutions of 1.0 M NaCl buffered with 50 mM NaH_2PO_4 in mono-layer graphene as measured by the G_{MONO}-SCEEG. The pH was adjusted using either 1.0 M HCl or 1.0 M NaOH. The identity of the adsorbed ion was deduced from the sign of the induced image charge. The solutions are arranged in order of increasing pH. Data are displayed in Fig. 3.5 (p. 138).

In addition to graphene, a symmetric SCEEG device can be used to measure the surface charge density induced by electrolyte solutions in other electrode materials. Compared with both multi-layer and mono-layer graphene, a larger surface charge density is induced in gold by a 1.0 M NaCl solution as measured using the Au-SCEEG. This could be due to the larger density of states and number of charge carriers in the gold or to a stronger interaction between the gold and the chloride anion. Unlike graphene, 1.0 M HCl induces a smaller charge density in gold than 1.0 M NaCl. This could result from a small amount of surface etching of the gold by HCl.

Solution	Concentration (M)	pH (± 0.1)	Sign ($+/-$)	Charge density, σ (nC/cm^2)	Physically adsorbed ion	Surface density, σ_n ($\times 10^{10}$ ions/cm^2)
NaCl	0.0010	6.6	$-$	-3.3 ± 0.5	Na^+	2.1 ± 0.3
	0.0032	6.1	$+ \rightarrow -$	5.3 ± 0.5	$Cl^- \rightarrow Na^+$	3.3 ± 0.3
	0.010	6.5	$+$	9 ± 2	Cl^-	6 ± 1
	0.032	6.6	$+$	16 ± 1	Cl^-	10 ± 1
	0.10	7.0	$+$	22 ± 2	Cl^-	14 ± 1
	0.32	5.6	$+$	23 ± 3	Cl^-	14 ± 2
	1.0	5.9	$+$	26 ± 3	Cl^-	16 ± 2
	3.1	6.3	$+$	35 ± 2	Cl^-	22 ± 1
	6.1	5.4	$+$	24 ± 4	Cl^-	15 ± 3

Table 3.3: Induced surface charge densities vs. concentration. The density and sign of the charge induced by NaCl solutions of different concentrations in mono-layer graphene as measured by the G_{MONO}-SCEEG. The identity of the adsorbed ion was deduced from the sign of the induced image charge. The symbol $+ \rightarrow -$ indicates that the sign briefly changes from $+$ to $-$ during half a period of oscillation. The solutions are arranged in order of increasing concentration. Data are displayed in Fig. 3.6 (p. 144).

Electrode material	Solution	Sign ($+/-$)	Charge density, σ (nC/cm^2)	Physically adsorbed ion	Surface density, σ_n ($\times 10^{10}$ ions/cm^2)
Multi-layer graphene	HCl (6.0 M)	$+$	900 ± 10	Cl^-	560 ± 10
	HNO_3	$+$	720 ± 20	$[NO_3]^-$	450 ± 10
	HCl	$+$	570 ± 10	Cl^-	360 ± 10
	NaCl	$+$	200 ± 10	Cl^-	130 ± 10
	$EMIMBF_4$	$+$	85 ± 6	$[BF_4]^-$	53 ± 4
	DNA	$-$	-45 ± 4	$[Tris]^+$	28 ± 3
Au	NaCl	$+$	430 ± 20	Cl^-	270 ± 10
	HCl	$+$	190 ± 10	Cl^-	120 ± 10

Table 3.4: Induced surface charge densities in other electrodes. The density and sign of the charge induced by different solutions in graphene with multi-layer regions and Au as measured by the G_{MULTI}-SCEEG and Au-SCEEG, respectively. The identity of the adsorbed ion was deduced from the sign of the induced image charge. All concentrations are 1.0 M unless otherwise noted. Solutions are listed in descending order of σ for each device. The values in red indicate the largest charge and surface densities that were measured by a SCEEG device in this work.

3.5 Capacitance per unit area, c_0

Not only can the G-SCEEG be used to determine the sign and magnitude of surface charge induced in graphene by electrolyte solutions and other polar liquids, it can also be used to determine the capacitance per unit area of the graphene-solution interface. The capacitance is determined using the experimental setup illustrated in Fig. 2.10 (p. 61). Current vs. time is measured as an AC voltage ramp is applied across the device. Because the voltage ramp is linearly in time, the independent variable of time in Fig. 2.10 (**b**) can be substituted for voltage to create a cyclic voltammogram as shown in Fig. 3.10. Like Fig. 2.10 (**b**), Fig. 3.10 shows the current response of the multi-layer G-SCEEG device with a $15\ \mu$L droplet of 1.0 M HCl as the voltage is ramped from $-\,250$ mV to $+\,250$ mV, and vice versa, in 5 ms, giving a ramp rate of $\nu = 100$ V/s.[10] The data presented in Fig. 3.10 were taken under normal atmospheric conditions and without sparging the solution with He.

Using this data the capacitance per unit area, c_0, can be calculated in two ways. The first is by fitting the model represented by Eq. (2.73) (p. 63) to the current transient that is generated by the applied voltage ramp. The value of the variable C that gives the best fit of Eq. (2.73) to the current vs. time data of Fig. 2.10 (**b**) is the capacitance of the interface between the droplet and a single graphene electrode. Dividing C by the area of overlap between the droplet and the electrode gives c_0. Because the rate of the voltage ramp, ν, the faradaic resistance, R_{F}, and the solution's resistance, R_{S} where $R = 2\,R_{\mathrm{G}} + R_{\mathrm{S}}$, are explicitly treated in Eq. (2.73), this way of calculating c_0 is valid regardless of the voltage ramp rate that is used.

[10] As mentioned in Chapter 2, Sect. 2.3.3 (p. 60), such a fast ramp rate over a narrow potential range was used in order to capture the current resulting from capacitative charging without subsequently causing electrochemical reactions to occur between the graphene and the electrolyte. However, in normal applications of cyclic voltammetry, the ramp rate is made slow enough (1–100 mV/s), and the potential range is made large enough, to avoid measuring the capacitive current while still retaining the ability to measure the current resulting from the electrochemical reactions of interest [59, 70]. On the other hand, if the ramp rate is too fast, the ions do not have sufficient time to diffuse to the electrode-solution interface, ultimately causing this technique to underestimate the interfacial capacitance [98].

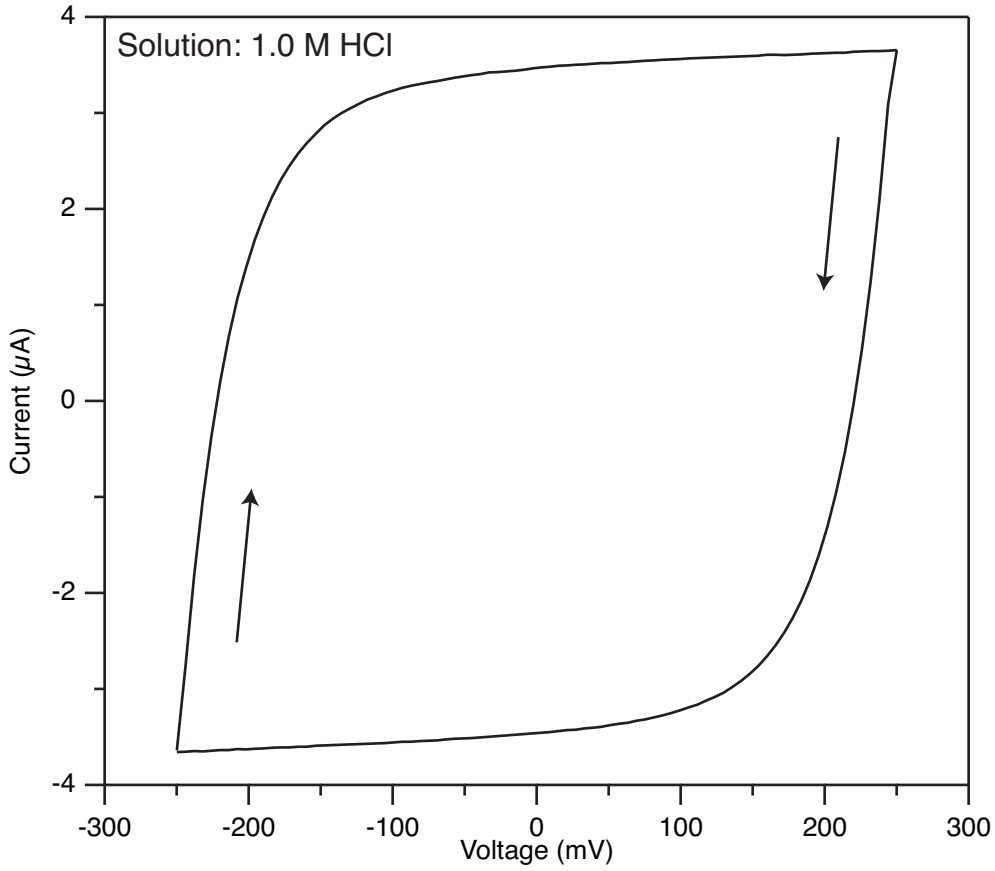

Figure 3.10: Cyclic voltammogram. Cyclic voltammogram of a 15 μL droplet of 1.0 M HCl taken using the G_{MULTI}-SCEEG device. Arrows indicate the direction of the voltage sweep. Voltage ramp rate, $\nu = 100$ V/s. Data was taken from Fig. 2.10 (p. 61).

The second way is by determining the average charge per unit surface area, $\langle\sigma\rangle_{\text{avg}}$, that accumulates at the electrode's surface during one cycle of an applied AC voltage ramp. This is done by integrating the magnitude of the current, $I(t)$, over the period, T, of the cycle and then dividing by both the area of overlap, A, between the droplet and one of the graphene electrodes (assuming the droplet overlaps each graphene electrode with equal area). This is equivalent to integrating the current, $I(V)$, in the cyclic voltammogram of Fig. 3.10 over the full cycle of the voltage ramp and then dividing by both the voltage ramp rate, ν, and the overlap area, A [98]:

$$\langle\sigma\rangle_{\text{avg}} = \frac{1}{2\,A}\int_0^T |I(t)|\;dt = \frac{1}{2\,A\,\nu}\oint I(V)\,dV \tag{3.18}$$

The factor of $1/2$ in Eq. (3.18) accounts for the fact that although the average over a complete cycle is being calculated, σ is determined from the current over only one-half of the cycle. This serves to eliminate most of the error due to faradaic current [70]. The capacitance per unit area is then estimated by dividing $\langle\sigma\rangle_{\text{avg}}$ by the total charge by the peak-to-peak voltage of the ramp, $V_{\text{p-p}}$:

$$c_0 = \frac{\langle\sigma\rangle_{\text{avg}}}{V_{\text{p-p}}} \tag{3.19}$$

In order to ensure that the external potential is applied predominately over the interfacial capacitor and that the faradaic current is minimized, the rate of the voltage ramp should be selected such that the resulting capacitive impedance is much greater than the resistance of the solution but much less than the faradaic resistance. For the most accurate results using this method, however, $\langle|I|\rangle_{\text{avg}}$ should be measured for several values of ν and c_0 determined from the slope of $\langle|I|\rangle_{\text{avg}}$ vs. ν [70].

In both of the ways for determining c_0 that are outlined above, c_0 is assumed to be independent of the applied potential. As seen in the expressions for the diffuse layer (Eq. (3.12), p. 124) and quantum (Eq. (3.14), p. 125) capacitances, however, this is only strictly valid when the potential

drops across these capacitors are much less than the thermal voltage ($\simeq$ 26 mV at $T = 300$ K). Because their potentials drops are likely much larger than the thermal voltage, this assumption introduces a source of error in c_0. Based on the quality of the fit in Fig. 2.10 (**b**), this error seems to be small.

Table 3.5 summarizes the capacitances per unit area of different electrolytes on graphene as measured using the multi-layer G-SCEEG. The capacitances were determined by fitting Eq. (2.73) (p. 63) to $I(t)$, as shown in Fig. 2.10 (p. 61), and by then dividing the result by the area of overlap between the droplet and an individual graphene sheet. Note that the value reported here for the capacitance of 1.0 M NaF on graphene ($\simeq$ 10 nF/mm^2) is approximately an order of magnitude less than that which was reported in the literature for 1 mM NaF on graphene using a normal hydrogen reference electrode ($\simeq$ 50–100 nF/mm^2) [81]. This discrepancy could be due to differences in the way in which the two capacitances were measured. In further work, electrochemical impedance spectroscopy could be used to resolve this discrepancy as it provides the most accurate measurement of the interfacial capacitance over a wide range of experimental conditions [70].

Electrode material	Concentration (M)	Solution	Capacitance, c_0 (nF/mm^2)
Multi-layer graphene	6.0	HCl	13 ± 1
	1.0	acetic acid	12 ± 1
	1.0	HCl	10 ± 1
	1.0	NaF	10 ± 1
	1.0	$ZnCl_2$	9.3 ± 0.9
	1.0	LiCl	9 ± 1
	1.0	KCl	9 ± 1
	1.0	NaBr	9 ± 1
	0.0010	trisodium citrate	9 ± 1
	1.0	NaI	8.8 ± 0.9
	1.0	$MgCl_2$	8.8 ± 0.9
	0.10	NaCl	8.8 ± 0.9
	1.0	NaCl	8.7 ± 0.9
	1.0	RbCl	8.5 ± 0.9
	1.0	$CaCl_2$	8.5 ± 0.9
	6.1	NaCl	8.3 ± 0.8
	1.0	CsCl	8.3 ± 0.9
	0.010	NaCl	7.2 ± 0.8
	0.0010	NaCl	6.8 ± 0.7
	55	H_2O	1.7 ± 0.2

Table 3.5: Capacitances per unit area. The capacitance per unit area of the electrolyte-graphene interface for different electrolyte solutions on graphene containing multi-layer regions. The experimental setup that was used is illustrated in Fig. 2.10 (p. 61). The capacitances were calculated by fitting the data to Eq. (2.73) (p. 63). The voltage ramp rate that was used was $\nu = 100$ V/s. Solutions are arranged in order of decreasing capacitance.

3.6 Surface potential, Φ, and effective surface binding energy per ion, E_{B}

Because one can measure both the surface charge density, σ, induced in graphene by an electrolyte solution and the capacitance per unit area, c_0, of the graphene-solution interface using the G-SCEEG, one is then able to determine the surface potential, Φ, across the interface using Eq. (2.7) (p. 26), *i.e.* $\Phi = \sigma \,/ c_0$.

Furthermore, if one makes the simplification of treating the entire interface as a parallel-plate capacitor and assumes each unit of charge, e, induced in graphene is effectively due to a single adsorbed ion, *i.e.* $\sigma \;=\; e\,N/A$ where N is the number of ions and A the area of overlap, one can calculate an effective surface binding energy per ion, $E_{\mathrm{B}} \;=\; W \,/\, N$. Starting with Eq. (2.1) (p. 25) for the energy, W, stored in a parallel-plate capacitor and dividing by $N \;=\; \sigma\, A \,/\, e$, the expression for E_{B} is:

$$E_{\mathrm{B}} = \frac{W}{N} = \frac{1}{2}\,\frac{\sigma\, e}{c_0} \tag{3.20}$$

Note that the form of Eq. (3.20) ignores the fact that the quantum and diffuse layer capacitances of the interface are defined differentially. Because of this, Eq. (3.20) is only strictly accurate if the capacitance of the Stern layer (the only capacitance that is like that of a parallel-plate capacitor) dominates the equivalent interfacial capacitance, something it can do only if it is significantly smaller than both the quantum and diffuse layer capacitances. The equation is used here only as a means to approximate the effective binding energy per ion because the relative magnitudes of the quantum, diffuse layer, and Stern layer capacitances are unknown.

Table 3.6 below lists values of Φ and E_{B} for several different electrolyte solutions when they are in contact with graphene electrodes containing regions of multi-layers. For each of these solutions, E_{B} represents the effective surface binding energy per Cl^- anion as it was previously determined that Cl^- is responsible for the the charge that is induced by each.

Comparing the values of Φ in Table 3.6 to the measured values of the surface potential at the

Electrode material	Concentration (M)	Solution	Surface potential, Φ (mV)	Cl^- binding energy, E_B (meV/ion)
Multi-layer graphene	6.0	HCl	690 ± 50	350 ± 30
	1.0	HCl	570 ± 60	290 ± 30
	1.0	NaCl	230 ± 30	110 ± 10

Table 3.6: Surface potential and binding energy per Cl^- ion. The surface potential across the interface and the effective surface binding energy per chloride ion, Cl^-, for different electrolyte solutions on graphene containing multi-layer regions.

interface between air and an electrolyte solution from Ref. [99], one finds that they are of the same order of magnitude ($230-690$ mV vs. $70-200$ mV).[11] They are also comparable to the zeta (ζ) potential, *i.e.* the potential difference between the bulk of an electrolyte solution and the hydrodynamic slip plane near that solution's interface with a solid surface, that was measured above glass and polydimethylsiloxane ($66 - 110$ mV) in Ref. [100].

The values of E_B, however, are approximately an order of magnitude smaller than those calculated by Yin et al. (Ref. [7]) using density functional theory ($0.11 - 0.35$ eV vs. $\simeq 1$ eV). Additionally, it is important to note that the sign of the values of E_B, *i.e.* $+$ and $-$ signify attraction and repulsion, respectively, in Table 3.6 only agrees with that of Yin et al.'s calculation when the calculation explicitly includes chemically adsorbed hydronium ions.

[11] Note that the surface potentials in Ref. [99] were measured using an ionizing electrode.

3.7 Chapter summary

1. Upon exposure of graphene to an electrolyte solution, an electric double layer of ions forms at the interface and extends out into the bulk of the solution as described by the modified Gouy-Chapman model.

2. The short-circuit current generated by the G-SCEEG can be used to determine the surface charge density induced in graphene by the hydrated ions of an electrolyte solution. The G-SCEEG, when subject to an external potential, can also be used to measure the capacitance per unit area of the capacitor that forms at the graphene-solution interface. The identity of adsorbed ion can be deduced from the sign of the short-circuit current.

3. The surface charge density is influenced by the species of the ion, the pH and ionic strength of the solution, and the presence of graphene multi-layers. The pH of the solution seems to be the most dominant factor, likely due to surface transfer doping between aqueous protons and graphene. The Cl^- anion in 6.0 M HCl induces the greatest surface charge density in both mono-layer graphene and graphene with regions of multi-layers.

4. The surface potential across the graphene-solution interface and the effective surface binding energy of ions adsorbed on graphene can both be calculated from the experimentally-determined values for the surface charge density and the capacitance per unit area.

... The mountains are dead stone, the people

Admire or hate their stature, their insolent quietness,

The mountains are not softened nor troubled

And a few dead men's thoughts have the same temper.

– Robinson Jeffers

4

Suspended, large-grain graphene

4.1 Chapter overview

This chapter details the fabrication and analysis of free-standing membranes of monocrystalline graphene. Despite being the strongest material ever measured [30], large areas of freestanding graphene are still fragile and difficult to manipulate because its atomic thinness and its inherent lattice defects leave it vulnerable to macroscopic tearing and rupturing. Additionally, although graphene is very rigid on a molecular scale, it becomes increasingly more pliable on length scales greater than a micron and is prone to folding and rolling up upon itself [101]. For these reasons

creating areas of freestanding graphene that are large enough to be experimentally accessible is a formidable challenge and is why graphene has commonly been studied while being placed upon another material. Such supporting substrates can reduce graphene's charge carrier mobility and dope it [102, 103]. They also preclude its use as a membrane for encasing, separating, or filtering different chemical species. Specifically, these membranes are becoming important as support films for transmission electron microscopy [104–106], as starting material for patterning various microscopic mechanical devices [107], and as ion-selective membranes for future filtration applications [108–110].

The difficulty involved in creating freestanding graphene has been well documented in the literature. Many previous studies have claimed varying degrees of success in suspending small areas (< 80 μm^2) of graphene [14, 30, 102, 111–113], whereas notably fewer studies have had success in suspending graphene over larger areas [104, 106, 114–116]. More difficult still has been the creation of large areas of freestanding graphene by transferring chemical vapor deposition (CVD)-grown graphene from the catalytic surface on which it is grown to a supporting substrate containing pits, trenches, or apertures [111, 114]. Most of this prior work has been limited by the use of either small areas (100 μm^2) of mechanically exfoliated monocrystalline graphene, or small grain sizes (80 μm^2) of polycrystalline CVD graphene. The choice of using either mechanically exfoliated or CVD graphene for creating suspended membranes plays an important role in the success and the ease of the fabrication process. Mechanically exfoliated graphene is attractive because it is less defective, and is hence less prone to tearing while unsupported, than CVD graphene. Its lack of defects and grain boundaries also ensures that its physical properties are relatively unperturbed. However, only small areas up to 100 μm^2 of exfoliated graphene are routinely attainable. This limits the total achievable freestanding area as well as prevents parallel and scalable membrane fabrication [117]. On the other hand, large areas of CVD graphene are usually polycrystalline and the prevalence of grain boundaries and the common need for harsh

post-synthesis transfer processes tend to weaken, and to eventually rupture, suspended membranes during the transfer [113]. The grain-boundary and transfer-induced defects also degrade graphene's unique electrical and thermal properties in freestanding membranes that do survive.

In this work, I, with help from T. Zhou, improved the probability and scalability of successfully suspending pristine mono- and multi-layer graphene on an insulating substrate and established the largest achievable freestanding area. We accomplished this by greatly reducing grain-boundary defects in CVD graphene and by optimizing commonly used wet and dry transfer methods. Based on recent advances in CVD graphene [118–120], I developed an improved CVD recipe for synthesizing continuous sheets (2×7 cm^2) of large grains (1 mm average diameter) of mono- and multi-layer graphene. With this advance we demonstrated that membranes can be suspended over arrays of apertures 5-30 μm in diameter (20–700 μm^2) in an insulating SiO_2/Si_3N_4 support substrate. We also demonstrated that optimized wet and dry transfer methods can be used to create suspended-graphene membranes with a similar area-dependent probability of success between 1–60%. We used optical microscopy, scanning electron microscopy (SEM), Raman spectroscopy, and electron diffraction (ED) to determine the presence and quality of the suspended graphene. Furthermore, because the large-grain CVD synthesis recipe I developed results in the formation of areas containing multi-layer graphene crystals, we also showed that individual crystals of bi- and tri-layer graphene can be successfully suspended over SiO_2/Si_3N_4 apertures up to 30 μm in diameter.

The 700 μm^2 areas of freestanding, pristine mono- and multi-layer graphene described below represent the current upper bound for suspended-graphene membranes formed by transferring graphene to an insulating substrate. This is of interest because large areas of freestanding graphene on insulating substrates are especially well suited for electromechanical resonator applications where electrically-isolated, freestanding graphene is essential and where investigators have shown that the resonance frequency and the quality factor of the graphene resonator

scale with the resonator's area [114, 121]. Graphene filtration and desalination devices made from arrays of freestanding membranes will also benefit from larger suspended areas of pristine graphene that are supported by electrochemically-inert substrates because the flux through such devices depends on both the number of defects in and the overall area of freestanding membranes [108, 109, 122]. Large-area, freestanding graphene membranes on insulating supports will also contribute to studies of graphene electrochemistry.

4.2 Fabrication and characterization of suspended membranes

Fabrication of suspended-graphene membranes begins with the synthesis of continuous sheets of large-grain, polycrystalline graphene grown on 25-μm thick copper foils using a home-built low-pressure CVD system (see Section A.1 in Appendix A for a complete description). The supporting, silicon-based substrate was fabricated by T. Zhou by creating 9×12 arrays of circular apertures in a 4 in. silicon wafer with a 300-nm thick capping layer of low-stress Si_3N_4. Each array was designed such that all 108 apertures are of identical diameter (either 5, 10, 20, 30 or 50 μm). Standard photolithography, reactive ion etch (RIE), and KOH silicon etch protocols were used to first create square, freestanding Si_3N_4 membranes and then to create circular apertures in those membranes. Finally, a 300-nm thick layer of SiO_2 was deposited on top of the Si_3N_4. SiO_2 was added to promote graphene adhesion [123] and to allow for the visualization of graphene on the substrate.

Multiple suspended-graphene membranes were created in parallel by transferring a 1×1.5 cm^2 section of graphene from Cu foil to a single 9×12 array of identically-sized apertures in the substrate. In order to assess the effect of the transfer method on the suspension yield, as well as to enhance the applicability of the fabrication methods, wet and dry graphene transfer methods were each separately developed and optimized. The wet transfer method that was developed is similar to one previously described [14] but was modified to contain three, 30 min. liquid CO_2-flush cycles during the critical point drying (CPD) step to more slowly and more gently reduce the surface tension across the suspended-graphene membranes after their MMA-polymer support layer had been removed (see Section A.2 in Appendix A for a complete description). The dry transfer method that was developed is similar to the method described by Suk et al [111]. It was deliberately modified, however, to improve graphene adhesion to the substrate by reducing the thickness of the PMMA-polymer support layer and by softening the PMMA layer using an acetone vapor

humidor prior to thermal PMMA removal. The method of Suk et al. was further modified by using ethanol to reduce the surface tension on the PMMA-supported graphene caused by residual H_2O that remained from the final rinsing step. This modification allows for a larger area of graphene to be transferred to the target substrate per transfer attempt by reducing surface tension-induced tearing of the PMMA-supported graphene (see Section A.2 in Appendix A for a complete description). The dry transfer method is of interest because it allows graphene to be transferred to hydrophobic substrates, to substrates that chemically react with H_2O, and to substrates containing wells or cavities without trapping pockets of H_2O.

Results from optical microscopy, SEM, and Raman spectroscopy analysis of successfully suspended graphene are shown in Fig. 4.1 (p. 168). Fig. 4.1 (**a**) is a grayscale optical image of graphene suspended over a 30-μm aperture using the wet transfer method. Inside the aperture, the lack of contrast indicates the suspended area is free of tears, particles, large areas of residual polymer contamination, and multiple graphene layers. A single Raman spectrum taken at the center of the aperture is shown in Fig. 4.1 (**b**). All Raman data were taken with laser excitation photon energy of 2.33 eV at 8 mW and a laser spot size of 1-2 μm. The shape, spectral position, and relative intensity of the G and G' peaks indicate that the graphene is monolayer. The D peak is nearly absent, confirming that the graphene is pristine with very few defects. For further confirmation of the uniformity of monolayer graphene over the entire aperture, a Raman area scan was taken. Fig. 4.1 (**c**) shows the resulting map of the Raman shift of the G' peak. Inside the aperture the Raman shift is fairly constant and is centered at 2665 cm^{-1}. Outside the aperture, the presence of the supporting SiO_2/Si_3N_4 substrate causes the G' peak to mostly blue shift to 2675–2680 cm^{-1}, although small regions of red shifting are also observed. These results are typical for most of the membranes that were made.

In addition to the suspended-graphene membranes being uniform, it is assumed that they are very likely mono-crystalline because the area of the average graphene crystal in the polycrys-

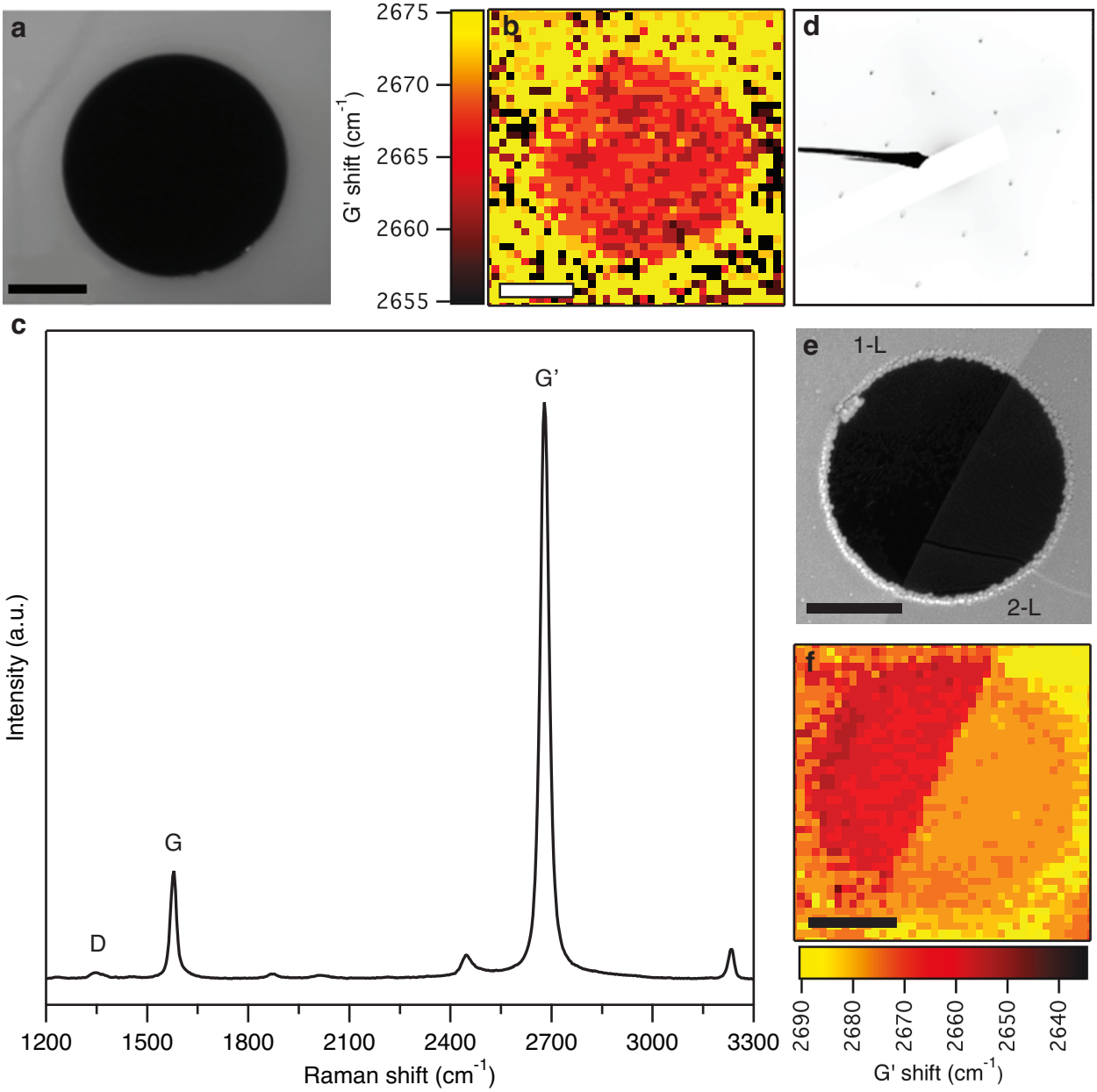

Figure 4.1: Optical, Raman, SEM, and electron diffraction (ED) analysis of suspended-graphene membranes. **a**, Grayscale optical microscope image of freestanding, mono-layer graphene over a 30-μm diameter aperture (scale bar: 10 μm). **b**, Spatial Raman map of the same graphene membrane showing the Raman shift of the G' peak over the entire 30-μm aperture (scale bar: 10 μm). **c**, Raman point spectrum taken at the center of the 30-μm aperture. **d**, ED pattern of a 10-μm diameter suspended mono-layer graphene membrane recorded using a 5-μm spot size (200 kV). **e**, SEM image of a 10-μm diameter suspended-graphene membrane bisected by the edge of a bi-layer graphene crystal. 1-L and 2-L denote the graphene layer number (scale bar: 3 μm). **f**, Spatial Raman map of the bisected membrane highlighting the difference between the G' peak Raman shift of the mono-layer and bi-layer regions (scale bar: 3 μm). For the Raman data, laser excitation photon energy = 2.33 eV at 8 mW and laser spot size = 1–2 μm.

talline sheet is at least 10^3 times larger than the area of the largest aperture. This assumption was confirmed using electron diffraction (ED). Fig. 4.1 (**d**) shows the electron diffraction pattern of monolayer graphene suspended over a 10-μm aperture. The diffraction pattern was taken at low magnification with a 5-μm diameter beam spot size and an acceleration voltage of 200 kV. The diffraction pattern indicates that the suspended graphene is indeed mono-crystalline because only one set of hexagonal spots with constant intensity is observed. Additionally, it shows that the graphene is pristine because the spots are clearly defined with only a very small amount of amorphous diffraction from contaminants and adsorbates. This is in contrast to the data presented by Zhou et al [118]. As part of their CVD graphene synthesis work, they demonstrated single crystals of graphene over many 100×100 μm^2 windows in an amorphous carbon film TEM grid. While no description is provided for how the graphene was transferred to the grid or whether the graphene is truly freestanding, the amorphous diffraction in the electron diffraction patterns and the areas of dark contrast in the bright-field TEM images they provide suggest that the graphene is in contact with either the amorphous carbon film on the grid or a separate amorphous film such as a polymer resist. One or both of these films is likely helping to support the graphene crystal. During the course of this work, T. Zhou attempted to suspend pristine mono-crystalline graphene over many 90×90 μm^2 windows in a molybdenum TEM grid using the optimized wet transfer technique, but all suspended areas ruptured after the removal of the polymer support layer and the subsequent CPD step.

With the CVD synthesis protocol I developed I was also capable of forming regions of multilayer graphene, which allowed for the fabrication of suspended multilayer graphene membranes. The ability to synthesize multilayer graphene crystals is advantageous because it eliminates both the need to transfer monolayer graphene multiple times to form multilayers and the contamination and defects that multiple transfers produce. The size of the multilayer grains (50–200 μm) as well as the contrast difference on SiO_2 between areas with differing numbers of graphene lay-

ers allowed for facile identification of the layer number (up to 5–6 layers) using either optical microscopy or SEM. An example of a 10 μm aperture spanned by both mono- and bi-layer graphene is provided in the SEM image of Fig. 4.1 (**e**). This membrane was created using the dry transfer method and the number of layers has been labeled as 1-L and 2-L. Fig. 4.1 (**e**) shows that the aperture is bisected by the edge of a bilayer graphene crystal with the left half consisting of monolayer graphene and the right half of bilayer graphene. The lack of particles and residual contamination helps confirm that the membrane is pristine. The line in the lower portion of the bilayer region is likely the result of a fold in the membrane. In the Raman map of Fig. 4.1 (**f**), which plots the Raman shift of the G' peak over the entire bisected aperture, a clear blue shift is seen when moving from the left mono-layer region (2665 cm^{-1}) to the right bi-layer region (2675–2680 cm^{-1}) as is expected [69, 124].

4.3 Yield of suspended membranes

Fig. 4.2 (p. 172) shows a plot of the suspension yield for the wet transfer method as a function of aperture diameter. graphene suspension was attempted over arrays of circular apertures with diameters of 5, 10, 20, 30, and 50 μm. As previously mentioned, graphene was transferred to a single 9×12 array of apertures at a time and all apertures in a given array had the same diameter. A yield, i.e. a probability of success expressed as a percent, was calculated for each array of apertures to which graphene was transferred. This was done by dividing the number of apertures that contained an intact freestanding graphene membrane after the polymer support layer had been removed by the total number of apertures that were initially covered by polymer-supported graphene. Because polymer-supported graphene is fairly resistant to tearing and can be suspended over areas of several square centimeters, we only observed tearing and rupturing of suspended-graphene membranes after the removal of this support layer. The total number of suspensions attempted in parallel per graphene transfer was typically between 95-105 due to some difficulty in initially covering all 108 apertures. Both optical microscopy and Raman spectroscopy were used to verify the presence and layer number of suspended graphene over each aperture. Because 10–20% of the area of the continuous graphene sheets on Cu contain multilayer crystals, we make a distinction between total suspension yield, i.e. the total number of apertures with either suspended mono- or multi-layer graphene, and mono-layer suspension yield, i.e. the total number of apertures with only monolayer graphene. Total suspension yield decreases from 62% for 5-μm diameter apertures to 13% for 30-μm apertures. We attempted suspending graphene over 50-μm apertures using this method, but we were unsuccessful. It is apparent from these yield data that as aperture diameter increases, the percentage of the total suspended-graphene membranes that are multi-layer tends to also increase. Despite variations in the amount of multi-layer areas between each piece of graphene transferred, this trend suggests that multi-layer membranes are more read-

ily suspended over larger apertures than are monolayer membranes. It is important to note that the CPD step is critical for the success of the wet transfer method. The total yield for 10-μm diameter apertures decreases from 44% to 7% if this step is omitted.

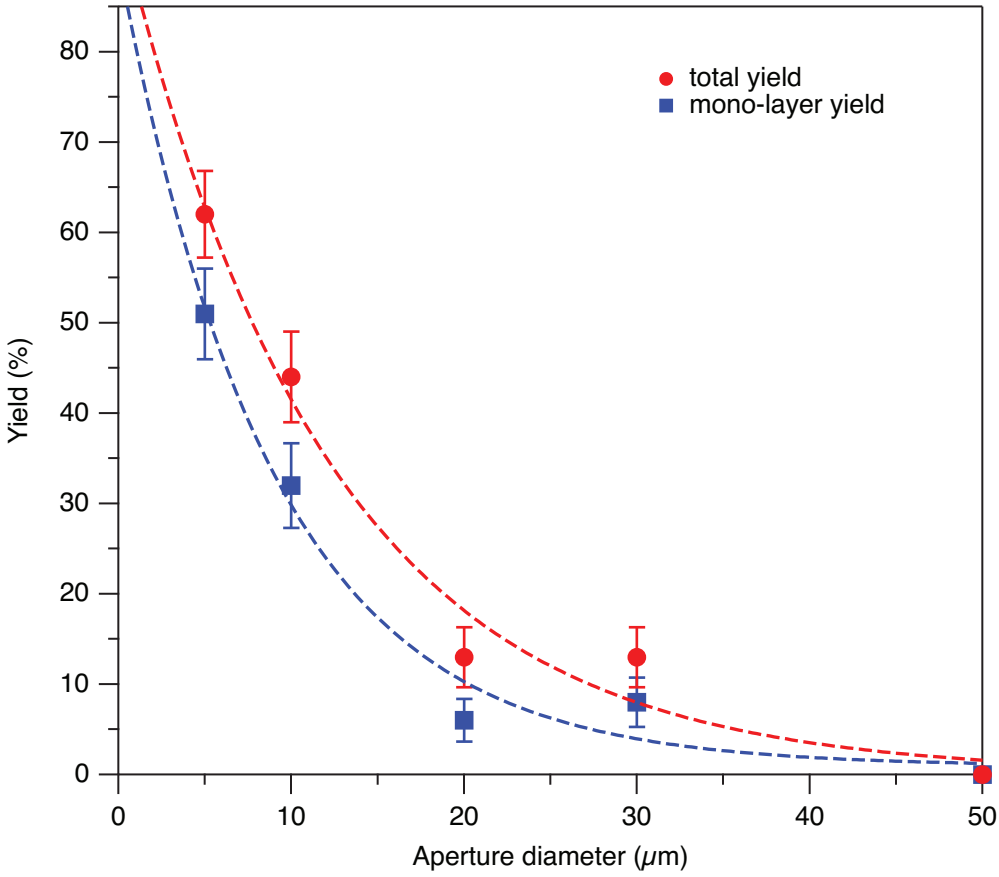

Figure 4.2: Suspended-graphene fabrication yield for the wet transfer method as a function of aperture diameter. Each red dot represents the total suspension yield (mono-layer + multi-layer graphene membranes) for a single array of 108 apertures, whereas each blue dot represents only the monolayer membrane yield for the same array. The red and blue dashed lines represent decaying exponential functions that have been fitted to the total and mono-layer yield data, respectively. Error bars depict standard deviations that were calculated by assuming that each aperture of an array represents an identical and independent attempt at forming a graphene membrane and that the probability of successfully suspending multiple membranes in parallel follows a binomial distribution.

Due to the relative complexity of the dry transfer method, it was used only to suspend graphene over 10- and 30-μm diameter apertures. The total suspension yield for the dry transfer method

for 10- and 30-μm apertures was 33% (15/46) and 1% (1/93), respectively, whereas the monolayer suspension yield was 28% (13/46) and 1% (1/93), respectively. Reducing the PMMA thickness and adding an acetone vapor PMMA softening step were determined to be crucial for successfully suspending graphene using this method, as graphene adhesion to the substrate was very poor otherwise (see Experimental section). Although both wet and dry transfer methods gave somewhat similar yields for 10-μm apertures (44% for the wet transfer vs. 33% for the dry transfer), the wet transfer yield was more than an order of magnitude greater than the dry transfer yield for 30-μm apertures (13% vs. 1%).

Overall, the wet transfer method produced consistently higher yields and was easier to implement than the dry transfer method. The results show that key steps in each of the transfer processes can greatly affect the yield of suspended-graphene membranes, but that membranes can nevertheless be successfully fabricated using either method. The intrinsic strength of large grain, mono-crystalline graphene is likely a major reason for this robustness. Comparing our data to the data reported by Suk et al. [111], we found that our yield for 5-μm diameter apertures (62%) was more than double their best yield for 5.1-μm diameter wells (26%) and that our yield for 30-μm apertures (13%) was similar to their best for 7.3-μm wells (13%). The reduction of grain-boundary defects and the optimization of the graphene transfer methods were likely responsible for this improvement. Although we only attempted to form freestanding graphene membranes over circular apertures in SiO_2/Si_3N_4, apertures of different geometries will likely reduce suspension yields because of the decreased axial symmetry of non-circular geometries.

4.4 Raman analysis of multi-layer suspended membranes

Despite the presence of some multi-layer grains containing > 7 layers in the polycrystalline graphene sheets, we observed suspended multi-layer graphene membranes with only bi- and tri-layers. Fig. 4.3 (**a**) shows a typical grayscale optical microscope image of a tri-layer region of graphene that is completely spanning a 10-μm aperture (the number of layers has again been labeled as 1-L, 2-L, etc.). A comparison of the Raman point spectra of suspended mono-, bi-, and tri-layer graphene over separate 10-μm apertures is given in Fig. 4.3 (**b**). Traces labeled as "bi-layer a" and "bi-layer b" represent Raman spectra that were observed for two different and distinct bi-layer membranes. The differences in the bi-layer spectra are likely caused by differences in the stacking order of the bi-layers, as CVD grown graphene often produces bi-layers that are randomly rotationally disordered [125, 126]. The changes in the G and G' bands for the different graphene types are explicitly shown in Fig. 4.3 (**c**) and (**d**), respectively. As expected, the energy and width of the G band change only slightly for the different types of multi-layers, with bi-layer b displaying the largest red shift compared to mono-layer graphene. The G' band, however, shows appreciable blue shifting and a slight peak narrowing, except in the case of the bilayer b trace which exhibits a broadening of the G' band.

To demonstrate the significance of the change in the G' band energy in identifying multilayer graphene, density histograms of the distribution of the G' band energy over the suspended graphene area for mono-layer, bi-layer a, bi-layer b, and tri-layer membranes are plotted in Fig. 4.4 (**a**). Each histogram represents data from an individual 10-μm membrane and each has been fitted with a normal distribution. To exclude changes caused by the surrounding SiO_2/Si_3N_4 substrate, the histograms include only those scan points that are within a 4-μm radius of the center of the aperture. A clear separation is seen between the distributions for the mono-layer and the multi-layer graphene membranes ($\Delta\omega$ = 13–30 cm^{-1}), which allows mono-layer graphene to be readily

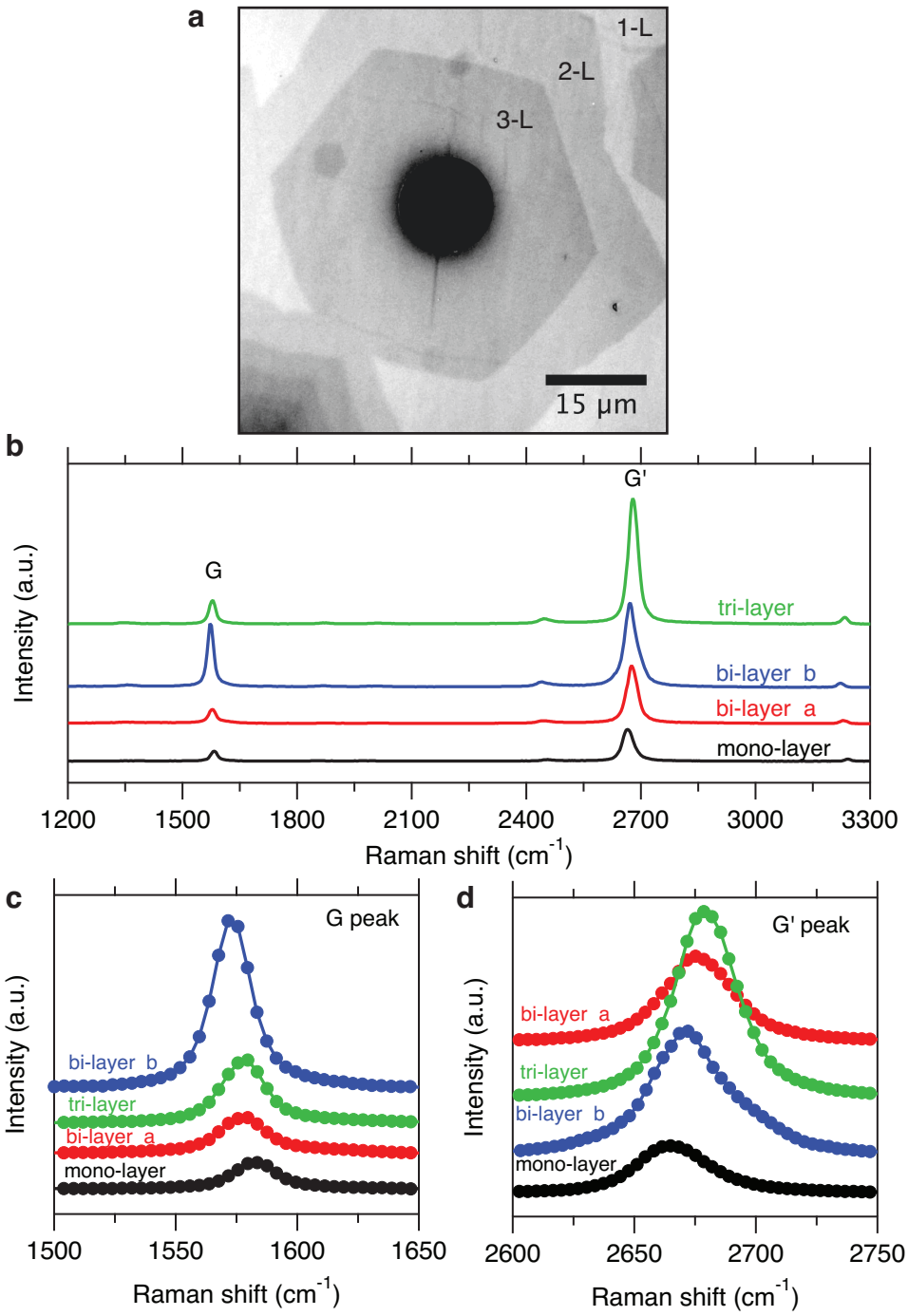

Figure 4.3: Suspended multi-layer graphene membranes and Raman analysis. a, Grayscale optical microscope image of tri-layer graphene suspended over a 10-μm aperture. 1-L, 2-L, and 3-L denote the graphene layer number. **b**, Comparison of Raman point spectra for suspended mono-, bi-, and tri-layer graphene. Bi-layer a and bi-layer b are two separate and distinct bi-layer membranes, likely exhibiting differing degrees of inter-layer rotational misalignment. The relative changes in the G and G' bands as a function of graphene type are emphasized in (**c**) and (**d**), respectively. For the Raman data, laser excitation photon energy = 2.33 eV at 8 mW and laser spot size = 1–2 μm.

distinguished from multi-layer graphene. Because the magnitude of the G' blue shift for multi-layer graphene depends on both the layer number and on the relative stacking orientation between the individual mono-layers, however, neither the layer number nor the stacking orientation can be determined by the shift alone [69].

In addition to the change in energy of the G' band, the shape of the band also provides information regarding the stacking order of multi-layer graphene [124]. Fig. 4.4 (**b**) gives the results of a Lorentz distribution fit to the G' band for (i) monolayer, (ii) bi-layer a, (iii) bi-layer b, and (iv) tri-layer membranes. All the traces were best fitted with a single Lorentzian peak, except for the bi-layer b trace, which was fitted with two Lorentzian peaks. For each of these multi-layer membranes, this demonstrates that the multi-layer graphene exhibits rotational misalignment between its individual mono-layers [69,127]. All of the suspended multi-layer graphene membranes that we examined showed this inter-layer rotational misalignment. Taken together, the shape of the G' peak, the change in energy of the G' band, and the optical micrographs allowed us to identify the number of graphene layers present in each membrane as well as to classify the rotational order between the layers of multi-layer membranes.

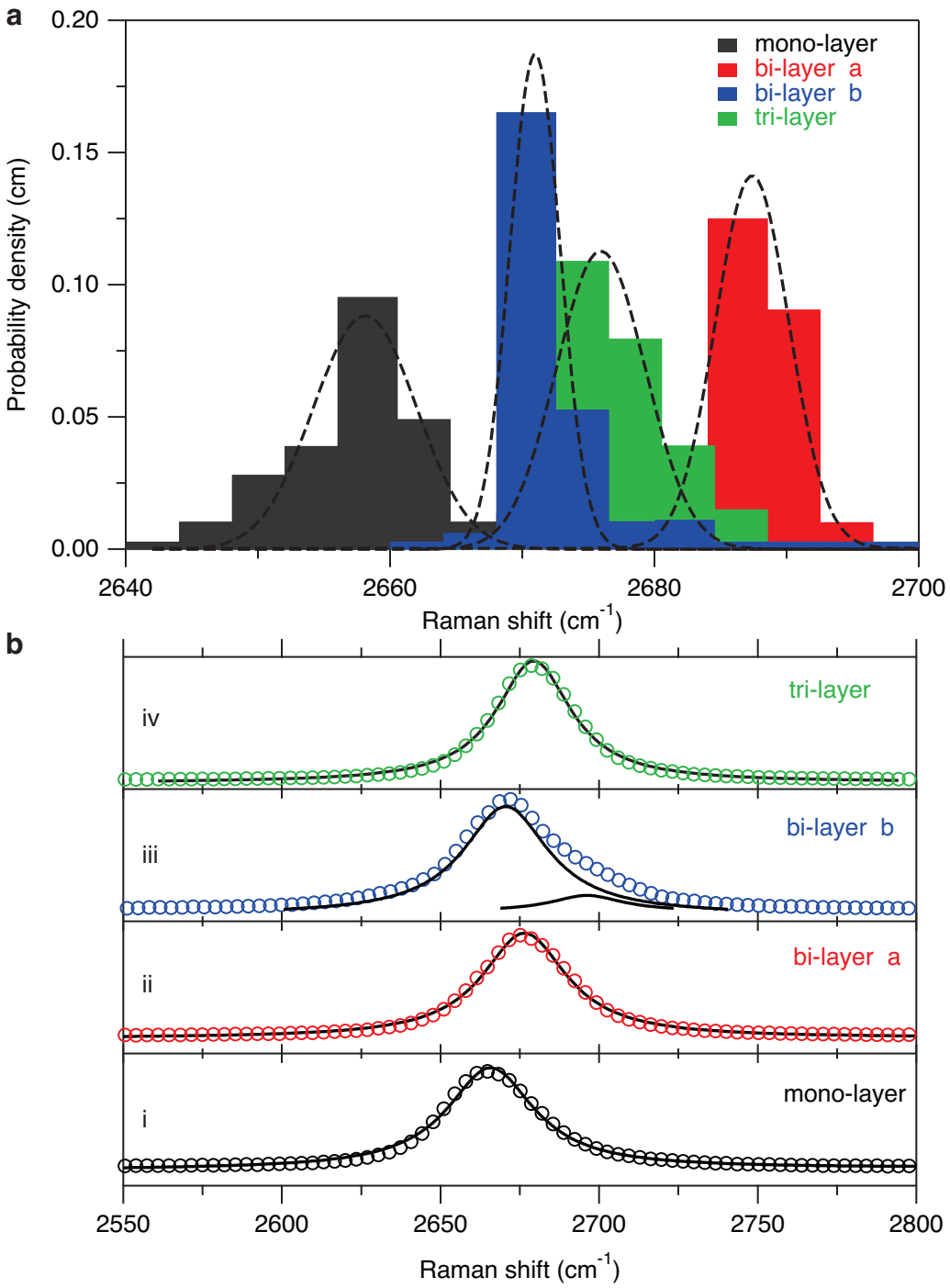

Figure 4.4: Further Raman analysis of suspended-graphene membranes. a, Density histograms of the distribution of the G' Raman shift over the suspended region for different graphene membranes. A normal distribution has been fitted to each histogram. **b**, G' peak shape for different suspended-graphene membranes: mono-layer (i), two different bi-layer (ii) and (iii), and tri-layer (iv) membranes. Black traces show the fitting of one [(i), (ii), and (iv)] and two (iii) Lorentz distributions to the data. These fits suggest that the multi-layer membranes exhibit inter-layer rotational misalignment. For the Raman data, laser excitation photon energy = 2.33 eV at 8 mW and laser spot size = 1–2 μm.

4.5 Chapter summary

In summary, we were able to demonstrate that the probability and scalability of creating pristine, freestanding mono- and multi-layer graphene membranes on an insulating substrate can be significantly enhanced as a result of an advanced CVD synthesis recipe and the optimization of common transfer methods. Optical microscopy, SEM, Raman spectroscopy, and ED characterizations of the suspended membranes prove their continuous and pristine nature. The fact that both wet and dry graphene transfer methods can be used to successfully suspend graphene with roughly similar yields improves the applicability and throughput of these methods and reduces the overall difficulty involved in membrane fabrication.

Although freestanding-graphene membranes as large as 700-8,000 μm^2 in area have been previously reported [104, 106, 114–116], these membranes have largely been limited to metallic support substrates that restrict the utilization of graphene's superior electrical properties and prevent the use of the membranes in environments that are incompatible with most metals, such as aqueous electrolyte solutions. Similarly, prior work describing large-area freestanding graphene on non-metallic support substrates has been limited by low yields, grain-boundary defects, and harsh fabrication conditions that chemically modify graphene [106, 114]. To my knowledge this work describes the largest suspended areas of pristine single crystals of intact and chemically unmodified, mono- and multi-layer graphene on insulating substrates yet reported. This work will be especially beneficial for using graphene as an electromechanical resonator, an electron microscopy support film, an electrochemical trans-electrode, and a desalination filtration membrane.

There are no lines in nature, only areas of color, one against another.

Edouard Manet

5

Trapping and repelling DNA

5.1 Chapter overview

Results from preliminary experiments aimed at electrostatically trapping DNA on, repelling DNA off, and moving DNA along graphene are provided in this chapter. As previously stated in Chapter 1, the goal was to overcome several limitations of using graphene nanopores for DNA sequencing, namely to reduce both the magnitude of and the thermally-induced fluctuations in the velocity of DNA as it translocates a graphene nanopore and to find a way to ratchet DNA through the pore a single nucleotide at a time.

5.2 Trapping DNA on and repelling DNA from graphene

The device used as a DNA trap is shown in Fig. 5.1. To make the device, a 1×1 cm piece of standard, CVD-grown graphene was transferred, using the wet transfer method, to a borosilicate-glass microscope coverslip such that it overlapped the Ti/Au (5/100 nm thick) metal contacts that had been evaporated on the glass' surface. Oxygen plasma was used to etch away an area of graphene from one Au contact. Silver paste was used to connect the metal contacts to an external power supply. A microfluidic channel (length = 2 mm, width = 50 μm, depth = 100 μm) made from polydimethylsiloxane (PDMS) was placed across the device such that it overlapped both Au contacts and the graphene.

The device was placed on an inverted spinning-disk confocal fluorescence microscope with an electron-multiplying charge-coupled device (EM-CCD) camera. To better visualize the edge of the graphene and the DNA a TE buffer solution, *i.e* 10 mM Tris and 1 mM EDTA at pH 7.5, containing diluted (1:1000) YOYO-1 dye was added to the channel. Due to quenching of the dye by the graphene, the graphene appeared dark when observed through the fluorescence microscope whereas the bare glass appeared bright.

Molecules of fluorescently-labelled single-stranded DNA (5.3 kb) were added to the solution on the side of the channel without graphene. The DNA was specifically labeled with the fluorescent dye AlexaFluor 488 by covalently bonding it to guanosine residues. The DNA was slowly driven into the microfluidic channel using hydrostatic pressure. Once the DNA reached the edge of the graphene, the graphene was biased to +5 V relative to the buffer solution for 60 s. This created what appeared to be an electroosmotic flow in the solution and trapped the negatively charged DNA molecules on the graphene's surface. To repel the DNA, the graphene was biased to -5 V for 60 s. Micrographs in Fig. 5.2 show the results of the experiment. Part (**a**) is the edge of the graphene before the bias was applied. Part (**b**) is the same region after applying +5 V for

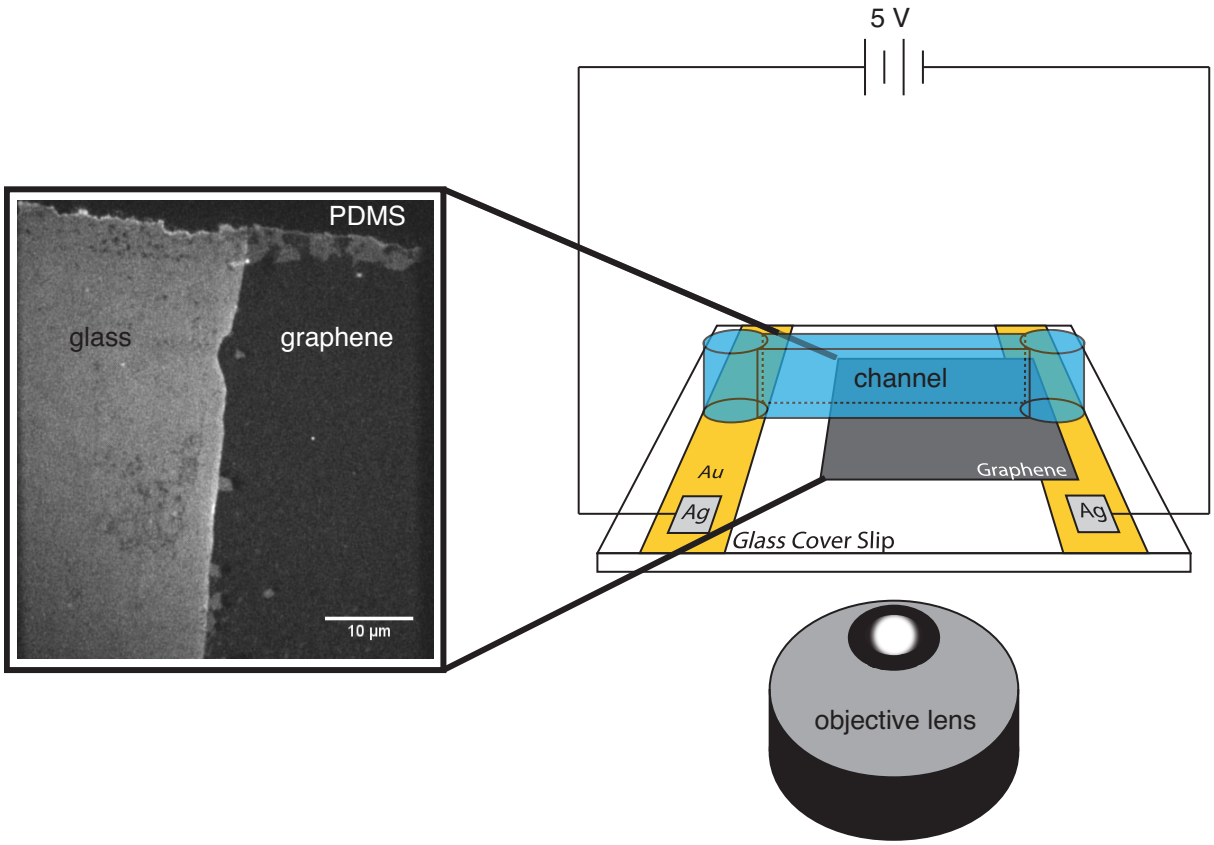

Figure 5.1: Trapping and repelling DNA from graphene. Fluorescence image of graphene on a glass cover slip (left). The contrast between the glass and the graphene is given by the fluorescence dye, YOYO-1. The dye is quenched on the graphene making it dark. DNA trapping device fabricated on a glass cover slip (right). One half of the graphene was then removed by O_2-plasma etching.

60 s. As evident by the white spots of bright contrast, DNA was successfully trapped on the surface of the graphene and remained on the surface after the bias was discontinued. Part (**c**) shows the adsorbed DNA that remained after a trapping event and Part (**d**) shows the same region after applying a -5 V for 60 s. Although not all the visible DNA molecules were desorbed by the negative bias, most of the molecules were repelled. Strong van der Waals interactions between the graphene and the single-stranded DNA were thought to prevent all the DNA molecules from desorbing.

Despite the success of trapping and repelling DNA electrostatically using graphene, this method is likely unsustainable because of the large voltages that are required. Biasing graphene to voltages over ± 2 V relative to an aqueous solution runs the risk of initiating electrochemical reactions to occur between the solution and the graphene. Because of graphene's extreme thinness, any uncontrolled chemical reactions on its surface are likely to destroy it.

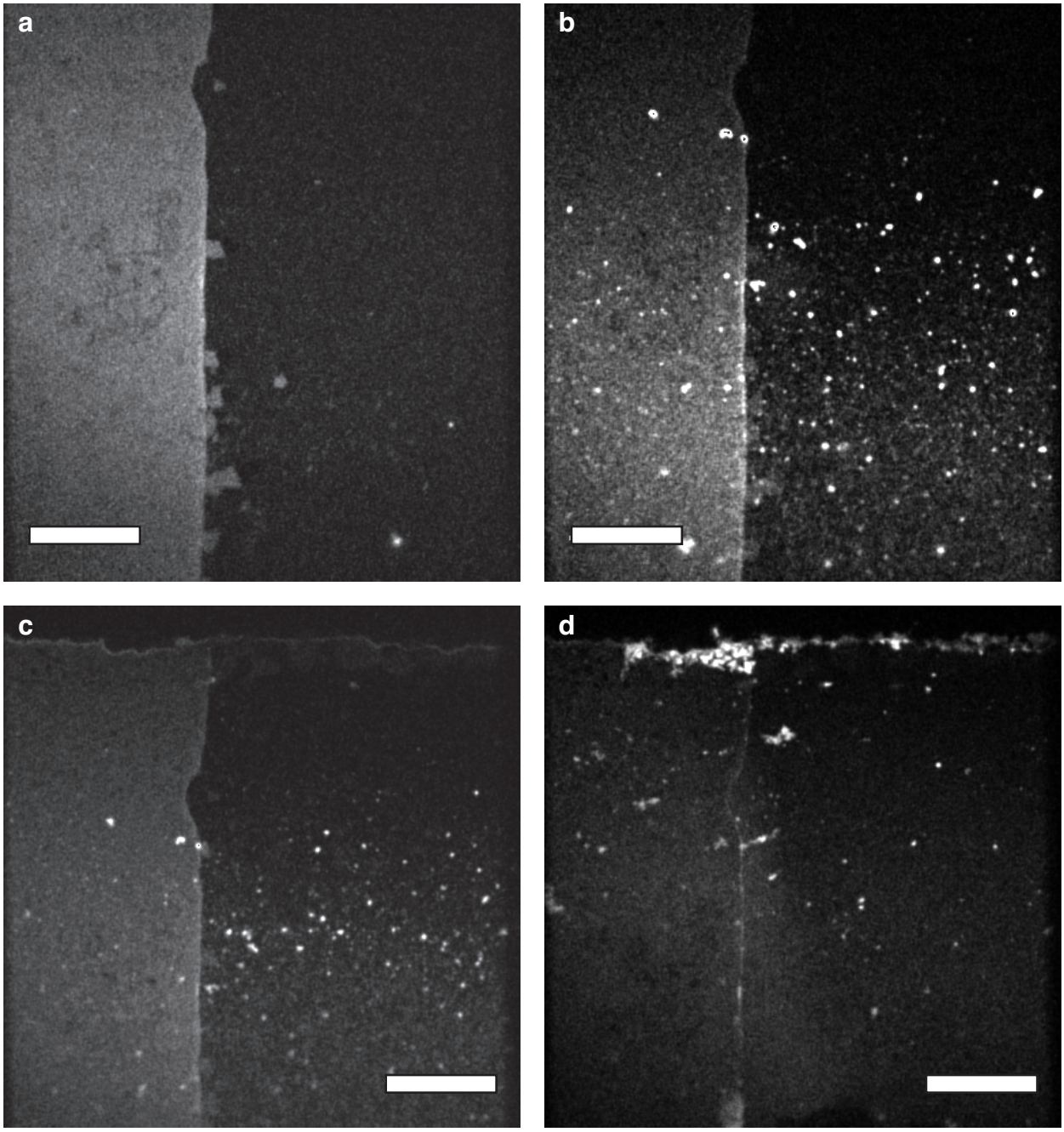

Figure 5.2: Fluorescence micrographs of DNA on the graphene trap. **a**, The graphene trap before applying a bias to it. **b**, The graphene trap after applying +5 V for 60 s. White spots are 5.3 kb single-stranded DNA molecules labeled with YOYO-1 and AlexaFluor 488 dyes (covalently bonded to guanosine residues). **c**, DNA molecules (white spots) adsorbed on the graphene trap after being electrostatically attracted to it. **d**, The graphene trap after applying V = -5 V bias to it for 60 s. A significant fraction of the DNA molecules have been repelled from the graphene surface. Scale bars: 10 μm.

5.3 Moving DNA along graphite with hydrostatic pressure

In addition to trapping and repelling DNA using graphene, the motion of DNA as it was driven over the surface of a freshly-cleaved piece of highly-oriented pyrolytic graphite (HOPG) was also analyzed. The device used for observing the motion of single-stranded DNA (ssDNA) was similar to that shown in Fig. 5.1. Instead of a PDMS microfluidic channel, however, a channel was etched into the glass coverslip using photolithography. The channel's dimensions were: length $= 2$ mm, width $= 50$ μm, and depth $= 1$ μm. A PDMS cap containing the HOPG flake was then added over the top of the channel. Molecules of single-stranded DNA (ϕ-X174) that had been specifically labeled with three CdSe-ZnS quantum dots using short complementary strands of oligonucleotides and an avidin-biotin linker were added to one side of the channel. Hydrostatic pressure was used to drive the molecules towards and along the HOPG flake. The motion of the molecules was recorded using the inverted spinning-disk confocal fluorescence microscope.

Fig. 5.3 is a composite fluorescent micrograph showing the trajectory of a single molecule of ssDNA as it tumbled across an HOPG flake through positions 1 to 11. The time lapse between each position was 380 ms. Spots of bright contrast corresponding to the labelled DNA have been circled in red to help distinguish them from the background. At several positions, three separate spots of bright contrast can clearly be seen. This images proves that it is possible to drive a molecule of ssDNA across a graphene-like surface.

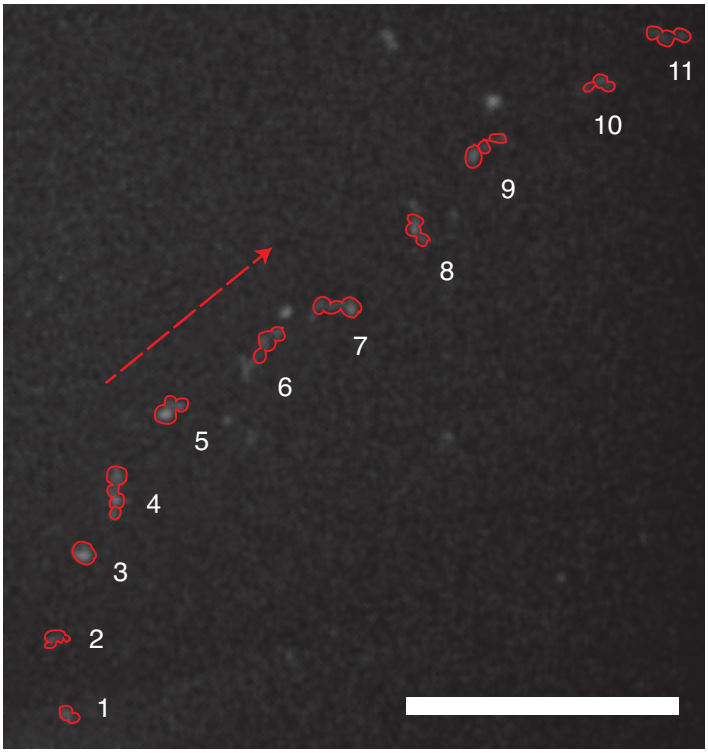

Figure 5.3: ssDNA tumbling along the surface of HOPG. A composite fluorescent micrograph of a single molecule of ϕ-X174 ssDNA, specifically labeled with three CdSe-ZnS quantum dots, tumbling along the surface of a freshly cleaved piece of HOPG. ssDNA motion from position 1 to 11 is a result of pressure-driven fluid flow. Time lapse between adjacent positions $= 380$ ms. Scale bar: 10 μm.

5.4 Linearization of DNA on graphene

Finally, Fig. 5.4 shows that DNA can be linearly stretched across graphene simply by flowing DNA over the surface of graphene using hydrostatic pressure.

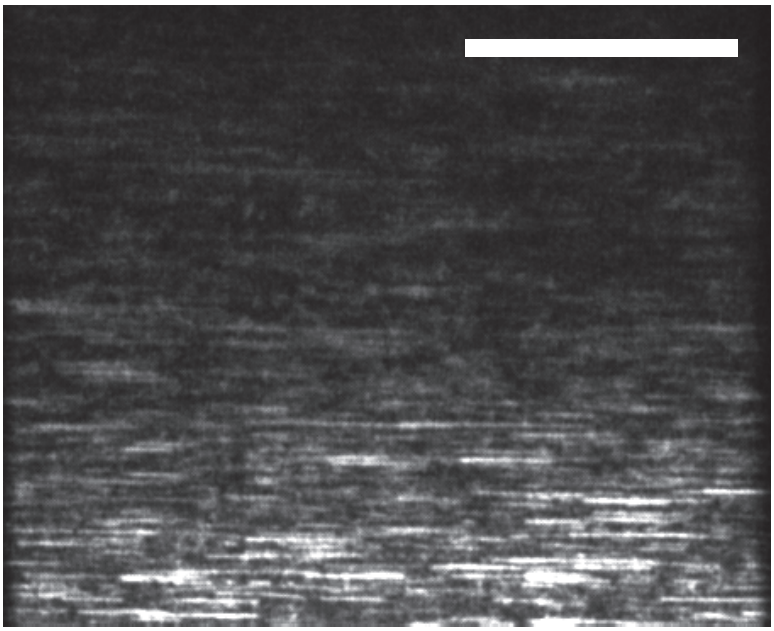

Figure 5.4: Adsorbed dsDNA on graphene. A fluorescent micrograph of dsDNA molecules, labeled with YOYO-1 dye, adsorbed on graphene in parallel rows along the direction of fluid flow, i.e left to right. Scale bar: 10 μm.

As to methods there may be a million and then some, but principles are few. The man who grasps principles can successfully select his own methods. The man who tries methods, ignoring principles, is sure to have trouble.

– Ralph Waldo Emerson

6

Unique Methods

6.1 Chapter overview

The two unique methods that were developed during the fabrication of the G-SCEEG devices are detailed in this chapter. Those methods are: the synthesis of large-grain graphene, both with and without multi-layers, on copper (Cu) foil using low-pressure chemical vapor deposition (CVD); and the transfer of CVD-grown graphene from Cu foil to hydrophobic, octadecyltrichlorosilane (OTS)-coated substrates. The development of these methods was based in part on the methods described in Refs. [118], [119] , [128] (synthesis) and [111] (transfer). In each case, the meth-

ods were significantly altered in order to optimize the successful fabrication of the G-SCEEG devices.

6.2 Synthesis of large-grain graphene using chemical vapor deposition

The work described in this section was motivated by the need for large areas ($\simeq 1$ cm^2) of high quality, *i.e.* defect free, mono-layer graphene. Although graphene isolated from exfoliated graphite has been shown to be exceptionally free of defects, multi-layers, and contaminants, it is difficult to obtain in areas greater than 100 μm^2 [117]. Not only does this prevent the use of high quality graphene in macroscopic experiments, it also makes it difficult to fabricate a scalable number of graphene-containing devices. Alternatively, CVD-grown graphene can be easily synthesized over large areas. The uncontrollable presence of multi-layers and grain-boundary defects, however, has been a persistent problem for CVD-grown graphene and has been blamed for its inferior physical properties [129].

The two CVD protocols presented here for synthesizing large-grain graphene significantly reduce the number of multi-layers and grain boundaries, thus allowing for the use of high-quality graphene in experiments requiring areas ≥ 1 cm^2. Because contamination has been shown to preferentially adhere to grain boundary defects [130], these protocols also produce a cleaner graphene surface by reducing the number of such defects. Furthermore, one of the protocols described in this section demonstrates that the method of chemical vapor deposition is capable of synthesizing continuous sheets ($\simeq 2 \times 5$ cm^2) of polycrystalline, mono-layer graphene, with an average grain size of $\simeq 2$ mm, on copper foil with negligible amounts of multi-layers. Results from several recent studies on CVD graphene growth were used to develop these protocols [118, 119, 128].

Based on these studies and on empirical evidence, it was determined that the main factors that control the synthesis of millimeter-scale grains are: the concentration of the carbonaceous source gas (controls the reaction rate and the number of nucleation sites); the flow rate of the gaseous

reactants (controls the reaction rate); the pressure inside the quartz reaction tube (controls the reaction rate); the temperature of the reaction (controls the reaction rate and the number of nucleation sites via sublimation of Cu); the duty cycle of the pulsed flow of the carbonaceous source gas (controls the amount of multi-layer graphene that forms); and the reaction time (controls the total amount of graphene that is synthesized). Below is a summary of the hypotheses that helped motivate and inform the development of the graphene synthesis protocols. Included on p. 190 is an illustration (Fig. 6.1) of the CVD setup that was used to test several of the hypotheses.

6.2.1 Hypotheses of graphene synthesis via CVD

1. Grain boundaries degrade graphene's electronic properties and attract contaminants [128–130].

2. CVD graphene synthesis is thought to begin with the catalytic decomposition of a carbonaceous gas, *e.g.* methane, ethylene, etc., by Cu (or another transition metal like nickel) into an activated carbon atom and H_2 gas. Activated carbon atoms adsorb onto the Cu and diffuse along the surface until they take part in the synthesis reaction by reaching either a nucleation site or a nascent graphene crystal. Cu is believed to also help catalyze the reaction between nascent graphene crystals and activated carbon atoms [119].

3. Reducing the density of nucleation sites on copper during the synthesis of CVD graphene leads to larger grain sizes. Nucleation-site density can be reduced by preserving the catalytically-inactive native oxide layer on the copper surface and by using a dilute concentration of the carbonaceous reactant gas. Desorption of carbon atoms from the Cu surface and sublimation of Cu also help to suppress nucleation site density [118–120].

4. Reducing the surface roughness of the Cu foil by electrochemically polishing it reduces the density of graphene nucleation sites [119].

5. Graphene grains can be made larger through controlled sublimation of copper surface layers that contain nucleation sites and/or small nascent graphene crystals [119].

6. Multilayers form when one or more layers of graphene traps reactive carbon species in defects on the copper surface. Once trapped, the carbon diffuses to a nucleation site where it nucleates the growth of a new graphene grain underneath the existing one [128].

7. The growth of multilayers can be suppressed by pulsing the carbonaceous reactant gas. This allows nearly all of the activated carbon species to be added to the edges of nascent graphene crystals before becoming trapped by them in surface defects [128].

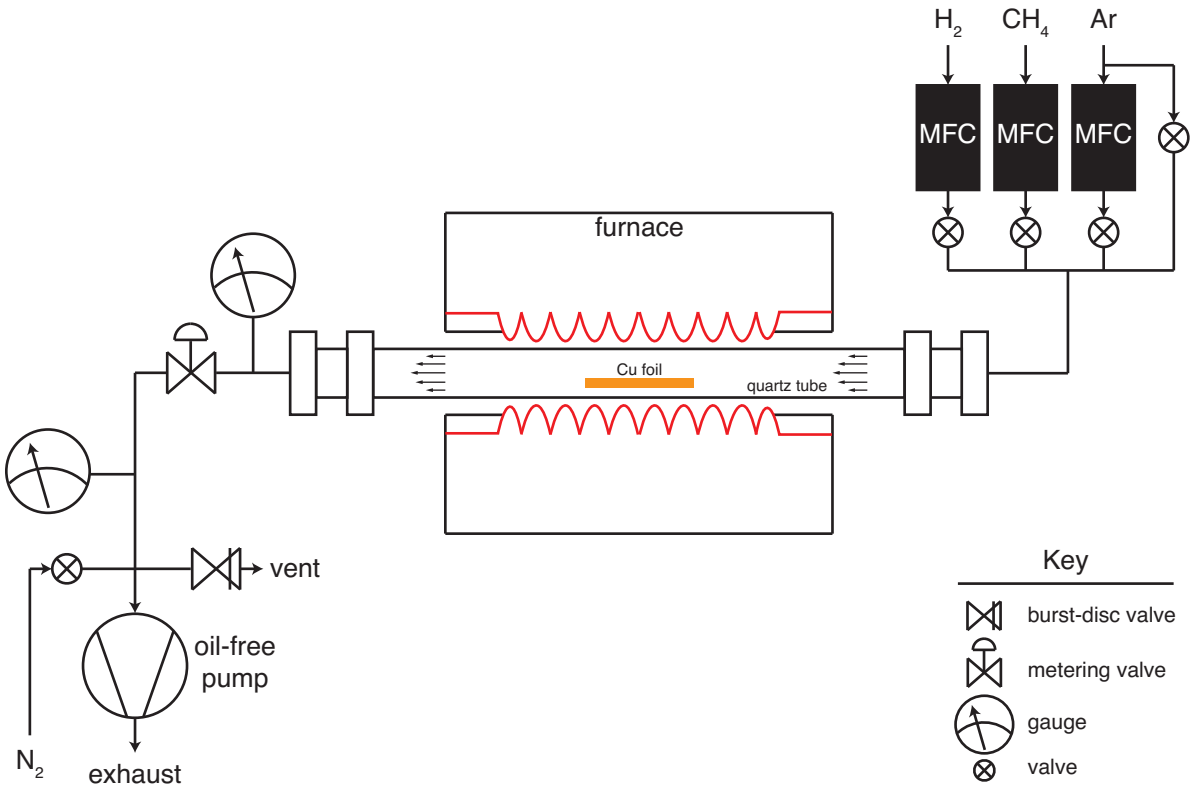

Figure 6.1: Low-pressure CVD setup. Illustration of the low-pressure CVD setup that was used for graphene synthesis. MFC stands for 'mass flow controller'. Not shown is the computer that controls the settings of the MFCs such as the flow rates and whether the internal valve is open or closed.

6.2.2 Protocol for synthesizing graphene with multi-layer regions

The protocol I developed for synthesizing continuous sheets of polycrystalline graphene, consisting of single grains between 200–3500 μm in diameter, on Cu foils using low-pressure chemical vapor deposition is a modification of the protocol described by Zhou et al. in Ref. [118]. Several modifications were made to ensure that a continuous sheet of large-grain graphene forms over the entire Cu foil surface. Those modifications include optimizing both the flow rate of the precursor gases and the synthesis reaction time as well as bending the Cu foil such that the bottom of the foil is 0.5 cm from the bottom of the quartz reaction tube during synthesis. I found that having the Cu foil in close proximity to the bottom of the tube was critical for forming a continuous graphene sheet on the bottom side of the foil. This is likely because of an increase in Cu vapor pressure and a decrease in gas flow velocity near the tube's wall. An illustration of the low-pressure chemical vapor deposition setup that was used to synthesize graphene is shown in Fig. 6.1.

The exact synthesis protocol is as follows:

1. A strip of 25-μm thick Cu foil (Alfa Aesar, 99.8%), 2×7 cm^2 in area, is first washed in 1 M HCl for 5 min., then sonicated in acetone for 15 min., triple rinsed with isopropyl alcohol, and blown dry with N_2 gas.

2. The strip is then inserted, length-wise, into the center of a quartz tube (22-mm inner diameter, 25-mm outer diameter, 62 cm in length) and slightly bent with a clean glass rod such that the shape of the foil matches the contour of the lower half of the tube but the middle of the foil remains 0.5 cm above the bottom surface of the tube.

3. The pressure in the tube is lowered to < 50 mTorr using an oil-free scroll pump. Ar (300 sccm) is flowed through the tube for 5 min., under the control of a mass flow controller, af-

ter which the pressure in the tube is increased to 750 mTorr using a metering valve located between the end of the tube and the pump.

4. While maintaining an Ar flow rate of 300 sccm, a Lindberg/Blue M Mini-Mite horizontal tube furnace is used to increase the temperature of the system to 1070°C over a period of 35 min. The Cu foil is annealed at 1070°C for 5 min.

5. Graphene synthesis starts with the introduction of H_2 and diluted CH_4 (500 ppm in Ar), each at a flow rate of 20 sccm, while the flow rate of Ar is changed to 310 sccm. The synthesis reaction is run for 4 hr. to ensure complete graphene coverage on the bottom side of the copper foil, i.e. the side of the foil facing the bottom surface of the quartz tube.

6. The reaction is arrested by cooling the system for 45 min. using an external fan until the temperature of the furnace is < 30°C. All gases used in the synthesis of graphene are ultra high purity grade.

Fig. 6.2 shows the progress of the graphene synthesis reaction over time. A series of SEM images demonstrates the growth of hexagonal graphene grains on Cu taken after synthesis times of (**a**) 30 min., (**b**) 60 min., (**c**) 120 min., and (**d**) 180 min. After 30 min., the majority of grains reach a diameter of 0.3–0.6 mm and fewer than 10% of the grains that were examined had yet to grow into other grains. By 60 min., most grains are > 1 mm and have begun to merge with adjacent grains. After 180 min., graphene covers most of the Cu foil and large graphene islands consisting of individual grains that are between 2–3.5 mm are common. Allowing the reaction to run for 4 hr. gives a continuous sheet of graphene on the surface of the Cu foil closest to the bottom of the quartz tube. The average grain diameter in the final polycrystalline sheet is estimated to be 0.75–1.5 mm. It is estimated that 10–20% of the area of graphene synthesized using the above protocol contains multi-layers.

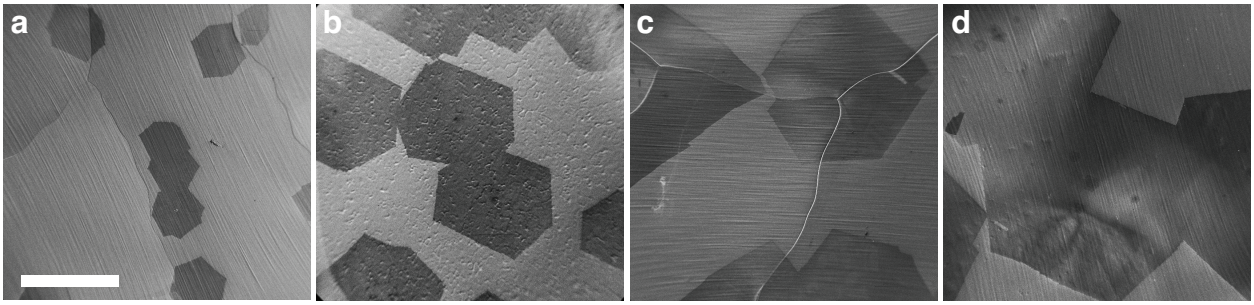

Figure 6.2: Graphene grain size. A time series of SEM micrographs reveals the size of hexagonal graphene grains on Cu foil after synthesis times of: **a**, 30 min., **b**, 60 min., **c**, 120 min., and **d**, 180 min. A continuous sheet of large-grain, polycrystalline graphene is achieved after 4 hr. Grains can reach diameters of 2–3.5 mm before growing into one another. Small hexagons seen within the larger hexagons of (**d**) are regions of multi-layer graphene. Scale bar: 1 mm.

Fig. 6.3 demonstrates the different optical techniques that were used to determine the presence, the size, and the number of layers of graphene grains that were grown on Cu foil. Fig. 6.3 (**a**) is a bright-field optical micrograph of graphene on Cu after oxidizing the Cu for ≥ 2 min. in an oven at 200°C. The area of the foil covered by graphene oxidizes more slowly and thus remains lighter in color than the area that is not covered. The rippled area on the upper left side of the graphene grain is a second layer of graphene, *i.e.* an add-layer. Fig. 6.3 (**b**) is an SEM micrograph of a single grain of graphene on Cu that contains add-layers near the nucleation site (bright dot). The graphene appears darker than the bare Cu under the given imagining conditions. Fig. 6.3 (**c**) is a dark-field micrograph of two conjoined graphene grains on Cu. Again, the graphene appears darker than the bare Cu. This is because the surface roughness of the bare Cu is much greater than that of the graphene (likely because the graphene does not completely follow the contour of the Cu surface), thus causing the Cu to scatter more light. If add-layers were present, they would show up as bright areas on the darker mono-layer grain because of their increased ability to corrugate.

As further verification that the synthesis protocol yields single grains of graphene with the occasional add-layer, graphene was transferred from the Cu foil that it was grown to a SiO_2/Si

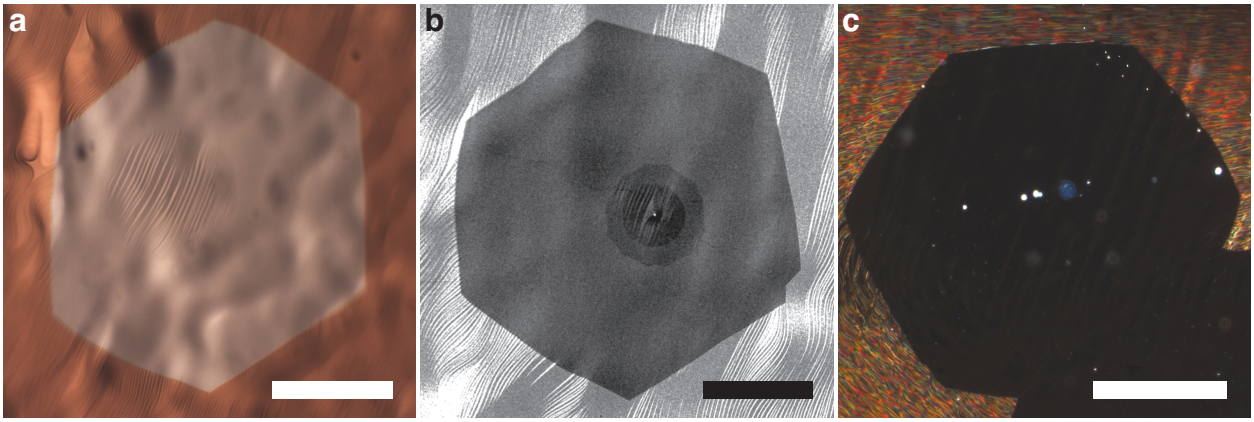

Figure 6.3: Imaging individual grains of graphene on Cu. a, Bright-field optical micrograph of hexagonal graphene grain on oxidized Cu. The wavy area on the grain is an add-layer. Scale bar: 100 μm. **b**, SEM micrograph of a single grain with add-layers (darker circles). Scale bar: 50 μm. **c**, Dark-field optical micrograph of two conjoined grains on Cu. Scale bar: 200 μm.

(300 nm) substrate and analyzed using Raman spectroscopy. Fig. 6.4 shows the results of the Raman analysis of a single graphene grain. Fig. 6.4 (**a**) is a bright-field optical micrograph of the single grain of graphene on SiO_2/Si. The edges of the graphene grain have been outlined for emphasis. The grain contains an add-layer near its center. Fig. 6.4 (**b**) is a Raman spectrum of the graphene grain at a point on the grain that does not contain the add-layer. The relative intensities of the D, G, and G' peaks in the spectrum are characteristic of mono-layer graphene. The small D peak is indicative of relatively defect-free graphene. Fig. 6.4 (**c**) is a series of spectral maps of the entire grain, depicting the intensity of the D, G, and G' peaks. The intensity of the peaks clearly changes over the area of the add-layer. To conclusively prove that the grain is mostly mono-layer, however, further analysis of the Raman data is needed, such as that performed in Chapter 2, Sect. 2.4.3 (p. 102) and shown in Fig. 2.30 (p. 106) [69].

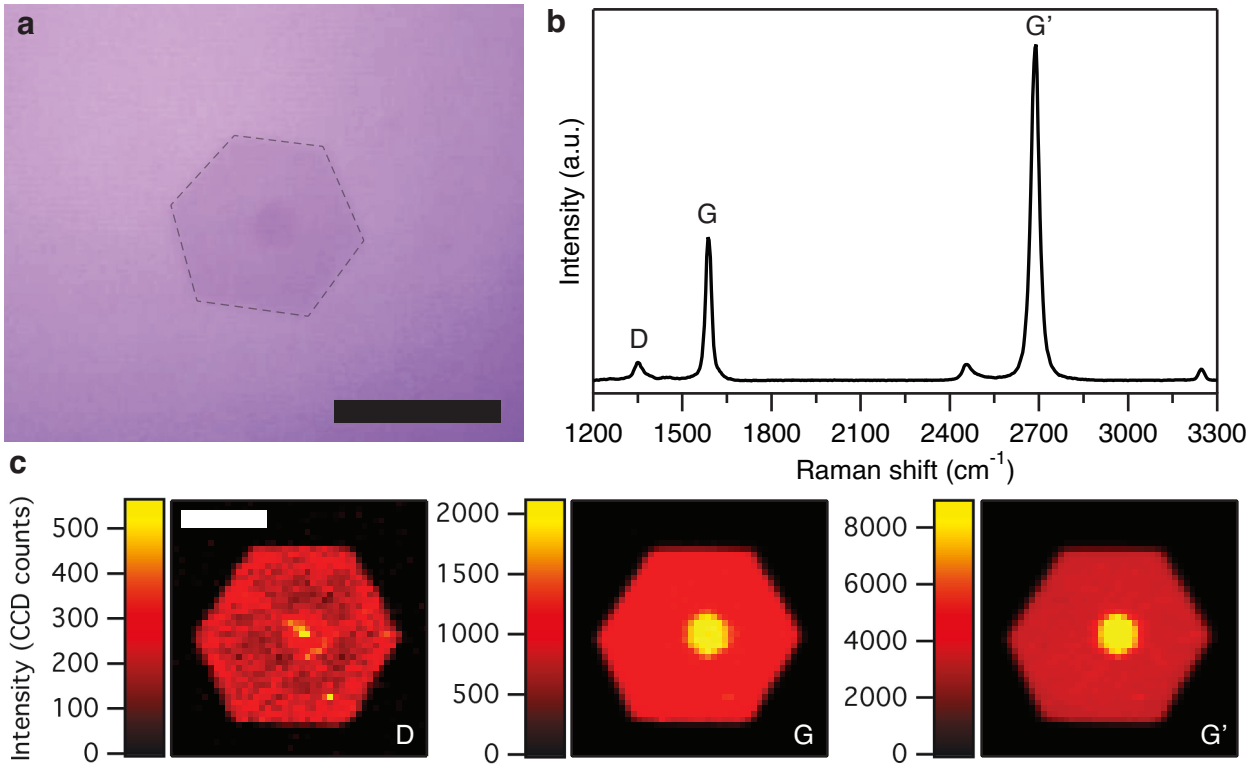

Figure 6.4: Raman analysis of an individual graphene grain on 300 nm SiO_2/Si. a, Bright-field optical micrograph of hexagonal graphene grain with add-layer on 300 nm SiO_2/Si. The grain has been outlined for emphasis. Scale bar: 10 μm. **b**, Raman spectrum of mono-layer region of grain. **c**, Raman spectral maps of the grain depicting the intensity of the D, G, and G' peaks. Scale bar: 5 μm. For the Raman data, laser excitation photon energy $= 2.33$ eV at 8 mW and laser spot size $= 1$–2 μm.

6.2.3 Protocol for synthesizing graphene without multi-layer regions

As stated before, multi-layer graphene growth has been hypothesized to result from the sequestration of activated carbon atoms in defects on the surface of Cu and the diffusion of the sequestered carbon underneath previously-nucleated mono-layer graphene sheet(s) until it eventually reaches a nucleation site and forms an additional graphene layer. If the source of carbon for the reaction is pulsed in a controlled manner, however, there is sufficient time for the activated carbon atoms to diffuse out of the Cu defects before becoming trapped by a growing grain of graphene. As demonstrated in Ref. [128], this significantly reduces, if not eliminates, the formation of multi-layer regions of graphene during the CVD process. This technique was successfully added to the protocol described previously in order to suppress multi-layer growth. Other parts of the protocol were also adjusted to allow large areas of this graphene ($\simeq 2 \times 5$ cm^2) to be synthesized.

The exact synthesis protocol is as follows:

1. A strip of 25-μm thick Cu foil (Alfa Aesar, 99.8%), 2×7 cm^2 in area, is first washed in 1 M HCl for 5 min., then sonicated in acetone for 15 min., triple rinsed with isopropyl alcohol, and blown dry with N_2 gas.

2. The strip is then inserted, length-wise, into the center of a quartz tube (22-mm inner diameter, 25-mm outer diameter, 62 cm in length) and slightly bent with a clean glass rod such that the shape of the foil matches the contour of the upper half of the tube and the middle of the foil is 1.5 cm above the bottom surface of the tube.

3. The pressure in the tube is lowered to < 50 mTorr using an oil-free scroll pump. Ar (300 sccm) is flowed through the tube for 5 min., under the control of a mass flow controller, after which the pressure in the tube is increased to 750 mTorr using a metering valve located between the end of the tube and the pump.

4. While maintaining an Ar flow rate of 300 sccm, a Lindberg/Blue M Mini-Mite horizontal tube furnace is used to increase the temperature of the system to $1070°$C over a period of 35 min. The Cu foil is annealed at $1070°$C for 24 hr.

5. The Cu foil is cooled for 45 min. using an external fan until the temperature of the furnace is $< 30°$C.

6. Once cooled, the furnace is again used to increase the temperature of the system to $1070°$C over a period of 35 min. The Cu foil is re-annealed at $1070°$C for 5 min.

7. Graphene synthesis starts with the introduction of H_2 and diluted CH_4 (500 ppm in Ar), each at a flow rate of 20 sccm, while the flow rate of Ar is changed to 250 sccm. The flow of diluted CH_4 gas is pulsed with a duty cycle of 30% per min. using a computer to control the valve of the mass flow controller, *i.e.* during each minute the valve is open for 18 s and closed for 42 s.

8. The synthesis reaction is run for 36 hr. to ensure complete graphene coverage on the bottom side of the copper foil, i.e. the side of the foil facing the bottom surface of the quartz tube.

9. The reaction is arrested by cooling the system for 45 min. using an external fan until the temperature of the furnace is $< 30°$C. All gases used in the synthesis of graphene are ultra high purity grade.

The long annealing time and subsequent cooling of the Cu foil is necessary to allow cracks to develop on the surface of the Cu along the grain boundaries in the polycrystalline foil. During the synthesis reaction, graphene growth then follows the contour of these cracks, preventing the graphene from tearing during its subsequent transfer to another substrate. For optical micrographs showing the reduction in the number of multi-layer regions that this protocol is able to achieve,

see Fig. 2.29 (p. 104). It is estimated that $< 0.02\%$ of the area of graphene synthesized using the above protocol contains multi-layers.

6.2.4 Summary of the CVD synthesis protocols

The values for the different parameters of the two graphene synthesis protocols described in this chapter are summarized in the table below.

Parameters		Protocol	
		w/ multi-layers	w/o multi-layers
Cu Anneal	Temperate (°C)	1070	1070
	Pressure (mTorr)	750	750
	Time (hr.)	0.083	24
	Ar flow rate (sccm)	300	300
Graphene Synthesis	Temperate (°C)	1070	1070
	Pressure (mTorr)	750	750
	Time (hr.)	4	36
	Ar flow rate (sccm)	310	250
	H_2 flow rate (sccm)	20	20
	CH_4 (500 ppm) in Ar flow rate (sccm)	20	20
	CH_4 (500 ppm) in Ar duty cycle (%)	-	30

Table 6.1: Parameters used in the synthesis of large-grain, CVD graphene. Parameters are listed for the protocols that were developed to synthesize large-grain, CVD graphene both with (w/) and without (w/o) regions of multi-layers.

6.2.5 Discussion on the necessity of electrochemically polishing the Cu foil

The idea behind electrochemically polishing, also known as electropolishing, the Cu foil before using it as a catalyst in the synthesis of CVD graphene is that it purportedly suppresses the density of graphene nucleation sites by reducing the foil's surface roughness. Generally speaking, the fewer nucleation sites there are, the larger the graphene grains are able to grow before merging into one another. In Ref. [119], Yan et al. use this argument to claim that electrochemically polishing the Cu foil is a critical step in the synthesis of millimeter-sized grains of graphene. A concerted effort was made to experimentally verify this claim.

The general protocol described in Ref. [131] for electropolishing copper was followed with only minor modifications. A home-built electropolishing cell consisting of a large Cu disk (5 cm in diameter, 3 mm-thick) as the cathode (negative electrode), a small piece of Cu foil (2×2 cm^2, 25 μm-thick) as the anode (positive electrode), ortho-phosphoric acid as the polishing solution, an orbital shaking table as the stirring mechanism, and a Keithley 2400 Sourcemeter as the power source was used for the reaction. Although Cu polishing typically produces the best results with an applied voltage of 1.5–2.5 V and an anode current density of 6–8 A/dm^2, the optimal voltage and anode current density for polishing the thin pieces of Cu foil were determined empirically according to the plot of the anode current density vs. voltage. An example of such a plot is provided in Fig. 6.5 (**a**).

As outlined in Ref. [131], the following regions are evident in the anode current density vs. voltage plot:

1. A $\rightarrow$ B: Cu etching

2. B $\rightarrow$ C: unstable region

3. C $\rightarrow$ D: stable plateau with polishing (optimal polishing at point D)

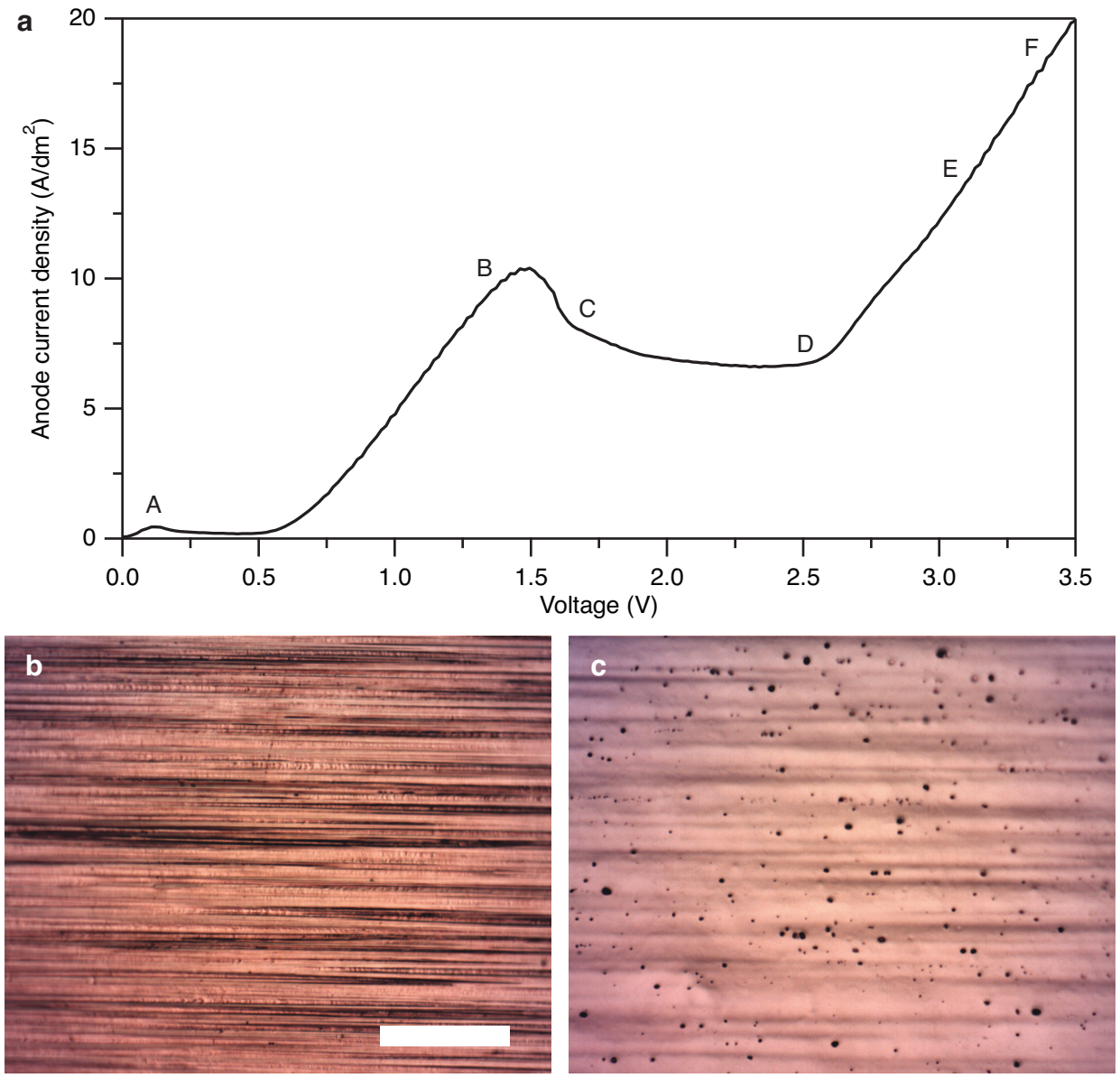

Figure 6.5: Electropolishing Cu foil. **a**, Plot of the anode current density vs. applied voltage of the home-built electropolishing cell. A 25 μm-thick piece of Cu foil was used as the anode. The voltage applied during electropolishing was kept in the 'stable plateau' range between points C and D. Optimal polishing conditions were achieved near point D. According to Ref. [131], etching occurs between points A and B; the reaction is unstable between points B and C; slow gas evolution with pitting occurs between points D and E; and polishing with rapid gas evolution occurs between points E and F. **b**, Cu foil before electropolishing. **c**, Cu foil after electropolishing for 5 min. at $\simeq 25^{\circ}$C. Scale bar: 100 μm.

4. D $\rightarrow$ E: slow gas evolution with pitting

5. E $\rightarrow$ F: polishing with rapid gas evolution

During the polishing reaction, the voltage and anode current density were kept as close to their optimal values as possible over reaction times of 5-30 min. The temperature of the ortho-phosphoric acid bath was kept at $\simeq$ 25°C. Upon completion of the reaction, the foil was rinsed with ethanol to remove residual phosphoric acid and to precipitate out any copper phosphate salts.

As is qualitatively evident in the optical micrographs of both Fig. 6.5 (**b**) (before polishing) and Fig. 6.5 (**c**) (after polishing), electrochemical polishing reduced the foil's overall surface roughness. In the process, however, small micron-scale holes developed on the surface, likely a result of bubble formation. Despite altering the electropolishing protocol several times and re-optimizing the voltage and anode current density, it was determined that the formation of holes could not be avoided.

Compared to the unpolished foil, the presence of the holes on the surface of the electropolished foil led to an increase in the number of multi-layer graphene areas that formed during synthesis. Because it was also empirically proven that large-grain graphene could be synthesized without electrochemical polishing the Cu foil, no further attempts at optimizing the polishing protocol were made. It is still possible, however, that electropolished Cu (without surface pitting) could reduce the number of nucleation sites during CVD graphene synthesis. According to Ref. [120], electropolishing is likely to have only a limited impact because the density of nucleation sites is most greatly affected by the presence of an oxide layer on the copper's surface.

6.2.6 Conclusions on the synthesis of large-grain graphene via CVD

1. Millimeter-scale grains of graphene, both with and without regions of multi-layers, can be successfully synthesized on thin pieces of copper foil using low-pressure chemical vapor deposition. The use of a dilute source of carbon and a sufficiently high reaction temperature are important factors.

2. Continuous sheets of large-grain graphene can be synthesized over most of the copper's surface by allowing the reaction to run for a sufficiently long amount of time.

3. Multi-layer graphene growth can be suppressed effectively by pulsing the flow of the carbonaceous reactant gas.

4. Electropolishing Cu is unnecessary for growing millimeter-scale (or larger), single grains of graphene but may still prove to be useful if the copper's surface roughness can be reduced without also causing surface pitting.

6.3 Transfer of large areas of graphene to a hydrophobic substrate

Fabrication of the G-SCEEG devices described in this thesis required the ability to transfer large, intact areas ($\geq$ 1 cm^2) of CVD-grown graphene to a glass substrate that had been functionalized with a self-assembled monolayer of octadecyltrichlorosilane (OTS). Because OTS-treated surfaces are hydrophobic, many of the protocols described in the literature are inadequate. These protocols invariably lead to poor adhesion of graphene to hydrophobic surfaces because they cause water to become trapped between graphene and the substrate. Although many dry-transfer techniques have been developed that avoid trapping water [111, 132–136], they inevitably yield only small pieces ($\simeq$ 1 mm^2) of continuous graphene, especially when graphene is transferred to OTS-treated substrates.

The transfer protocol I developed is based primarily on that described in Ref. [111] but contains several additional steps to ensure that $\simeq$ 1 cm^2 areas of continuous graphene can be transferred to an OTS-functionalized surface. The protocol also uses the series of modified 'standard clean' (SC*) solutions, *i.e.* SC-1* and SC-2*, which are described in Ref. [137].[1] The solutions aid in eliminating residual metal and organic contamination from the side of the graphene that ultimately is in contact with the OTS-functionalized substrate. The main parts of the transfer protocol are illustrated in Fig. 6.6 and a summary of the parameters involved in the protocol is provided in Table 6.2 (p. 208).

[1] The standard clean solutions used here are modified versions of those originally developed by the Radio Corporation of America (RCA). RCA used these solutions to clean silicon wafers that were then used in the manufacture of semiconductor devices. See Ref. [138] for more information regarding the original SC-1 and SC-2 solutions.

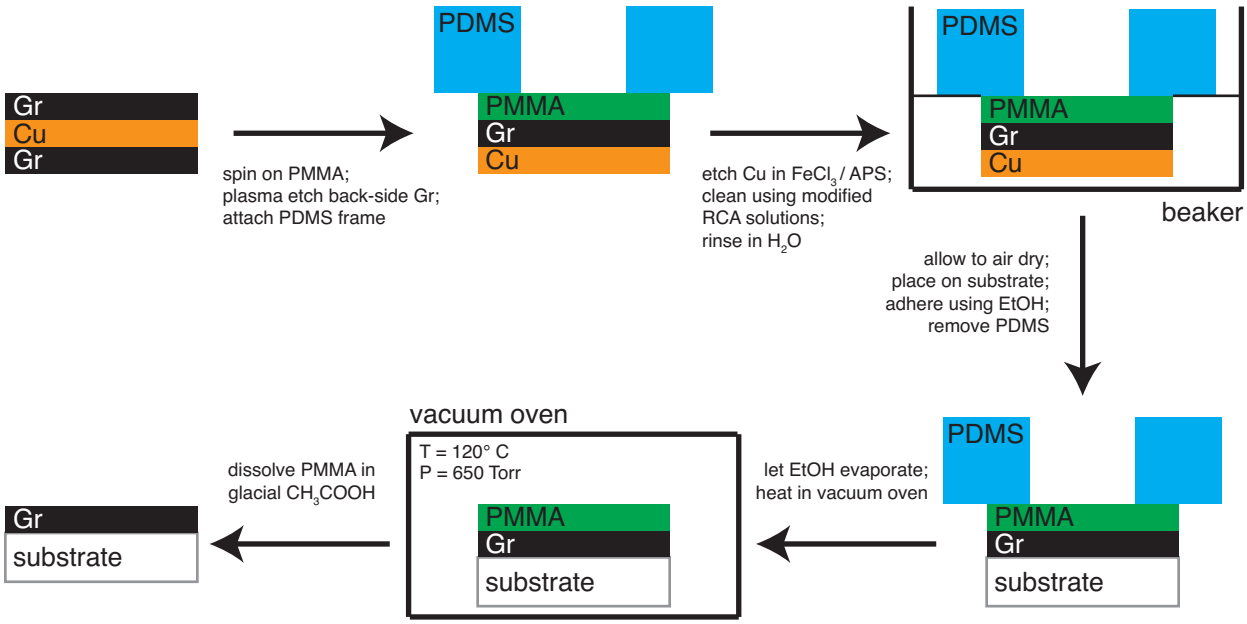

Figure 6.6: Diagram of the graphene transfer protocol. An illustration of the steps involved in transferring CVD-grown graphene from a piece of Cu foil to a hydrophobic substrate such as OTS-functionalized glass.

6.3.1 Protocol for graphene transfer

The exact transfer protocol is as follows:

1. A 2×2.5 cm^2 piece of graphene on Cu foil (Gr/Cu) is first spin coated with 6% (w/w) polymethyl methacrylate (PMMA) in anisole (MicroChem 950PMMA 11 A) for 40 sec. at 1000 RPM.

2. The PMMA is cured at 100°C for 5 min.

3. Graphene on the backside of the foil is removed by O_2 plasma (100 W, 1 min.).

4. The PMMA/Gr/Cu foil stack is then pressed onto the bottom of a 3-mm thick polydimethylsiloxane (PDMS) support frame containing a 1×1.5 cm^2 rectangular hole.

5. The Cu foil is partially etched in 1 M ferric chloride ($FeCl_3$; Transene CE-100) for 5 min. then rinsed in deionized H_2O (Millipore, 18MΩ) for 15 min. This is done to speed up the etching process.[2]

6. The remaining Cu foil is etched in 100 mM ammonium persulfate (APS; $(NH_4)_2S_2O_8$) for $\simeq 2$ hr.

7. After all the Cu has been etched, the graphene is subjected to the following sequence of rinses, all of which are carried out at 25°C:

   (a) deionized H_2O (15 min.)

   (b) SC-2* (20:1:1 ratio of deionized H_2O : 30% H_2O_2 : 12 M HCl, 15 min.)

   (c) deionized H_2O (15 min.)

[2] Because etching Cu with $FeCl_3$ can lead to the formation of insoluble copper chloride salt crystals, which can then tear any graphene residing on the surface of the Cu [108], ammonium persulfate is used to etch the remaining Cu.

(d) SC-1* (30:1:1 ratio of deionized H_2O : 30% H_2O_2 : 28% NH_4OH, 10 min.)[3]

(e) deionized H_2O (15 min.)

Note that a glass microscope slide is used to transfer the PDMS/PMMA/Gr stack between solutions because of the ease at which the suspended PMMA/Gr stack ripped while being pulled off of air/liquid interfaces.

8. After the final deionized H_2O rinse, the stack is lifted out of the solution with a glass microscope slide.

9. Several milliliters of ethanol (200 proof) are then pipetted around the PDMS frame on the glass microscope slide to replace the water trapped underneath the stack with ethanol. This is done to lower the surface tension and help prevent the stack from tearing.

10. The stack is carefully pulled off the microscope slide so as to avoid tearing the PMMA/Gr, flipped over such that the bare graphene is facing up, and gently blown dry with N_2 gas for 5 min. The stack is then allowed to air dry for at least 1 hr. to ensure all liquid has evaporated.

11. After cleaning the OTS-functionalized substrate with acetone and isopropyl alcohol, the substrate is covered in 2 mL of 200-proof ethanol. Using the PDMS frame as a handle, the PMMA/Gr stack is flipped onto the substrate using tweezers such that the bare graphene is facing down. The ethanol is then allowed to evaporate for at least 1 hr.[4]

[3] Note that the ratio used here for the volume of the solutes to the solvent is less than that described in Ref. [137]. This was done intentionally as a precautionary measure to ensure that the solution would not chemically react graphene during the rinse step.

[4] The use of ethanol in this step is absolutely crucial to the overall success of the transfer. The surface tension of the evaporating ethanol is thought to pull the PMMA/Gr stack down onto the substrate's surface, greatly enhancing the adhesion of graphene to the surface and ensuring that graphene does not delaminate as the PMMA layer is subsequently dissolved. Here, the role of the evaporating ethanol is the same as that of the evaporating water in protocols designed for transferring graphene to hydrophilic substrates like silicon dioxide [139].

12. The PDMS frame is cut from the PMMA/Gr using a finely pointed scalpel.

13. To promote adhesion of the graphene to the substrate, the sample is heated to $120°C$ for 1 hr. in a vacuum oven (650 Torr).

14. The PMMA layer is then dissolved over a period of 24 hr. using glacial acetic acid as prescribed in Ref. [140]. The graphene is subsequently rinsed in deionized H_2O to remove residual acetic acid.[5]

15. An optional step is to anneal the graphene in a tube oven (H_2 flow rate = 200 sccm; Ar flow rate = 400 sccm; T = $250°C$; P = 1 Torr; t = 2 hr.) according to the protocol described in Ref. [141]. Annealing has been shown to remove some of the residual PMMA that remains after the bulk of the PMMA was dissolved using an organic solvent. For transfers involving large-grain, mono-layer only graphene, however, this step was determined to create cracks in the graphene and was, therefore, omitted.

[5] It was discovered that using organic solvents, such as acetone or a mixture of dichloromethane and methanol, to dissolve the PMMA also led to delamination of the graphene from the OTS-functionalized substrate. It is recommended that only acetic acid be used for this step.

6.3.2 Summary of the hydrophobic transfer protocol

The steps and parameters involved in the transfer of graphene from a 25-μm thick Cu foil to a hydrophobic substrate are summarized in the table below.

Transfer step	Parameter	Value
Polymer coat	Polymer	PMMA
	Solvent	anisole
	Concentration	6% (w/w)
	Spin rate (RPM)	1000
	Spin time (sec.)	40
	Cure temperate (°C)	100
	Cure time (min.)	5
Polymer frame	Polymer	PDMS
	Thickness (mm)	3
O_2 plasma clean	Power (W)	100
	Time (min.)	1
Cu etch	Etchants	$FeCl_3$ / $(NH_4)_2S_2O_8$
	Concentrations	1.0 M / 0.1 M
	Times (min.)	5 / 120
Post-etch treatments	Rinse solutions	H_2O / SC-2* / H_2O / SC-1* / H_2O
	Rise times (min.)	15 / 15 / 15 / 10 / 15
	Drying method	air
	Drying temperature (°C)	25
Adhesion promotion	Solvent	ethanol (200-proof)
	Bake temperature (°C)	120
	Bake pressure (Torr)	650
	Bake time (min.)	60
Polymer coat removal	Solvent	acetic acid (glacial)
	Temperature (°C)	25
	Time (hr.)	24
Graphene anneal (optional)	Temperature (°C)	250
	H_2 flow rate (sccm)	200
	Ar flow rate (sccm)	400
	Pressure (Torr)	1
	Time (hr.)	2

Table 6.2: Parameters involved in the transfer of graphene to hydrophobic substrates.

7

Conclusions and future prospects

Most of my effort in this thesis has been dedicated towards providing a detailed description of the graphene supercapacitive electrical energy generator (G-SCEEG) and its ability to generate electricity from oscillating droplets of electrolyte solutions. While the idea of harvesting renewable energy from ocean waves may seem like an exciting future application, much more engineering must be done before SCEEGs and devices like them are suitable, and economical, for merely powering personal electronic devices. Increasing the surface area of the SCEEG's electrodes, by using carbon nanotubes for example, and altering the geometry of the moving electrolyte to re-

duce friction are logical first steps towards increasing both the SCEEG's electrical output and its efficiency.

More important than the G-SCEEG's ability to generate useful amounts of electric power, however, is the simple way in which it can be used to uniquely access basic information about the nature of the interaction between hydrated ions and graphene. Measurements involving the G-SCEEG are able to determine the identity of the ions that adsorb to graphene as well as the ion's surface charge density and binding energy. Additionally, the surface potential at the G-SCEEG's graphene electrodes relative to the bulk solution can be deduced from such measurements. From a scientific standpoint, this is what I find most exciting, the fact that a simple macro-scale device is capable of providing extensive insight into the nano-scale interactions between ions and solid-state materials.

To the best of my knowledge, no other experimental method or instrument can provide such extensive information about the interface between an electrode and an electrolyte solution. While methods such as the Kelvin probe method, Kelvin probe force microscopy, photoemission spectroscopy, and scanning electron microscopy can be used to measure the work function and surface potential of solids [142], they are ill suited to do so in the presence of aqueous solutions. Other methods such as the measurement of three-phase contact angles and the use of an ionizing, radioactive electrode are limited to studying the surface potential of only certain types of interfaces [99, 143, 144].

A

Standard Methods

A.1 Standard synthesis of graphene using chemical vapor deposition

Continuous sheets of polycrystalline graphene, consisting of single grains between 1–10 μm in diameter, were synthesized on Cu foils using low-pressure chemical vapor deposition.[1] Versions of this ”standard” recipe can be found throughout the literature, but it was first detailed in Ref. [68].

As shown in the Raman spectroscopic analysis of Chapter 2, Sect. 2.4.3.4, Fig. 2.30 (p. 106), the graphene that is synthesized using this protocol has a significant number of defects and multi-

[1] See Fig. 6.1 (p. 190) for an illustration of the CVD setup.

layer regions (at least 25% of its area has some number of multi-layers).

A.1.1 Protocol for synthesizing graphene

The synthesis protocol is as follows (note that all gases used in the synthesis of graphene are ultra high purity grade):

1. A strip of 25-μm thick Cu foil (Alfa Aesar, 99.8%), 2×7 cm^2 in area, is first washed in 1 M HCl for 5 min., then sonicated in acetone for 15 min., triple rinsed with isopropyl alcohol, and blown dry with N_2 gas.

2. The strip is then inserted into the center of a quartz tube (22-mm inner diameter, 25-mm outer diameter, 62 cm in length) such that it is 0.5 cm above the bottom surface of the tube.

3. The pressure in the tube is lowered to < 50 mTorr using an oil-free scroll pump.

4. H_2 (10 sccm) is flowed through the tube for 5 min.

5. While maintaining an H_2 flow rate of 10 sccm, a Lindberg/Blue M Mini-Mite horizontal tube furnace is used to increase the temperature of the system to 1000°C over a period of 15 min.

6. The Cu foil is annealed at 1000°C for 30 min.

7. Graphene synthesis is begun with the introduction of CH_4 at a flow rate of 4 sccm, while the flow rate of H_2 is unchanged.

8. The synthesis reaction is run for 40 min. to ensure complete graphene coverage on both the bottom and top sides of the copper foil.

9. The reaction is arrested by cooling the system for 45 min. using an external fan until the temperature of the furnace is < 30°C.

A.2 Graphene transfer protocols

A.2.1 Wet graphene transfer

The following protocol was based on that described in Ref. [139].

A.2.1.1 Protocol for transferring wet graphene

The transfer protocol was optimized by T. Zhou and is as follows:

1. Methyl methacrylate (MMA) polymer solutions (2%, 4%, and 6% MMA in ethyl lactate; diluted from a stock solution of MicroChem 9% MMA 8.5 in ethyl lactate) are each spun on a piece of graphene-containing copper foil (Gr/Cu) for 30 seconds at 3000 RPM and cured by baking at 180°C on a hot plate for 3 min.

2. To remove Gr on the side of the Cu foil not covered by MMA, the Gr is etched using O_2 plasma (100 W, 1–2 min.).

3. Scissors are then used to cut a piece of the MMA/Gr/Cu stack to fit the size specifications of the target substrate.

4. The copper foil is removed by placing the stack in a bath of ferric chloride solution ($FeCl_3$; Transene CE- 100) with the bare Cu side facing down on the solution's surface for 2 hr. to ensure that all the Cu is etched.

5. Once the Cu is completely removed, the MMA/Gr stack is then transferred to a deionized water bath (Millipore, 18 MΩ) using a piece of bare Si wafer that has been cleaned using O_2 plasma to make its surface hydrophilic.

6. After several minutes in the water bath, the same piece of Si wafer is used to move the stack to a solution of 1 M HCl and then to 6 more deionized water baths.

7. While the stack is in the last deionized water bath, it is scooped out using the hydrophilic target substrate, which has previously been O_2 plasma cleaned for 1 min. at 30 W.

8. The MMA/Gr/substrate stack is then placed under a halogen lamp for a minimum of 90 min. to allow the water to migrate out from underneath the stack and to eventually evaporate.

9. Once dry, the MMA layer is removed by submerging the MMA/Gr/substrate stack in acetone at 48°C overnight. Residual acetone is removed by repeated rinsing with isopropyl alcohol and deionized H_2O.

For suspended graphene membranes, the MMA layer is removed using the following protocol:

1. Once dry, the MMA layer is dissolved using acetone; a homemade aluminum jar is used to house the substrate during this process.

2. The substrate is first placed in the jar and the jar is then placed inside a large beaker. Acetone is added slowly and gently to the beaker until the jar is fully submerged.

3. The beaker is covered and left on a hotplate (48°C) overnight.

4. Acetone is then exchanged with 200-proof ethanol to facilitate critical point drying. The exchange is accomplished by removing the jar from the acetone-containing beaker and placing it in a beaker containing ethanol. The jar is allowed to sit in ethanol for 5 min. so that the acetone in the jar can be completely replaced with ethanol. This process is repeated three more times with ethanol to ensure that no acetone remains.

5. A critical point dryer (Tousimis 931 Series) was then used to remove the ethanol. Ethanol was replaced with liquid CO_2 over the course of three, 30 min. cycles. Three slow cycles

provided extra assurance that all the ethanol was gently replaced with liquid CO_2 during the drying process.

A.2.2 Dry graphene transfer

The following protocol was based on that described in Ref. [111].

A.2.2.1 Protocol for transferring dry graphene

The transfer protocol is as follows:

1. A 1.5×2 cm^2 piece of graphene on Cu foil (Gr/Cu) is first spin coated with 4% (w/w) polymethyl methacrylate (PMMA) in anisole (MicroChem 950PMMA 11 A) for 40 sec. at 1000 RPM.

2. The PMMA is cured at room temperature for 60 min.

3. Graphene on the backside of the foil is removed by O_2 plasma (100 W, 1 min.).

4. The PMMA/Gr/Cu foil stack is then pressed onto the bottom of a 3-mm thick polydimethylsiloxane (PDMS) support frame containing a 1×1.5 cm^2 rectangular hole.

5. The Cu foil is etched in ferric chloride ($FeCl_3$; Transene CE-100) for 30 min. then rinsed in deionized H_2O (Millipore, 18 MΩ) for 15 min., 2 M HCl for 30 min., and finally deionized H_2O again for 15 min. A glass microscope slide is used to transfer the PDMS/PMMA/Gr stack between solutions because of the ease at which the suspended PMMA/Gr stack rips while being pulled off of air/liquid interfaces.

6. After the final deionized H_2O rinse, the stack is lifted out of the solution with a glass microscope slide. Several milliliters of ethanol (200 proof) are then pipetted around the PDMS

frame to replace the water trapped underneath the stack with ethanol. This is done to lower the surface tension and help prevent the stack from tearing.

7. The stack is then carefully pulled off the microscope slide so as to avoid tearing the PMMA/Gr and gently blown dry with N_2 gas for 5 min.

8. The target substrate is placed face down on the PDMS/PMMA/Gr.

9. The PDMS frame is cut from the PMMA/Gr using a finely pointed scalpel.

10. To promote graphene adhesion the sample is placed in a home-built acetone vapor humidor for 15 min. followed by heating the sample to $180°$C for 2 hr. in an atmosphere of Ar (500 sccm) at a pressure of 500 Torr.

11. The PMMA is thermally removed by heating the sample to $350°$C for 4 hr. in an atmosphere of H_2 (500 sccm) and Ar (500 sccm) at a pressure of 1 Torr.

A.3 Fabrication of apertures in silicon-containing substrates

This method was developed and optimized by T. Zhou.

A.3.1 Protocol for fabricating apertures

All the steps outlined below are to be completed inside a clean room. The fabrication protocol is as follows:

1. A Si wafer (<100>; 4-in. diameter; 500-μm thick) is first cleaned using the standard RCA cleaning protocol.

2. A 300-nm thick layer of low stress ($<$ 200 MPa) Si_3N_4 is then grown on the top and bottom surfaces of the wafer using low-pressure CVD.

3. Standard photolithography and reactive ion etching (RIE) are used to remove sets of 9×12 arrays of squares from the top layer of Si_3N_4, thus exposing the underlying Si in each square.

4. A solution of KOH (40%) is then used to anisotropically etch the exposed Si, forming freestanding Si_3N_4 membranes (250×250 μm^2).

5. A second round of photolithography and RIE is done on the freestanding Si_3N_4 membranes to form circular apertures (5, 10, 20, 30, or 50 μm in diameter) at the center of each membrane.

6. After aperture formation, the wafer is thoroughly cleaned using a piranha etch solution.

7. Finally, a 300-nm thick layer of SiO_2 is deposited on top of the aperture-containing Si_3N_4 membranes using plasma-enhanced CVD.

A.4 Functionalization of oxide-containing substrates with octadecyltrichlorosilane

The protocol described below for forming a self-assembled monolayer (SAM) of octadecyltrichlorosilane (OTS) on oxide-containing substrates was based on Refs. [145] and [146]. The thickness of the OTS layer that forms on oxidized silicon depends on the reaction conditions and can vary between 1.5–4.3 nm [146]. However, the thickness of the OTS SAM is approximately 2.5 nm when the alkyl chains of OTS are fully extended and oriented normal to the substrate's surface [147, 148].

Although OTS forms covalent bonds with oxide-containing surfaces, it can physically adsorb to metals such as Au and Pt [149]. This physisorbed OTS layer can usually be removed, however, using the organic solvents acetone and isopropyl alcohol.

A.4.1 Protocol for OTS silanization

The silanization protocol is as follows:

1. The substrate is first cleaned using ultrasonication in acetone, isopropyl alcohol, and deionized water (in that order), each for five minutes; the substrate is then immersed in a piranha etch solution, *i.e.* a 3:1 mixture of concentrated H_2SO_4 and H_2O_2, for 20 min. at 100°C and washed with deionized water and dried with N_2 gas.

2. To activate surface oxide groups, the substrate is subjected to oxygen plasma cleaning (100 W for 5 min.).

3. A 10 mM solution of octadecyltrichlorosilane (OTS) is prepared in anhydrous toluene and is subsequently mixed using a magnetic stir bar for one minute. Because OTS is readily hydrolyzed when exposed to atmospheric water vapor, the solution of OTS must be prepared under an atmosphere of dry N_2 gas.

4. The substrate is submerged in the OTS solution and the functionalization reaction is allowed to run for 4–6 hr. at 25°C under an atmosphere of dry N_2 gas. According to Ref. [146], a reaction time of 6 hr. is optimal for forming a layer of OTS that completely coats the surface of the substrate.

5. The substrate is then removed from the reaction solution and submerged in chloroform for 5 min. It is rinsed with fresh chloroform and ethanol before being dried with N_2 gas.

6. To finish the reaction, the substrate is cured in a vacuum oven at 120°C for one hour (P $=$ 650 Torr).

B

Derivations

B.1 *Derivation of the parallel-plate capacitance*

The expression for the capacitance of a parallel-plate capacitor is relevant to the Stern layer capacitance, C_{s}, as described in Chapter 3 (beginning on p. 123). A version of the following derivation of C_{s} can be found in Ref. [36].

The derivation begins with Gauss' law:

$$\vec{\nabla} \cdot \vec{E} = \frac{\rho}{\epsilon_0} \tag{B.1}$$

where $\vec{E}$ is the electric field, ρ the volumetric charge density, and ϵ_0 the permittivity of a vacuum. Eq. (B.1) can be rewritten in integral form using the divergence theorem, *a.k.a.* Gauss' theorem:

$$\oint_S \vec{E} \cdot d\vec{a} = \frac{Q_{\text{enc}}}{\epsilon_0} \tag{B.2}$$

where Q_{enc} is the total charge enclosed in some volume v over which the surface integral, represented in the left-hand part of Eq. (B.2), is being taken. For a cylindrical Gaussian surface extending through an infinite plane of surface charge σ, the left side of Eq. (B.2) equals:

$$\oint_S \vec{E} \cdot d\vec{a} = 2\,|\vec{E}|\,a \tag{B.3}$$

where a is the area of the cylinder's ends that are parallel to the charged plane. The electric field extending above and below the infinite plane is then found by equating Eq. (B.2) and (B.3):

$$\vec{E} = \frac{\sigma}{2\,\epsilon_0}\,\hat{n} \tag{B.4}$$

where $Q_{\text{enc}} = \sigma\,a$. For two infinite planes of opposite surface charge, $+\sigma$ and $-\sigma$, that are separated by a dielectric of thickness d and relative permittivity ϵ, the electric field between the planes is:

$$\vec{E} = \frac{\sigma}{\epsilon\,\epsilon_0}\,\hat{n} \tag{B.5}$$

and everywhere else $\vec{E} = 0$. Using Eq. (B.5) and the definitions of capacitance, $q_{\text{s}} = C\,\Phi_{\text{s}}$, and electric potential, $\Phi_{\text{s}} = -\int \vec{E} \cdot d\vec{l}$, it can be shown that the Stern layer capacitance of the parallel planes, or plates, of charge is:

$$C_{\text{s}} = \frac{q_{\text{s}}}{\Phi_{\text{s}}} = \frac{\sigma\,A}{|\vec{E}|\,d} = \frac{\epsilon\,\epsilon_0}{d}A \tag{B.6}$$

$$\boxed{C_{\mathrm{s}} = \frac{\epsilon\,\epsilon_0}{d} A} \tag{B.7}$$

where q_{s} is the charge on the plates of the Stern layer, Φ_{s} is the potential difference across the Stern layer, and A represents the area of the layer. Eq. (B.6) is true so long as $A >> d^2$ and the fringe electric fields at the periphery of the area can be neglected.

B.2 *Derivation of the Debye diffuse layer capacitance*

The expression for the capacitance of Debye diffuse layer is relevant to the diffuse layer capacitance, C_{d}, as described in Chapter 3 starting on p. 124. Partial versions of the following derivation of C_{d} can be found in Refs. [37], [60], and [59].

Beginning again with Gauss' law, Eq. (B.1) on p. 220, and the definition of the electric potential in derivative form, $\vec{E} = -\,\vec{\nabla}\, V$, one obtains Poisson's equation:

$$\nabla^2\, \Phi_{\mathrm{d}} = -\,\frac{\rho}{\epsilon\,\epsilon_0} \tag{B.8}$$

where Φ_{d} is the potential drop across the diffuse layer and ϵ is the relative permittivity of the solution. According to the Maxwell-Boltzmann distribution, the spatial distribution of the concentration of the i-th ion, $n_{\mathrm{i}}(x)$, extending away from the electrode-solution interface at $x = 0$ is given by:

$$n_{\mathrm{i}}(x) = n_{\mathrm{i,0}}\, \exp\left(-\,\frac{U_{\mathrm{i}}(x)}{k_{\mathrm{B}}\, T}\right) \tag{B.9}$$

when the i-th ions are exposed to a the distance-dependent potential $U_{\mathrm{i}}(x)$. In Eq. (B.9), k_{B} is the Boltzmann constant, T the temperature, and $n_{\mathrm{i,0}}$ the bulk concentration of the i-th ion. When the i-th ion of charge state z_{i} is subject to the the distance-dependent, diffuse layer electric potential,

$\Phi_{\rm d}(x)$, Eq. B.9 becomes:

$$n_{\rm i}(x) = n_{\rm i,0}\ \exp\left(-\frac{z_{\rm i}\, e\, \Phi_{\rm d}(x)}{k_{\rm B}\, T}\right) \tag{B.10}$$

For a symmetric electrolyte, *i.e.* each ionic species has an equal and opposite charge state, $z = z_+ = -\, z_-$, and bulk concentration, $n_0 = n_{+,0} = n_{-,0}$, the charge density is then:

$$\rho = z\, e\ (n_+ - n_-) = -\, 2\, z\, e\, n_0\ \sinh\left(\frac{z\, e\, \Phi_{\rm d}}{k_{\rm B}\, T}\right) \tag{B.11}$$

One then obtains the Poisson-Boltzmann equation by substituting Eq. (B.11) into Eq. (B.8):

$$\nabla^2\, \bar{\Phi}_{\rm d} = k^2\ \sinh \bar{\Phi}_{\rm d} \tag{B.12}$$

where

$$k^2 \equiv \frac{2\, z^2\, e^2\, n_0}{\epsilon\, \epsilon_0\, k_{\rm B}\, T} \tag{B.13}$$

$$\bar{\Phi}_{\rm d} \equiv \frac{z\, e}{k_{\rm B}\, T}\, \Phi_{\rm d} \tag{B.14}$$

Note that $k^{-1} = \lambda_{\rm D}$. In general, Eq. (B.12) has no analytical solution and must be solved numerically [37]. Integrating the one-dimensional version of Eq. (B.12) once with respect to $\bar{x}$, how-

ever, in order to find the diffuse layer capacitance, C_{d}, proceeds via the following steps:

$$\frac{\partial^2 \bar{\Phi}_{\mathrm{d}}}{\partial \bar{x}^2} = \sinh \bar{\Phi}_{\mathrm{d}} \tag{B.15}$$

$$2\left(\frac{d\,\bar{\Phi}_{\mathrm{d}}}{d\bar{x}}\right)\frac{\partial^2 \bar{\Phi}_{\mathrm{d}}}{\partial \bar{x}^2} = 2\left(\frac{d\,\bar{\Phi}_{\mathrm{d}}}{d\bar{x}}\right)\sinh \bar{\Phi}_{\mathrm{d}} \tag{B.16}$$

$$\int_{\infty}^{\bar{x}} \frac{d}{d\bar{x}'}\left(\frac{d\,\bar{\Phi}_{\mathrm{d}}}{d\bar{x}'}\right)^2 d\bar{x}' = 2\int_{0}^{\bar{\Phi}_{\mathrm{d}}} d\bar{\Phi}'_{\mathrm{d}}\,\sinh \bar{\Phi}'_{\mathrm{d}} \tag{B.17}$$

where $\bar{x} \equiv k\,x$. Evaluating the integrals of Eq. (B.17) and assuming

$$\left.\frac{d\,\bar{\Phi}_{\mathrm{d}}}{d\bar{x}}\right|_{\bar{x}=\infty} = 0, \tag{B.18}$$

i.e. the gradient of the diffuse layer potential is zero in the bulk, one finds:

$$\left(\frac{d\,\bar{\Phi}_{\mathrm{d}}}{d\bar{x}}\right)^2 = \left[2\,\cosh \bar{\Phi}'_{\mathrm{d}}\right]\Bigg|_{0}^{\bar{\Phi}_{\mathrm{d}}} = 2\left(\cosh \bar{\Phi}_{\mathrm{d}} - 1\right) \tag{B.19}$$

Using the identity $\cosh(x) - 1 = 2\,\sinh^2(x/2)$ and simplifying gives:

$$\frac{d\,\Phi_{\mathrm{d}}}{dx} = -\left(\frac{8\,k_{\mathrm{B}}\,T\,n_0}{\epsilon\,\epsilon_0}\right)^{1/2}\sinh\left(\frac{z\,e\,\Phi_{\mathrm{d}}}{2\,k_{\mathrm{B}}\,T}\right) \tag{B.20}$$

where the negative sign comes from the assumption that $d\,|\Phi_{\mathrm{d}}|\,/\,dx < 0$ for $x > 0$, *i.e.* the magnitude of Φ_{d} decreases as one approaches the bulk solution because of the boundary condition $\lim_{x\to\infty} \Phi_{\mathrm{d}}(x) \to 0$.

Assuming that the diffuse layer is thin, the net charge per unit area of the diffuse layer, σ_{d}, is well defined and is balanced by an equal and opposite surface charge density, σ, at the electrode's

surface, *i.e.* $\sigma = -\sigma_{\mathrm{d}}$. Using the boundary condition relating the gradient of the potential normal to a conductive surface, $\partial V \,/\, \partial n$, to that surface's charge density, σ, the net surface charge density in the diffuse layer can be obtained from Eq. (B.20) by evaluating $\partial \Phi_{\mathrm{d}} \,/\, \partial x$ at the interface, *i.e.* $x = 0$.[1] This yields:

$$\sigma_{\mathrm{d}} = -\epsilon\,\epsilon_0 \left.\frac{\partial \Phi_{\mathrm{d}}}{\partial x}\right|_{x=0} = \left(8\,k_{\mathrm{B}}\,T\,\epsilon\,\epsilon_0\,n_0\right)^{1/2} \sinh\left(\frac{z\,e\,\Phi_{\mathrm{d},0}}{2\,k_{\mathrm{B}}\,T}\right) \tag{B.21}$$

where $\Phi_{\mathrm{d},0}$ is the diffuse layer potential at the electrode's surface, *i.e.* $\Phi_{\mathrm{d}}(x = 0) = \Phi_{\mathrm{d},0}$. Finally, the differential capacitance of the diffuse layer is found by taking the partial derivative of Eq. (B.21) with respect to Φ_{d} and evaluating the result at the interface, *i.e.* $\Phi_{\mathrm{d}}(x = 0) = \Phi_{\mathrm{d},0}$:

$$C_{\mathrm{d}}(\Phi_{\mathrm{d},0}) = A \left.\frac{\partial \sigma_{\mathrm{d}}}{\partial \Phi_{\mathrm{d}}}\right|_{\Phi_{\mathrm{d}}=\Phi_{\mathrm{d},0}} = \frac{\epsilon\,\epsilon_0}{\lambda_{\mathrm{D}}}\left[\cosh\left(\frac{z\,e\,\Phi_{\mathrm{d},0}}{2\,k_{\mathrm{B}}\,T}\right)\right] A \tag{B.22}$$

$$\lambda_{\mathrm{D}} \equiv \sqrt{\frac{\epsilon\,\epsilon_0\,k_{\mathrm{B}}\,T}{2\,z^2\,e^2\,n_0}} \tag{B.23}$$

$$\boxed{C_{\mathrm{d}}(\Phi_{\mathrm{d},0}) = \frac{\epsilon\,\epsilon_0}{\lambda_{\mathrm{D}}}\left[\cosh\left(\frac{z\,e\,\Phi_{\mathrm{d},0}}{2\,k_{\mathrm{B}}\,T}\right)\right] A} \tag{B.24}$$

where λ_{D} is, again, called the Debye length. The concept of differential capacitance is used to describe the capacitance of the diffuse layer because the charge, q, in this layer is not proportional to the potential, V, applied across it, *i.e.* the ratio of q to V is not constant. Unlike normal capacitors, the capacitance of the diffuse layer varies with the electric potential and the usual definition of capacitance does not accurately apply [80]. Instead, it is the derivative of the charge with re-

[1] Finding σ_{d} in this way is possible because of the discontinuity that occurs in the normal component of the electric field when it crosses a plane of surface charge, σ. The resulting boundary condition, in terms of the electric potential V, is given by $\sigma = -\epsilon\,\epsilon_0\,\partial V \,/\, \partial n$ [36]. Alternatively, the total charge in the diffuse layer can also be found by integrating the distribution of the net charge density over the entire diffuse layer [37].

spect to potential evaluated at a given value of the potential that best describes the capacitance.

If the electric potential energy of an ion is much less than its thermal energy, *i.e.* $k_{\mathrm{B}}\,T \;>> z\,e\,\Phi_{\mathrm{d},0}$, then C_{d} takes on a form resembling the capacitance of a parallel-plate capacitor and is no longer a function of $\Phi_{\mathrm{d},0}$:

$$\boxed{C_{\mathrm{d}} \simeq \frac{\epsilon\,\epsilon_0}{\lambda_{\mathrm{D}}}\,A} \tag{B.25}$$

This is the so-called Debye-Hückel approximation to the Poisson-Boltzmann equation. The results of the approximation are more thoroughly discussed in Sect. 3.2 of Chapter 3 (p. 115).

B.3 *Derivation of the quantum capacitance*

The quantum capacitance, C_{q}, of graphene is relevant for understanding the magnitude of the surface charge densities that are measured using G-SCEEG devices as well as for determining the reason those densities differ from the densities that are measured using an Au-SCEEG device. See Chapter 3 (beginning with p. 124) for a more complete explanation of the role quantum capacitance plays in the output of SCEEGs. Below is a derivation of the expression for C_{q}. Partial versions of this derivation can be found in Refs. [41], [44], [150], and [151].

The derivation of C_{q} begins with the expression for the density of states of graphene:

$$\rho_{\mathrm{s}}(E) = \frac{2\,|E|}{\pi\,\left(\hbar\,v_{\mathrm{F}}\right)^2} \tag{B.26}$$

The derivation of Eq. (B.26) using the tight-binding Hamiltonian approach is well documented elsewhere [151]. Here, the result is merely quoted. From Eq. (B.26) the density of intrinsic positive, p_{c}, and negative, n_{c}, charge carriers in graphene can be found using the Fermi-Dirac distri-

bution, $f(E)$:

$$p_{\mathrm{c}} = \int_0^\infty dE\, \rho_{\mathrm{s}}(E)\, f_+(E) \tag{B.27}$$

$$n_{\mathrm{c}} = \int_0^\infty dE\, \rho_{\mathrm{s}}(E)\, f_-(E) \tag{B.28}$$

where

$$f_\pm(E) = \frac{1}{1 + \exp\left(\frac{E \pm E_{\mathrm{F}}}{k_{\mathrm{B}}\, T}\right)} \tag{B.29}$$

Setting $u \equiv E \,/\, k_{\mathrm{B}}\, T$ and $\eta \equiv E_{\mathrm{F}} \,/\, k_{\mathrm{B}}\, T$, Eq. (B.27) and (B.28) become:

$$p_{\mathrm{c}} = \frac{2}{\pi}\left(\frac{k_{\mathrm{B}}\, T}{\hbar\, v_{\mathrm{F}}}\right)^2 J_1(-\eta) \tag{B.30}$$

$$n_{\mathrm{c}} = \frac{2}{\pi}\left(\frac{k_{\mathrm{B}}\, T}{\hbar\, v_{\mathrm{F}}}\right)^2 J_1(+\eta) \tag{B.31}$$

where $J_{\mathrm{j}}(\eta)$ is the Fermi-Dirac integral:

$$J_{\mathrm{j}}(\eta) = \frac{1}{\Gamma(\mathrm{j}+1)} \int_0^\infty du \frac{u^{\mathrm{j}}}{1 + \exp\,(u - \eta)} \tag{B.32}$$

$$\Gamma(x) = (x-1)! \tag{B.33}$$

When no external perturbation is added, *i.e.* $E_{\mathrm{F}} = 0$:

$$n_{\mathrm{c}} = p_{\mathrm{c}} = n_{\mathrm{i}} = \frac{\pi}{6}\left(\frac{k_{\mathrm{B}}\, T}{\hbar\, v_{\mathrm{F}}}\right)^2 \tag{B.34}$$

which is $\simeq 9 \times 10^{10}$ cm^{-2} at room temperature. Due to the law of mass action, at equilibrium:

$$n_{\mathrm{c}}\, p_{\mathrm{c}} = n_{\mathrm{i}}^2\, \frac{J_1(\eta)\, J_1(-\eta)}{J_1^2(0)} \tag{B.35}$$

When an external voltage $\Phi_{\mathrm{q,0}}$ is applied across the graphene, $E_{\mathrm{F}} = e\, \Phi_{\mathrm{q,0}}$ and the net charge density is:

$$\sigma_{\mathrm{q}} = e\, \big[J_1(-\eta) - J_1(\eta)\big] \tag{B.36}$$

Finally, the differential capacitance (Eq. (3.10) on p. 123) is:

$$C_{\mathrm{q}} = A\, \frac{\partial\, \sigma_{\mathrm{q}}}{\partial V_{\mathrm{c}}} = \left[\frac{2\, e^2}{\pi\, (\hbar\, v_{\mathrm{F}})^2}\right] \frac{\partial}{\partial \eta} \big[J_1(-\eta) + J_1(\eta)\big]\, A \tag{B.37}$$

Using the following relations:

$$\frac{d}{d\eta} J_{\mathrm{j}}(\eta) = J_{\mathrm{j}-1}(\eta) \tag{B.38}$$

$$J_0(\eta) = \int_0^\infty \frac{d\epsilon}{1 + \exp\,(\epsilon - \eta)} = \ln\,\big[1 + \exp\,(\eta)\big] \tag{B.39}$$

it can be shown that Eq. (B.37) can be written as:

$$\boxed{C_{\mathrm{q}}(\Phi_{\mathrm{q,0}}) = \frac{2\, e^2\, k_{\mathrm{B}}\, T}{\pi\, (\hbar\, v_{\mathrm{F}})^2}\, \ln\left[2\, \left(1 + \cosh\left[\frac{e\, \Phi_{\mathrm{q,0}}}{k_{\mathrm{B}}\, T}\right]\right)\right] A} \tag{B.40}$$

If $E_{\mathrm{F}} = e\, \Phi_{\mathrm{q,0}} >> k_{\mathrm{B}}\, T$, then C_{q} reduces to Eq. (3.13) (p. 125):

$$\boxed{C_{\mathrm{q}}(\Phi_{\mathrm{q,0}}) \simeq e^2 \left[\frac{2\, e\, \Phi_{\mathrm{q,0}}}{\pi\, (\hbar\, v_{\mathrm{F}})^2}\right] A = e^2\, \rho_{\mathrm{s}}(E_{\mathrm{F}})\, A} \tag{B.41}$$

B.4 *Derivation of the streaming potential*

It is useful to analyze the expression for the streaming potential, V_{str}, to determine whether V_{str} is responsible for the open-circuit voltage generated by the SCEEG device. As explained in Chapter 2, Sect. 2.3.4 (p. 74), V_{str} is generated when a solution of electrolyte solution, which is in contact with a solid surface, flows parallel to that surface. The flow of the solution is usually treated as arising from a hydrostatic pressure gradient that is applied to the electrolyte in a direction parallel to the solid surface. Versions of this derivation can be found in both Refs. [60] and [152].

The derivation of V_{str} begins when a hydrostatic pressure gradient, $\vec{\nabla} P$, is applied to an electrolyte solution in a cylindrical capillary of radius R_c and length l along the cylinder's axis (oriented in the $\hat{z}$ direction):

$$\vec{\nabla} P = -\frac{\Delta P}{l}\,\hat{z} \tag{B.42}$$

where ΔP is the difference in pressure between the two ends of the capillary. It is assumed that the concentration of the electrolyte is such that the diffuse layer is thin, *i.e.* $R_c >> \lambda_D$ where λ_D is the Debye length. The pressure gradient causes the solution to flow with a velocity, $\vec{v}(r)$. The radial distribution of the velocity along the cylinder's axis in the $\hat{z}$ direction is given by:

$$v_z(r) = \Delta P\,\frac{R_c^2 - r^2}{4\,\eta_s\,l} \tag{B.43}$$

where η_s is the viscosity of the solution.

Because the solution near the wall of the capillary has a net charge density, $\rho(r)$, the flow of fluid also creates a flow of current called the streaming current, I_{str}. I_{str} is found by integrating the current density, $\vec{J} = \rho\,\vec{v}$, over cross-sectional area of the cylinder:

$$I_{str} = 2\,\pi \int_0^{R_c} r\,v_z(r)\,\rho(r)\,dr \tag{B.44}$$

Due to the assumption that the thin diffuse layer is thin, $\rho(r)$ is approximately zero everywhere except in a narrow cylindrical shell close to the capillary's wall. This permits one to treat $v_z(r)$ as linear in r because only the form of $v_z(r)$ for $r \simeq R_\mathrm{c}$ is of interest. The expression of $v_z(r)$ then becomes:

$$v_z(r) \simeq \frac{\Delta P\, R_\mathrm{c}}{2\,\eta_\mathrm{s}\, l}\,(R_\mathrm{c} - r) = \frac{\Delta P\, R_\mathrm{c}}{2\,\eta_\mathrm{s}\, l}\,x \tag{B.45}$$

where $x \equiv R_\mathrm{c} - r$. Inserting Eq. (B.45) into Eq. (B.44) and neglecting higher order terms of x, I_str is:

$$I_\mathrm{str} = -\,\frac{\pi\, R_\mathrm{c}^2\, \Delta P}{\eta_\mathrm{s}\, l} \int_{R_\mathrm{c}}^{0} x\, \rho(x)\, dx \tag{B.46}$$

The expression for $\rho(x)$ is then found by using Poisson's equation and by applying the Debye-Hückel approximation to the Poisson-Boltzmann equation. From Eq. (3.8) (p. 121), the potential drop across the diffuse layer, $\Phi_\mathrm{d}(x)$, according to the Debye-Hückel solution to the Poisson-Boltzmann equation is:

$$\Phi_\mathrm{d}(x) = \Phi_{\mathrm{d},0}\, \exp\left(-\,\frac{x}{\lambda_\mathrm{D}}\right)$$

Then, from Poisson's equation, the form of $\rho(x)$ is:

$$\rho(x) = -\,\epsilon\,\epsilon_0\,\frac{d^2\,\Phi_\mathrm{d}(x)}{dx^2} = -\,\frac{\epsilon\,\epsilon_0\,\Phi_{\mathrm{d},0}}{\lambda_\mathrm{D}^2}\,\exp\left(-\,\frac{x}{\lambda_\mathrm{D}}\right) \tag{B.47}$$

Inserting Eq. (B.47) into Eq. (B.46) and integrating yields:

$$I_{\text{str}} = -\frac{\pi\, R_{\text{c}}^2\, \Delta P}{\eta_{\text{s}}\, l}\ \frac{\epsilon\, \epsilon_0\, \Phi_{\text{d,0}}}{\lambda_{\text{D}}^2} \int_0^{R_{\text{c}}} x\, \exp\left(-\frac{x}{\lambda_{\text{D}}}\right) dx \tag{B.48}$$

$$= -\frac{\pi\, R_{\text{c}}^2\, \Delta P}{\eta_{\text{s}}\, l}\ \epsilon\, \epsilon_0\, \Phi_{\text{d,0}}\ \left[-\exp\left(-\frac{x}{\lambda_{\text{D}}}\right)\left(\frac{x}{\lambda_{\text{D}}}+1\right)\right]\Bigg|_0^{R_{\text{c}}} \tag{B.49}$$

$$\simeq -\frac{\epsilon\, \epsilon_0\, \pi\, R_{\text{c}}^2}{\eta_{\text{s}}}\ \frac{\Delta P}{l}\ \Phi_{\text{d,0}} \tag{B.50}$$

where the final form of the streaming current is:

$$\boxed{I_{\text{str}} \simeq -\frac{\epsilon\, \epsilon_0\, \pi\, R_{\text{c}}^2}{\eta_{\text{s}}}\ \frac{\Delta P}{l}\ \Phi_{\text{d,0}}} \tag{B.51}$$

In the steady state, a conduction current, I_{c}, arises in response to I_{str}. From Ohm's law, I_{c} is due to a streaming potential, V_{str}, *i.e.* $V_{\text{str}} = I_{\text{c}}\, R$. The expression for I_{c} is:

$$I_{\text{c}} = \sigma_{\text{c,0}}\, \pi\, R_{\text{c}}^2\, \frac{V_{\text{str}}}{l} \tag{B.52}$$

where the following relation was used for R, the resistance of the solution in the capillary: $R = \rho_0\, l\, /\, A = l\, /\, \pi\, R_{\text{c}}^2\, \sigma_{\text{c,0}}$. ρ_0 and $\sigma_{\text{c,0}}$ are the resistivity and conductivity of the bulk solution, respectively. Because the streaming current is equal but opposite to the conduction current, *i.e.* $I_{\text{str}} + I_{\text{c}} = 0$, one can use this fact and Eqs. (B.51) and (B.52) to obtain the expression for V_{str} (Eq. (2.82), p. 74):

$$\boxed{V_{\text{str}} = \frac{\epsilon\, \epsilon_0}{\eta_{\text{s}}\, \sigma_{\text{c,0}}}\, \Phi_{\text{d,0}}\, \Delta P} \tag{B.53}$$

C

Nomenclature

Symbol	Meaning
α	amplitude of area change
a	area
A	area
A_{c}	cross-sectional area
$A_{\mathrm{p\text{-}p}}$	peak-to-peak area
$A_{\mathrm{L},0}$	initial overlap area between droplet & left electrode
$A_{\mathrm{R},0}$	initial overlap area between droplet & right electrode
$\vec{B}$	magnetic field

Symbol	Meaning
c_0	capacitance per unit area
c_d	drag coefficient
C	capacitance
$\mathbf{C}$	capacitance matrix
C'	differential capacitance
C_d	diffuse layer capacitance
C_eq	equivalent capacitance
C_q	quantum capacitance
C_s	Stern layer capacitance
C_EDL	capacitance of electric double layer
C_I	capacitance of interface
C_L	capacitance of left capacitor
C_R	capacitance of right capacitor
C_LR	mutual capacitance between left and right electrodes
d	distance
δ	phase angle
D	diffusivity, diffusion constant
e	charge of an electron
$\vec{E}$	electric field
E_d	activation energy of desorption
E_F	Fermi level
E_B	effective binding energy per ion
ϵ	relative permittivity
ϵ_0	vacuum permittivity
f	frequency
$\vec{f}_\mathrm{k}$	force of kinetic friction
$\vec{f}_\mathrm{d}$	drag force
g	gravitational constant
G_s	surface conductance
I	current
$\mathbf{I}$	current phasor
I_0	initial current

Symbol	Meaning
I_{c}	conduction current
I_{ex}	excess current
I_{L}	current through a load
$\langle I_{\mathrm{L}} \rangle_{\mathrm{RMS}}$	RMS current through a load
I_{sc}	short-circuit current
$\langle \lvert I_{\mathrm{sc}} \rvert \rangle_{\mathrm{avg}}$	average magnitude of short-circuit current
$\langle I_{\mathrm{sc}} \rangle_{\mathrm{RMS}}$	RMS short-circuit current
I_{SD}	source-drain current
I_{str}	streaming current
j	imaginary unit, $\sqrt{-1}$
$\vec{J}$	current density
k	(a) reaction rate constant (b) $\lambda_{\mathrm{D}}^{-1}$
k_{B}	Boltzmann constant
k_{d}	desorption rate constant
l	length
L	inductance
λ	charge per unit length
λ_{D}	Debye length (characteristic screening length)
Λ	displacement amplitude
m	mass
n	number of droplets
n	surface wave mode number
$\hat{n}$	normal unit vector
N	number of ions
n_{c}	negative charge carrier density
n_{e}	electron concentration
n_0	average ion concentration
n_∞	ionic concentration of bulk solution
η	power transfer efficiency
η_{c}	mechanical–electrical energy conversion efficiency
η_{s}	viscosity of solution

Symbol	Meaning
Θ	number of occupied binding sites
Θ_0	initial number of occupied binding sites
Θ_r	relative concentration of bound ions
Θ_{sat}	total number of bound ions at saturation
p_c	positive charge carrier density
P	(a) power
	(b) pressure
PF	power factor
P_L	power dissipated in a load
P_{TOT}	total generated power
$\langle P_L \rangle_{avg}$	average power dissipated in a load
ρ	charge density
ρ_m	mass density
ρ_s	density of states
ϕ	phase angle between alternating current and voltage
Φ	surface potential
Φ_d	electric potential across diffuse layer
Φ_{EDL}	electric potential across electric double layer
Φ_q	electric potential across graphene
Φ_s	electric potential across Stern layer
q	electric charge
q_0	initial charge
q_{ex}	excess electric charge
Q_{enc}	total electric charge enclosed by a given volume
r	(a) reaction rate
	(b) radial distance
	(c) radius, radius of curvature
r_d	desorption rate
R	(a) resistance
	(b) equivalent device resistance
R_c	radius of capillary
R_E	electrode resistance

Symbol	Meaning
R_{L}	load resistance
R_{S}	solution resistance
S	ratio of changes in total energy
σ	charge per unit area
σ_{c}	conductivity
$\sigma_{\mathrm{c,0}}$	bulk conductivity
σ_{d}	charge per unit area of the diffuse layer
σ_{n}	number of adsorbed ions per unit area
σ_{q}	charge per unit area of graphene
t	time
T	(a) temperature
	(b) period of oscillation
τ_{d}	characteristic timescale of ionic desorption
τ_{D}	Debye time
τ_{RC}	RC time constant
U	potential energy
μ	electrochemical potential
μ_0	vacuum permeability
μ_{k}	coefficient of kinetic friction
ν	(a) slope of voltage ramp
	(b) frequency factor
v	volume
$\vec{v}$	velocity
v_{F}	Fermi velocity
v_{z}	velocity along z axis
V	voltage
$\mathbf{V}$	voltage phasor
V_0	initial voltage
V_{ex}	excess voltage
V_{BG}	backgate voltage
V_{L}	voltage across a load
$\langle V_{\mathrm{L}} \rangle_{\mathrm{RMS}}$	RMS voltage across a load

Symbol	Meaning
V_{oc}	open-circuit voltage
$\langle V_{\text{oc}} \rangle_{\text{RMS}}$	RMS open-circuit voltage
$V_{\text{p-p}}$	peak-to-peak voltage
V_{R}	voltage drop across device's equivalent resistance
V_{str}	streaming potential
V_{X}	voltage drop across device's equivalent reactance
w	energy density
W	potential energy
W_{TOT}	total potential energy
ω	angular frequency
x	distance
$\vec{x}$	displacement
$\hat{x}$	x axis unit vector
γ	surface tension
z	ionic charge state, valency
$\hat{z}$	z axis unit vector
Z	impedance
Z^*	time-dependent internal impedance
$\langle Z^* \rangle_{\text{avg}}$	average internal impedance
Z_{L}	load impedance

References

[1] Ghosh, S. *et al.* Carbon Nanotube Flow Sensors. *Science* **299**, 1042–1044 (2003).

[2] Sood, A. K. *et al.* Direct Generation of a Voltage and Current by Gas Flow Over Carbon Nanotubes and Semiconductors. *Physical Review Letters* **93**, 086601–(1–4) (2004).

[3] Ghosh, S. *et al.* Flow-induced voltage and current generation in carbon nanotubes. *Physical Review B* **70**, 205423–(1–5) (2004).

[4] Dhiman, P. *et al.* Harvesting Energy from Water Flow over Graphene. *Nano Letters* **11**, 3123–3127 (2011).

[5] Yin, J. *et al.* Harvesting Energy from Water Flow over Graphene? *Nano Letters* **12**, 1736–1741 (2012).

[6] Yin, J. *et al.* Generating electricity by moving a droplet of ionic liquid along graphene. *Nature Nanotechnology* **9**, 378–383 (2014).

[7] Yin, J. *et al.* Waving potential in graphene. *Nature Communications* **5**, 3582–3587 (2014).

[8] Moon, J. K., Jeong, J., Lee, D. & Pak, H. K. Electrical power generation by mechanically modulating electrical double layers. *Nature Communications* **4**, 1487–1492 (2013).

[9] Branton, D. *et al.* The potential and challenges of nanopore sequencing. *Nature Biotechnology* **26**, 1146–1153 (2008).

[10] Manrao, E. A. *et al.* Reading DNA at single-nucleotide resolution with a mutant MspA nanopore and phi29 DNA polymerase. *Nature Biotechnology* **30**, 349–353 (2012).

[11] Laszlo, A. H. *et al.* Decoding long nanopore sequencing reads of natural DNA. *Nature Biotechnology* **32**, 829–833 (2014).

[12] Hayden, E. Nanopore genome sequencer makes its debut. *Nature News* (2012). DOI: 10.1038/nature.2012.10051.

[13] Hayden, E. Data from pocket-sized genome sequencer unveiled. *Nature News* (2014). DOI: 10.1038/nature.2014.14724.

[14] Garaj, S. *et al.* Graphene as a subnanometre trans-electrode membrane. *Nature* **467**, 190–193 (2010).

[15] Garaj, S. *et al.* Molecule-hugging graphene nanopores. *PNAS* **110**, 12640–12645 (2013).

[16] Geim, A. K. & Novoselov, K. S. The Rise of Graphene. *Nature Materials* **6**, 183–191 (2007).

[17] Fologea, D. *et al.* Slowing DNA Translocation in a Solid-State Nanopore. *Nano Letters* **5**, 1734–1737 (2005).

[18] Krishnakumar, P. *et al.* Slowing DNA Translocation through a Nanopore Using a Functionalized Electrode. *ACS Nano* **7**, 10319–10326 (2013).

[19] Lu, B. *et al.* Origins and Consequences of Velocity Fluctuations during DNA Passage through a Nanopore. *Biophysical Journal* **101**, 70–79 (2011).

[20] Gowtham, S. *et al.* Physisorption of nucleobases on graphene: Dentity-functional calculations. *Physical Review B* **76**, 033401–(1–4) (2007).

[21] Manohar, S. *et al.* Peeling Single-Stranded DNA from Graphite Surface to Determine Oligonucleotide Binding Energy by Force Spectroscopy. *Nano Letters* **8**, 4365–4372 (2008).

[22] Taherian, F. *et al.* What Is the Contact Angle of Water on Graphene? *Langmuir* **29**, 1457–1465 (2013).

[23] Ho, T. A. *et al.* Molecular dynamics simulation of the graphene–water interface: comparing water models. *Molecular Simulation* **40**, 1190–1200 (2014).

[24] Cole, D. J., Ang, P. K. & Loh, K. P. Ion Adsorption at the Graphene/Electrolyte Interface. *J. Phys. Chem. Lett.* **2**, 1799–1803 (2011).

[25] Rafiee, J. *et al.* Wetting transparency of graphene. *Nature Materials* **11**, 217–222 (2012).

[26] Shih, C. *et al.* Breakdown in the Wetting Transparency of Graphene. *Physical Review Letters* **109**, 176101–(1–5) (2012).

[27] Li, Z. *et al.* Effect of airborne contaminants on the wettability of supported graphene and graphite. *Nature Materials* **12**, 925–931 (2013).

[28] Thomson, W. Kinetic Theory of the Dissipaiton of Energy. *Nature* **9**, 441–444 (1874).

[29] Dressen, D. G. Oscillating droplet: Pulsed-induced resonances experiment #1: Resonance Sample #2 (OTS) (2012). Laboratory Notebook Entry.

[30] Lee, C., Wei, X., Kysar, J. W. & Hone, J. Measurement of the elastic properties and intrinsic strength of monolayer graphene. *Science* 385–388 (2008).

[31] Plume, A. Graphene: ten years of the 'gold rush'. *Research Trends* **38** (2014).

[32] Winter, M. & Brodd, R. J. What Are Batteries, Fuel Cells, and Supercapacitors? *Chemical Reviews* **104**, 4245–4270 (2004).

[33] Pandolfo, A. G. & Hollenkamp, A. F. Carbon properties and their role in supercapacitors. *Journal of Power Sources* **157**, 11–27 (2006).

[34] Bazant, M. Z., Thornton, K. & Ajdari, A. Diffuse-charge dynamics in electrochemical systems. *Physical Review E* **70**, 021506–24 (2004).

[35] Friedberg, R. The electrostatics and magnetostatics of a conducting disk. *Am. J. Phys.* **61**, 1084–1096 (1993).

[36] Griffiths, D. J. *Introduction to Electrodynamics* (Prentice Hall, New Jersey, 1999), 3rd edn.

[37] Kirby, B. *Micro- and Nanoscale Fluid Mechanics: Transport in Microfluidic Devices* (Cambridge University Press, New York, 2010), 1st edn.

[38] Jackson, J. D. *Classical Electrodynamics* (Wiley, New York, 1998), 3rd edn.

[39] Alexander, C. & Sadiku, M. *Fundamentals of Electric Circuits* (McGraw Hill, New York, 2009), 4th edn.

[40] Ambrosi, A., Chua, C. K., Bonanni, A. & Pumera, M. Electrochemistry of Graphene and Related Materials. *Chemical Reviews* **114**, 7150–7188 (2014).

[41] Luryi, S. Quantum capacitance devices. *Applied Physics Letters* **52**, 501 (1988).

[42] Oster, G., Perelson, A. & Katchalsky, A. Network Thermodynamics. *Nature* **234**, 393–399 (1971).

[43] Bisquert, J. Chemical capacitance of nanostructured semiconductors: its origin and significance for nanocomposite solar cells. *Phys. Chem. Chem. Phys.* **5**, 5360–5 (2003).

[44] Kim, C.-H. & Frisbie, C. D. Determination of Quantum Capacitance and Band Filling Potential in Graphene Transistors with Dual Electrochemical and Field-Effect Gates. *J. Phys. Chem. C* **118**, 21160–21169 (2014).

[45] Zhang, S. Analysis of Some Measurement Issues in Bushing Power Factor Tests in the Field. *IEEE Transactions on Power Delivery* **21**, 1350–1356 (2006).

[46] Whitehill, J., Neild, A., Ng, T. W., Martyn, S. & Chong, J. Droplet spreading using low frequency vibration. *Applied Physics Letters* **98**, 133503 (2011).

[47] Rayleigh, L. On the Capillary Phenomena of Jets. *Proc. R. Soc. Lond.* **29**, 71–79 (1879).

[48] Lai, M., Lee, C., Liao, C. & Wei, Z. Oscillation spectrums and beat phenomenon of a water droplet driven by electrowetting. *Applied Physics Letters* **94**, 154102 (2009).

[49] Sejdić, E., Djurović, I. & Jiang, J. Time–frequency feature representation using energy concentration: An overview of recent advances. *Digital Signal Processing* **19**, 153–183 (2009).

[50] Baraniuk, R. G. & Jones, D. L. A Signal-Dependent Time-Frequency Representation: Optimal Kernal Design. *IEEE Transactions on Signal Processing* **41**, 1589–1602 (1993).

[51] Taylor, J. R. *Classical Mechanics* (University Science Books, Sausalito, California, 2005).

[52] Hamer, W. J. & DeWane, H. J. Electrolytic Conductance and the Conductances of the Halogen Acids in Water. Publication NSRDS-NBS 33, National Bureau of Standards (1970).

[53] McNaught, A. D. & Wilkinson, A. *IUPAC Compendium of Chemical Terminology*. doi:10.1351/goldbook.O04322 (Blackwell Scientific Publications, Oxford, 1997), 2nd. edn.

[54] Masel, R. I. *Principles of Adsorption and Reaction on Solid Surfaces* (Wiley, New York, 1996).

[55] Israelachvili, J. *Intermolecular and Surface Forces* (Academic Press, Boston, 2011), 3rd edn.

[56] Riley, K. F., Hobson, M. P. & Bence, S. J. *Mathematical Methods for Physics and Engineering* (Cambridge University Press, Cambridge, 2006), 3rd edn.

[57] Zhdanov, V. P. Arrhenius parameters for rate processes on solid surfaces. *Surface Science Reports* **12**, 183–242 (1991).

[58] Wang, Z. & Seebauer, E. G. Estimating pre-exponential factors for desorption from semiconductors: consequences for a priori process modeling. *Applied Surface Science* **181**, 111–120 (2001).

[59] Bockris, J. O., Reddy, A. K. N. & Gamboa-Aldeco, M. E. *Modern Electrochemistry 2A: Fundamentals of Electrodics* (Springer, New York, 2000), 2nd. edn.

[60] Delgado, Á. V. (ed.) *Interfacial Electrokinetics and Electrophoresis*, vol. 106 of *Surfactant Science Series* (Marcel Dekker, New York, 2001).

[61] Shih, C.-J., Strano, M. S. & Blankschtein, D. Wetting translucency of graphene. *Nature Materials* **12**, 866–869 (2013).

[62] Priya, S. & Inman, D. (eds.) *Energy Harvesting Technologies* (Springer, New York, 2009).

[63] Wang, Z. L. Nanogenerators for Self-Powered Devices and Systems. SMARTech digital repository; http://hdl.handle.net/1853/39262, Georgia Institute of Technology (2011).

[64] Raju, M. ULP meets energy harvesting: A game-changing combination for design engineers. Tech. Rep., Texas Instruments (2008).

[65] Vatamanu, J. & Bedrov, D. Capacitive Energy Storage: Current and Future Challenges. *J. Phys. Chem. Lett.* **6**, 3594–3609 (2015).

[66] Lorenz, C. D., Chandross, M., Lane, J. M. D. & Grest, G. S. Nanotribology of water confined between hydrophilic alkylsilane self-assembled monolayers. *Modelling Simul. Mater. Sci. Eng.* **18**, 034005–14 (2010).

[67] Wang, S., Lin, L. & Wang, Z. L. Nanoscale Triboelectric-Effect-Enabled Energy Conversion for Sustainably Powering Portable Electronics. *Nano Lett.* **12**, 6339–6346 (2012).

[68] Li, X. *et al.* Large-Area Synthesis of High-Quality and Uniform Graphene Films on Copper Foils. *Science* **324**, 1312–1314 (2009).

[69] Kim, K. *et al.* Raman spectroscopy study of rotated double-layer graphene: Misorientation-angle dependence of electronic structure. *Phys. Rev. Lett.* **108**, 1–6 (2012).

[70] Gileadi, E. *Physical Electrochemistry* (Wiley, Weinheim, 2011).

[71] Pope, M. A. & Aksay, I. A. Four-Fold Increase in the Intrinsic Capacitance of Graphene through Functionalization and Lattice Disorder. *J. Phys. Chem. C* **119**, 20369–20378 (2015).

[72] Ang, P. K., Chen, W., Wee, A. T. S. & Loh, K. P. Solution-Gated Epitaxial Graphene as pH Sensor. *J. Am. Chem. Soc.* **130**, 14392–14393 (2008).

[73] Dankerl, M. *et al.* Graphene Solution-Gated Field-Effect Transistor Array for Sensing Applications. *Adv. Funct. Mater.* **20**, 3117–3124 (2010).

[74] Robinson, R. S., Sternitzke, K., McDermott, M. T. & McCreery, R. L. Morphology and Electrochemical Effects of Defects on Highly Oriented Pyrolytic Graphite. *J. Electrochem. Soc.* **138**, 2412–2418 (1991).

[75] Zhou, H., Preston, M. A., Tilton, R. D. & White, L. R. Calculation of the dynamic impedance of the double layer on a planar electrode by the theory of electrokinetics. *Journal of Colloid and Interface Science* **292**, 277–289 (2005).

[76] Oschatz, M. *et al.* *Annual Reports on NMR Spectroscopy*, vol. 87, chap. 4: Interactions Between Electrolytes and Carbon-Based Materials–NMR Studies on Electrical Double-Layer Capacitors, Lithium-Ion Batteries, and Fuel Cells, 237–318 (Academic Press, 2016).

[77] von Helmholtz, H. L. F. *Ann. Physik* **89** (1853).

[78] von Helmholtz, H. L. F. *Ann. Physik* **7** (1879).

[79] Bard, A. J. & Faulkner, L. R. *Electrochemical Methods: Fundamentals and Applications* (Wiley, New York, 2001), 2nd. edn.

[80] Grahame, D. C. The Electrical Double Layer and the Theory of Electrocapillarity. *Chemical Reviews* **41**, 441–501 (1947).

[81] Xia, J., Chen, F., Li, J. & Tao, N. Measurement of the quantum capacitance of graphene. *Nature Nanotechnology* **4**, 505–509 (2009).

[82] Badiali, J.-P. & Goodisman, J. The Lippmann Equation and the Ideally Polarizable Electrode. *J. Phys. Chem.* **79**, 223–232 (1975).

[83] Randin, J. P. & Yeager, E. Differential Capacitance Study of Stress-Annealed Pyrolytic Graphite Electrodes. *Journal of the Electrochemical Society* **118**, 711–714 (1971).

[84] Marx, D., Tuckerman, M. E., Hutter, J. & Parrinello, M. The nature of the hydrated excess proton in water. *Nature* **397**, 601–604 (1999).

[85] Volkov, A. G., Paula, S. & Deamer, D. W. Two mechanisms of permeation of small neutral molecules and hydrated ions across phospholipid bilayers. *Bioelectrochemistry and Bioenergetics* **42**, 153–160 (1997).

[86] Fajans, K. Polarizability of Alkali and Halide Ions, Especially Fluoride Ion. *J. Phys. Chem.* **74**, 3407–3410 (1970).

[87] Conway, B. E. & Ayranci, E. Effective Ionic Radii and Hydration Volumes for Evaluation of Solution Properties and Ionic Adsorption. *J. Soln. Chem.* **28**, 163–192 (1999).

[88] Yang, K. L., Yiacoumi, S. & Tsouris, C. *Dekker Encyclopedia of Nanoscience and Nanotechnology*, vol. 2, chap. E: Electric Double-Layer Formation, 1001–1014 (CRC Press, New York, 2004).

[89] Tan, X. Edge Effects on the pH Response of Graphene Nanoribbon Field Effect Transistors. *J. Phys. Chem. C* **117**, 27155–27160 (2013).

[90] Hu, S. Proton transport through one-atom-thick crystals. *Nature* **516**, 227–230 (2014).

[91] Ristein, J. Surface Transfer Doping of Semiconductors. *Science* **313**, 1057–1058 (2006).

[92] Liu, H., Liu, Y. & Zhu, D. Chemical doping of graphene. *J. Mater. Chem.* **21**, 3335–3345 (2011).

[93] Zhu, Y. *et al.* A solid dielectric gated graphene nanosensor in electrolyte solutions. *Applied Physics Letters* **106**, 123503–05 (2015).

[94] Mailly-Giacchetti, B. *et al.* pH sensing properties of graphene solution-gated field-effect transistors. *J. Appl. Phys.* **114**, 084505 (2013).

[95] Fu, W. *et al.* Graphene Transisitors Are Insensitive to pH Changes in Solution. *Nano Lett.* **11**, 3597–3600 (2011).

[96] Lim, C. X., Hoh, H. Y., Ang, P. K. & Loh, K. P. Direct Voltammertic Detection of DNA and pH Sensing on Epitaxial Graphene: An Insight into the Role of Oxygenated Defects. *Anal. Chem.* **82**, 7387–7393 (2010).

[97] Ohno, Y., Maehashi, K., Yamashiro, Y. & Matsumoto, K. Electrolyte-Gated Graphene Field-Effect Transistors for Detecting pH and Protein Adsorption. *Nano Lett.* **9**, 3318–3322 (2009).

[98] Wang, H. & Pilon, L. Physical interpretation of cyclic voltammetry for measuring electric double layer capacitances. *Electrochimica Acta* **64**, 130–139 (2012).

[99] Jarvis, N. L. Effect of Various Salts on the Surface Potential of the Water-Air Interface. *J. Geophys. Res.* **77**, 5177–5182 (1972).

[100] Sze, A., Erickson, D., Ren, L. & Li, D. Zeta-potential measurement using the Smoluchowski equation and the slope of the current–time relationship in electroosmotic flow. *Journal of Colloid and Interface Science* **261**, 402–410 (2003).

[101] Wolf, E. L. *Applications of Graphene: An overview*. Springer Briefs in Materials (Springer, New York, 2013).

[102] Bolotin, K. I. *et al.* Ultrahigh electron mobility in suspended graphene. *Solid State Communications* 351–355 (2008).

[103] Joshi, P., Romero, H. E., Neal, A. T., Toutam, V. K. & Tadigadapa, S. A. Intrinsic doping and gate hysteresis in graphene field effect devices fabricated on sio_2 substrates. *J. Phys.: Condens. Matter* **22**, 1–6 (2010).

[104] Alemán, B. *et al.* Transfer-free batch fabrication of large-area suspended graphene membranes. *ACS Nano* 4762–4768 (2010).

[105] Russo, C. J. & Passmore, L. A. Controlling protein adsorption on graphene for cryo-em using low-energy hydrogen plasmas. *Nat Meth* **11**, 649–652 (2014).

[106] Buckhout-White, S. *et al.* Tem imaging of unstained dna nanostructures using suspended graphene. *Soft Matter* 1414–1417 (2013).

[107] Blees, M., Rose, P., Barnard, A., Roberts, S. & McEuen, P. L. Graphene kirigami. In *Bulletin of the American Physical Society*, vol. 59 (American Physical Society March Meeting, Denver, CO, 2014).

[108] O'Hern, S. C. *et al.* Selective molecular transport through intrinsic defects in a single layer of cvd graphene. *ACS Nano* 10130–10138 (2012).

[109] O'Hern, S. C. *et al.* Selective ionic transport through tunable subnanometer pores in single-layer graphene membranes. *Nano Lett.* 1234–1241 (2014).

[110] Joshi, R. K. *et al.* Precise and ultrafast molecular sieving through graphene oxide membranes. *Science* 752–754 (2014).

[111] Suk, J. W. *et al.* Transfer of cvd-grown monolayer graphene onto arbitrary substrates. *ACS Nano* 6916–6924 (2011).

[112] Meyer, J. C. *et al.* The structure of suspended graphene sheets. *Nature* 60–63 (2007).

[113] Lee, G. H. *et al.* High-strength chemical-vapor-deposited graphene and grain boundaries. *Science* 1073–1076 (2013).

[114] Barton, R. A. *et al.* High, size-dependent quality factor in an array of graphene mechanical resonators. *Nano Lett.* 1232–1236 (2011).

[115] Faugeras, C. *et al.* Thermal conductivity of graphene in corbino membrane geometry. *ACS Nano* 1889–1892 (2010).

[116] Booth, T. J. *et al.* Graphene membranes and their extraordinary stiffness. *Nano Lett.* 2442–2446 (2008).

[117] Novoselov, K. S. *et al.* Roadmap for graphene. *Nature* 192–200 (2013).

[118] Zhou, H. *et al.* Chemical vapor deposition growth of large single crystals of monolayer and bilayer graphene. *Nature Communications* **4**, 2096–2103 (2013).

[119] Yan, Z. *et al.* Toward the synthesis of wafer-scale single-crystal graphene on copper foils. *ACS Nano* 9110–9117 (2012).

[120] Hao, Y. *et al.* The role of surface oxygen in the growth of large single-crystal graphene on copper. *Science* 720–723 (2013).

[121] Bunch, J. S. *et al.* Electromechanical resonators from graphene sheets. *Science* 490–493 (2007).

[122] Cohen-Tanugi, D. & Grossman, J. C. Water desalination across nanoporous graphene. *Nano Lett.* 3602–3608 (2012).

[123] Koenig, S. P., Boddeti, N. G., Dunn, M. L. & Bunch, J. S. Ultrastrong adhesion of graphene membranes. *Nature Nanotechnology* 543–546 (2011).

[124] Jorio, A., Dresselhaus, M. S., Saito, R. & Dresselhaus, G. *Raman Spectroscopy in Graphene Related Systems* (John Wiley & Sons, Weinheim, 2011).

[125] Lenski, D. R. & Fuhrer, M. S. Raman and optical characterization of multilayer turbostratic graphene grown via chemical vapor deposition. *J. Appl. Phys.* **110**, 1–4 (2011).

[126] Diaz-Pinto, C., De, D., Hadjiev, V. G. & Peng, H. Ab-stacked multilayer graphene synthesized via chemical vapor deposition: a characterization by hot carrier transport. *ACS Nano* 1142–1148 (2012).

[127] Cong, C. *et al.* Raman characterization of aba- and abc-stacked trilayer graphene. *ACS Nano* 8760–8768 (2011).

[128] Han, Z. *et al.* Homogeneous Optical and Electronic Properties of Graphene Due to the Suppression of Multilayer Patches During CVD on Copper Foils. *Adv. Funct. Mater.* **24**, 964–970 (2013).

[129] Petrone, N. *et al.* Chemical Vapor Deposition-Derived Graphene with Electrical Performance of Exfoliated Graphene. *Nano Letters* **12**, 2751–2756 (2012).

[130] Huang, P. *et al.* Grains and grain boundaries in single-layer graphene atomic patchwork quilts. *Nature* **469**, 389–392 (2011).

[131] McG. Tegart, W. J. *The Electrolytic and Chemical Polishing of Metals in research and industry* (Pergamon Press, New York, 1959), 2nd. edn.

[132] Caldwell, J. D. *et al.* Technique for the Dry Transfer of Epitaxial Graphene onto Arbitrary Substrates. *ACS Nano* **4**, 1108–1114 (2010).

[133] Song, J. *et al.* A general method for transferring graphene onto soft surfaces. *Nature Nanotechnology* **8**, 356–362 (2013).

[134] Wang, D.-Y. *et al.* Clean-Lifting Transfer of Large-area Residual-Free Graphene Films. *Adv. Mater.* **25**, 4521–4526 (2013).

[135] Shin, W. C. *et al.* Doping suppression and mobility enhancement of graphene transistors fabricated using an adhesion promoting dry transfer process. *Applied Physics Letters* **103**, 243504 (2013).

[136] Feng, Y. & Chen, K. Dry transfer of chemical-vapor-deposition-grown graphene onto liquid-sensitive surfaces for tunnel junction applications. *Nanotechnology* **26**, 035302 (2014).

[137] Liang, X. *et al.* Toward Clean and Crackless Transfer of Graphene. *ACS Nano* **5**, 9144–9153 (2011).

[138] Kern, W. *Handbook of Semiconductor Wafer Cleaning Technology: Science, Technology, and Applications*. Materials Science and Process Technology (Noyes Publications, New Jersey, 1994).

[139] Reina, A. *et al.* Transferring and Identification of Single- and Few-Layer Graphene on Arbitrary Substrates. *J. Phys. Chem. C* **112**, 17741–17744 (2008).

[140] Her, M., Beams, R. & Novotny, L. Graphene transfer with reduced residue. *Physics Letters A* **377**, 1455–1458 (2013).

[141] Lin, Y.-C. *et al.* Graphene Annealing: How Clean Can It Be? *Nano Lett.* **12**, 414–419 (2012).

[142] Melitz, W., Shen, J., Kummel, A. C. & Lee, S. Kelvin probe force microscopy and its application. *Surface Science Reports* **66**, 1–27 (2011).

[143] Jarvis, N. L. & Scheiman, M. A. Surface Potentials of Aqueous Electrolyte Solutions. *J. Phys. Chem.* **72**, 74–78 (1968).

[144] Horiuchi, H., Nikolov, A. & Wasan, D. T. Calculation of the surface potential and surface charge density by measurement of the three-phse contact angle. *Journal of Colloid and Interface Science* **385**, 218–224 (2012).

[145] McGovern, M. E., Kallury, K. M. R. & Thompson, M. Role of Solvent on the Silanization of Glass with Octadecyltrichlorosilane. *Langmuir* **10**, 3607–3614 (1994).

[146] Rezaee, A. *et al.* Octadecyltrichlorosilane (OTS): a resist for OMCVD gold nanoparticle growth. *Surface and Interface Analysis* **41**, 615–623 (2009).

[147] Linford, M. R. & Chidsey, C. E. D. Alkyl Monolayers Covalently Bonded to Silcon Surfaces. *J. Am. Chem. Soc.* **115**, 12631–12632 (1993).

[148] Angst, D. L. & Simmons, G. W. Moisture Absorption Characteristics of Organosiloxane Self-Assembled Monolayers. *Langmuir* **7**, 2236–2242 (1991).

[149] Finklea, H. O., Robinson, L. R., Blackburn, A. & Richter, B. Formation of an Organized Monolayer by Solution Adsorption of Octadecyltrichlorosilane on Gold: Electrochemical Properties and Structural Characterization. *Langmuir* **2**, 239–244 (1986).

[150] Fang, T., Konar, A., Xing, H. & Jena, D. Carrier statistics and quantum capacitance of graphene sheets and ribbons. *Applied Physics Letters* **91**, 092109 (2007).

[151] Castro Neto, A. H., Guinea, F., Peres, N. M. R., Novoselov, K. S. & Geim, A. K. The electronic properties of graphene. *Reviews of Modern Physics* **81**, 109–162 (2009).

[152] Hunter, R. J. *Zeta Potential in Colloid Science: Principles and Applications*. Colloid Science Series (Academic Press, New York, 1981).